TECHNISCHE UNIVERSITÄT WIEN
Vienna University of Technology

DISSERTATION

Identifying, Visualizing and Modifying Reaction Pathways of Oxygen Reduction on Sr-Doped Lanthanum Manganite (LSM) Model Electrodes

ausgeführt zum Zwecke der Erlangung des akademischen Grades eines Doktors der technischen Wissenschaften unter der Leitung von

Univ.Prof. Dipl.-Phys. Dr. rer. nat. Jürgen Fleig

E164

Institut für Chemische Technologien und Analytik,

Fachbereich Elektrochemie

eingereicht an der Technischen Universität Wien

Fakultät für Technische Chemie

Tobias Martin Huber
0426703
Rottmayrgasse 17/29

Wien 16. Dezember 2014

Abstract

Sr-doped lanthanum manganite (LSM) is the most commonly used cathode material in solid oxide fuel cells (SOFC). Nevertheless, many aspects of the oxygen reduction at LSM electrodes are not yet completely understood. Particularly important in this respect is the resistance of oxygen reduction kinetics (ORK), which often exhibits the highest loss in thin film electrolyte SOFCs. As a consequence, substantial optimization becomes possible when finding the rate limiting steps and understanding ORK of the reaction mechanisms. The aim of this thesis is to reveal, visualize, quantify and modify the reaction pathways of oxygen reduction on LSM, to identify the rate limiting steps and to find correlations between structural or chemical properties and ORK. In order to facilitate these experiments, several new measurement set-ups were designed and constructed to extend the experimental prospects, to combine existing measurement techniques, analytical methods and experimental tools.

In the present thesis, oxygen reduction kinetics of LSM on yttria stabilized zirconia (YSZ) was investigated by means of geometrically well defined, dense LSM microelectrodes and thin films on YSZ (100) single crystals. For the sake of comparison, also Pt/YSZ systems were analyzed. LSM was deposited by pulsed laser deposition (PLD), Pt by means of magnetron sputter deposition. Both types of thin films were subsequently microstructured by photolithography and chemical or ion beam etching. The electrochemical characterization of the resulting electrochemical half cells was performed by impedance spectroscopy, current-voltage measurements and ^{18}O tracer

experiments, combined with time of flight secondary ion mass spectrometry (ToF-SIMS) analysis.

Impedance measurements on differently shaped and sized macroscopic and microscopic LSM electrodes identified two parallel reaction pathways of ORK, a surface and a bulk path. By adding an oxygen blocking Pt capping layer, the LSM bulk path could partly be blocked. By varying the three phase boundary (3PB) length, the polarization resistance of the surface path was shown to scale with the 3PB length. On circular microelectrodes in the lower temperature region (< ca. 700 °C), most of the current is carried by the 3PB length related surface path, while at high temperatures (> ca. 700 °C) the bulk path is dominating.

It is shown experimentally, e.g. by thermovoltage measurements, impedance spectroscopy and infrared camera pictures, as well as by finite element modelling, that substantial temperature gradients may arise in asymmetrically heated microelectrode experiments. For a complete avoidance of the temperature inhomogeneity problem, a novel symmetrically heated vacuum-micro-contact set-up was built. This was essential for accurate impedance measurements on microelectrodes and also facilitated quantitative ^{18}O tracer exchange experiments on polarized microelectrodes in controlled atmosphere.

Tracer exchange measurements on both, polarized and non-polarized polycrystalline microelectrodes, exhibit resoluble contributions from diffusion and surface exchange kinetics of grains and grain boundaries. The two parallel and interacting diffusion pathways, via grains (D_b and k_b) and grain boundaries (D_{gb} and k_{gb}) were also successfully

4

simulated by a 3D finite element model. These investigations showed that grain boundaries may not only facilitate fast oxygen diffusion, but also fast oxygen exchange kinetics. Variation from stoichiometric LSM to A-site non-stoichiometric LSM (($La_{0.8}Sr_{0.2}$)$_{0.95}$MnO$_3$) did not lead to large changes of the kinetic parameters. Experiments were also performed on epitaxial layers without grain boundaries, where properties (D_b and k_b) are close to those of the grains in polycrystalline layers. Additionally, cathodically polarized microelectrodes showed a tremendous increase of ^{18}O concentration in the LSM films with an apparent uphill diffusion, which could be explained and simulated.

The novel measurement set-up was also used to verify a bulk path through Pt microelectrodes with an electrode polarization resistance depending on the Pt grain size in the low temperature region (<450 °C). The corresponding activation energy is 0.15 eV and the rate limiting step most probably oxygen diffusion along the Pt grain boundaries.

Kurzfassung

Sr-dotiertes Lanthan-Manganat (LSM) ist das am häufigsten verwendete Kathodenmaterial in Festoxid-Brennstoffzellen (SOFC); dennoch sind viele Aspekte der Sauerstoffreduktion an LSM-Elektroden noch nicht vollständig verstanden. Besonders wichtig sind in diesem Zusammenhang die elektrischen Verluste der Sauerstoffreduktionskinetik (SRK), die den höchsten Beitrag zum Innenwiderstand in Dünnschicht-Elektrolyt-Brennstoffzellen aufweisen. Daher birgt das Identifizieren des ratenbestimmenden Schritts und das Verstehen des Reaktionsmechanismus ein großes Optimierungspotenzial. Das Ziel dieser Arbeit ist es, die Reaktionswege der Sauerstoffreduktion an LSM zu visualisieren, zu quantifizieren und zu modifizieren. Zusätzlich sollen die ratenbestimmenden Schritte identifiziert und der Zusammenhang zwischen strukturellen und chemischen Eigenschaften der SRK geklärt werden.

Um die nötigen Experimente zur Klärung dieser Fragestellung zu ermöglich, wurden mehrere neue Messaufbauten konstruiert und gebaut. Dadurch wurde es möglich, bestehende Messmethoden zu erweitern, zu kombinieren und gemeinsam mit analytischen Methoden neuartige Experimente zu realisieren.

In der vorliegenden Arbeit wurde die Sauerstoffreduktionskinetik von LSM auf Yttrium-stabilisierten Zirkoniumoxid (YSZ) mittels geometrisch wohldefinierten, dichten LSM-Mikroelektroden und dünnen Schichten auf YSZ (100)-Einkristallen untersucht. Vergleichend wurde auch das System Pt/YSZ analysiert. LSM wurde mittels Laserabscheidung (PLD), Pt mittels Magnetron-Sputtern abgeschieden. Anschließend

wurden die Schichten mit Photolithographie mikrostrukturiert und chemisch bzw. ionenstrahlgeätzt. Die elektrochemische Charakterisierung dieser elektrochemischen Halbzellen wurde mittels Impedanzspektroskopie, Stromspannungsmessungen und mit ^{18}O-Tracer-Experimenten in Kombination mit Flugzeit-Sekundärionen-Massenspektrometrie (ToF-SIMS-Analyse) durchgeführt.

Impedanzmessungen an verschieden geformten und verschieden großen makroskopischen und mikroskopischen LSM-Elektroden identifizierten zwei parallele Reaktionswege der Sauerstoffreduktion (Oberflächenpfad und Volumenpfad). Mittels LSM-Elektroden mit sauerstoffblockierenden Pt-Deckschichten konnte der Volumenpfad teilweise blockiert werden. Durch Variation der Länge der Dreiphasengrenze (3PG) konnte gezeigt werden, dass der Polarisationswiderstand des Oberflächenpfades mit der 3PG skaliert. Auf kreisförmigen Mikroelektroden im unteren Temperaturbereich (unter ca. 700 °C) dominiert der Dreiphasenlängen-bezogene Oberflächenpfad, während bei hohen Temperaturen (über ca. 700 °C) der Volumenpfad dominiert.

Es wurde experimentell durch Thermospannungsmessungen, Impedanzspektroskopie und Infrarotkamerabilder, sowie durch Finite-Element-Modellierung gezeigt, dass erheblichen Temperaturgradienten in asymmetrisch beheizten Mikroelektrodenexperimente in der kontaktieren Mikroelektrode entstehen. Für eine vollständige Vermeidung der Temperaturinhomogenität in der Probe wurde ein neuartiger, symmetrisch geheizter Vakuum-Mikrokontaktaufbau konstruiert und gebaut. Mit diesem Versuchsaufbau ist es erstmals möglich, quantitative ^{18}O Austauschexperimente in kontrollierter Atmosphäre auf polarisierten Mikroelektroden durchzuführen.

Die Tiefenprofile dieser Mikroelektroden zeigten deutlich eine spannungsinduzierte Änderung der Oberflächenkinetik und eine tiefenabhängige Änderung der Diffusionseigenschaften. Sowohl polarisierte als auch nicht-polarisierte polykristalline Mikroelektroden zeigen Beiträge von Diffusion und Oberflächenaustausch von zwei parallelen und wechselwirkenden Diffusionswegen über Körner (D_b und k_b) und Korngrenzen (D_{GB} und k_{GB}) und wurden erfolgreich mittels eines 3D-Finite-Elemente-Modells (FEM) simuliert. Es konnte gezeigt werden, dass Korngrenzen nicht nur den Einbau des Sauerstoffs erheblich erleichtern, sondern auch, dass ihre Sauerstoffdiffusion, verglichen zu Körnern, erheblich schneller ist. A-Platz-unterstöchiometrisches LSM ($(La_{0.8}Sr_{0.2})_{0.95}MnO_3$) zeigte lediglich kleine Unterschiede in den Diffusions- und Oberflächenaustauscheigenschaften. Die kinetischen Parameter epitaktischer Schichten ohne Korngrenzen (D_b und k_b) waren fast ident mit denen der Körner aus polykristallinen Schichten. Kathodisch polarisierte Mikroelektroden zeigten eine stark erhöhte ^{18}O-Konzentration in den LSM-Filmen mit einem überraschenden Anstieg der ^{18}O Konzentration von der Oberfläche zur Mitte der Schichten. Dieses Verhalten konnte mittels FEM erklärt und simuliert werden.

Die neuen Messaufbauten wurden auch genutzt, um zu verifizieren, dass Pt-Mikroelektroden im Niedertemperaturbereich (<450 °C) durch einen Volumenpfad mit Sauerstofftransport durch Pt dominiert sind. Der Elektrodenpolarisationswiderstand skalierte mit der Pt-Korngröße der Mikroelektrode. Die entsprechende Aktivierungsenergie betrug 0,15 eV und der ratenbestimmende Schritt ist aller Wahrscheinlichkeit nach die Sauerstoffdiffusion entlang der Pt-Korngrenzen.

8

Content

1. Introduction and Status of Research

Problems associated with electrical energy production and conversion are among the main challenges of our century. One big issue is to scope with the increasing energy demand of the growing world population. To provide sustainable energy without destroying our natural resources and minimizing the further increase of global warming is another big issue. The International Energy Agency (IEA) designates one of its main objectives to promote sustainable energy policies that spur economic growth and environmental protection in a global context – particularly in terms of reducing greenhouse-gas emissions that contribute to climate change [1]. As the source of two-thirds of global greenhouse-gas emissions, the energy sector will be pivotal in determining whether or not climate change goals are achieved [2]. More than $1600 billion were invested in 2013 to provide the world's consumers with energy, a figure that has more than doubled in real terms since 2000; and a further $130 billion was spent to improve energy efficiency [1]. Maintaining the status quo leaves the world in the best case on a trajectory consisting of a long-term average temperature increase of 3.6 °C, far above the internationally agreed 2 °C target [2]. The UN's Intergovernmental Panel on Climate Change (IPCC) estimates global temperature rises by the end of the century between 1.1 °C and 6.4 °C. Already with a warming between 1 °C and 4 °C, some physical systems or ecosystems are at high risk of abrupt and drastic changes with unpredictable consequences [3]. This example shows that improvement of existing technologies and implementing new technologies is urgently needed, to

challenge our energy exposure and change our handling of available resources. One of these "new" technologies for high efficiency electrical energy conversion are ceramic fuel cells (solid oxide fuel cells, SOFCs). They convert chemical energy directly into electrical energy and exhibit the highest fuel flexibility, allowing to work directly on hydrocarbons [4]. Further benefits are high efficiency, long-term stability, low emissions and appropriate costs [5]. Furthermore, the greenhouse gas emission is much lower than that from conventional power generation technologies [6]. SOFCs work at relatively high operation temperatures (typically 700-1000 °C) [7, 8] and their theoretical efficiency is not limited by the Carnot's cycle. Commercially produced SOFCs achieved already an efficiency of 60% [5]. The high operation temperature also offers high tolerance to typical catalyst poisons, produces high-quality heat for reforming hydrocarbons or combined power heat units and offers the possibility of direct utilization of hydrocarbon fuels [6].

A sketch of the functional principle of a SOFC operated with hydrogen as fuel gas is shown in Fig. 1.1. Oxygen is reduced at the cathode on the r.h.s. according to Eq. 1.1, transported through the electrolyte to the l.h.s., where the anode is located. There, the hydrogen molecule together with the transported oxygen ion forms water (according to Eq. 1.2) and provides two electrons for the utilizable electrical current. The electrolyte between anode and cathode has to fulfill three properties: First, it has to satisfy sufficient ion and negligible electronic conductivity. Second, it has to be gas tight. And third, it has to be chemically and structurally stable [6]. These three major parts, namely the anode, the cathode and the electrolyte, have to be chemically and thermally compatible with each other.

16

$$\frac{1}{2}O_2 + 2e^- \rightleftharpoons O^{2-} \qquad\qquad 1.1$$

$$O^{2-} + H_2 \rightleftharpoons H_2O + 2e^- \qquad\qquad 1.2$$
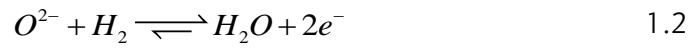
The overall reactions are chemically driven by the difference in oxygen chemical potential between the two electrodes. This leads to a voltage between cathode and anode which can be used for electrical power generation. Moreover, the SOFC increases its efficiency, compared to other fuel cells, by using the heat emitted by the exothermic electrochemical oxidation [6].
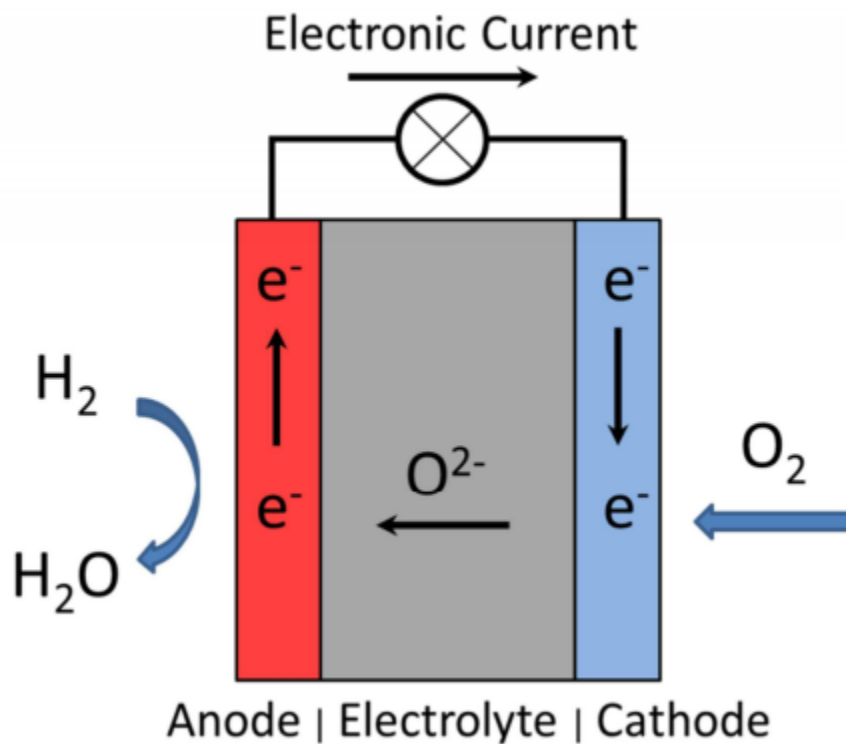
Fig. 1.1 Sketch of a solid oxide fuel cell operated with oxygen and hydrogen. (Figure from Ref. [9])

The electrolyte of state of the art SOFCs often consists of a free-standing or supported membrane of oxygen-ion-conducting yttria-stabilized zirconia (YSZ) [5, 10]. Cathodes in

such cells are fabricated from perovskite-type ceramics [5, 6]. Mostly they consist of a mixture of porous Sr-doped lanthanum manganite (LSM) with open gas pores for oxygen supply and YSZ [10]. Alternatives to LSM include Sr-doped lanthanum cobaltite and lanthanum ferrite [10]. LSM as well as this alternatives crystallize as ABO_3 in the perovskite structure, which is displayed in Fig. 1.2. The anode consists of a porous Ni/Y_2O_3-ZrO_2 (Ni/YSZ) cermet and is used for fuel gas oxidation [11].
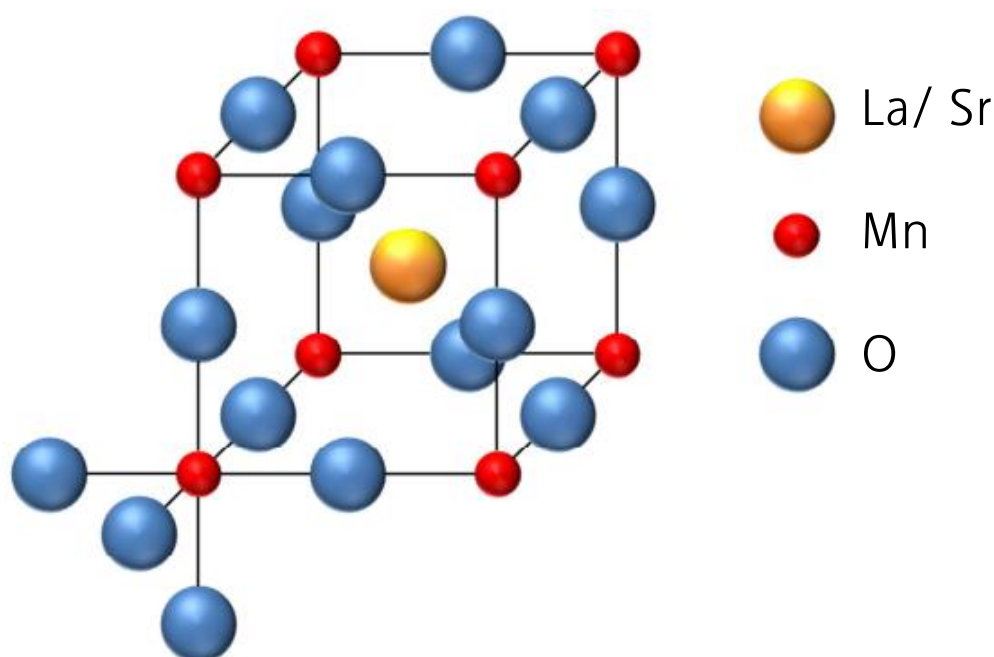
Fig. 1.2 Model of the crystal structure of LSM. The cubic perovskite structure is shown; slight lattice distortion can occur depending on stoichiometry, temperature and substrate. (Figure from Ref. [9])

LSM is not only the most used cathode material in commercially produced SOFCs [6], it is also among the most investigated ones. However, contributions of the different reaction mechanisms - and the parameters affecting their individual relevance - to the total oxygen reduction rate are still under debate. Particularly important in this respect is the electrochemical resistance of the cathodic reaction which often exhibits the

highest loss in thin film electrolyte SOFCs [12]. Therefore developing more efficient cathodes by finding better materials and improvement of existing materials implies high optimization potential.

$LaMnO_3$ is an intrinsic p-type conductor. Electronic conductivity is enhanced by substitution of the La^{3+} A-site by Sr^{2+} in the perovskite lattice. Thus an electronic hole is formed on the B-site to maintain the electroneutrality [6]. LSM thereby shows sufficient electronic hole conduction necessary for the cathode reaction, since the reduction of oxygen requires electrons, which must be provided by the cathode material [6]. Between 700 und 1000 °C $La_{0.8}Sr_{0.2}MnO_3$ has an electric conductivity of 175-300 S cm^{-1} [13], but only a very low oxygen ion bulk conductivity of 5.8·10^{-6} Scm^{-1} at 1000 °C [14]. $La_{1-x}Sr_xMnO_3$ with x=~0.1-0.2 generally provides sufficient electronic conductivity while maintaining mechanical and chemical stability with YSZ [15, 16]. One of the most important advantages is the similar thermal expansion coefficient (TEC) of LSM (between 11.2·10^{-6} K^{-1} and 12.7·10^{-6} K^{-1} [17, 18]) and the most commonly used YSZ, which exhibits a TEC of 10.3·10^{-6} K^{-1} in the temperature range from 50 to 1000 °C in air or H_2 atmosphere [7, 19].

Oxygen reduction on LSM is mostly believed to take place at the three phase boundary (3PB) were electrolyte, electrode and gas phase are in contact (Fig. 1.3a). In the corresponding so called surface path the oxygen incorporation takes place only in a very narrow active area very close to the 3PB (Fig. 1.3a).
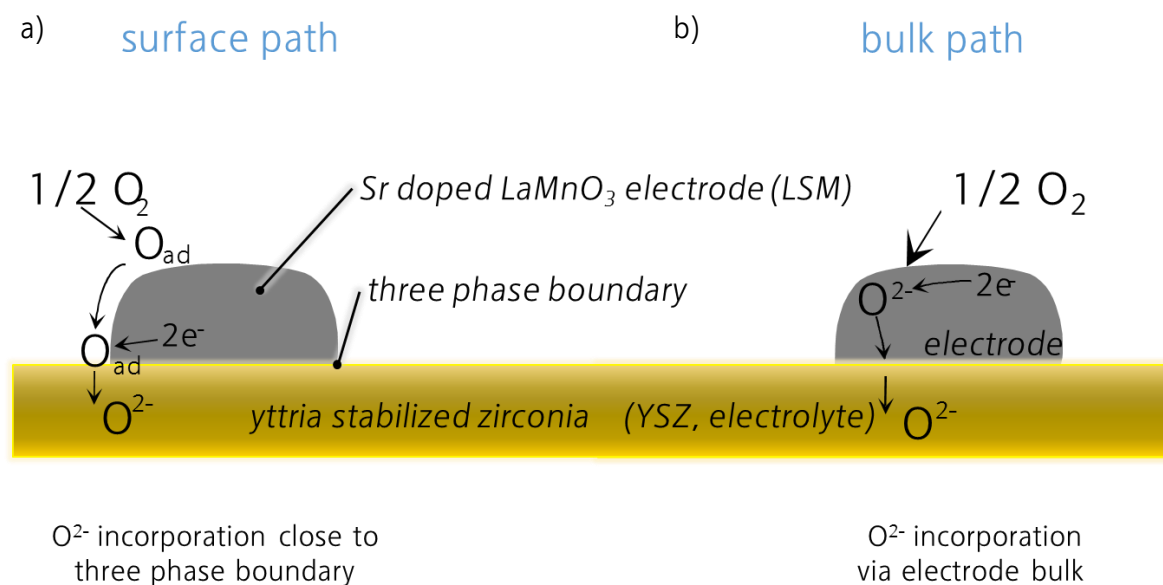
Fig. 1.3 Reaction paths of oxygen reduction on LSM electrodes at the three phase boundary (a) and via bulk path (b).

However, LSM thin film electrodes were found to be limited by ambipolar diffusion of oxygen through the bulk [20-22]. This suggested relevance of a second path, called bulk path, where the oxygen reduction and incorporation occurs at the entire LSM surface (Fig. 1.3b). The corresponding complex oxygen ion transport in a mixed conducting oxide can be described by a transmission line model derived by Jamnik and Maier [23].

LSM is a special perovskite-type oxide, since in contrast to most others it can have oxygen-excess and oxygen–deficient non-stoichiometries [6]. Mizusaki et al. described the non-stoichiometry independence of oxygen partial pressure, temperature and composition [24-26]. At moderate oxygen partial pressure $>10^{-3}$ atm LSM contains more oxygen than is consistent with the formal ABO_3 unit cell [10]. Neutron diffraction studies showed that this behavior results from cation vacancy formation on the A and B sites while the oxygen sub-lattice remains fully occupied [27]. Also the structure, shape and

microstructure of LSM electrodes influences its oxygen reduction kinetics and transport properties. De Souza et. al. reported enhanced oxygen diffusion along grain boundaries [28]. Accordingly, the electrochemical electrode performance and characteristics of LSM are subject to changes and strongly depend on the exact details of processing and operating history [10]. Also the interaction between LSM and environmental factors during sample cooling appears to be critical to mechanical properties [6]. One reason for the long-term stability of LSM is most likely the low cation vacancy concentration under SOFC operation conditions leading to a high sintering resistance [29]. In some commercially produced SOFCs metallic interconnects made of Fe-Cr containing alloys Cr poisoning effects of LSM electrodes can occur [30]. More details on properties of LSM and on its electrochemical performance and reaction mechanisms can be found in chapter 2.

Adler summarizes four relevant highlights of LSM [10]: 1. Surface path at low over-potential. 2. Bulk path at moderate to high overpotential. 3. Pronounced non-stationary behavior. 4. Extreme sensitivity to processing and operation history. Adler further states: "Many points remain unclear and further work of impedance and other quantitative measurements would undoubtedly help clarify the questions dealing with oxygen reduction on LSM." In another paper dealing with the defect chemistry of LSM [31] Finn Willi Poulson states: "Since the defect chemistry and conduction mechanism in LSM are still controversial issues, several questions are left open for the scientists of the next millennium to crack." This open questions triggered many studies presented in this thesis. The main goal of the thesis can thus be summarized as the identification of the rate limiting steps of oxygen reduction on LSM thin films and their determining factors.

The experiments on LSM and their (partly numerical) analysis also advance the understanding of oxygen exchange kinetics in solid state materials in general. The corresponding results are presented in chapter 2, 4 and 5.

Moreover, platinum microelectrodes on YSZ were investigated (chapter 6). This system is highly interesting as reference system for fundamental investigations of solid state reactions in SOFCS. It is also highly technological relevant for applications, for example in micro-SOFCs and oxygen gas sensors also called lambda sensors.

The investigation methods used in this thesis include:

- Electrochemical impedance spectroscopy

- DC measurements

- Oxygen ^{18}O tracer gas exchange experiments

- Numerical finite element simulations

Several studies required development of novel measurement set-ups and new equipment extending the measurement range and experimental possibilities. Among others, this required a detailed analysis of shortcomings caused by temperature gradients in microelectrode experiments. Those are summarized in chapter 3. Developing new measurement equipment was therefore also an important part of this thesis and details are given in chapter 3 and 7.

2. Identifying and Modifying Oxygen Reduction Pathways of La$_{0.8}$Sr$_{0.2}$MnO$_3$ (LSM) Thin Film Model Electrodes

This chapter consists to a large extend of a scientific paper published in "Journal of the Electrochemical Society" [32]. Some parts (section 2.5) have been published in "Journal of Materials Research" [33].

2.1   Abstract

Sr-doped lanthanum manganite (LSM) is a widely used cathode material in solid oxide fuel cells (SOFC). Despite being a poor ion conductor, LSM electrodes can reduce oxygen via two pathways: a surface path which includes surface diffusion of oxygen species and oxide ion incorporation at the three phase boundary (3PB), and a bulk path based on oxygen bulk diffusion. In this chapter, the kinetics of both paths and their dependence on temperature and electrode geometry is investigated by impedance spectroscopy on micro-patterned LSM thin film electrodes. Differently shaped and sized macroscopic and microscopic LSM electrodes as well as LSM electrodes with oxygen blocking Pt capping layers are employed to identify two parallel reaction pathways of oxygen reduction. On circular microelectrodes in the lower temperature region (below ca. 700 °C) the 3PB length related surface path carries most of the current, while at high temperatures (above ca. 700 °C) the bulk path is dominating. The significance of each reduction path also depends on the microstructure of the columnar LSM films which can be changed by varying pulsed laser deposition (PLD) parameters or by post-annealing.

Moreover, relevance of a pseudo-3PB path across edges of the LSM electrodes is discussed.

2.2   Introduction

Solid oxide fuel cells (SOFCs) are promising devices for environmentally friendly energy conversion systems [34, 35]. They are not limited to the Carnot efficiency of heat engines and emit less greenhouse gases than conventional power generators. To further improve the efficiency of SOFCs the polarization resistances of cathode, electrolyte and anode have to be reduced. Particularly important in this respect is the resistance of the cathode [12]. Sr-doped lanthanum manganite (LSM) is still the most commonly used material in SOFC cathodes and thus is also among the best investigated ones [10, 28, 32, 36-57]. Oxygen reduction at an oxide cathode mainly proceeds via two pathways. Either oxide ions are incorporated into the electrolyte close to the three phase boundary (3PB) (surface path including surface diffusion), or ions enter the cathode material and are transported through the cathode to the electrode/electrolyte interface (bulk path) [6, 10, 33, 58-62]. Owing to its good electronic and poor ionic conductivity under high oxygen partial pressure, LSM is often assumed to be restricted to the surface path when employed in porous and composite LSM/YSZ electrodes [10]. However, cathodic bias enhances ion conduction in LSM, due to the reduced chemical potential of oxygen, and may lead to an increased contribution of the bulk path to the oxygen reduction kinetics. Improved performance of a bulk path under cathodic bias was demonstrated [62] and simulated [63] for porous LSM electrodes. Moreover, tracer studies on LSM bulk material showed fast ionic grain boundary conduction in LSM [28,

64]. Hence, significance of a bulk path in LSM and the parameters affecting the importance of each path are still under debate [10].

The relevance of the bulk path should strongly increase in investigations on thin film electrodes [22, 40, 42, 43, 65-69] due to the very different ratios of surface area to 3PB length compared to porous electrodes. Such thin film electrodes can be prepared by pulsed laser deposition, and micro-patterning leads to electrodes with defined and still significant 3PB length. Several studies report oxygen transport via a bulk path in LSM thin films [20, 21] and the variation of LSM microelectrode area and thickness indicated a dominating bulk path at temperatures of ca. 800 °C [40, 66]. A separation of the bulk path polarization resistance into surface and transport related resistances was shown in Refs. [44, 65] for low oxygen partial pressures. Measurements in a broader temperature range gave indication that the surface path may also be relevant for microelectrodes [40, 43, 66]. Patterned LSM thin film electrodes showed a dominating surface path with a 3PB related rate limiting step at lower temperatures, and appearance of an oxygen bulk transport contribution around 800°C [42]. Oxygen incorporation at the 3PB was also concluded from voltage driven [18]O reduction on micro-patterned LSM electrodes [33, 68, 69]. Obviously, both reaction paths may be relevant for LSM thin film electrodes and additional information on the parameters affecting the relevance of the two reaction pathways is therefore needed for a clear picture of oxygen reduction kinetics on LSM.

This chapter presents the results of investigations to identify the relevant paths and to analyze their dependence on several parameters such as temperature and electrode geometry (3PB length and electrode surface area). Highly reliable and reproducible data

were obtained by using a symmetrically heated microelectrode measurement set-up referred to as "MiMa" (**Mi**croelectrode measured in a tube furnace normally used for **Ma**croscopic samples) [70]. Surface and bulk path of oxygen reduction on LSM microelectrodes could thus be successfully identified, separated and modified.

2.3   Experimental

2.3.1 Sample Preparation

$(La_{0.8}Sr_{0.2})MnO_3$ powder (Sigma Aldrich, USA) was isostatically pressed, sintered for 12 h at 1200 °C in air and used as target for the PLD process. Films were deposited on polished YSZ (1 0 0) single crystals (9.5 mol% Y_2O_3, CrysTec GmbH, Germany) using a KrF excimer laser (248 nm, COMPex Pro 201 F, Lambda Physics, Germany). Laser beam energy was set to 400 mJ per pulse at 10 Hz pulse frequency. The deposition was performed in $4 \cdot 10^{-2}$ mbar O_2 atmosphere at substrate temperatures of 600 °C, 700 °C and 850 °C. The temperature at the YSZ surface was monitored by a pyrometer (Heitronics KT-19.99, Germany). The film thickness (between 100 nm and 240 nm) was controlled via deposition time and measured by scanning electron microscopy (SEM, FEI Quanta 200 FEG, Netherlands) and digital holographic microscopy (DHM, Lyncee Tec, Switzerland). Gas tightness of the films was investigated by ^{18}O tracer exchange and subsequent time-of-flight secondary ion mass spectrometry (ToF-SIMS 5, ION-TOF GmbH, Germany). Microstructure and film growth was investigated by SEM and transmission electron microscopy (TEM, FEI TECNAI F20). All LSM films showed a

columnar film growth with varying grain diameters, dependent on the substrate temperature in the PLD [71].

Platinum capping layers (thickens about 400 nm) were deposited on top of some LSM films via DC magnetron sputtering (MED 020 Coating System, BAL-TEC, Germany) of Pt (99.95 % pure, OGUSSA, Austria) at room temperature. Film thickness was determined by ex-situ calibration using a quartz crystal micro-balance and checked by SEM measurements. Micro-patterning of the LSM films and LSM/Pt bilayers was performed by photolithography and subsequent chemical etching in 30% concentrated hydrochloric acid or ion beam etching with 2 keV Ar+ ions. The following samples with different shapes of LSM and/or LSM/Pt electrodes were thus prepared (Fig. 2.1):

- (a) Circular shaped LSM and LSM/Pt microelectrodes from $\varnothing$=90 µm to $\varnothing$=300 µm, deposited on one side polished $10 \cdot 10 \cdot 0.5$ mm^3 YSZ single crystals with pasted porous Pt counter electrodes.

- (b) Finger-type LSM and LSM/Pt microelectrodes of nominally identical surface area (0.0675 mm^2) and different 3PB length (from 1.2 mm to 7.2 mm), deposited on one side polished $10 \cdot 10 \cdot 0.5$ mm^3 YSZ single crystals with pasted porous Pt counter electrodes.

- (c) Macroscopic LSM/Pt electrodes with grid-type pattern, deposited on both sides of double side polished $5 \cdot 5 \cdot 0.5$ mm^3 YSZ single crystals. Either both LSM and Pt are etched away between the mesh (A), or only Pt was microstructures and a dense LSM layer remained on top of YSZ (B).
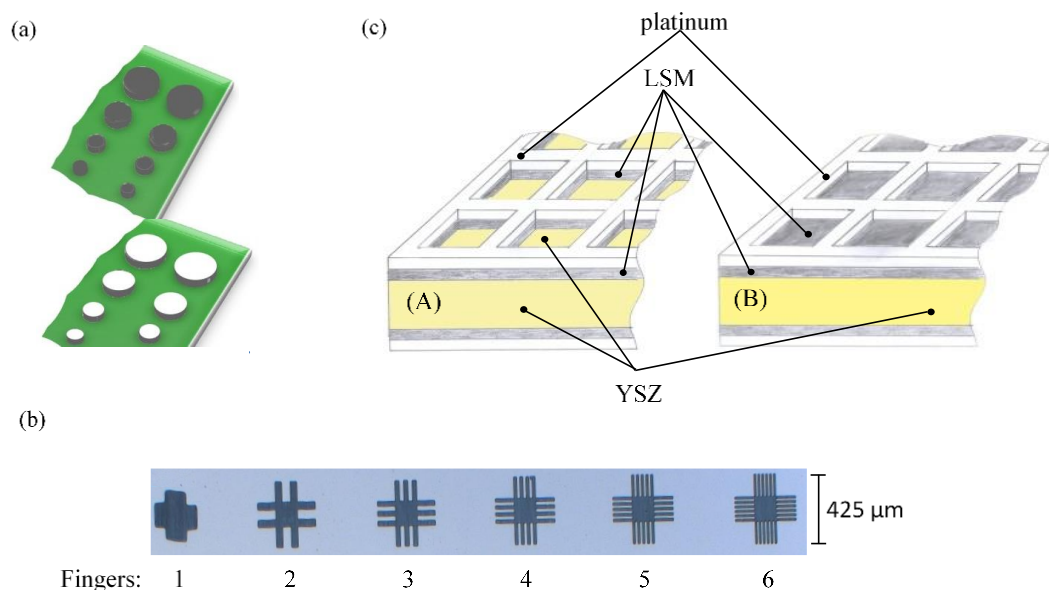
Fig. 2.1 Electrode shapes used in this chapter: (a) sketch of circular LSM microelectrodes with and without Pt capping layer, (b) micro photograph of finger-type LSM and LSM/Pt electrodes, (c) sketch of macroscopic LSM/Pt electrodes with free YSZ layer in between the grid (A) or with LSM remaining on YSZ (B).

2.3.2 Impedance Spectroscopy

Electrochemical characterization of the Pt, LSM and LSM/Pt microelectrodes was done by means of two point impedance measurements using an Alpha-A High Resolution Dielectric Analyzer (Novocontrol, Germany). Impedance spectra were recorded at temperatures from 280 °C to 950 °C in the frequency range between 10^6 and 10^{-3} Hz (if required) with a resolution of 5 points per frequency decade. An equivalent circuit of the bulk path in a mixed conducting electrode with surface resistance, based on a transmission line for bulk transport and interfacial impedance elements, is given in Ref. [23]. However, according to Ref. [44], this model yields meaningful fit parameters

for LSM thin film electrodes only for low and medium oxygen partial pressures due to similar relaxation frequencies of bulk and surface processes. Owing to the fact that all measurements were performed in air (i.e. at high O_2 pressure), an alternative simplified equivalent circuit, shown in Fig. 2.2, was therefore used to quantify the impedance data in this chapter. It was not only used for measurements with predominant bulk path but also for surface path data. The authors are aware that for both pathways the circuit it is not backed by a clear mechanistic model. However, it offers a robust model and leads to accurate fits of the shoulder mostly occurring in the medium frequency part of the spectra.
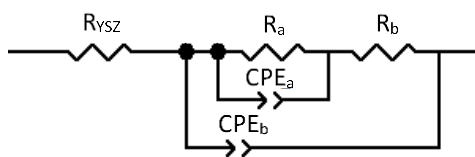
Fig. 2.2 Equivalent circuit used for the complex nonlinear least square fits; CPE=constant phase element.

A bulk path with negligible transport resistance would indeed be reflected by this circuit [72], but this situation is not expected for LSM. The reason for still using the nested circuit instead of two serial RC-elements is the following: For a bulk path with a resistive bulk contribution, also two serial RC-elements are mechanistically incorrect and for a surface path the LSM/YSZ interfacial capacitance is indeed parallel to all resistive contributions as indicated by CPE_b in Fig. 2.2. Hence, by using the given circuit we can fit data at all temperatures and sample geometries without caring about the exact mechanism and for a predominant surface path CPE_b should have a simple meaning (interfacial capacitance). In most Arrhenius plots and comparisons, only the total

polarization resistance ($R_{tot}=R_a+R_b$) is therefore considered. Parameterization of the spectra was carried out by the complex nonlinear least square (CNLS) fit software Z-View2 (Scribner, USA).

Constant phase elements (CPE) rather than ideal capacitances were used with the complex impedance of a constant phase element Z_{CPE} being given by

$$Z_{CPE} = \frac{1}{(i \cdot \omega)^{p_{CPE}} Q_{CPE}} \; .$$
2.1

Therein ω denotes the angular frequency of the AC signal, and p_{CPE} and Q_{CPE} are fitting parameters. If n equals one, the constant phase element represents an ideal capacitor with Q_{CPE} being its capacitance C. For n<1 a capacitance value can be estimated from Q_{CPE} with its parallel resistance R using the equation [73]

$$C = (R^{1-p_{CPE}} \cdot Q_{CPE})^{\frac{1}{n}} \; .$$
2.2

2.3.3 Measurement Set-ups

Two different micro-contact set-ups were used for the experiments. An asymmetrically heated measurement set-up see Fig. 2.3a. It was used for quick measurements since it allows fast heating and a change of the contacted electrode within seconds. It can thereby provide reasonable statistical information over a large number of different microelectrodes on one and the same sample within relatively short times. It also allows monitoring optical changes of the contacted microelectrode in real time during the

measurement. The second measurement set-up is the symmetrically heated chamber sketched in Fig. 2.3b, called MiMa.
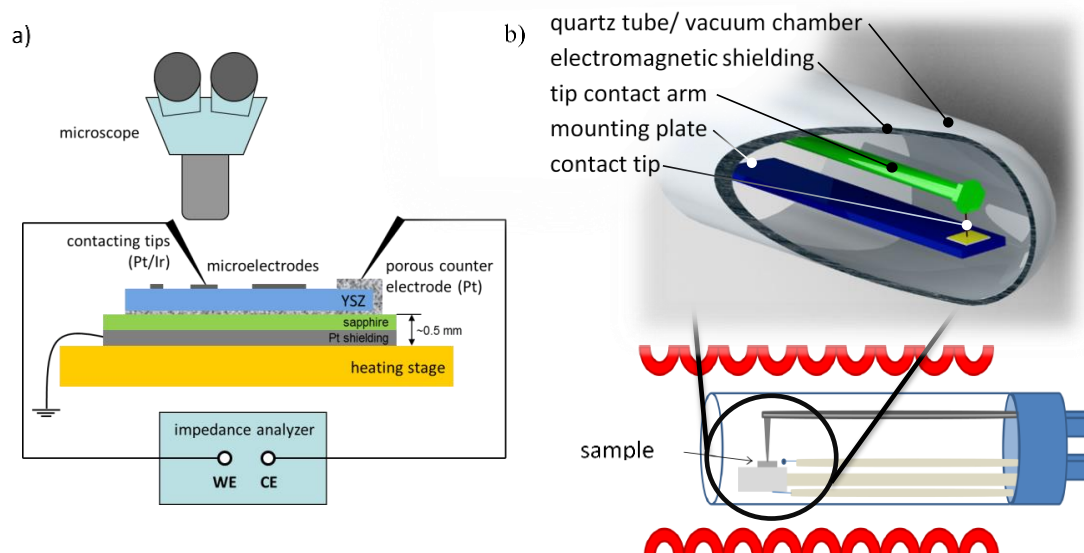
Fig. 2.3 (a) Conventional asymmetrically heated micro-contact set-up, (b) symmetrically heated measurement set-up (MiMa).

It is characterized by a homogeneous, precisely measureable temperature with negligible temperature gradients in the contacted sample. This set-up enables continuous measurements on one and the same microelectrode from room temperature up to 1000 °C without losing contact. Minimizing the temperature gradient also minimizes the thermo-voltages, which prevents unintended polarization and thus undefined measurement conditions [58, 70]. Since during the measurement all contacting parts of the symmetrically heated set-up are inside the tube furnace, the contacting procedure has to be done outside the hot zone at room temperature. This contacting is performed with a micromanipulator and is monitored by a USB

microscope [70]. Then the sample with the contacted electrode is moved into the hot zone of the tube furnace. Detailed information and discussion of the two micro-contact set-ups can be found in Ref. [70].

2.4   Results and Discussion

2.4.1 LSM Microelectrodes

Circular shaped 240 nm thick LSM microelectrodes ($\varnothing$=90 μm and $\varnothing$=190 μm, deposited at 600 °C) were electrochemically characterized in air from 450 °C to 950 °C in the symmetrically heated micro-contact set-up MiMa (Fig. 2.3b). The measured impedance spectra are depicted in Fig. 2.4 and in the Nyquist they plot consist of a large semicircle in the low frequency range, a shoulder in the medium frequency range and a high frequency intercept. For low temperatures (ca. 500 °C) the high frequency intercept becomes a separate arc, it can be assigned to the spreading resistance of ion conduction in YSZ [74, 75]. In all temperature regimes, the electrode part of the spectra can be fitted to the circuit given in Fig. 2.2. In the lower temperature regime the two semicircles strongly overlap and form one distorted arc in the Nyquist plot (Fig. 2.4a). For high temperatures, the two "semicircles" are more separated (Fig. 2.4b). The different separation of arcs at high and low temperatures is a first hint of two different mechanisms of oxygen reduction on LSM.
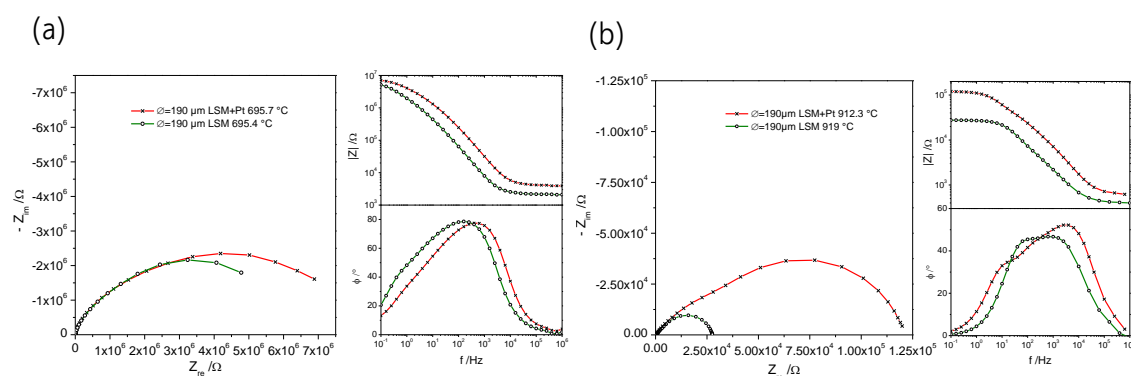
Fig. 2.4 (a) Impedance spectra of an Ø=190 µm LSM microelectrode at 695.4 °C (green line with circles) and a LSM microelectrode with platinum capping layer at 695.7 °C (red line with crosses); (b) Impedance spectra of measurements on the same microelectrodes at 919.0 °C (LSM, green circles) and 912.3 °C (LSM/Pt, red crosses), LSM thickness 240 nm; l.h.s.: Nyquist plot, r.h.s: Bode plot.

The temperature dependence of the total polarization resistance ($R_{tot}= R_a+R_b$) of an Ø=190 µm circular LSM electrode is shown in Fig. 2.5. It clearly exhibits a higher activation energy at higher temperatures. Such a bending in an Arrhenius plot can only be caused by two parallel reaction pathways and a change of the dominant path with temperature, see Fig. 2.6c [58, 76, 77]. Two differently activated serial processes in a single path cannot cause such a curve (see Fig. 2.6b). Accordingly, the changing slope is another strong hint for a mechanistic change –namely a path change – with varying temperature. For LSM the situation is further complicated since both parallel pathways seem to contain two serial processes as indicated by the two arcs in the impedance spectra and already proven for the bulk path in Ref [44]. In the following analysis of the Arrhenius plots we still approximate each path by one admittance element (Y_1 and Y_2).
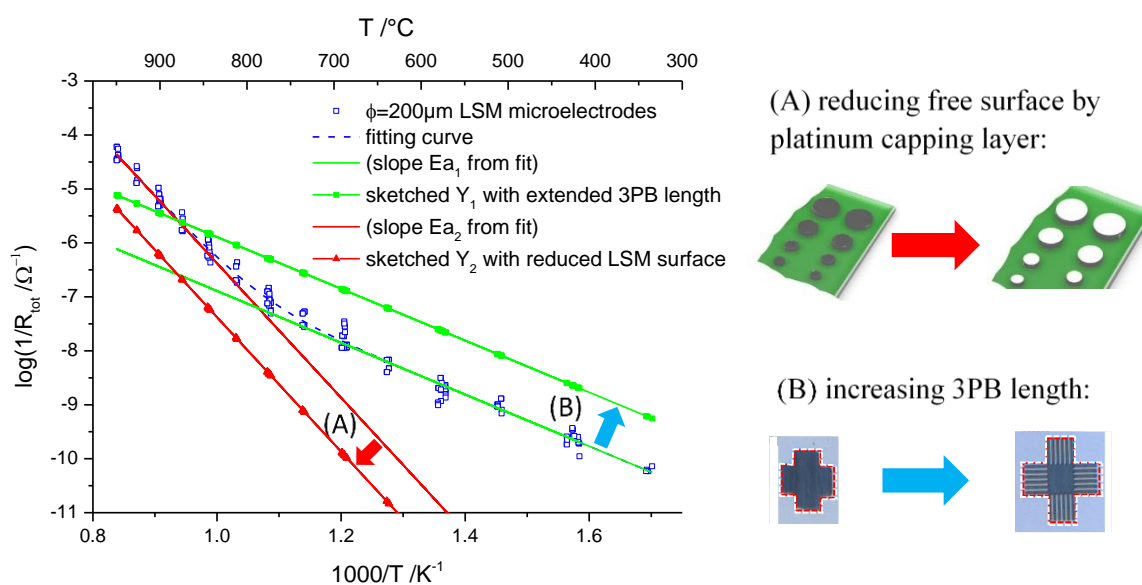
Fig. 2.5 Arrhenius plot of R_{tot} ∅=190 µm LSM electrode (240 nm thick) and related fit curve (Eq. 2.3) given with green squares and green lines, respectively. The straight solid lines correspond to Y_1 or Y_2, solely. By reducing the free LMS surface, e.g. by a platinum capping layer, the high temperature part of the curve is expected to shift to higher resistance values indicated by dashed red line (A). By increasing the 3PB length the low temperature part of the curve is expected to shift to lower resistance values indicated by dashed blue line (B).
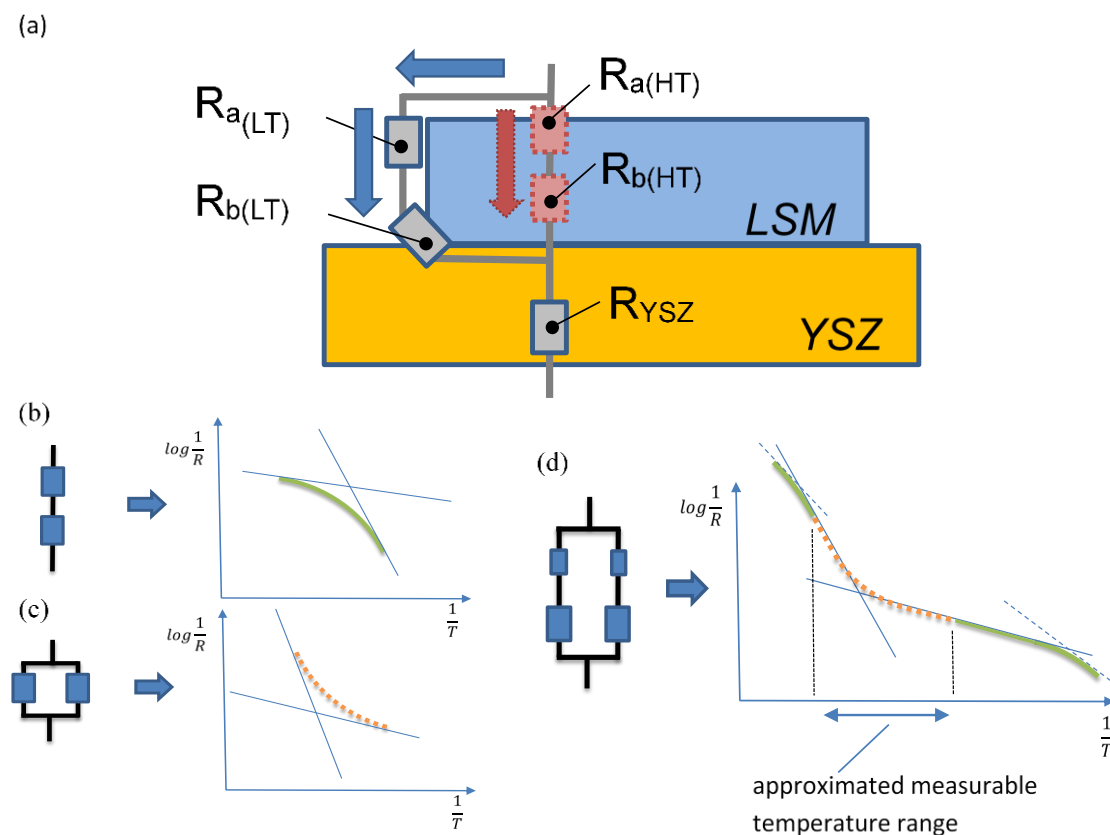
Fig. 2.6 (a) Sketch of two parallel reaction pathways for circular shaped LSM microelectrodes for high (HT) and low (LT) temperature. Each path consists of two serial electrode processes, R_a and R_b and the same R_{YSZ}. Owing to the insufficient fit model R_a and R_b of the circuit in Fig. 2.2 do not necessarily coincide with the resistance location indicated here. (b) Two serial processes with different activation energies and the resulting Arrhenius plot. (c) Two parallel processes with different activation energies and the resulting Arrhenius plot. (d) Two parallel paths, each with two serial processes and the resulting Arrhenius plot if all four activation energies are sufficiently different. In a certain temperature range only two activation energies are visible.

Precisely, Y_1^{-1} and Y_2^{-1} represent the sum of $R_{a(HT)}$ plus $R_{b(HT)}$ and $R_{a(LT)}$ plus $R_{b(LT)}$, respectively with HT and LT indicating the predominant path at high and low temperature, cf. Fig. 2.6a. However, for our circular shaped microelectrodes, one resistance is approximately one order of magnitude smaller than the other one in both

temperature regimes i.e. from 500 °C - 950 °C in ambient air. Owing to this dominance of one resistor in each path a single activation energy should approximately describe the admittance of each path, at least in the parameter range under investigation, (see also sketch in Fig. 2.6d). Hence, the following equation is used to quantify the Arrhenius plots:

$$\log(Y) = \log\left(\frac{1}{R_{tot}}\right) = \log\left(Y_1^0 \cdot e^{\frac{-Ea_1}{k_B T}} + Y_2^0 \cdot e^{\frac{-Ea_2}{k_B T}}\right). \qquad 2.3$$

Therein the pre-exponential factors Y_1^0 and Y_2^0 as well as the activation energies Ea_1 and Ea_2 are fitting parameters; k_B an T denote Boltzmann's constant and temperature, respectively. The total fitting curve and both slopes representing the activation energies Ea_1 and Ea_2, are shown in Fig. 2.5. For circular LSM microelectrodes (Ø=190 μm) deposited at 600 °C, the activation energies are 2.47 eV ± 0.06 eV and 0.95 eV ± 0.02 eV in the high and low temperature regime, respectively. For microelectrodes of Ø=90 μm, the measured activation energy values are almost identical to microelectrodes of Ø=190 μm. For the sake of completeness one may mention that both paths lead to the same R_{YSZ} and any local current constriction in YSZ close to the 3PB is included in $R_{a(LT)}+R_{b(LT)}$ [78].

This interpretation in terms of high temperature bulk path and low temperature surface path is in line with results in Refs. [42-44, 66]. For other electrode geometries the influence of different reaction pathways is expected to change. For example, finger electrodes (Fig. 2.1b) with constant surface area but varying 3PB length should reduce the polarization resistance in the low temperature region by increasing the 3PB length.

This is sketched in (Fig. 2.5(B)). A covering layer on top of the LSM microelectrodes reduce the free LSM surface and should thereby increase the polarization resistance in the high temperature (bulk path) region (Fig. 2.5(A)). Both cases are experimentally verified in the next sections.

2.4.2 Effect of a Platinum Capping Layer on LSM Microelectrodes

LSM microelectrodes with and without platinum capping layer (LSM deposited at 600 °C) were measured at temperatures between 600 °C and 920 °C in air in the symmetrically heated MiMa set-up. At low temperatures (LT, below 700 °C), impedance spectra of capped and uncapped LSM electrodes exhibit a very similar shape with two strongly overlapping semicircles (Fig. 2.4a). Also the total polarization resistance is very similar for both types of electrodes. At high temperatures (HT, above 700 °C), both types of electrodes similarly show two more separated semicircles in the impedance spectra (Fig. 2.4b), but the total polarization resistance of the platinum capped LSM/Pt microelectrode is significantly increased. Above 900 °C capped electrodes show a more than five times higher total polarization resistance.

The Arrhenius plot in Fig. 2.7 summarizes results of five LSM and three LSM/Pt microelectrodes. The trend caused by the capping layer is the following: Similar polarization resistances was observed at low temperatures and higher resistances of capped LSM/Pt microelectrodes at higher temperatures. The averaged activation energy in the high temperature regime is 2.47 ± 0.06 eV for LSM microelectrodes and 2.0 ± 0.05 eV for LSM/Pt. In the low temperature regime 0.95 ± 0.02 eV are found for

LSM and 0.89 ± 0.02 eV for the LSM/Pt microelectrodes. The large data scattering at low temperatures might be caused by some degradation of 3PB regions during the long measurement time (≈1 week for each electrode), at high temperatures the measured values are very reproducible.

The 3PB region and the 3PB length are not affected by the Pt capping layer while the bulk path becomes strongly blocked. On LSM/Pt electrodes only the sides, illustrated in Fig. 2.8 b/c, can incorporate oxide ions, while an LSM microelectrodes the entire surface is open and thus exhibit an area which is ca. 100 times larger. Hence, similarity of the polarization resistance at low temperatures is a strong indication for a predominant surface path (unaffected by the Pt capping layer). Also the polarization resistance increase of the capped electrode at high temperature is in qualitative agreement with the prediction sketched in Fig. 2.5(A). However, in case of LSM/Pt the situation is somewhat more complicated, since the polarization resistance is much lower than that of a surface path extrapolated to higher temperatures and also not 100 times higher than for LSM without Pt, despite nominally 100 times less LSM surface area. Moreover, the activation energy of 2.0 eV is much higher than that of the supposed surface path (~0.9 eV) but still lower than the 2.47 eV measured for the bulk path in LSM electrodes without Pt.
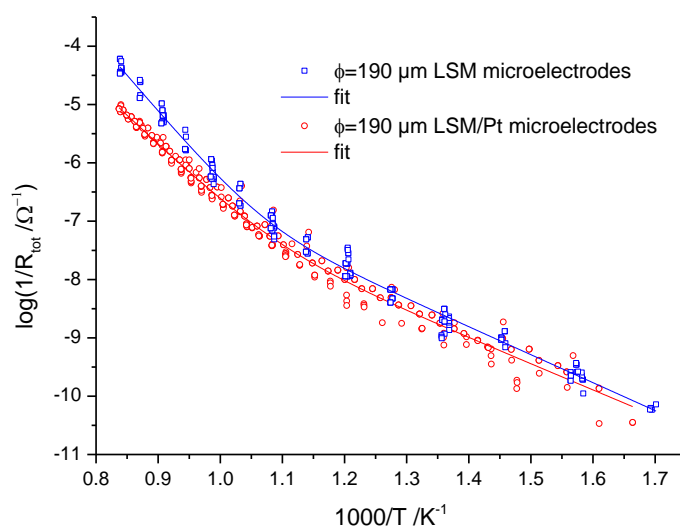
Fig. 2.7 Arrhenius plot of 5 LSM microelectrodes and 3 LSM/Pt microelectrodes with platinum capping layer Ø =190 μm, 240 nm LSM thickness.

We cannot completely exclude some catalytic effect of Pt on LSM at high temperatures, but control experiments with porous Pt capping layers showed practically the same polarization resistance at higher temperatures as with dense Pt capping layers. We therefore conclude that for LSM/Pt there is most probably also a transition to a bulk path at higher temperatures. This edge related bulk path, however, has different properties and a different activation energy, simply because current lines in LSM are very different compared to the standard bulk path of LSM electrodes. Short bulk diffusion distances across/at the edge are possible, see Fig. 2.8b/c.

This edge related bulk path – which scales with the 3PB length [79] and thus is a kind of pseudo-3PB path can significantly contribute to oxygen reduction of LSM electrodes. The relevance of such bulk path edge effects was quantified in Ref [79] for electrodes with sides perpendicular to the YSZ surface, see Fig. 2.8b. In the case of ion beam

etched LSM/Pt electrodes, the contribution of such a pseudo-3PB path is even more pronounced, since a thinner LSM rim is formed during preparation (Fig. 2.8c, d, e). Despite blocking the main part of the surface by a Pt layer, the edge remains bulk path active and becomes relevant at higher temperatures. Here, diffusion lengths in the LSM are rather short and the relative importance of surface resistance and transport resistance ($R_{a(HT)}$, $R_{b(HT)}$ in Fig. 2.6) are very different compared to the main part of the LSM electrode. This can change the rate limiting resistance in the bulk path. Possibly the surface reaction dominates the bulk path "across the edges", while ion transport is most resistive for the large area of uncapped LSM electrodes. This could explain the activation energy difference between LSM/Pt and LSM at high temperatures see sketch in Fig. 2.8a. Please note that $R_{a(HT)}$ and $R_{b(HT)}$ in Fig. 2.6 may not really correspond to R_a and R_b of the mechanistically insufficient fit model in Fig. 2.2; rather they are a good approximation of the physically more complicated situation.
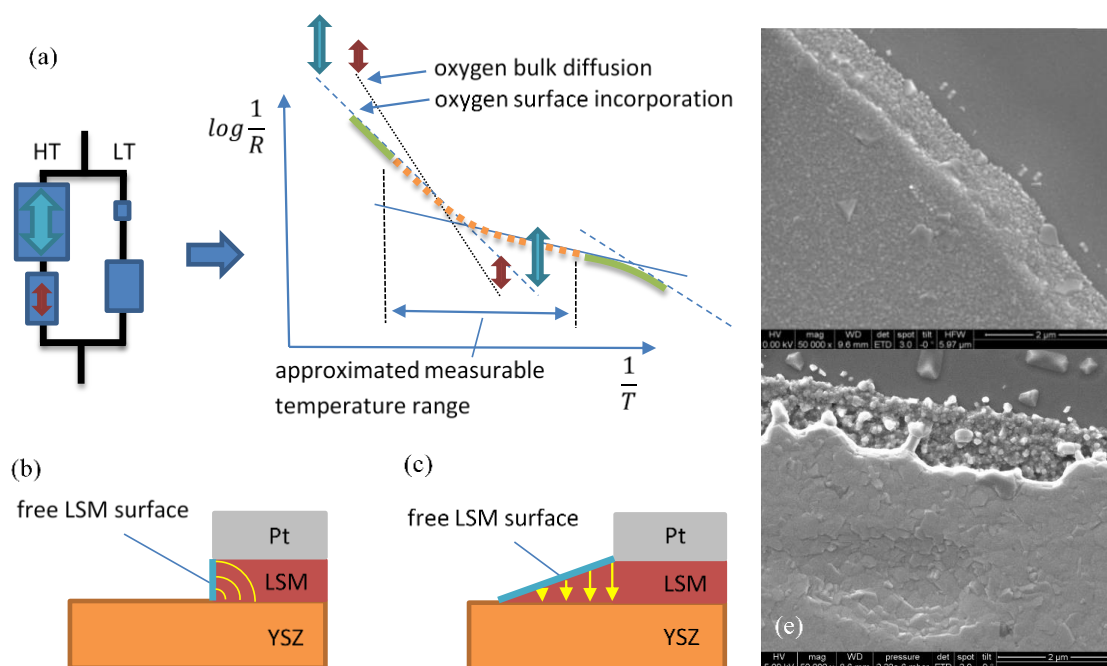
Fig. 2.8 (a) Sketch of Pt capped microelectrode with two parallel reaction pathways for high (HT) and low (LT) temperature with different ratios of the two high temperature resistors, compared to Fig. 2.6. Arrows in the corresponding Arrhenius plot indicate the relative resistive increase caused by the added Pt capping layer compared to uncapped LSM electrodes. (b) Sketch of a cross-section from the 3PB region of an idealized LSM layer with Pt capping layer. (c) Sketch of the cross-section of a real LSM layer with platinum capping layer. Owing to preparation reasons a wedge-shaped LSM rim on top of the YSZ single crystal remains. (d) SEM picture of the 3PB region of an LSM electrode prepared by ion beam etching. (e) SEM picture of the 3PB region of an LSM electrode with Pt capping layer, prepared by ion beam etching.

2.4.3 Effect of Varying Three Phase Boundary Length

LSM finger-type electrodes (see Fig. 2.1b prepared at 700 °C) were measured in the symmetrically heated MiMa set-up in air from 450 °C to 950 °C. All six electrodes have the same surface area of 0.0675 mm^2, while the 3PB length varies from 1.2 mm (one finger per side) to 7.2 mm (six fingers per side). In Fig. 2.9 Arrhenius plots of the

polarization resistance are compared for electrodes with one and six fingers per side (a). Particularly at lower temperatures strongly different values are found. However, when scaling the polarization resistance to the 3PB length the normalized resistances fall together in the lower temperature region (Fig. 2.9b). This strongly supports the conclusion above that at lower temperatures the surface path is active, cf. sketched Y_2 in Fig. 2.5(B).

Above ca. 730 °C the normalized polarization resistances in Fig. 2.9b become different and at 940 °C the total (absolute) polarization resistances of the two electrodes in Fig. 2.9a exhibit rather similar values. Since the two electrodes have the same free surface, this again suggests a predominant bulk path at higher temperatures. The slight difference even for the highest temperature is most probably due to a still remaining surface path contribution for electrodes with 6 fingers per side. The activation energies Ea_i and Y_i^0 parameters obtained from double logarithmic fitting according to Eq. 2.3 are displayed in Tab. 2.1 for 6 and 1 finger electrodes, both for 120 and 240 nm thin LSM films. Activation energies at lower temperatures (ca. 1.3-1.6 eV) are in accordance with the values found in section 3.1. The high temperature Ea values are much higher, namely of the order of 3 eV (except for the 2.4 eV found for 6 fingers, 120 nm see also below).
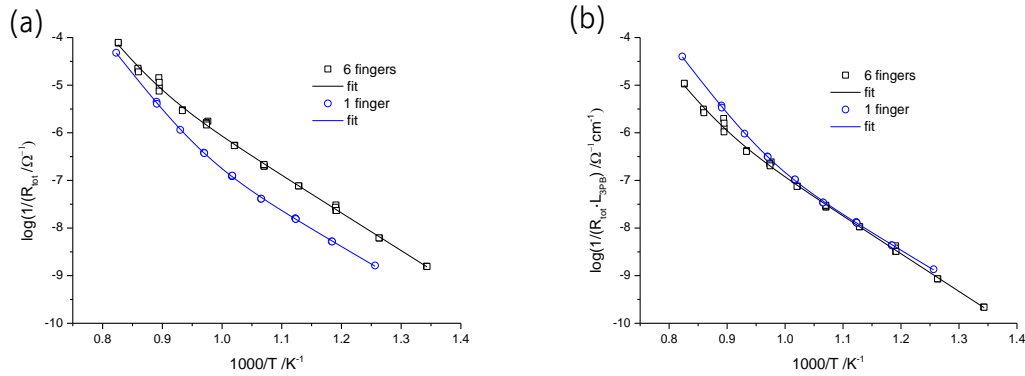
Fig. 2.9 (a) Arrhenius plot of the total polarization resistance of 240 nm thick LSM microelectrodes with 1 and 6 fingers, the electrode shape is shown in Fig. 2.1b). b) Arrhenius plot normalized to the 3PB length (L_{3PB}).

	6 fingers 240 nm	1 finger 240 nm	6 fingers 120 nm	1 finger 120 nm
Y_1^0	$4.59 \cdot 10^9 \ \Omega^{-1}$	$1.04 \cdot 10^9 \ \Omega^{-1}$	$3.24 \cdot 10^5 \ \Omega^{-1}$	$1.04 \cdot 10^7 \ \Omega^{-1}$
Ea_1	3.35 eV	3.22 eV	2.38 eV	2.83 eV
Y_2^0	$7.31 \cdot 10^1 \ \Omega^{-1}$	$2.36 \cdot 10^0 \ \Omega^{-1}$	$7.49 \cdot 10^{-1} \ \Omega^{-1}$	$5.17 \cdot 10^{-1} \ \Omega^{-1}$
Ea_2	1.58 eV	1.45 eV	1.25 eV	1.35 eV

Tab. 2.1 Fit values of Eq. 2.3 for 120 nm and 240 nm thick electrodes with 1 and 6 fingers on each side. Fit curves are shown in Fig. 2.10.

A more detailed comparison of measurements on LSM finger microelectrodes with two different film thicknesses reveals a further effect (Fig. 2.10). All curves of 3PB normalized resistances coincide at low temperatures and – as above mentioned - support our interpretation in terms of a predominant surface path. At high temperatures different resistances are found for identical finger numbers but different thicknesses: In both cases, i.e. for 1 and for 6 fingers, the thinner microelectrodes exhibit higher resistances. This seems to contradict a bulk path interpretation since either both thicknesses should

lead to the same resistance (rate limiting surface kinetics) or the thicker film should have a higher resistance (transport limitation). Moreover, the fit value Ea_1 (high temperature) of the 120 nm thin electrodes, with six fingers, is much lower (2.38 eV) compared to the 240 nm thick electrodes (>3 eV).
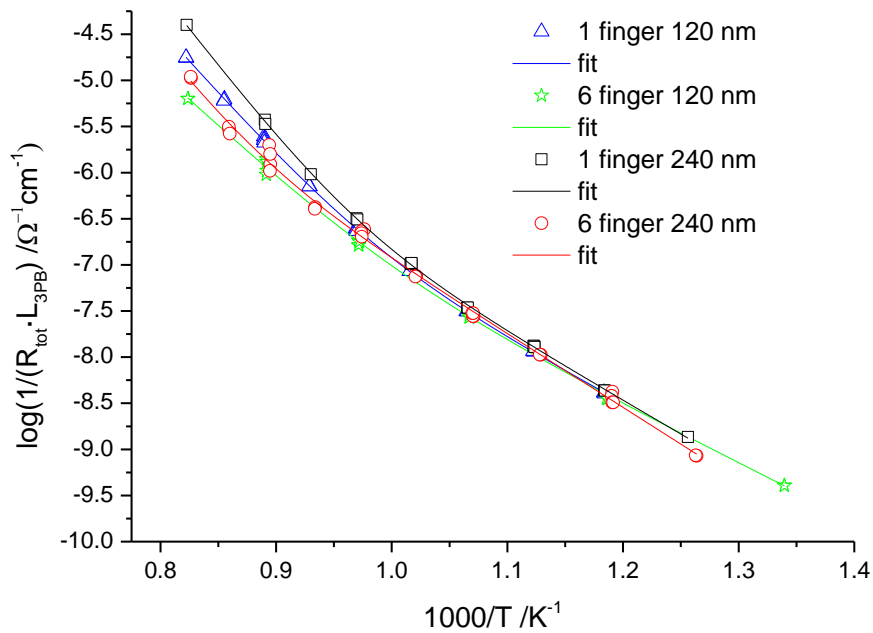
Fig. 2.10 Arrhenius plot of L_{3PB} normalized polarization resistances of 6 and 1 finger–type electrodes with different LSM thickness of 120 nm and 240nm, electrode shape is shown in Fig. 2.1b.

Most probably this has a rather simple reason: Reducing the film thickness also reduces the cross-section for in-plane electron follow in the LSM layer and thereby the electronic sheet resistance [80] in the LSM electrode is increased. For the thinner electrodes, the increased electronic sheet resistance has two sequent effects. It adds an additional resistor and it reduces thereby the active surface area, i.e. the area to which electrons are supplied and thus contributes to the reaction via bulk path. The bulk path reaction

reduction of LSM is much stronger thermally activated than electronic conductivity in LSM, which has an activation energy of only 0.1 eV [81]. Accordingly, the electronic sheet resistance becomes less important the lower the temperature is, and it is irrelevant in the low temperature 3PB regime. However, it affects electrode properties at high temperatures, particularly for thinner films and many fingers, where it causes a lowering of the effective activation energy and an increase of the polarization resistance.

The same effect is also seen when comparing measurements on circular Ø=190 µm LSM and LSM/Pt electrodes. For LSM microelectrodes with platinum capping layer, the spreading resistance of YSZ calculated from the known temperature dependent conductivity (σ_{ion}(T)) of a YSZ single crystal is in good agreement with the measured R_{YSZ} value. LSM microelectrodes without capping layers show higher spreading resistances and the error increases towards higher temperatures. For true microelectrode temperatures of 607 °C and 922 °C, measured with thermocouple type K in the symmetrically heated MiMa set-up, the measured spreading resistance is equal and exceeds the calculated one by a factor 1.5, respectively. The higher YSZ spreading resistance for LSM electrodes compared to LSM/Pt electrodes reflects a smaller active electrode area caused by the lateral sheet resistance in the microelectrode. This also means that the high temperature activation energy of LSM electrodes in Figs. 5 and 7 might be slightly underestimated.

All these considerations and interpretations are in line with the following test: Finger electrodes with one or two fingers per side and additional Pt capping layers were measured in the symmetrically heated MiMa set-up. The total polarization resistance scales with the 3PB length over the entire temperature range (660 °C – 880 °C)

(Fig. 2.11). Here, the electronic sheet resistance in the LSM film is short-circuited by the platinum layer. A change in activation energy from low to high temperature regime is again found but less pronounced than in Fig. 2.9 (LSM), since the Pt restricts the bulk path to the rim of the Pt capped microelectrode. Therefore, also the high temperature resistance scales with the 3PB length (pseudo-3PB path).

For a more detailed analysis of the effect of different 3PB lengths, all 6 electrodes of Fig. 2.1b were investigated at the same temperature in the asymmetrically heated micro-contact set-up. Intermediate temperature measurements were performed on different microelectrodes at ca. 700 °C electrode temperature (800 °C hot stage set temperature) in air, subsequently changing from low 3PB length (1.2 mm) to high 3PB length (7.2 mm). The impedance spectra were again fitted to the equivalent circuit in Fig. 2.2. The decrease of the total polarization resistance correlates with an increasing 3PB length (Fig. 2.12a) even though the normalized polarization resistance ($R_{tot} \cdot L_{3PB}$) is not really constant.
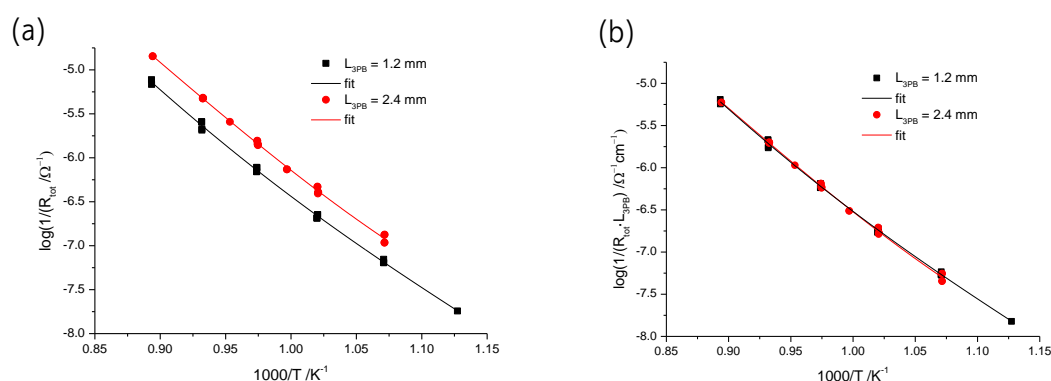
Fig. 2.11 (a) Arrhenius plot of the total polarization resistance of finger-type electrodes with Pt capping layer; (b) values normalized to the 3PB length.

Irreversible changes which occurred during the measurements on these LSM microelectrodes (second measurement cycle in Fig. 2.12a) can be caused by the repeated contacting procedures but also by degradation effects due to temperature gradients resulting from the local cooling of the current collecting tip and the asymmetrical heating. Such degradation effects were also observed for Pt microelectrodes [82] when measuring in set-ups with temperature gradients caused by asymmetrical heating [70]. This effect partly explains the slight increase of $R_{tot} \cdot L_{3PB}$ with finger numbers.
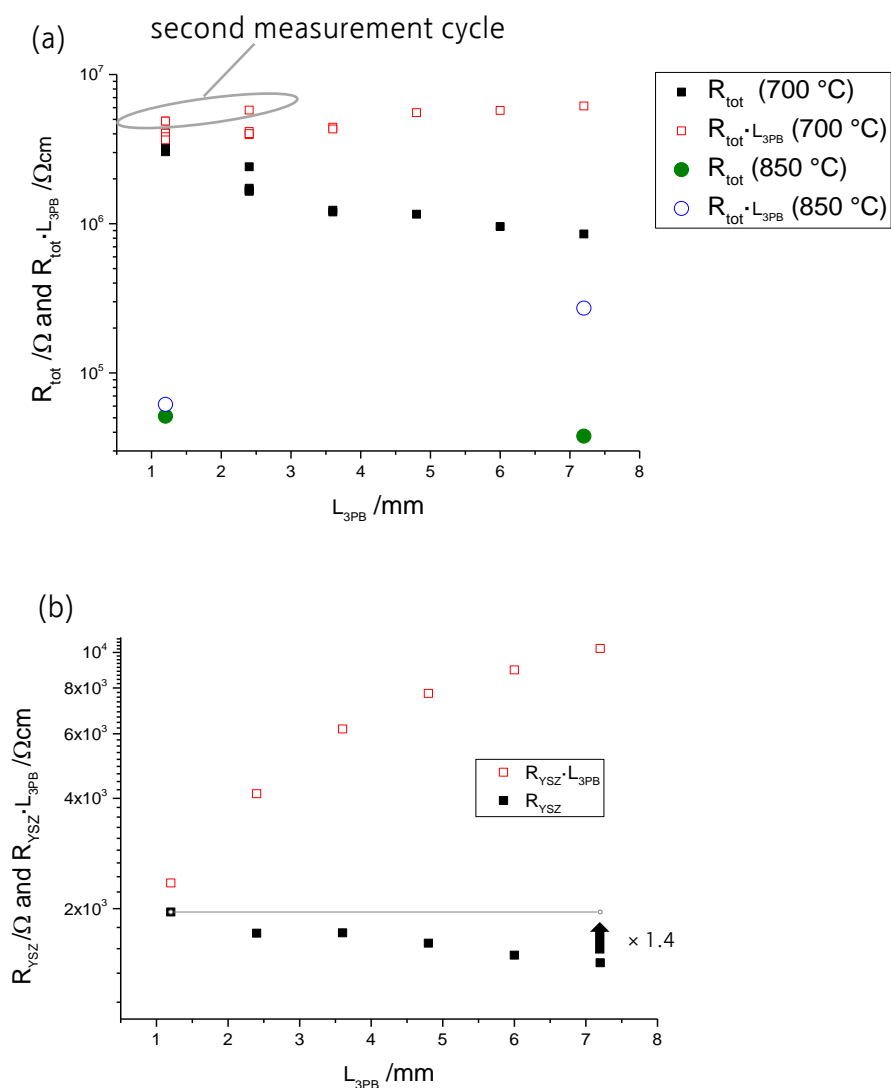
Fig. 2.12 (a) Total polarization resistances and total polarization resistances scaled to the 3PB length of finger-type LSM microelectrodes with different 3PB lengths (for microelectrodes see Fig. 2.1b) measured at ca. 700 °C and 850 °C average electrode temperature in an asymmetrically heated micro-contact set-up (hot stage set temperature 800 °C and 1000 °C). (b) Electrolyte resistance R_{YSZ} of the microelectrodes at 800 °C hot stage set temperature. The arrow indicates the decrease of the electrolyte resistance with increasing number of fingers.

Additional high temperature measurements at 1000 °C set temperature (ca. 850 °C average electrode temperature) were performed on two electrodes with 1.2 mm and 7.2 mm 3PB length (Fig. 2.12a). It can be clearly seen that there is little effect of the

strong difference in 3PB length which supports the interpretation of a change from surface to bulk path between measurements at lower temperatures (ca. 700 °C) and higher temperatures (ca. 850 °C).

At 700 °C the resistance R_{YSZ}, representing the high frequency intercept in the spectrum, decreases by a factor of 1.4 (Fig. 2.12b) when increasing the number of fingers per side from one to six. This is simply due to the fact that in terms of current constriction in YSZ the 6 finger electrode acts as if it were larger than the 1 finger electrode, thus lowering R_{YSZ}. At 850 °C the electrolyte resistance R_{YSZ} decreases only by a factor of 1.1 with increasing finger number. This might be caused by a reduced active electrode surface area for a 6 finger electrode at high temperatures due to the electronic sheet resistance.

For the sake of completeness we also analyzed the geometry dependence of the individual fitting elements R_a and R_b of the equivalent circuit in Fig. 2.2. At 700 °C the resistance values are similar for the one finger electrode with small 3PB length. R_a almost scales with the 3PB length while resistance R_b is less dependent on the 3PB length (Tab. 2.2). This might also be an effect of a different sensitivity of R_a and R_b to degradation during measurements. For high temperatures neither R_a nor R_b shows a pronounced dependence on the 3PB length (Tab. 2.3).

3PB length	R_{YSZ} /Ω	$R_{YSZ} \cdot L_{3PB}$ /Ωm	R_a /Ω	$R_a \cdot L_{3PB}$ /Ωm	R_b /Ω	$R_b \cdot L_{3PB}$ /Ωm
1.2 mm	$1.96 \cdot 10^3$	$2.35 \cdot 10^3$	$1.80 \cdot 10^6$	$2.17 \cdot 10^6$	$1.49 \cdot 10^6$	$1.79 \cdot 10^6$
7.2 mm	$1.42 \cdot 10^3$	$1.03 \cdot 10^4$	$2.64 \cdot 10^5$	$1.90 \cdot 10^6$	$6.08 \cdot 10^5$	$4.38 \cdot 10^6$

Tab. 2.2 R_a, R_b and R_{YSZ} of finger-type microelectrodes (ca. 200 nm thickness) at 800 °C hot stage set temperature ($\approx$700 °C electrode temperature).

3PB length	R_{YSZ} /Ω	$R_{YSZ} \cdot L_{3PB}$ /Ωm	R_a /Ω	$R_a \cdot L_{3PB}$ /Ωm	R_b/Ω	$R_b \cdot L_{3PB}$ /Ωm
1.2 mm	$5.73 \cdot 10^2$	$6.88 \cdot 10^2$	$6.12 \cdot 10^3$	$7.34 \cdot 10^3$	$4.51 \cdot 10^4$	$5.41 \cdot 10^4$
7.2 mm	$5.13 \cdot 10^2$	$3.70 \cdot 10^3$	$6.95 \cdot 10^3$	$5.01 \cdot 10^4$	$3.08 \cdot 10^4$	$2.21 \cdot 10^5$

Tab. 2.3 R_a, R_b and R_{YSZ} of finger-type microelectrodes (ca. 200 nm thickness) at 1000 °C hot stage set temperature, averaged over 6 measurements ($\approx$850 °C electrode temperature).

2.4.4 Macroscopic Electrodes With and Without Extended 3PB

In order to further test the interpretations given so far, measurements were also performed on symmetrically deposited macroscopic electrodes of type A and B, see Fig. 2.1c. Sample A exhibits a grid of 200 nm thick LSM (deposited at 700°C) and 400 nm thick platinum (deposited at room temperature) with free YSZ surface in between. The 3PB length of these electrodes is roughly 2.5 m for a mesh of 10 µm distance between 10 µm wide stripes (Fig. 2.1c (A)). The platinum film acts both as current collector and as oxygen blocking layer on top of LSM. Only the 200 nm high LSM side walls are remaining as free surface. Samples of type B consist of a dense 200 nm thick LSM film with a 400 nm thick platinum grid on top. The platinum mesh covers more than 75% of the LSM surface and acts as current collector but large free LSM surfaces are still present.

The 3PB length is very short and determined by the edge length of the YSZ substrate, i.e. 2 cm per electrode. These two sample types combine very different 3PB lengths (also achieved by finger-type microelectrodes) and very different LSM surface area (as in the case of LSM and LSM/Pt microelectrodes). Hence, both relevant geometrical parameters rather than only one are varied. Both sample geometries were measured by a pseudo 4-point wiring [83] (Pt foil current collectors) in the symmetrically heated MiMa set-up. Measurement cycles (450 °C to 900 °C and back to 450 °C) lasted up to 5 days. Sample type B with small 3PB length was only measurable above 600 °C owing to the very high polarization resistance.

Macroscopic LSM samples of type A with very large 3PB length exhibit a significant change in the shape of the impedance spectra from low temperature (475 °C) to high temperature (850 °C) cf. Fig. 2.13a. At low temperatures only one distorted semicircle is visible, while for high temperatures clearly two different contributions can be observed in the Nyquist and in the Bode plot. Less shape change is found for samples of type B (Fig. 2.13b). Irrespective of the exact shape, an impedance analysis in terms of the equivalent circuit in Fig. 2.2 was performed and the total polarization resistances of two electrodes are plotted in the Arrhenius diagram of Fig. 2.14a. LSM samples with negligible 3PB length (type B) exhibit a much higher total polarization resistance in the low temperature regime (450 °C - 700 °C) compared to R_{tot} of the sample with large 3PB length (type A). This is in accordance with the interpretation of a predominant surface path at lower temperatures.
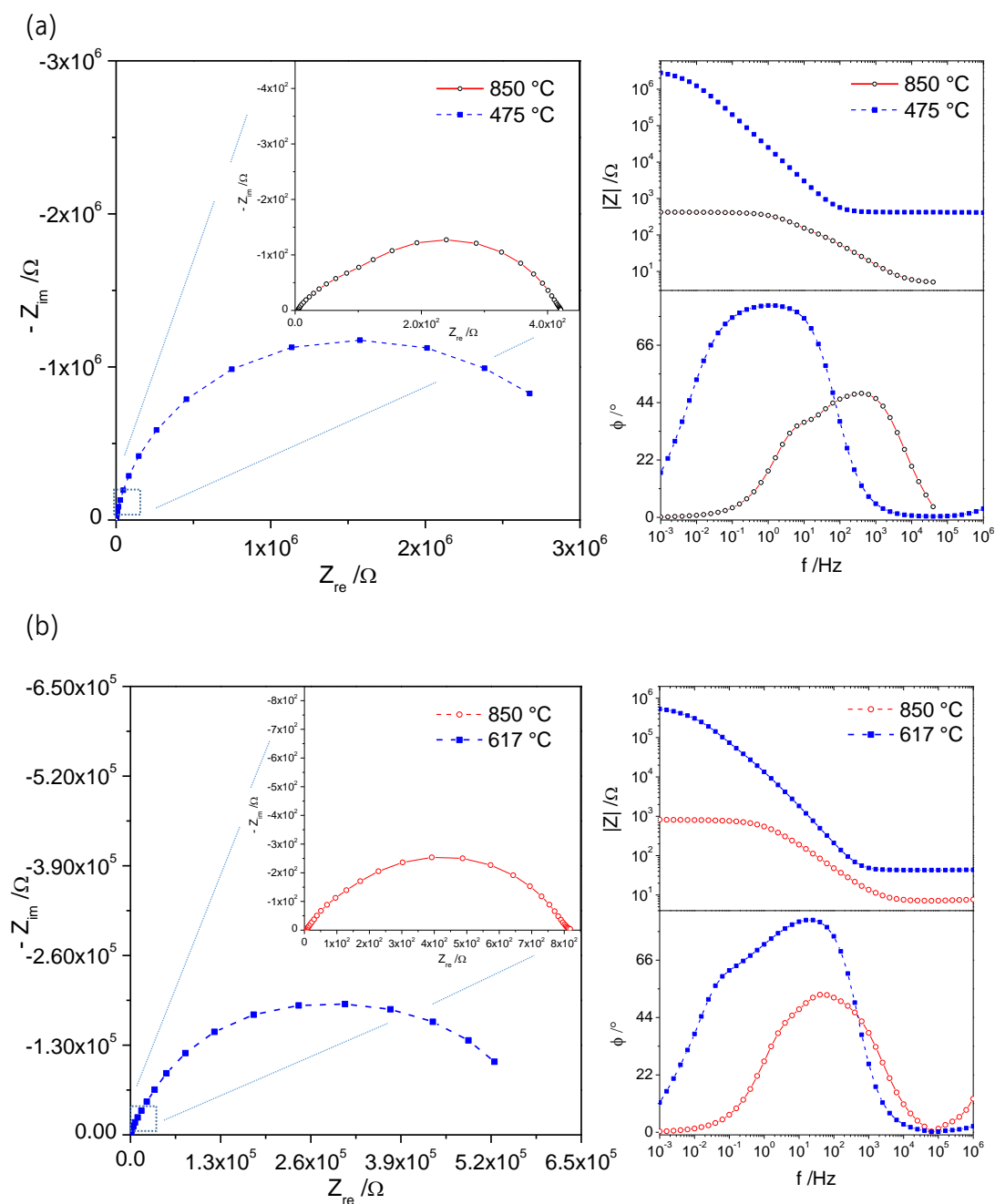
Fig. 2.13 Impedance spectra of macroscopic symmetric 5·5 mm^2 LSM electrodes. (a) Type A with extended 3PB at 475 °C and 850 °C and (b) type B at 850 °C and 617°C.

Both samples show comparable resistance values at 900 °C, which seems surprising since one may expect that sample type A with very small LSM surface area exhibits a

negligible bulk path contribution. However, as for LSM/Pt microelectrodes this is also not the case here, since the free LSM edges of sample type A, sketched in Fig. 2.15, still enable a bulk path. Hence, both pathways are active on both samples, though with different weighting. Therefore, again an analysis via Eq. 2.3 is feasible and extrapolated fit values of Y_1 and Y_2 are shown in Fig. 2.14b. Activation energies and Y_i^0 values from both types of samples are summarized in Tab. 2.4 for different measurement series. Very consistently activation energies at high and low temperatures differ substantially with values of the order of 1.4 eV at lower temperature and 2.6 eV at high temperature. This is in good accordance with the microelectrode measurements discussed so far.

(a)

(b)

Fig. 2.14 (a) Arrhenius plot of the total polarization resistance of two 5·5 mm² symmetrical LSM samples, one with extended L_{3PB} (LSM_A) and one without extended L_{3PB} (LSM_B). Absolute polarization resistances of both electrodes on a YSZ electrolyte are plotted. (b) Fitted admittances Y_1 and Y_2 according to Eq. 2.3 for both samples types.

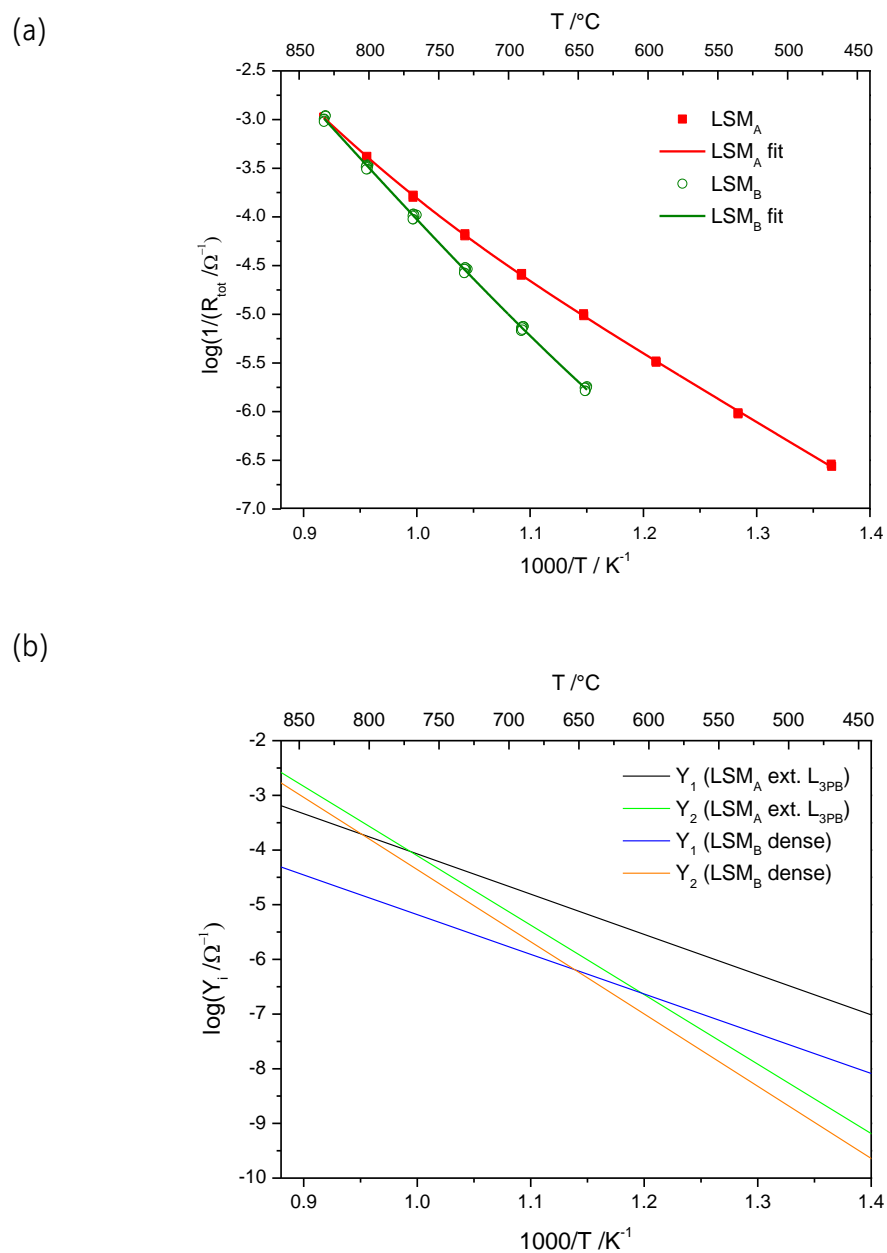| LSM sample & series	Type	Ea_1	Ea_2	Intersection temperature
LSM_1 series 1, green in Fig. 2.15a	B	2.60eV	1.58eV	597 °C
LSM_1 series 2	B	2.62eV	1.44eV	604 °C
LSM_2 series 1, red in Fig. 2.15a	A	2.51eV	1.46eV	727 °C
LSM_2 series 2	A	2.52eV	1.37eV	754 °C
LSM_2 series 3	A	2.31eV	1.43eV	679 °C
LSM_3 series 1	A	2.39eV	1.35eV	717 °C
LSM_4 series 1, blue in Fig. 2.16a	B	2.54eV	1.34eV	598 °C
LSM_4 series 2, orange in Fig. 2.16a	B	2.67eV	1.74eV	588 °C

Tab. 2.4 Activation energies of 4 macroscopic LSM samples with sample names LSM_1 to LSM_4 ($5 \cdot 5$ mm^2). For most samples several measurement series were performed.

The surface path ratio between the two samples ($Y_{2\,(Type\,A)}$ and $Y_{2\,(Type\,B)}$, Fig. 2.14b) is ca. 10 (between 6 and 17 in the temperature range of 450 °C - 850 °C), while the 3PB length differs by a factor of 100. This apparent inconsistency may partly be caused by uncertainties in the true 3PB length (cf. shape of 3PB in Fig. 2.8). Possibly even more important is the different preparation procedure of the 3PBs: the inner 3PBs of sample A are prepared by photo-lithography and ion beam etching, while the outer 3PB of both samples is simply prepared by grinding. The similarity of the polarization resistance at high temperatures, despite different surface areas, is most probably again caused by the short transport distances of the pseudo-3PB path of sample type A, see Fig. 2.15. The importance of this path is again aggravated by the fact that side walls are far from perpendicular, cf. Fig. 2.7.
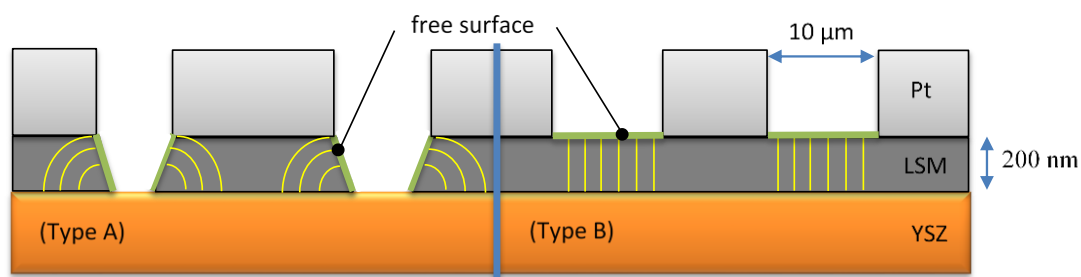
Fig. 2.15 Sketch indicating the free LSM surface and possible ion flux lines for both samples A and B. Please note: film thickness and Pt grid distance are not drawn to scale.

2.4.5 Changing Paths by Heat Treatment and Aging

A macroscopic sample (type A) with LSM prepared in the PLD at 700°C can be repeatedly measured up to ca. 850 °C without significant changes of the polarization resistance (Fig. 2.16 blue line). Increasing the temperature to a higher maximal value changes the LSM electrode irreversibly (decrease of R_{tot}^{-1} at high temperatures, Fig. 2.16b). The low temperature resistance, however, is not affected by this heat treatment. After the change occurs at high temperature, again reproducible cycles are possible when not exceeding the maximal temperature reached before (here 940 °C). This modification of the high temperature part of the Arrhenius plot is most probably correlated with microstructural changes in LSM: the microstructure of LSM films not only
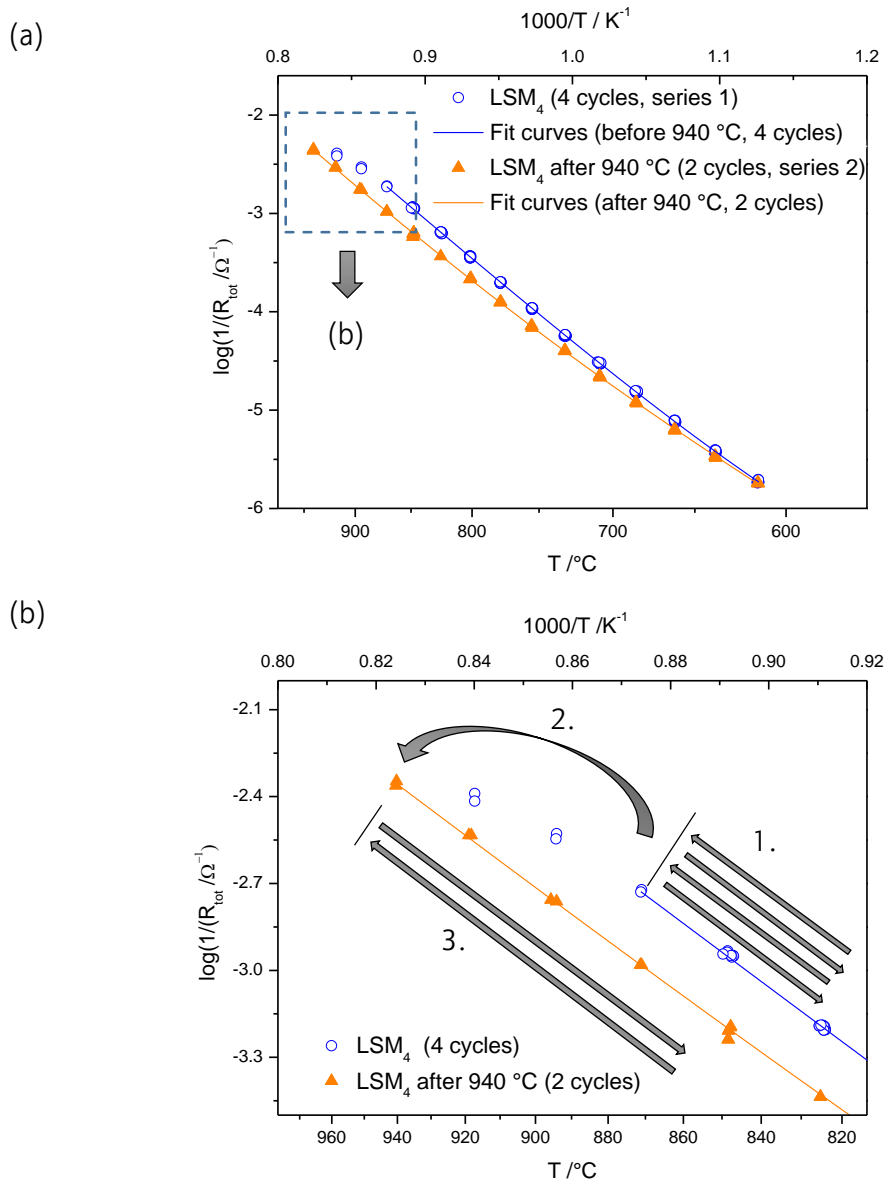
Fig. 2.16 (a) Arrhenius plot of the total electrode polarization resistance of a macroscopic LSM sample (type B, sample name LSM$_4$), deposited at 700 °C. Reproducible measurements during 4 cycles before heating to 940 °C and 2 cycles after heating to 940 °C. (b) Magnification of the high temperature range, indicating changes caused by heating up to 940 °C (2.). Reproducible cycles can be measured before the additional heating step (1.) and after this step (3.). Arrows indicate the heating measurement sequence: 1. Four cycles between 620°C and 870 °C, 2. increasing temperature from 870 °C to 940 °C, 3. two cycles between 940 °C and 620 °C. Two measurement points were taken at each temperature.

depends on the PLD deposition temperature but also on the annealing temperature with grain sizes increasing from a few 10 nm without annealing to more than 100 nm after annealing at 1000 °C, see Fig. 2.17. Such an increase of the grain size is also expected during the measurements when extending the temperature range to 940 °C (Fig. 2.16).
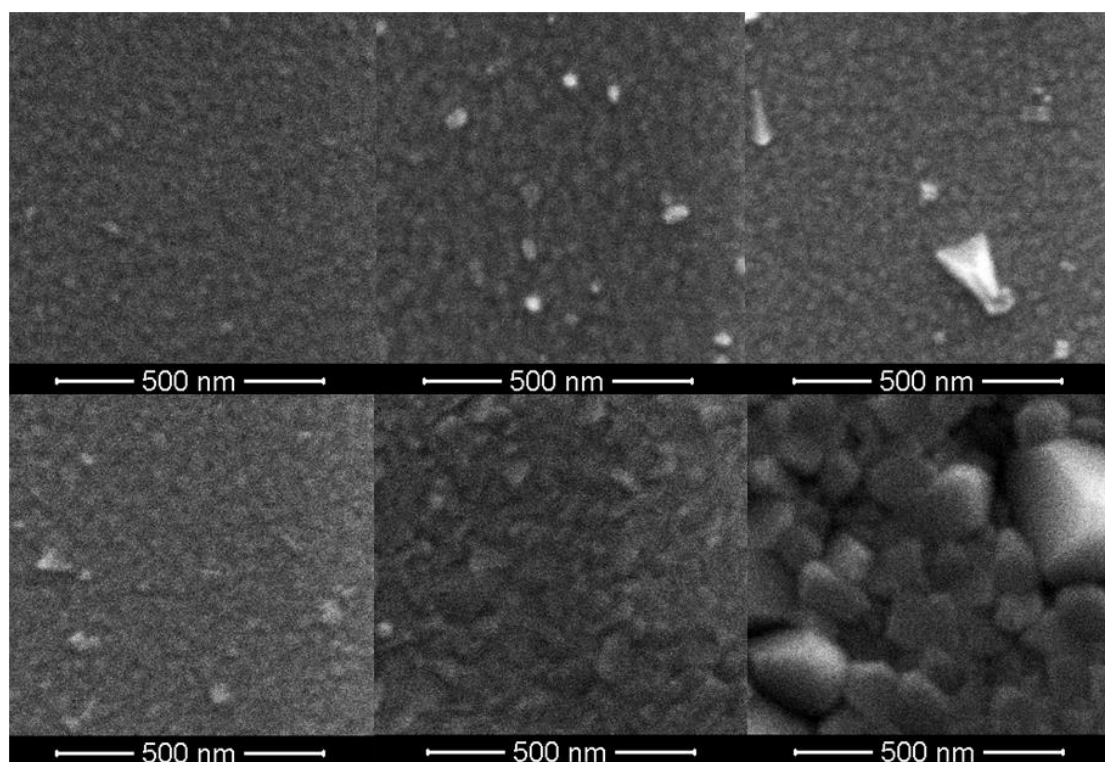
Fig. 2.17 SEM pictures of LSM films prepared by PLD at 580 °C on YSZ (100), (a) without additionally heat treatment and annealed for 12 h at (b) 600 °C, (c) 700 °C, (d) 800 °C, (e) 900 °C, (f) 1000 °C.

For LSM grain boundaries contributing to the oxygen exchange kinetics of LSM, the resistance of the electrode should increase with increasing grain size. Indeed, strongly enhanced tracer exchange and diffusion coefficients of grain boundaries were found in a tracer study presented in chapter 4 on very similar LSM films. Hence, most probably microstructural changes are responsible for the observed high temperature changes of

R_{tot}. At high temperatures the electrode is simply switched to a new "stable" resistive state with a different average grain size and thus a different polarization resistance. The absence of a resistance change at low temperatures indicates that LSM grain boundaries do not play a significant role for the surface path.

This interpretation is confirmed by two additional experiments: In Fig. 2.18 the temperature dependent polarization resistances of two differently prepared and differently sized LSM microelectrodes are shown (700 °C and 861 °C deposition temperature). They exhibit the same absolute polarization resistance in the bulk path dominated high temperature regime, although the $\varnothing$=300 µm electrode has a 9 times bigger surface area. SEM and TEM [71] analysis revealed average grain sizes of 35 nm and 85 nm for the films deposited at 700 °C and 861 °C, respectively. This cannot fully explain the factor of 9 difference in the area specific polarization resistance, but a different grain size distribution with many small grains for lower deposition temperature may also play a role. At low temperatures with 3PB related surface path, the measured polarization resistances scale by a factor of almost 3, which excellently matches the 3PB length ratio of 3.

In a final experiment, an $\varnothing$=300 µm LSM microelectrode deposited at 600 °C PLD substrate temperature was measured in the symmetrically heated MiMa set-up. The first heating cycle of the freshly prepared LSM microelectrode showed severe degradation (Fig. 2.19). This effect is stronger than for LSM thin films deposited at higher temperatures (see Fig. 2.16), but after this first heating very reproducible cycles can be measured without significant further degradation (as long as the subsequently used maximal temperature is not exceeded).
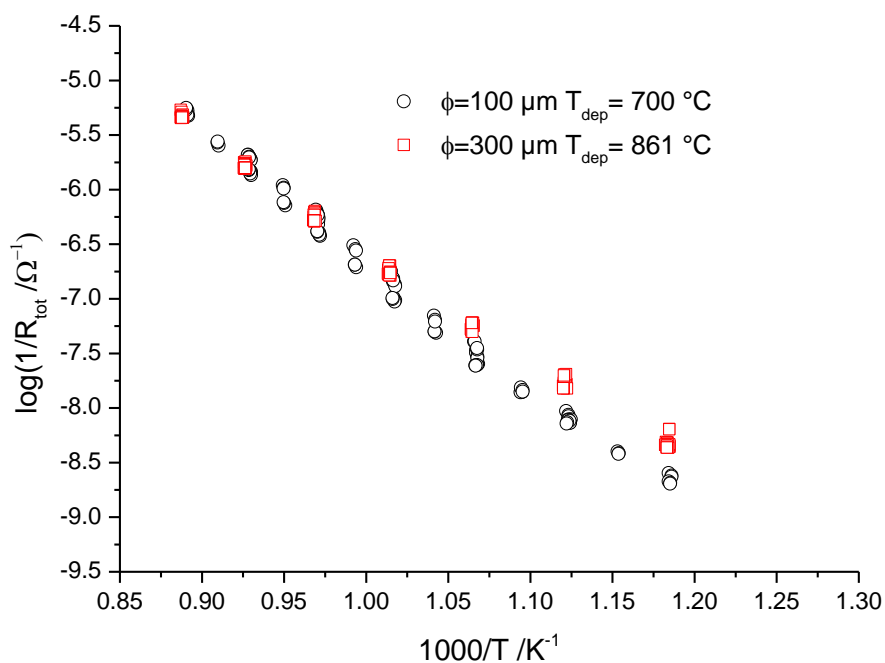
Fig. 2.18 Arrhenius plot (R$_{tot}$) of an Ø=300 µm (deposition temperature of 861 °C) and an Ø=100 µm (deposition temperature of 700 °C) LSM microelectrode, thickness ≈200 nm.

Please note: Such a stable state was first established in all measurements of chapter 3. This irreversible change during the very first heating is again most probably the result of a modified LSM microstructure and thus of the grain boundary contribution to the bulk path. It should be mentioned that in this case also the resistances at low temperatures are affected, which might have other reasons than grain growth.
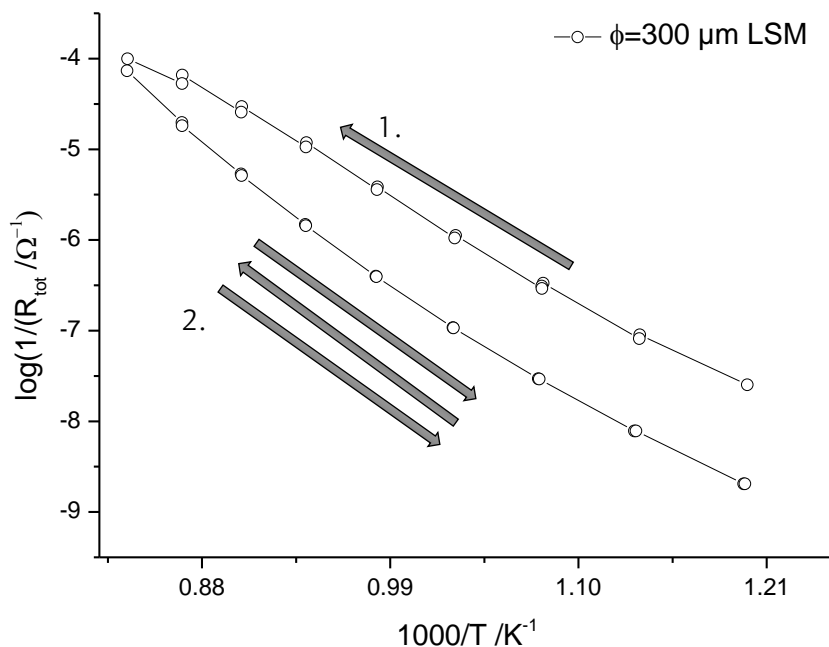
Fig. 2.19 Resistance change of an Ø=300 µm LSM electrode with 240 nm thickness (deposition temperature of 600 °C) during a first heat treatment, arrows indicate the measurement sequence (1. First heating, 2. Three cycles in the entire temperature range).

2.5 Capacitances

2.5.1 Theoretical Issues of Capacitances

2.5.1.1 Electrostatic Capacitance

Capacitance is the ability of a given material to store electrical charge. The capacitance is defined by

$$C = \frac{q}{V} \qquad\qquad 2.4$$

where q denotes the charge (+q on one –q on the other plate) and V the applied voltage. The simplest form of an electrostatic capacitance is the double layer capacitance. This capacitance of two parallel plates can be calculated by

$$C = \varepsilon_r \varepsilon_0 \frac{A}{d} \qquad\qquad 2.5$$

using A as plate area, d as distance between the plates, ε_r as the relative static permittivity and the vacuum permittivity as ε_0. These electrostatic capacitances are found in ideal interfacial double layer capacitances.

Small capacitances, visible in impedance spectra, not necessarily originate from the measured sample. They can also include stray capacitances from the measurement set-up, in microelectrode experiments, for example, typically 100 fF are found. In the case of the symmetrically heated MiMa set-up this stray capacitances can reach some pF (detailed description of measurement set-ups in chapter 3).

2.5.1.2   Electrochemical Double Layer Capacitance

Experimentally obtained values of interfacial capacitances in YSZ based systems are in the range of 50 µF/cm^2 [84, 85]. Such electrochemical interface capacitances, commonly still referred to as double layer capacitances, seem to have also non-electrostatic contributions [23, 83] and are therefore also often called "pseudo capacitive". These capacitances also imply electrochemical reactions and thereby also chemical storage effects on a microelectrode [85]. Values of 100 µF/cm^2 were measured in Ref. [86] for metallic microelectrodes (Ag, Pt, Au, and Ni) on 10 mol% Y_2O_3 containing

YSZ. Double layer capacitances between 120 and 330 µF/cm were found for Pt/LSM on

YSZ with 8 mol% yttria [84, 87]. A detailed mechanistic understanding of such solid state

double layer capacitors is still missing.
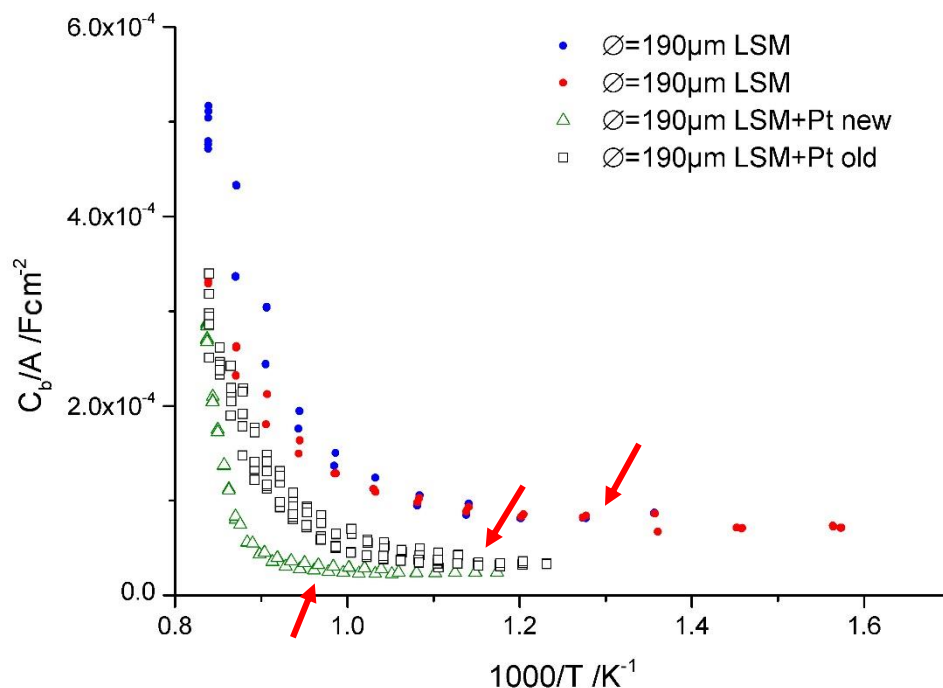
Fig. 2.20 Temperature dependent capacitance C_b calculated from CPE_b of LSM and LSM/Pt Ø=190 µm microelectrodes. Red arrows indicate the approximated ending of the temperature invariant part of the capacitances.

2.5.1.3   Chemical Capacitance

Chemical capacitances (also known as faradaic or pseudo capacitance, C_{Chem}) are

associated with the bulk oxidation/reduction of the electrode material. As discussed in

the following, this chemical capacitance can become much larger than surface or

interfacial capacitances. Thus it is a useful measure of how much of the bulk is involved

in a reaction, even when we step away from thin films to more complex microstructures [10]. C_{Chem} often has a negative formal activation energy, i.e. it increases with temperature. An increase of the chemical capacitance corresponds to an increase of the "readiness" of the material to undergo stoichiometric changes upon oxygen partial pressure variation [88]. A generalized equivalent circuit for mixed conductors including chemical capacitances was derived in Ref. [23]

2.5.1.4   Interfacial Capacitances of LSM/YSZ and LSM/Pt of Circular Microelectrodes

A final fact supporting the interpretation of oxygen reduction on LSM/Pt microelectrodes in terms of two parallel paths comes from the analysis of capacitances C_b. This capacitance was calculated according to Eq. 2.5, using fit values Q_{CPE} and p_{cpe} from CPE_b and total polarization resistance $R_{tot}=R_1+R_2$ as R. Exemplary, we consider the capacitance of the circular shaped 240 nm thick LSM and LSM/Pt microelectrodes (Ø=190 µm, deposited at 600 °C) measured in air from 450 to 950 °C in the symmetrically heated micro-contact set-up MiMa (Fig. 2.3b). Temperature dependence of total polarization resistance and shape of measured impedance spectra are depicted in Figs. 2.7 and 2.4 and described above.

For Ø=190 µm LSM microelectrodes, C_b shows a temperature independent value of ca. $8.5 \cdot 10^{-5}$ Fcm^{-2} below 650 °C (Fig. 2.20). At higher temperatures it increases up to $4.7 \cdot 10^{-4}$ Fcm^{-2} at 900 °C (Fig. 2.20 blue and red circles). For LSM/Pt microelectrodes the temperature invariant part of the capacitance at lower temperatures is drastically extended (from around 650 to 750 °C) by applying a dense Pt capping layer on top of

the LSM microelectrode. A freshly prepared $\varnothing$=190 µm LSM/Pt microelectrode shows a temperature independent value of $4.5 \cdot 10^{-5}$ Fcm^{-2} up to ca. 750 °C (Fig. 2.20 green triangles). At higher temperatures, the capacitance again increases drastically to $2.5 \cdot 10^{-4}$ Fcm^{-2} at 900 °C. Additionally the temperature invariant part of C_b of the LSM/Pt microelectrode shows a time dependent behavior. After several hours at high temperatures (up to 950 °C), the intersection temperature (change from surface to bulk path) shifts to lower temperature values (Fig. 2.20 black unfilled squares).

Irrespective of the exact meanings and locations of the two serial resistors (R_a, R_b) from the fitting model of the surface path, an YSZ/LSM interfacial capacitance has to exist in parallel to both resistors. Hence, at least this part of the equivalent is expected to be correct, as long as the surface path prevails in oxygen reduction. In the low temperature region, C_b shows reasonable values for an interfacial capacitance [84, 85] and also exhibits temperature independence as expected for an interfacial capacitance. Since the predominant oxygen reduction process changes from surface to bulk path for increasing temperature, we interpret the change of the capacitance in Fig. 2.20 not as an increase of the interfacial capacitance, but simply in terms of the reaction mechanism change. In the bulk path and in the transition temperature range, C_b has either another meaning or no simple meaning at all. The extension of the temperature independent part of C_b by adding the Pt layer can again be a hint for a change of the intersection temperature. This is in very good agreement with the interpretation given above: The Pt capping layer reduces the free LSM surface and thereby extends the validity range of the surface path, in which it is not affected by the platinum capping layer. The changing of the intersection temperature, caused by enhancing 3PB length, was demonstrated

above for resistances of macroscopic electrodes. The total polarization resistance change of the same LSM and LSM/Pt microelectrodes used for the analysis of C_b, however, shows no significant changes of the intersection temperature (Fig. 2.7). The fact that this effect is only visible in the capacitive, but not in the resistive part of the impedance spectra might be caused by the complicated interaction of the different reaction pathways and changing rate limiting steps as sketched in Fig. 2.21.
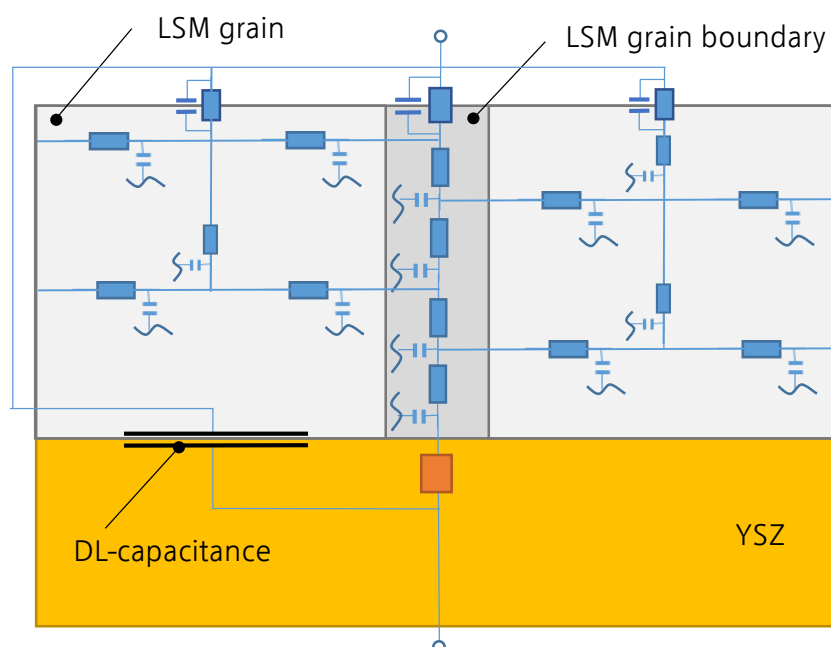
Fig. 2.21 Sketch of LSM grain gain boundary transmission lines for high temperature bulk path. The electronic rail is only partly shown except for the double layer capacitance.

The reason, why C_b of LSM/Pt microelectrodes is substantially smaller than for LSM, is not known yet; possibly another serial interfacial capacitance at the Pt/LSM interface plays a role. We may assume that the interface capacitance at the LSM/YSZ interface has a second interface capacitance at the LSM/Pt interface connected in series. Thus

the value of the measured total capacitance would be reduced. Both capacitances are in the same order of magnitude, however, fitting values are different for electrodes with and without platinum cover layer (Fig. 2.20). After subtracting the capacitance of a $\varnothing$=190 µm LSM/Pt microelectrode (C_{DL+Pt}=24 µF/cm^2) from the measured total double layer capacitance of a $\varnothing$=190 µm LSM microelectrode (C_{DL}=85 µF/cm^2), the remaining capacitance at the LSM/Pt interface would be C_{Pt}=33 µF/cm^2. PtO$_x$ as third "phase" between Pt and YSZ is discussed in several studies as a potential source for electrochemical processes [65, 82, 83, 89-91]. Thus platinum oxide is assumed to play an important role also at the LSM/Pt interface.

The temperature induced change of C_b of LSM/Pt microelectrodes correlates with optical degradation of the Pt capping layer. After several hours at high temperature, the Pt capping layer gets pin holes, hence, not covering the entire LSM electrode surface anymore (Fig. 2.22b). By increasing the free LSM surface of the microelectrode, the temperature invariant part of C_b is shifted to lower temperatures. The interface capacitance, however, is expected to be relatively small compared to the chemical capacitance [87, 92].

a)

b)
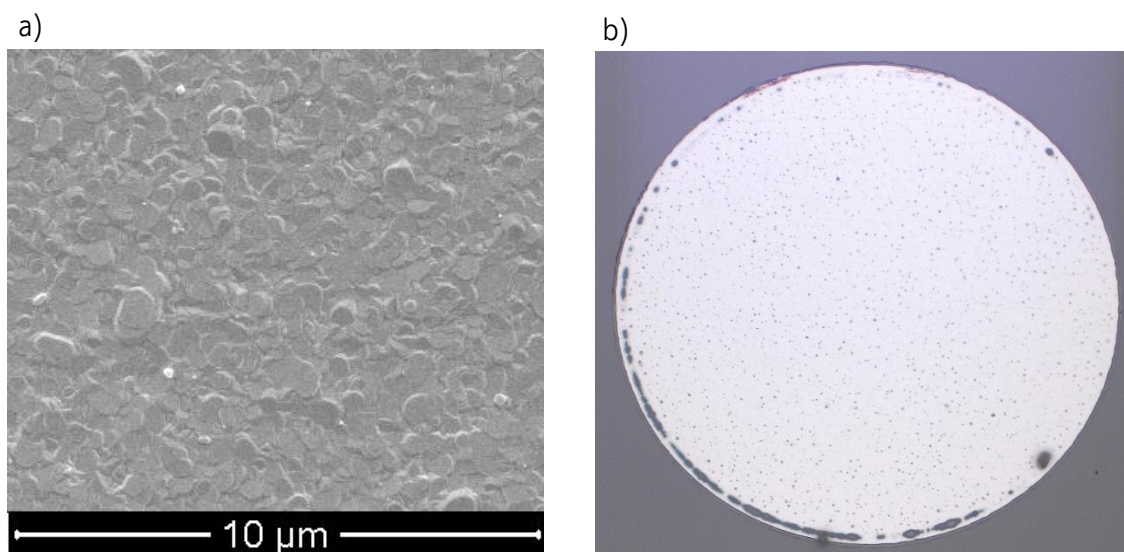
Fig. 2.22 a) SEM picture of dense part of the Pt capping layer on top of a microelectrode after high temperature treatment (900 °C). b) SEM picture of a Ø=190 µm LSM/Pt microelectrode after several weeks at high temperature, (up to 900 °C). Dark spots at the microelectrode surface indicate pin holes and holes in the Pt capping layer.

2.5.2 Chemical Capacitances of LSM and LSM/Pt Microelectrodes

Oxygen transport and electronic hole conduction in LSM, described by a transmission line derived by Jamnik and Maier [23], is only valid for isotropic and homogeneous single crystals. However, we assume grain boundary diffusion being the dominating process for oxygen transport in polycrystalline columnar thin film LSM electrodes (3D model in Fig. 2.23). Due to the complex microstructure of our LSM thin films, the transmission line mentioned before is expected to be rather complicated.
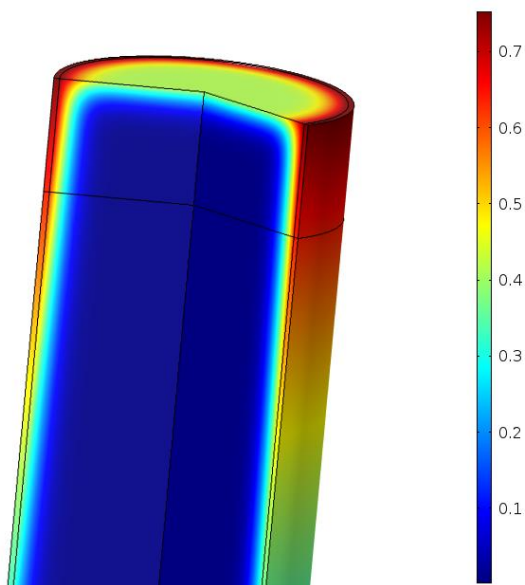
Fig. 2.23 3D finite element simulation of Ø=50 nm LSM grain with 1 nm thick grain boundary. Color indicating incorporated ^{18}O tracer concentration.

The fast grain boundaries carry the major part of the oxygen ions, but also "feed" the LSM grains of the film in perpendicular direction (Fig. 2.21 horizontal transmission lines). Capacitances, obtained from fitted impedance spectra (calculated from the constant phase element CPE_a or CPE_b after Eq. 2.2) give only qualitative information, since the used equivalent circuit (Fig. 2.2) is an even more simplified version of a transmission line and not a mechanistical correct model.

2.6   Imaging of Active Zones of LSM Thin Film Electrodes

To visualize both electrochemical oxygen incorporation pathways, the surface and the bulk path, cathodic ^{18}O tracer incorporation experiments were conducted at lower temperatures (about 370 °C) and for different cathodic polarizations. Experiments were carried out in the asymmetrically heated micro-contact set-up depicted in Fig. 2.24. This

method was first applied to Sr-doped $LaMnO_3$ electrodes though at high temperatures [68].

The p-type electronic conductivity of LSM is rather high for LSM [93] and the total polarization resistance of the microelectrode was only moderately decreased by the applied voltages. Therefore an electronic sheet resistance should not play a significant role in these experiments. Owing to the much larger electrode resistance compared to the electrolyte resistance secondary current distributions only determined by the electrochemical electrode activity can be expected. A detailed discussion and comparison of similar experiments on Pt are published in Ref. [83]. The impedance spectrum at 375 °C consists of a high frequency arc which can be attributed to the spreading resistance of ion conduction in YSZ [94] and the onset of a huge electrode feature in the low frequency region (Fig. 2.25a).

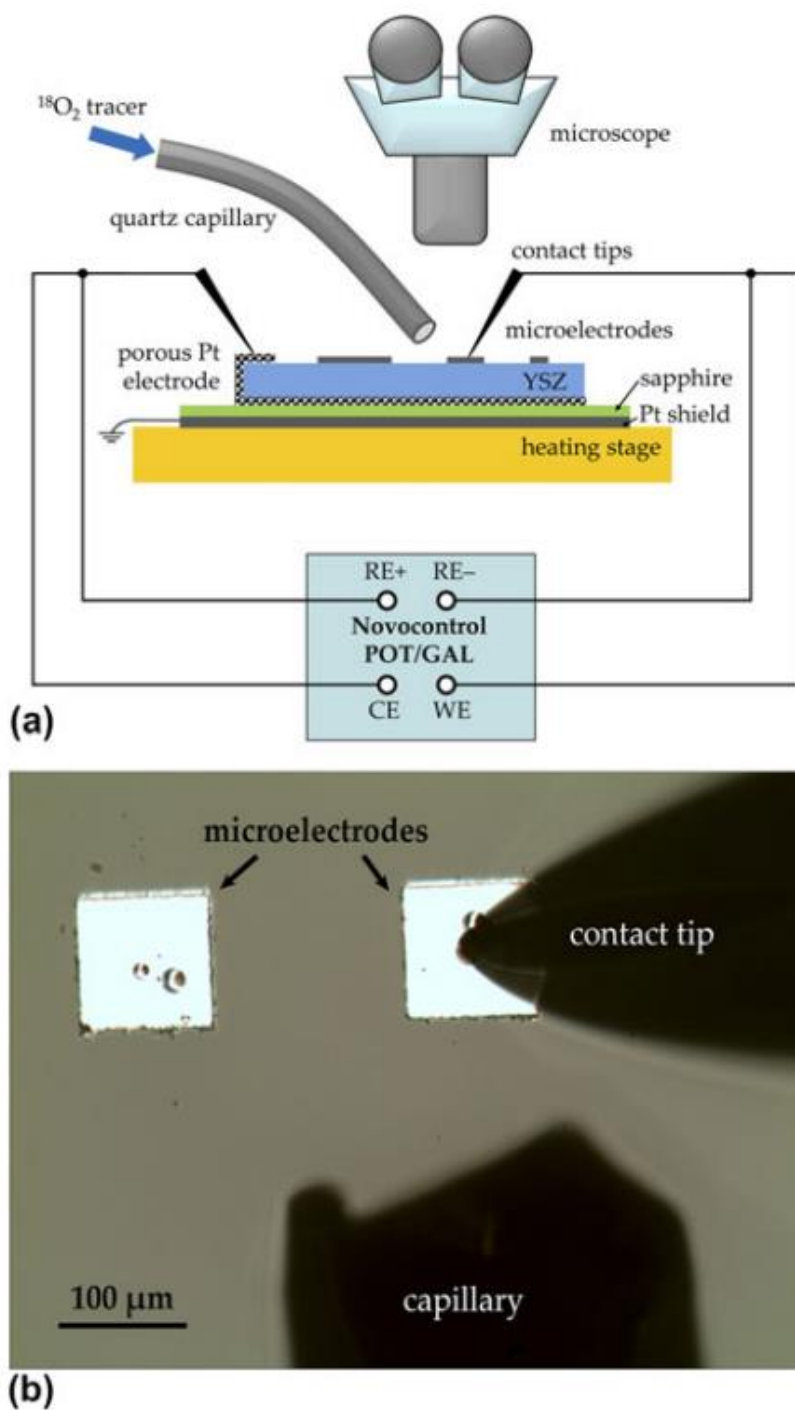**Fig.** 2.24 (a) Sketch of the experimental micro-contact set-up. The quartz capillary was used for $^{18}O_2$ tracer gas supply. (b) View through the microscope during ^{18}O incorporation experiment.

Tracer incorporation experiments were carried out on squarish 100×100 µm^2 LSM electrodes – an SEM image is depicted in Fig. 2.25c. Impedance measurements with and without applied bias were performed before exchange experiments at the same microelectrode. Bias was applied for 1000 s. $^{18}O_2$ tracer gas was supplied by a quartz capillary (Fig. 2.24) in the last 600 s of the polarization experiment to ensure a steady state of the current (Fig. 2.25d).

The DC currents during ^{18}O incorporation at 375 °C and η=-0.71 V as well as 369 °C and η=-0.85 V are shown in Fig. 2.25d. A highly resolved ^{18}O distribution image of the 3PB region of the electrode polarized with η=-0.71 V is shown in Fig. 2.26d – the SIMS image was recorded in CBA mode [95, 96] after removing the LSM electrode. In this image, three different regions can be distinguished: (i) An area with low tracer intensity on the left hand side where the LSM electrode was located, (ii) a narrow zone with high ^{18}O intensity in the middle of the image corresponding to the 3PB and (iii) a region with intermediate intensity on the right hand side reflecting the free YSZ surface. These three zones with different tracer content are even better visible in the lateral tracer fraction profile in Fig. 2.26e, which was calculated by line integration from the entire distribution image. The significant increase of ^{18}O at the 3PB shows that in this region pronounced oxygen incorporation via an electrode surface pathway took place, whereas the tracer fraction beneath the LSM film is only slightly increased indicating lower electrochemical activity. The moderate tracer increase on the free YSZ surface can be attributed to conventional (thermally driven) tracer exchange on a solid oxide ion conductor [97, 98]. A contribution of an electrolyte surface path can be ruled out owing to the considerably lower overpotential during tracer incorporation.
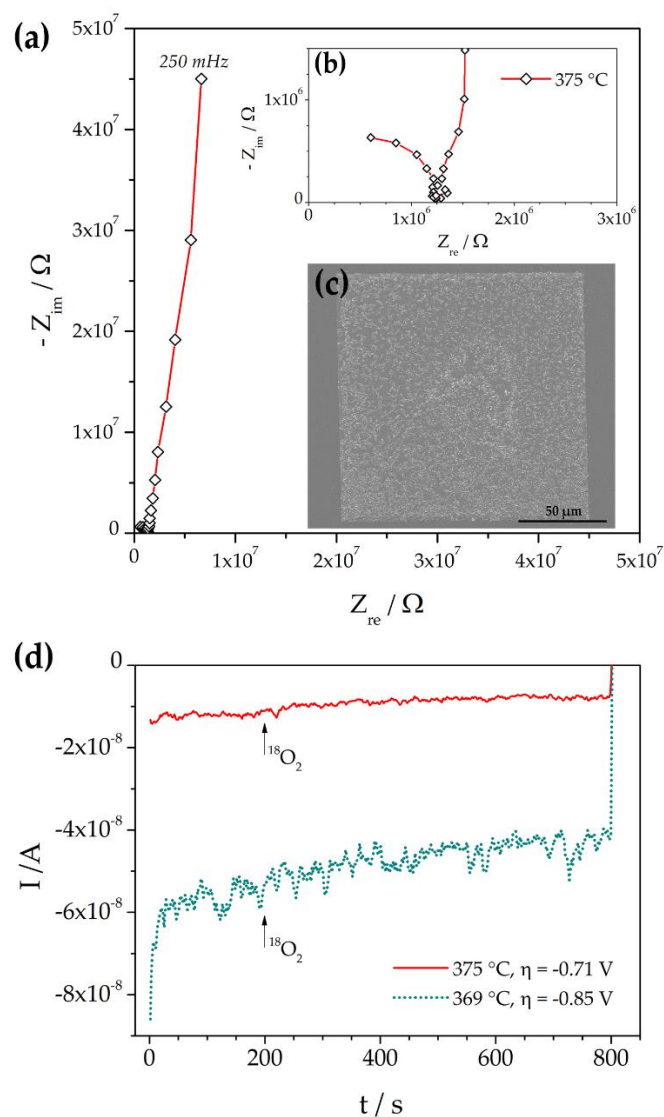
Fig. 2.25 (a) Impedance spectrum of a square-shaped 100·100 µm² LSM electrode at 375 °C. (b) Magnification of the high frequency region from (a) showing the electrolyte arc. (c) SEM image of a comparable LSM electrode, the light dots are larger, slightly protruding crystallites of the polycrystalline thin film. (d) Cathodic dc currents during tracer incorporation at 375 °C and η=0.71 V (solid curve) as well as 369 °C and η=0.85 V (dotted curve). The arrows denote the beginning of tracer gas supply.

However, the situation tremendously changed when increasing the cathodic polarization to -0.85 V. In Fig. 2.26a an overview of the tracer distribution in YSZ (after removing LSM) is given. In contrast to the situation discussed above the tracer intensity

beneath LSM is now significantly higher than on the free YSZ surface; see the high resolution image in Fig. 2.26b. The latter measurement was carried out in the area indicated by the square in Fig. 2.26a. Thus it reflects the tracer incorporation beneath LSM on the left hand side and conventional tracer exchange on free YSZ on the right hand side of the distribution image. From the integration zone indicated by the frame in Fig. 2.26b, the lateral tracer fraction profile in Fig. 2.26c was calculated. The amount of tracer incorporated on the free YSZ surface is in good agreement with that found for the less polarized sample. However, the tracer fraction incorporated beneath the LSM electrode is significantly higher – compare Figs. 26c and 26e. Possibly the increase in tracer fraction towards the 3PB is still caused by oxygen incorporated via a surface path, but for unambiguous interpretation a temperature gradient within the LSM electrode induced by the contact tip has to be ruled out. Nevertheless, it can be definitely concluded from comparison of both measurements that an increase of the cathodic polarization led to a significant increase of the importance of the bulk path.
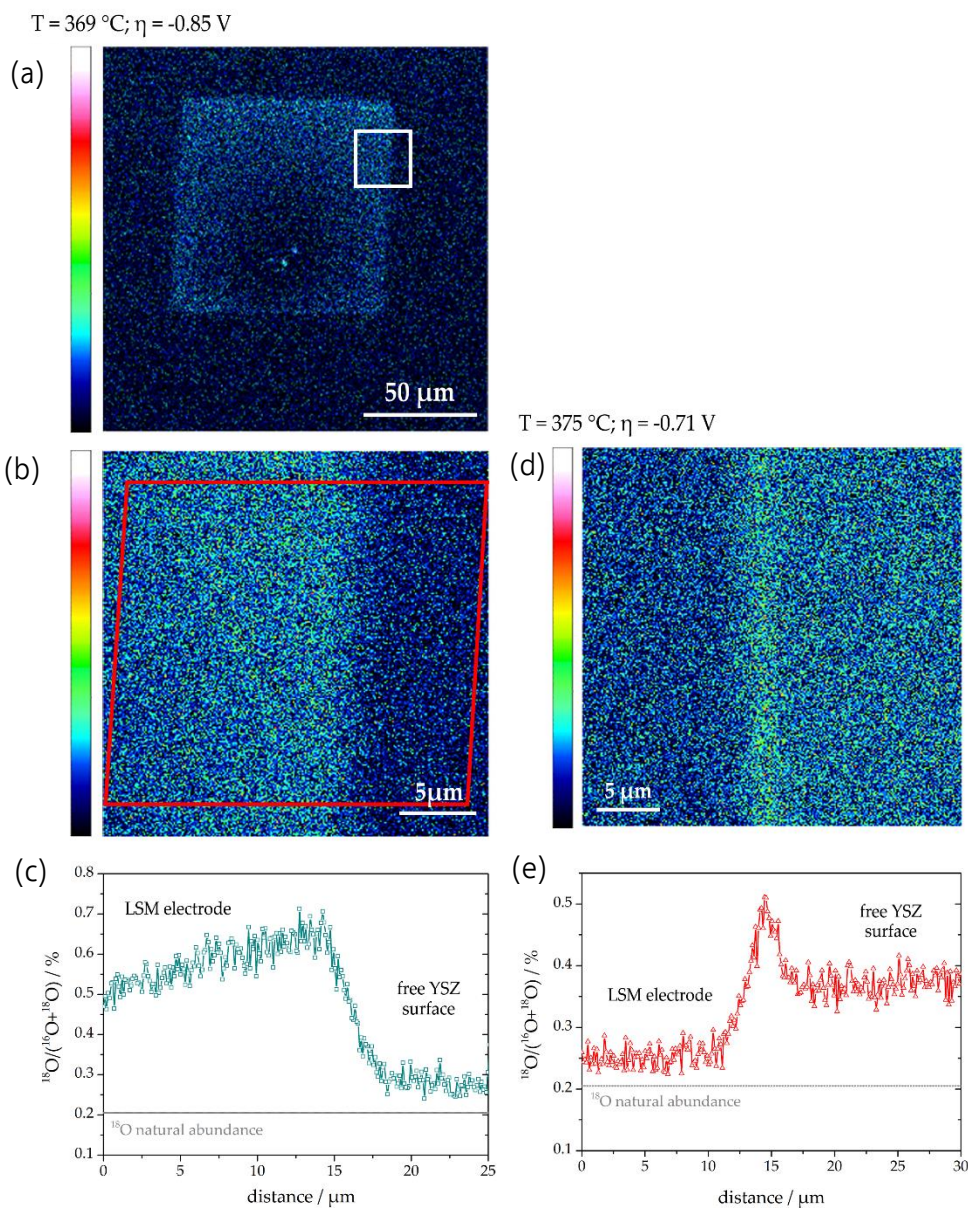
Fig. 2.26 (a) Overview image (intensity plot) showing the ^{18}O distribution measured in YSZ after removal of LSM. The tracer was incorporated at 369 °C with cathodic polarization of -085 V. The lower tracer intensity around the contacted region was most likely caused by a cooling of the thin film due to the tip. (b/d) High-resolution ^{18}O distribution image (intensity plot) measured in YSZ after removing the LSM electrode. The tracer was incorporated at (b) 369 °C with a cathodic polarization of η=–0.85 V and (d) 375 °C with a cathodic polarization of η=-0.71 V. (c) The LSM electrode was on the left hand side. Lateral tracer fraction profile calculated by line integration from the region indicated by the frame in (b). (e) Lateral tracer fraction profile calculated from (d) by line integration over entire height of the image.

This behavior is in excellent agreement with the interpretation of paths given so far. At low temperatures the surface path via 3PB dominates the oxygen reduction and rather high polarization is required to "activate" the bulk path at such low temperatures. Ultimately, i.e. for -0.9 V in our case, the application of a cathodic dc voltage (i.e. reducing conditions) leads to such a strong increase in oxygen vacancy concentration in LSM that the bulk path outperforms the surface path. Owing to the moderate cathodic overpotential used in this study, the concentration of electronic holes is still high enough to provide sufficient lateral conductivity. Hence, a homogeneous polarization of the thin film is possible – a sharp drop of incorporated ^{18}O within the electrode is not found here.

2.7   Conclusion

Two independent reaction pathways of oxygen reduction on lanthanum strontium manganite (LSM) thin films were successfully identified, quantified and modified. A surface path for oxygen reduction is found in a low temperature regime (below ca. 700 °C, depending on geometrical parameters). Here, the polarization resistance scales with the 3PB length and has an activation energy of ca. 1.4 eV. At high temperatures, a parallel bulk path with a much higher activation energy of the corresponding resistance (typically between 2.4 and 3.3 eV) becomes predominant. The transition temperature between the paths depends on the exact geometrical properties such as 3PB length and free LSM surface area and could be varied by more than 150 °C. Modifications of the paths were realized by variations of the microelectrode shape and by reducing the free LSM surface via a platinum capping layer. However, also a strong reduction of the

available LSM surface by a Pt capping layer cannot completely block the bulk path. Rather, a pseudo-3PB path across edges of LSM becomes relevant at high temperatures, probably with a change of the rate limiting step within the bulk path. Moreover, the film microstructure - in particular the grain size - affects the LSM bulk path and indicates an important role of grain boundaries in oxygen reduction on LSM. Accordingly, a variation of grain sizes by different deposition temperatures or high temperature annealing causes resistance changes of the LSM bulk path.

3. Temperature Gradients in Microelectrode Measurements: Relevance and Solutions for Studies of SOFC Electrode Materials

This chapter consists in large parts of a scientific paper published in "Solid State Ionics" [70].

3.1 Abstract

Microelectrodes on solid electrolytes, contacted by current-collecting tips, have become increasingly important for analyzing electrochemical properties of electrode materials in solid state ionics. In currently employed micro-contact set-ups for electrochemical impedance spectroscopy (EIS) measurements at elevated temperatures, samples are usually asymmetrically heated from the bottom side. It is shown experimentally, e.g. by thermovoltage measurements, impedance spectroscopy and infrared camera pictures, as well as by finite element modelling that substantial temperature gradients may arise in these experiments. Consequences in terms of data analysis are discussed and ways to alleviate the problem are described. For a complete avoidance of the temperature inhomogeneity problem, a novel symmetrically heated micro-contact set-up was built. This set-up allows fully automated measurements on one single microelectrode from room temperature to 1100 °C in varying gas atmosphere and with pressures from 2 bar to 0.01 mbar. Compared to experiments with asymmetric heating, electrodes measured in the novel set-up showed less degradation and no artifacts caused by thermovoltage.

This makes a mechanistic interpretation of the impedance spectra easier and allows long time measurements on single microelectrodes over weeks. Advantages of this new set-up are exemplified by EIS measurements on $(La_{0.8}Sr_{0.2})MnO_3$ (LSM) and platinum microelectrodes, both deposited on a single-crystalline yttria stabilized zirconia electrolyte. Different activation energies at high and intermediate temperatures could be quantified by accurate measurements on single LSM and Pt microelectrodes.

3.2   Introduction

Electrochemical impedance spectroscopy (EIS) is a key method in solid state electrochemistry and frequently applied not only to separate electrode and electrolyte impedance contributions but also to obtain mechanistic details of electrochemical reactions, for example in solid oxide fuel cells (SOFCs), solid oxide electrolysis cells (SOECs), and gas sensors. Electrodes optimized in terms of electrochemical performance are usually porous. However, since electrode kinetics also depends on geometrical parameters such as particle size, porosity, exact morphology and phase distribution (in composite electrodes), measurements on porous electrodes are often difficult to interpret in terms of reaction pathways and rate limiting steps. Progress has recently been made by 3D reconstruction studies to clarify geometrical details of composite electrodes [99-104] but efforts to obtain such details of porous electrodes are considerable. For an effective comparison of different materials and mechanistic studies, model electrodes were therefore successfully introduced. Two types of model electrodes are employed: macroscopically sized dense thin film electrodes and microelectrodes, which themselves may or may not consist of dense thin films.

Thin film electrodes can be deposited with defined structure on single crystalline electrolyte substrates. Often symmetrical samples with two identical electrodes are prepared, which can be investigated in a homogeneously heated furnace without problems caused by temperature gradients. However, this approach is not very flexible in terms of electrode geometry, and analysis of three phase boundary effects requires additional micro-patterning [42, 65, 74, 91, 105, 106]. Moreover, meaningful DC measurements can only be obtained when applying a reversible counter electrode or a three electrode arrangement. The latter is highly non-trivial in solid state electrochemistry due to difficulties in positioning the reference electrode [107, 108]. Also microelectrodes are commonly used in the field of solid state electrochemistry and a main advantage is simply the fact that minimizing the size maximizes the polarization resistance of the studied microelectrode. Hence, compared to the much larger counter electrode, a microelectrode has an orders of magnitude higher polarization resistance. Only the influence of the measured microelectrode is therefore seen in impedance spectra [65] and the counter electrode acts as a reference electrode. This geometry thus also enables measurements of the current-voltage characteristics of single electrodes.

A simple microelectrode experiment can be realized by pressing a metal wire or an oxide "pyramid" onto a single crystal [109-112]. Such experiments have been successfully performed in homogeneously heated furnaces and again avoid inhomogeneous temperature distributions in the samples. However, the corresponding microelectrode preparation and variation is elaborate, and even more important, the geometry of the point contact is rather ill-defined or hardly controllable. Therefore, geometrically well-defined thin film microelectrodes with sizes down to 10 µm in diameter have been

introduced [40]. This method combines the advantages of highly defined thin film electrodes with the advantages of microelectrodes. Mostly, films with known growth properties are deposited on single crystals and micro-structured by photolithography. A current collecting contact is established under a microscope by means of a contact tip. Since generally many microelectrodes, partly of different size and shape, exist on a single sample, the method is highly flexible and quick in terms of obtaining reasonable statistics, for example for varying geometrical parameters. Moreover, three phase boundary (3PB) and electrode surface are easily accessible to complementary analytical measurements.

However, to the best of the authors' knowledge such experimental set-ups are so far only realized by using asymmetrically heated hot stages [72, 113-115]. This asymmetrical heating (from the bottom side) and cooling (by convection, radiation and the contacting tip acting as a heat sink) is known to cause temperature gradients [83]. Those can lead to measurement artifacts and inconveniences including unknown exact temperature of the measured electrode, inhomogeneous temperature distribution within one electrode, additional degradation [82] and sample polarization. These uncertainties make identification of different or changing reaction pathways [65, 74, 83, 116-121] highly nontrivial. Additionally, temperature dependent measurements on one and the same microelectrode turn out to be difficult in such set-ups due to frequent contact loss during heating. Despite these problems, there is no study available that quantifies the local temperature inhomogeneity and analyzes its effects in electrochemical measurements in more detail.

In Ref. [83] an effective temperature (T_{spr}) of the measured electrode with diameter d_{ME} was calculated from the spreading resistance of the single crystalline electrolyte (YSZ=yttria stabilized zirconia). From the YSZ bulk (spreading) resistance R_0 and the known conductivity (σ_{ion})-temperature (T) relation with parameters E_a and σ^*, a temperature is calculated from

$$\sigma_{ion} = \frac{1}{2 d_{ME} R_{bulk}} = \sigma^* \cdot e^{-\frac{E_a}{k_B T}} \qquad\qquad 3.1$$

according to

$$T_{spr} = \frac{E_a}{k_B \cdot \ln(2 d_{ME} R_0)} \; . \qquad\qquad 3.2$$

This calculated temperature, however, is only an average temperature in the electrolyte region close to the microelectrode. It does not give exact information on the electrode surface temperature and the lateral thermal gradient inside the electrode itself. Moreover, this estimation via Eq. 3.2 is limited to circular electrodes.

In this chapter, the inhomogeneous temperature distribution in electrodes on asymmetrically heated samples is analyzed. Several methods are used to quantify the problem, including impedance measurements, micro-thermocouple measurements, and infrared camera visualization. Moreover, finite element calculations are employed to further analyze the temperature distribution. The influence of parameters such as temperature range, electrode size and contact tip diameter are investigated. In the second part, we introduce a novel micro-contact set-up (named MiMa) is introduced. It allows combination of the advantages of symmetrically heated samples and

microelectrode measurements on well-defined thin film microelectrodes with sizes down to 30 µm. The performance is demonstrated by different examples. For comparison, measurements are also conducted on a new, computer controlled, asymmetrically heated micro-contact set-up.

3.3 Experimental

3.3.1 Sample Preparation

$(La_{0.8}Sr_{0.2})MnO_3$ powder from Sigma Aldrich was isostatically pressed, sintered for 12 h at 1200 °C in air and used as target for the pulsed laser deposition (PLD) of thin films. Films were deposited on polished YSZ (100) single crystals (9.5 mol% Y_2O_3, CrysTec GmbH, Germany) using a KrF excimer laser (248 nm, COMPex Pro 101 F, Lambda Physics, Germany). Laser beam energy was set to 400 mJ per pulse at 10 Hz pulse frequency. The deposition was performed in $4 \cdot 10^{-2}$ mbar O_2 atmosphere at substrate temperatures up to 900 °C. The temperature at the YSZ surface was monitored by a pyrometer (Heitronics KT-19.99, Germany). The film thickness (between 100 nm and 240 nm) was controlled via deposition time and measured by scanning electron microscopy (SEM, FEI Qianta 200 FEG, Netherlands) and digital holographic microscopy of microelectrodes (DHM, Lyncee Tec, Switzerland). The microstructure and film growth was analyzed by SEM and transmission electron microscopy (TEM, FEI TECNAI F20). 400 nm platinum cover layers were deposited on top of the LSM films via DC magnetron sputtering (MED 020 Coating System, BAL-TEC, Germany) of Pt (99.95 % pure, OGUSSA, Austria) at room

temperature. The thickness of the platinum films was measured by ex-situ calibration using a quartz crystal micro-balance as well as by SEM. Platinum films without LSM were also deposited on YSZ (100) by DC magnetron sputtering. A detailed description of the platinum thin film fabrication is given in Ref. [58]. From the films, LSM, LSM/Pt and Pt microelectrodes were prepared by photolithography and subsequent ion beam etching with 2 keV Ar ions (LSM and LSM/Pt), or chemical etching in concentrated hydro chloric acid in case of LSM and in nitro hydrochloric acid for platinum.

3.3.2 Impedance Spectroscopy

Electrochemical characterization of the Pt, LSM and LSM/Pt microelectrodes was done by means of two point impedance measurements using an Alpha-A High Resolution Dielectric Analyzer with ZG-2 interface (Novocontrol, Germany). Impedance spectra were recorded at temperatures between 280 °C and 950 °C in the frequency range of $1 \cdot 10^6$ Hz to $1 \cdot 10^{-3}$ Hz with a resolution of 5 points per frequency decade. Parameterization of the spectra was carried out by the complex nonlinear least square (CNLS) fit software Z-View2 (Scribner, USA). The equivalent circuits used to fit the experimental data are shown in Fig. 3.1 (CPE means constant phase element). No attempt was undertaken to interpret R_1, R_2, (R_3), fitting was thus only performed to determine the DC polarization resistance of the electrode, given by the sum of R_1 + R_2 + (R_3).
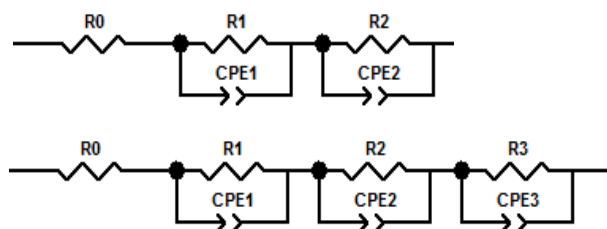
Fig. 3.1 Equivalent circuits used for the complex nonlinear least square fits

3.3.3 Optimized Asymmetrically Heated Micro-Contact Stage

An improved micro-contact set-up (Fig. 3.2) was used for measurements with asymmetrically heated hot stage. It allows set temperatures up to 1000 °C and experiments in variable gas atmosphere with pressures from 2 bar to $5 \cdot 10^{-2}$ mbar. Moreover, a high pressure washing bottle is included to control the humidity during the measurements. Possibility of highly accurate and reliable contacting of microelectrodes is achieved by placing all moving parts for contacting inside the heated vacuum chamber. These moving parts are designed with minimum size and fabricated of stiff materials, making the set-up less prone to vibration induced decontacting of the microelectrodes. Nine computer controlled piezo actuators (Agilis Newport, USA) are applied with step size of 50 nm in X- Y-, and Z-direction for positioning up to three contacting tips. Electrical contact to the measured electrodes is established under a microscope (Mitutoyo, Japan) using a USB camera. The set-up allows contacting of small structures down to the µm scale and changing the contacted electrode within seconds. The hot stage for asymmetric heating was mounted on a water cooled stage as heat

protection for the piezo actuators. The whole set-up is placed on a vibration damping table.
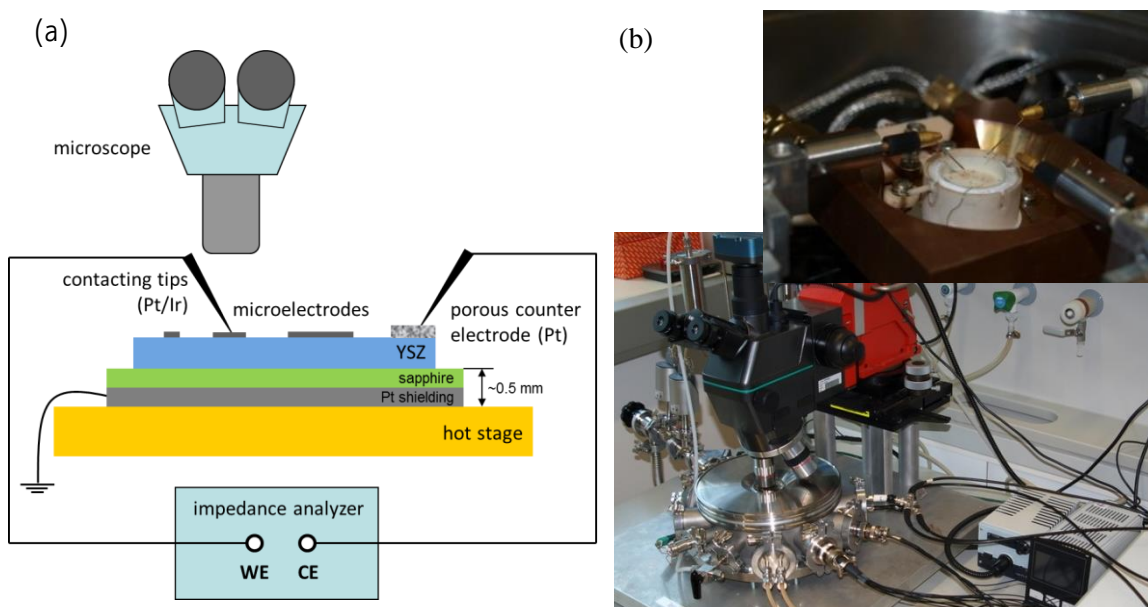
Fig. 3.2 (a) Sketch of the conventional micro-contact set-up with asymmetric heating. (b) Photograph of the improved set-up and view on the hot stage mounted on a cooling stage inside the vacuum chamber.

Even though the vacuum chamber acts as Faraday cage, the hot stage inside the vacuum chamber can influence the impedance spectroscopy measurements. Stray fields can be minimized with an electrically grounded shielding plate between sample and hot stage but only at the expense of a decrease of the sample temperature compared to the set temperature. Despite all optimizations it remains difficult to perform measurements on one single microelectrode without losing electrical contact while increasing (high) temperatures: Since the contacting needle is fixed at the cold end and is not exactly perpendicular to the sample surface (to retain visibility of the electrode in the

microscope), thermal expansion of all parts during temperature increase often causes disconnection of a microelectrode.

3.4 The Temperature Distribution in an Asymmetrically Heated Sample and Visualization of its Consequences

3.4.1 Measurements of Local Temperature Distributions and Their Consequences

For temperature measurements a sample set-up was chosen consisting of a 400 nm Pt film on a 0.5 mm thick YSZ single crystal. The film was micro-structured (circular microelectrodes of $\emptyset$=50-300 µm) with a remaining continuous platinum film (ca. 1 mm in width) at the edges of the YSZ crystal. Two different contact tips were used, one platinum (a) and one platinum (90%)/rhodium (10%) (b). Both tips are the ends of long thin wires directly connected to type S thermocouple compensation wires. The first experiment is based on thermovoltage measurements in an asymmetrically heated micro-contact set-up. The hot stage temperature was set to 800 °C ($T_{hot\ stage}$) and both contacting tips were placed in a distance of several millimeters on the continuous Pt film at the sample edge (Fig. 3.3 (1.)). The platinum tip (a) together with the platinum film on the YSZ sample acts as negative part of a thermocouple type S, the Pt/Rh tip (b) as the positive one. The thermovoltage measured between the two wires is determined by the exact local temperature of the Pt/Rh tip (b) on the Pt film (marked with arrow (A) in Fig. 3.3). The reference point of the thermocouple was at room temperature.

This measurement reveals how much the contact tip affects the local temperature by cooling. For a hot stage set temperature of 800 °C the measured thermovoltages reveal local temperatures (T_{TC}) far below this set value: For a contact tip with a tip radius of 2 μm 580 °C are found, while a blunt tip (>10 μm radius) causes even 570 °C. Reducing convection by an additional cover plate above the sample reduces the difference to the set temperature (606 °C for 2 μm tip radius) and indicates that the local cooling is not entirely caused by the contact tip. However, this local temperature at the tip is the lowest one in the entire sample and calculations (see below) as well as a second type of "temperature measurement" show that large parts of the microelectrode and the bulk beneath the microelectrode are much closer to the set temperature.
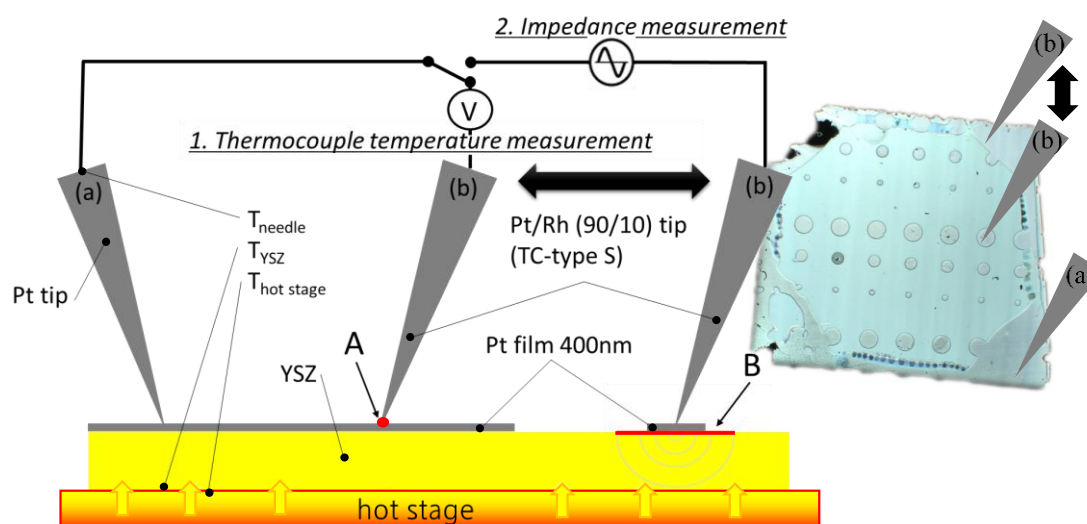

Fig. 3.3 Measurement of the temperature distribution for platinum microelectrodes and a continuous platinum film on YSZ, using micro-thermocouple measurements (1) and impedance spectroscopy (2). Arrow A and arrow B point on a red spot or line, thus on red area indicating the relevant region of the measurement.

The second estimate of the "local" temperature was obtained indirectly from a measured resistance: The impedance was measured between the microelectrode being contacted by the Pt/Rh tip and the extended Pt film counter electrode (Fig. 3.3 (2.)). The YSZ electrolyte resistance was extracted from the impedance spectrum and a temperature (T_{spr}) was calculated from Eq. 3.2 [83]. The bulk resistance of such a microelectrode experiment is largely determined by a small sample region which roughly corresponds to a hemisphere with a radius of the microelectrode diameter [122] (Fig. 3.3b below red area B).

Smaller electrodes lead to lower average temperatures, with values of 710 °C (740 °C) measured with 2 µm contact tip radius and Ø=50 µm (200 µm) microelectrode for 800 °C set temperature of the hot stage. For comparison, also a blunt tip with a tip radius of >10 µm was used for impedance measurements on the same microelectrodes. Those showed much stronger cooling effects with a temperature of 660 °C for an Ø=50 µm microelectrode. Obviously, differences between sharp and blunt tips are more pronounced for T_{spr} compared to T_{TC} since the large contact area between tip and microelectrode draws more heat out of the sample.

Hindering the convective cooling by closing the vacuum chamber again decreased the difference to the set temperature by a few degrees. The cooling also strongly depends on the contacting force which presumably changes the contact area between tip and microelectrode but also heat transfer from the hot stage to the sample. Calculated temperature values (T_{spr}) for microelectrode diameters from Ø=50 µm to Ø=200 µm, measured with sharp and blunt contacting tip for open and closed cover plate, are summarized in Fig. 3.4a. In this diagram, also the local temperature at the contact tips

(T_{TC}) is shown, measured in the micro-thermocouple experiment described above. Not surprisingly this local temperature is substantially lower than T_{spr} since it is the lowest temperature of the entire sample while T_{spr} averages over a certain bulk region.
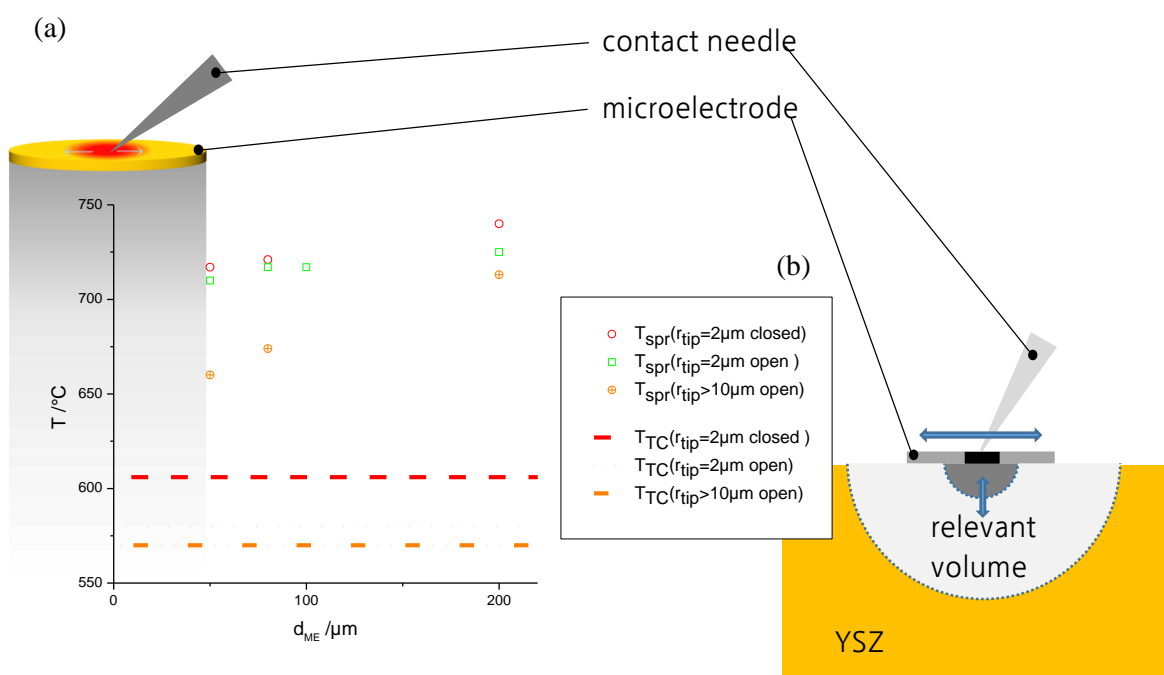
Fig. 3.4 (a) Temperatures determined for different Pt microelectrodes of radius r_{ME} on an asymmetrically heated sample with set temperature $T_{hot\ stage}$=800 °C. Lines indicate temperatures T_{TC} measured with a micro-thermocouple. "Open" and "closed" indicate whether or not the vacuum chamber is closed by its cover plate. (b) Sketch indicating the volume relevant for T_{spr} (approximation according to Ref. [83]) and its dependence on the microelectrode size.

3.4.2 Simulation of the Local Temperature Distribution

Finite element calculations were performed with COMSOL Multiphysics® (COMSOL, Sweden) for a cylindrical YSZ sample, 5 mm in diameter and 0.5 mm thickness. In the center of the top side there was a microelectrode with varying diameter (d_{ME}) from

Ø=20 µm to Ø=300 µm (thickness of 200 nm) and a current collecting tip with varying contact radius from 0.5 µm to 10 µm. The geometry is shown in Fig. 3.5 (cylindrical electrolyte only partly visible), together with typical temperature distributions. The shape of the tip resembles that of the tips used in the experiments. A counter electrode was placed on the bottom side. Temperature and current distributions were calculated in the sample. The model also includes cooling effects by convection in air, thermal conduction in the Pt tip and radiation to the ambiance. The temperature distribution in the sample was calculated by solving the equation

$$\rho C_p \frac{\partial T}{\partial t} - \nabla \cdot (k_T \nabla T) = Q \qquad\qquad 3.3$$

which includes the following material properties: density ρ (ρ=5680 kg·m^{-3} for YSZ and ρ=21450 kg·m^{-3} for Pt), the heat capacity C_p (C_p=0.6 J·kg^{-1}·K^{-1} for YSZ and C_p=130 J·kg^{-1}·K^{-1} for Pt), thermal conductivity k_T (k_T=2.5 W·m^{-1}·K^{-1} for YSZ and 71.6 W·m^{-1}·K^{-1} for Pt), heat source (or sink) Q=0. If not mentioned otherwise, the microelectrode is assumed to be an oxide microelectrode with ρ, C_p, and k values approximated by those of YSZ. The boundary conditions

$$-n \cdot (-k_T \nabla T) = h \cdot (T_{amb} - T) \qquad\qquad 3.4$$

describes convection of the surfaces with normal vector n. The heat transfer coefficient h depends on the dimensions of the exposed surface, air pressure and the ambient temperature T_{amb}; it was calculated according to the model implemented in Comsol [123] for natural convection of a horizontal plate aligned upside in air of 1 atm. Radiation to ambiance is described by

$$-n \cdot (-k_T \nabla T) = \varepsilon k_B (T_{amb}^4 - T^4) \qquad\qquad 3.5$$

including the surface emissivity ε, and Boltzmann's constant k_B. In all simulations the bottom side of the YSZ (T_{YSZ} in Fig. 3.3) was set to 800 °C, i.e. any temperature step between hot stage and sample bottom side (Fig. 3.3) was neglected. All other surfaces included a convection term (Eq. 3.4) and thermal radiation (Eq. 3.5) with surface emissivity ε=0.7 for YSZ and oxide microelectrode and ε=0.5 for platinum.

Typical temperature distributions are shown in Fig. 3.5 and reveals very strong temperature gradients close to the contact tip. Fig. 3.6 displays temperature distributions along the surface of the microelectrode for different tip radii of the contact needle and different microelectrode diameters. Most obvious is the very strong temperature drop by more than 200 °C directly beneath the contact tip. This result is in excellent agreement with the thermocouple measurements shown in section 3.4.3. However, this does not mean that the entire microelectrode is at low temperature. Rather, the temperature sharply increases within a few µm to much higher values and large parts of the microelectrode exhibit temperature variations of "only" 10 to 30 °C. Particularly for very sharp tips most of the lateral temperature inhomogeneity can be localized to a very small region in the center of the microelectrode. Fig. 3.6c displays temperature distributions in Z-direction (into the YSZ beneath the contact tip, perpendicular to the microelectrode surface) for 1 and 9 µm tip radii. Also the cooling in the YSZ depth is strongly influenced by the tip radius. The fact that the surface T is lower than the set temperature of the hot stage also for sharp tips (and even without tips) is due to heat losses caused by radiation and convective cooling at the entire sample surface, see also (Fig. 3.5 color gradient in Z-direction/ in tip direction).
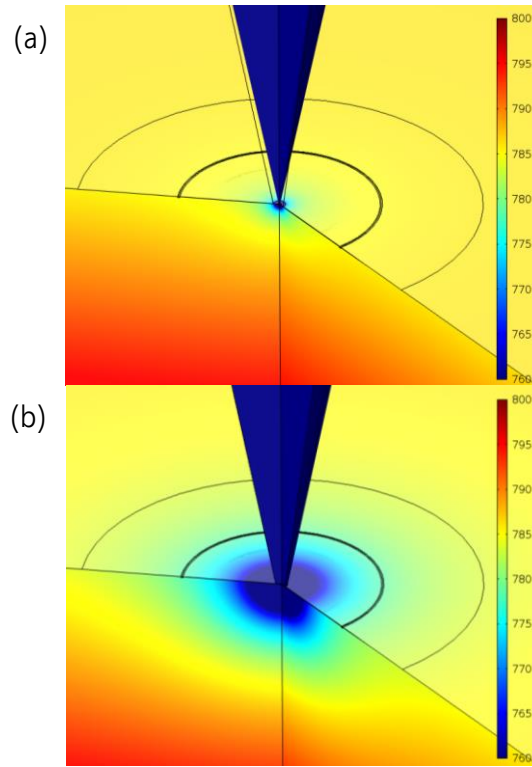
Fig. 3.5 3-D picture of the temperature distribution of an Ø=200 μm microelectrode calculated by the finite element method, hot stage set temperature of 800 °C, contact tip radius of (a) 1 μm and (b) 9 μm, temperature range from 760 °C to 800 °C. The inner circle represents the ø=200 μm microelectrode, the outer circle corresponds to the distance of two times the electrode diameter (2·d_{ME}=400 μm).

This calculated temperature distribution was then used to determine the local conductivity of YSZ according to Eq. 3.1 with E_a=0.767 eV and σ_0 =157.9± 16.3 Ω^{-1} cm^{-1}. E_a and σ_0 were experimentally obtained from impedance measurements and are valid in the temperature range from 675 to 1000 °C. For the sake of simplicity, these parameters were used for all temperatures considered here, accepting small errors (e.g. 3% error of YSZ conductivity at 550°C). More specific, a second finite element simulation was simultaneously performed by solving

$$div(-\sigma \cdot grad(\varphi)) = 0 \qquad\qquad 3.6$$

93

which includes the temperature dependent electrical conductivity σ and the electrical potential φ. Boundary conditions were φ=-1 V at the contacting tip and φ=0 V at the hot stage. The resulting current density distribution was used to calculate the effective YSZ bulk (spreading) resistance and then an averaged temperature was determined from Eq. 3.2, as in the experiment. These temperatures (T_{spr}) are plotted in Fig. 3.7. The cooling power of the current collecting tip and the holding clamp was estimated from temperature measurements by a thermocouple. For 800 °C hot stage set temperature a clamp temperatures of 200 °C was measured in a distance of 15 mm from the hot stage.

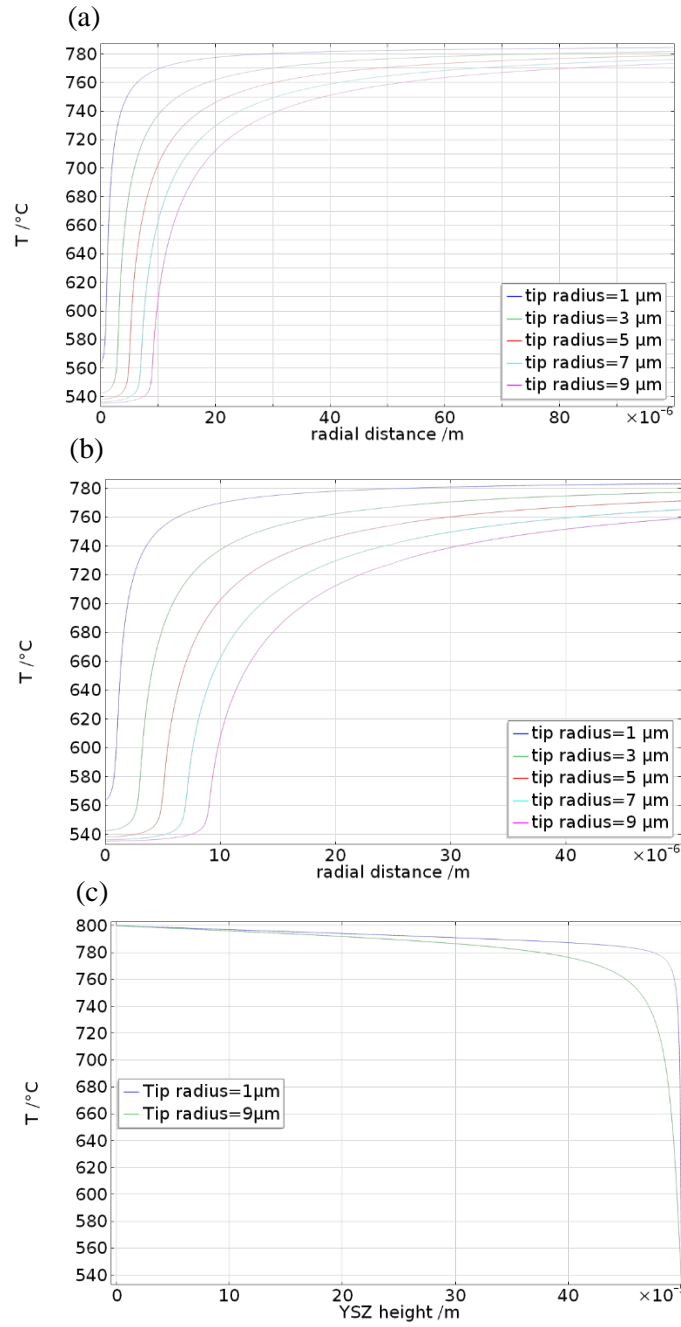**Fig.** 3.6 Calculated temperature distribution along the YSZ microelectrode interface showing the influence of the contact tip radius for (a) an ø=200 μm and (b) an ø=50 μm electrode at 800 °C set temperature (T_{YSZ}). (c) Temperature distribution along the Z-axis, perpendicular to the microelectrode surface into YSZ, beneath the contact tip, for two different tip radii of 1 and 9 μm.
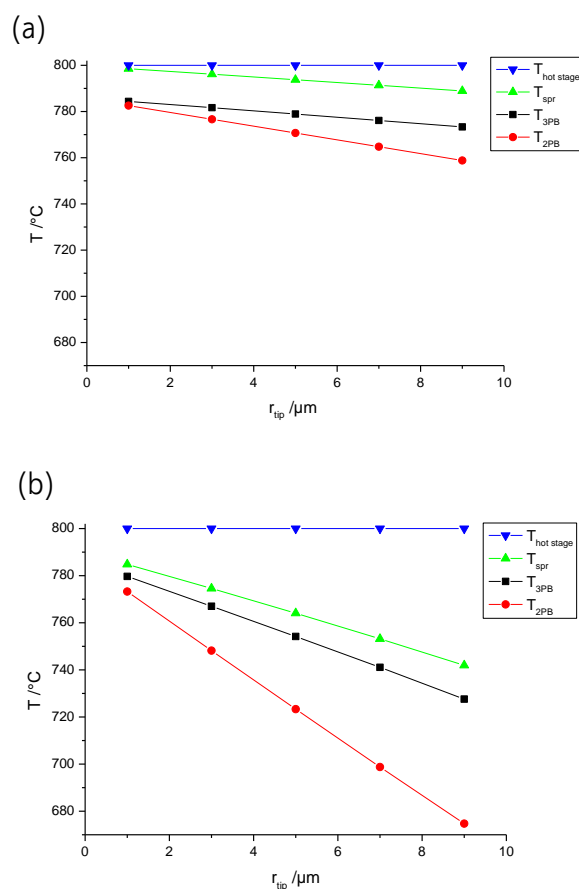
Fig. 3.7 Calculated temperatures for (a) $\varnothing$=200 µm and (b) $\varnothing$=50 µm LSM electrodes at 800 °C hot stage temperature contacted with different tip radii. All calculated temperatures result from simulated current distributions in the YSZ.

Despite the unavoidable temperature gradient it might be reasonable to define also a kind of "effective" temperature of the microelectrodes. The most appropriate approach, however, depends on the mechanism of the electrochemical electrode reaction. For systems with prevailing three phase boundary (3PB) mechanism the temperature of the outer rim of the microelectrode is relevant. Fig. 3.7 displays how much this temperature (T_{3PB}) depends on tip radius and microelectrode diameter. The difference between T_{spr} and T_{3PB} is not very pronounced (5.5 K for an $\varnothing$=80 µm electrode with r_{tip}=1 µm and

13.3 K for an Ø=200 µm electrode with r_{tip}=9 µm, both 800 °C hot stage set temperature) with T_{3PB} being always lower than T_{spr}. Therefore T_{spr} is indeed a reasonable estimate of the true 3PB temperature. Moreover the temperature distribution is only slightly influenced by the electrode material. The simulation for a LSM microelectrode gives a slightly higher three phase boundary temperature compared to a Pt microelectrode, caused by the better thermal conduction of Pt.

For a bulk path with oxygen exchange taking place at the entire surface [20, 21, 40, 66], it is more appropriate to calculate an area-weighted temperature similar to the way of determining effective temperatures from the spreading resistance. We therefore define

$$T_{2PB} = \frac{4}{d_{ME}^2} \int T(r) \cdot r \cdot 2 \cdot dr \, .$$

3.7

It would be even more accurate to also include an Arrhenius type weighting factor in the integral. Then the result would depend on the activation energy. The calculated temperature T_{2PB} is always lower than the 3PB temperature (Fig. 3.7) and is more sensitive to the tip cooling power. The influence of the needle cooling decreases with increasing electrode diameter since the local cooling beneath the tip is almost independent of the microelectrode and its size. However, the averaged cooling effect, reflected by T_{2PB}, is stronger on smaller microelectrodes. Particularly for large contact tip radii and small microelectrodes T_{spr} might significantly overestimate T_{2PB}. Moreover, the exact value of T_{2PB} is strongly influenced by the convection behavior.

 All together two rules of thumb might be given. The temperature of the heavily cooled sample part beneath the contact tip is mainly determined by the hot stage set

temperature and the mere fact of using a contact tip but much less by the tip radius. The size of the cooled area on the microelectrode, however, strongly depends on the contact tip size. A small tip radius (1-2 µm) only lowers the temperature in a small area while a blunt tip (r_{tip}>5 µm) can affect a significant area, of a microelectrode and can cause considerable temperature errors at high measurement temperatures, particularly for small microelectrodes with a bulk path.

3.4.3 Visualizing the Temperature Inhomogeneity

A cathodic DC voltage of -900 mV was applied to a LSM microelectrode at 372 °C set temperature. After a time span of 200 s a steady state current could safely be assumed. Then a $^{18}O_2$ gas stream (97.1 % isotopic enrichment, Cambridge Isotope Laboratories, UK) with 1.5 ml·min^{-1} was locally supplied to a contacted LSM microelectrode for 600 s by means of a quartz capillary [124]. After such a voltage driven oxygen tracer incorporation the sample was quenched on a cold metal block. Only the contacted microelectrode was removed in hydro-chloric acid. The YSZ region beneath the former LSM electrode was investigated by time-of-flight secondary ion mass spectrometry (ToF-SIMS 5 instrument, ION-TOF GmbH, Germany). Fig. 3.8a and 8b display the ^{18}O tracer distribution and a cross-section profile in the near-surface region, with a sputter depth of ca. 3 nm in YSZ. The ^{18}O tracer is very asymmetrically distributed with maxima at both 3PBs and much higher fraction on one side of the former microelectrode.

In principle, the enhanced tracer level at the three phase boundary could reflect the dominance of a 3PB related surface path, compared to oxygen reduction through the LSM bulk. However, under strong cathodic bias oxygen reduction on LSM

microelectrodes can be expected to takes place mainly via the bulk path [66]. This is confirmed by tracer measurements performed in the novel MiMa set-up (chapter 4) and thus without a temperature gradient in the sample Fig. 3.8c and d. An almost flat concentration profile is found in the latter case. The drastic variation in ^{18}O content in Fig. 3.8a, b therefore visualizes the temperature gradient, caused by the contacting tip. The tip creates a local cooling with a lateral temperature distribution in the microelectrode. Lower temperatures decrease the thermally activated oxygen reduction and incorporation into the YSZ. The needle was located on the left part of the microelectrode and thus the oxygen incorporation was lowest close to this point. Towards the 3PB the temperature again increases and higher tracer fractions are found, particularly on the right hand side. Bright spots at the needle contact point in the center of the dark area of Fig. 3.8a indicate higher ^{18}O concentration due to holes in the film. (The needle can damage the LSM film during the contacting procedure). Further information on such experiments, also revealing true 3PB related effects, are given in Ref. [33].
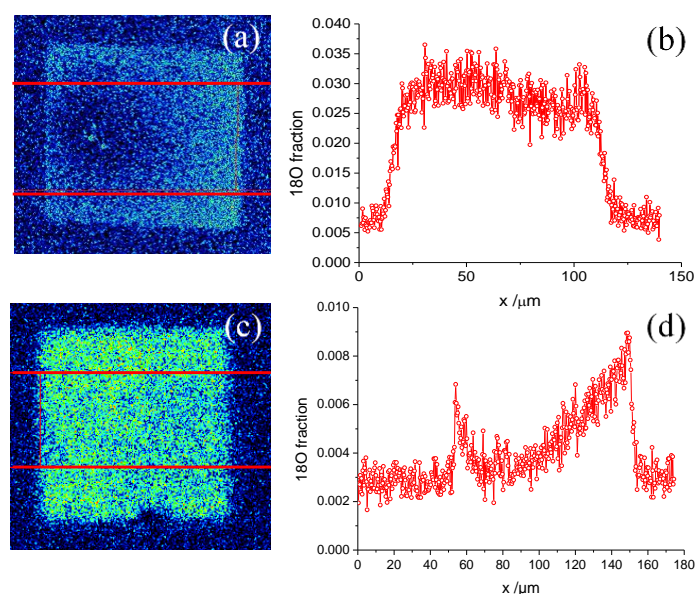
Fig. 3.8 (a)/(b) ^{18}O content beneath a 100·100 µm^2 LSM electrode polarized at in the conventional set-up with asymmetric heating at T_{spr}=372 °C, -900 mV, ca. 5·10^{-8} A. (c)/(d) ^{18}O content beneath a 100·100 µm^2 LSM electrode measured in MiMa at 466 °C, -900 mV, 8·10^{-7} A. Red lines in (a) and (c) show the integration area for (b) and (d), respectively. Red lines in (a) and (c) indicating integration areas.

In a second experiment to visualize the temperature distribution, an infrared camera with high spatial resolution was used (Infratec, ImageIR® 9300). A color coded temperature distribution is given in Fig. 3.9 with one microelectrode being contacted (r.h.s). The corresponding temperatures in cross-sections of a non-contacted and a contacted microelectrode are given in Fig. 3.9. True temperatures may be somewhat different since materials emission properties are not considered. At 300 °C hot stage set temperature the contacted 200 µm LSM electrode shows a gradient of approximately 6 K from the 3PB to the needle. This difference seems to be small but the steepest part of the gradient is expected below the needle, and was not visible in this experiment. Indeed a finite element calculation of the expected temperature distribution for 2 µm

tip radius results in a temperature decrease of 10 °C between 20 µm and 100 µm distance to the needle (center). Therefore good agreement of experiment and simulation can be concluded.
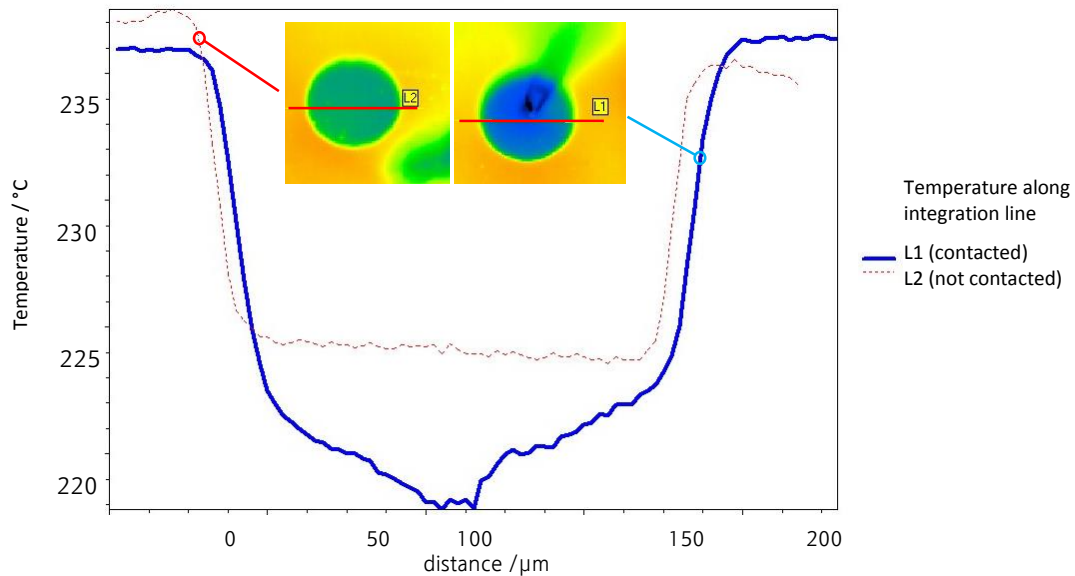
Fig. 3.9 Infrared camera picture of LSM microelectrodes (Ø=200 µm) on YSZ, the microelectrode on the r.h.s. was contacted by a tip at hot stage set temperature of 300 °C. Material emission properties are not included. The varying temperature distribution at the YSZ surface could be caused by infrared transition through the YSZ from the inhomogeneous Pt counter electrode on the back side of the sample. Line scans show the temperature distribution of a contacted (blue) and a not contacted (red dotted) LSM microelectrode (lines are indicated) in the infrared picture.
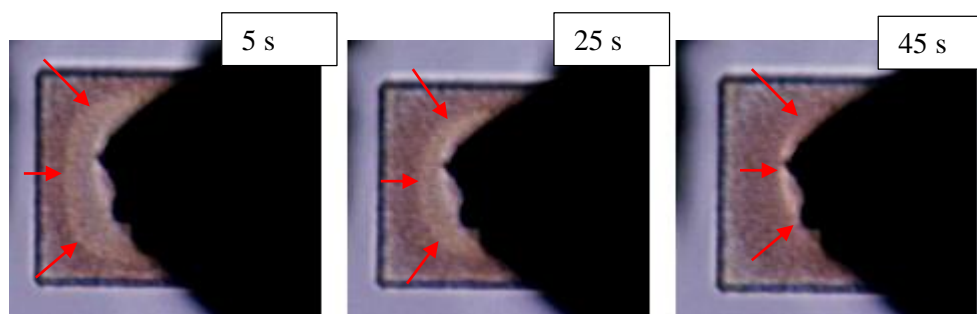
Fig. 3.10 100·100 µm^2 squared LSM electrode at T_{set}=400 °C after exposing to -3 V bias for different times (5, 25 and 45 s). Reduction starts near to the 3PB and is slower close to the cold contacting tip. The contrast is determined by reflection rather be the true LSM color.

A last experiment indicating existence of a lateral temperature profile is the following: In Fig. 3.10 the reduction process of a LSM thin film microelectrode, caused by high cathodic bias starts from the 3PB region (T_{set}=400 °C, -3 V bias). In this parameter regime (bias, temperature) oxygen reduction takes place via a bulk path [33, 66] and from this one might expect a homogeneous discoloration (reduction) upon strong cathodic bias. However, discoloration in Fig. 3.10 is faster near the 3PB and becomes slower towards the contact tip which is in good agreement with the temperature decrease due to local cooling found in measurements and finite element temperature calculations.

3.5 Novel Symmetrically Heated Micro-Contact Stage "MiMa"

3.5.1 Experimental Realization

In order to perform microelectrode measurements in a homogeneously heated surrounding, a novel micro-contact set-up was designed (Fig. 3.11). In the following it

is named "MiMa", which reflects the fact that microelectrodes (Mi) can be measured in a set-up usually employed for macroscopic (Ma) electrodes. Samples are essentially the same as for asymmetrically heated microelectrode measurements with microelectrodes on one side of a solid electrolyte (here YSZ single crystal) and a counter electrode on the other side (here porous platinum). The main difference to earlier microelectrode measurements in homogeneously heated set-ups [109] is the fact that in MiMa the contact tip is not used as micro-contact/microelectrode but rather only to contact well-defined thin film microelectrodes already deposited on the electrolyte.

The vacuum chamber consists of stainless steel and quartz parts. All inner parts in the heated chamber are fabricated of platinum and corundum or quartz. A corundum tube is mounted on an expansion bearing near the cold end of the vacuum tube and acts as tip contact arm. A Pt/Ir tip is fixed on the other side of the corundum tube with a corundum screw. The contact between the microelectrode and the Pt/Ir tip is established under a microscope with a micro-manipulator outside of the heated area (Fig. 3.11a and b). For this purpose a micro-manipulator is moved to lift-up the tip contact arm with a blade. After the needle is aligned to the center of the selected microelectrode the tip contact arm is lowered. As soon as contact is established, blade and micro-manipulator are removed, a tube furnace is moved over the sample and the vacuum chamber is closed. A properly contacted microelectrode can now be measured from room temperature up to 1100 °C and from $1 \cdot 10^{-2}$ mbar up to 2 bar in different gas atmospheres without losing contact. The temperature is monitored with a thermocouple type S or type K positioned next to the sample. The oxygen partial pressure can be monitored with a lambda sensor (MicroPoas Setnag France).
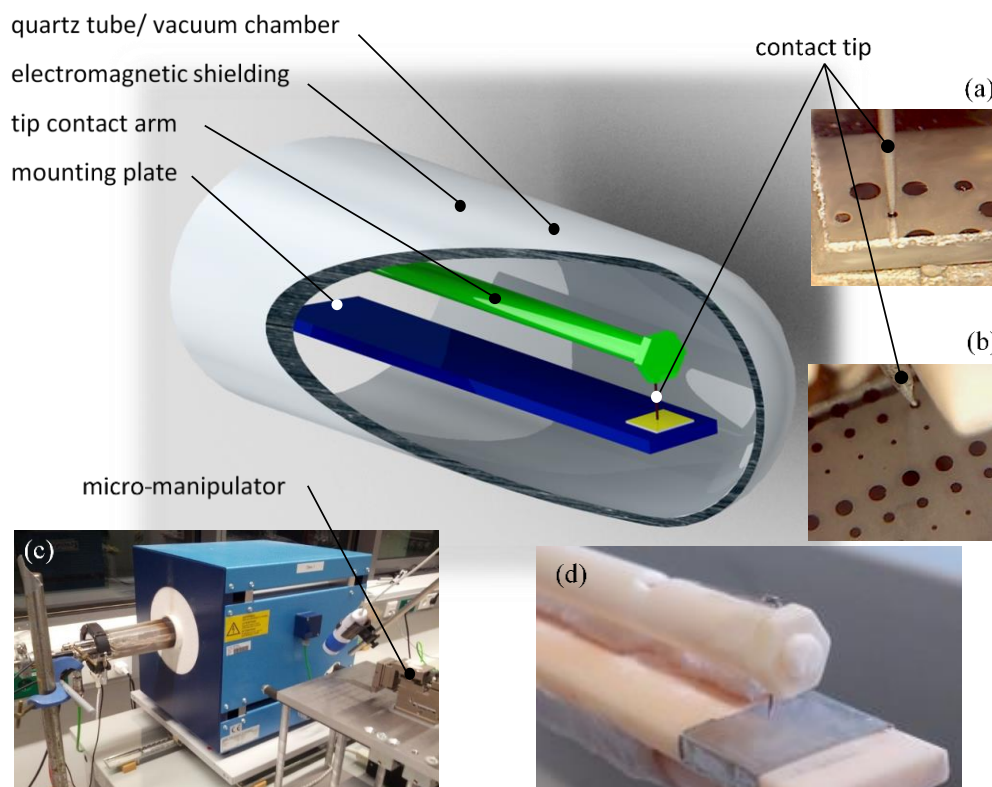
Fig. 3.11 3D sketch of the tip contact arm, mounting plate and quartz tube of the symmetrically heated micro-contact set-up MiMa. Small pictures (a) & (b) show contacted microelectrodes before the tube furnace is moved over the sample. (c) Whole measurement set-up with contacting device. (d) Tip contact arm with Pt/Ir contacting tip on mounting plate with platinum foil (without sample).

3.5.2 Reproducibility and Measurement Stability of Microelectrode Measurements in MiMa

The stability and high flexibility of MiMa microelectrode measurements in terms of temperature variations is demonstrated by an impedance measurement series on a LSM microelectrode (d_{ME}=300 µm).
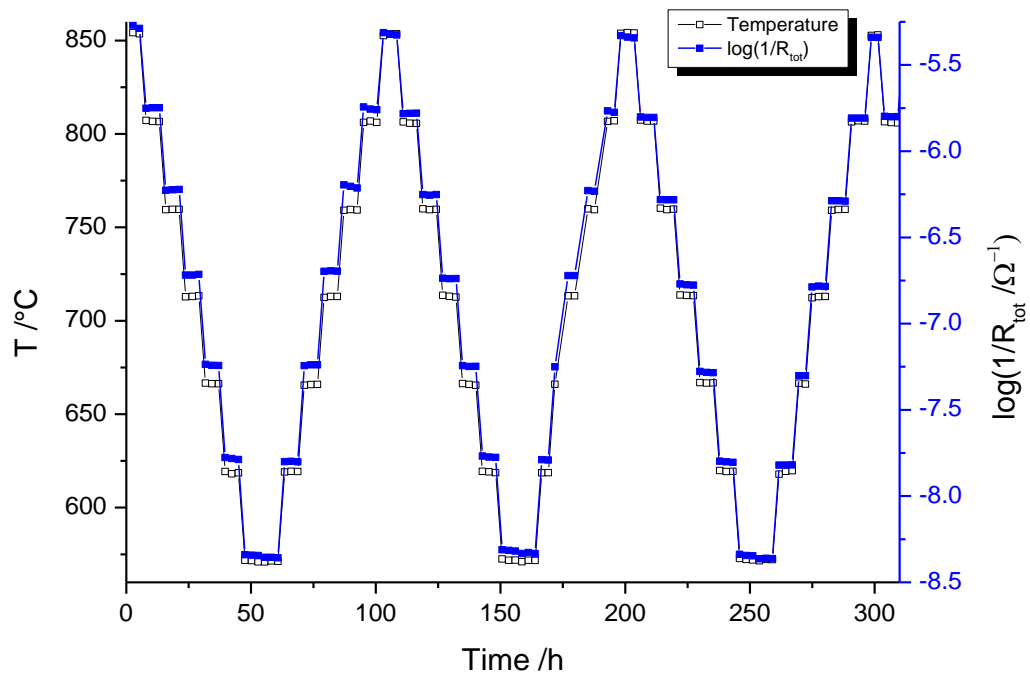
Fig. 3.12 Temperature and electrode polarization resistance (R_{tot}) variation of an Ø=300 μm LSM microelectrode for a long time measurement (>300 h).

Several temperature sweeps between 560 and 860 °C and a measurement time of more than 300 h on one and the same microelectrode did not cause significant changes of the polarization resistance R_{tot} (Fig. 3.12). R_{tot} was obtained from the measured impedance spectra by fits to the equivalent circuit of Fig. 3.1, see above. It should again be emphasized that such temperature cycles are not possible in the asymmetrically heated set-up presented above due to frequent loss of contact during heating and destruction of the microelectrode by several contacting procedures.

3.5.3 Comparison Between Asymmetrically and Symmetrically (MiMa) Heated Set-up for Bulk Path Kinetics

In a second experiment, one and the same square LSM electrode (145 µm edge length) was analyzed by impedance spectroscopy at different temperatures in both set-ups. The series in MiMa was obtained after a single contacting procedure while in the asymmetrically heated set-up a careful contacting and de-contacting had to be performed for each temperature to avoid microelectrode damage. In a pseudo-Arrhenius plot (Fig. 3.13), the electrode polarization resistance is plotted versus the logarithm of the inverse high frequency off-set R_0 obtained from fits to the circuits in Fig. 3.1. In case of circular microelectrodes, the YSZ bulk resistance is analytically given by Eq. 3.1, at least in the semi-infinite case. Here, however, rather large square microelectrodes were employed and the numerical factor relating R_0 and σ_{ion} is unknown. Hence, we use $\log(1/R_0)$, which is still proportional to a nominal T_{spr}, as X-axis in order to compare results from the two set-ups. The resistance measured in MiMa shows a change of the slope from low to high temperatures, indicating a reaction mechanism change from surface to bulk path [32]. The same is true for the measurement in the asymmetrically heated contact stage, but there the resistance decreases stronger towards higher temperatures.
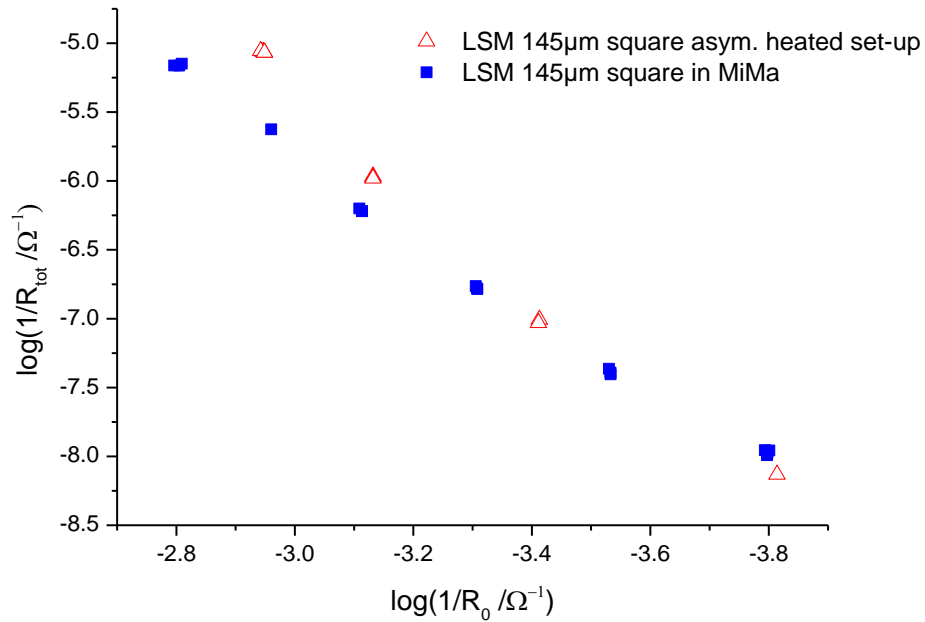
Fig. 3.13. log $1/R_{tot}$ vs. log $1/R_0$ from a 145·145 μm^2 squared LSM microelectrode measured in MiMa and in the asymmetrically heated set-up (impedance spectra are shown in Fig. 3.14), temperature range is approximately 550 °C (at log $1/R_0$=-3.8) to 850 °C (at log $1/R_0$=-2.8).

This stronger change in slope is most probably a systematic error of the asymmetrically heated micro-contact set-up and related to the thermovoltage resulting from temperature gradients in the sample. For a Pt/YSZ/Pt system a thermoelectric power of 0.486 mV·K^{-1} was reported [125, 126]. Thermovoltages of several 10 mV, often measured in our asymmetrically heated micro-contact set-ups, are in good agreement with this value. The additional thermovoltage causes a shift of the electrode reaction out of equilibrium and changes the polarization resistance R_{tot} of an impedance experiment. For LSM thin film electrodes (and many other materials) R_{tot} becomes smaller upon bias, and thus is in accordance with the result in Fig. 3.13. This thermovoltage induced resistance change becomes stronger towards high

temperatures since the temperature gradient also increases. Complete absence of a difference between MiMa measurements and the experiment in the asymmetrically heated se-up case at lower temperatures might be caused by the fact that here the three phase boundary becomes relevant for LSM microelectrodes [32], see also section 4.4. In general, details of the contacting procedure may affect the local temperatures and thus thermovoltages may vary significantly. Therefore different electrode resistances can easily be found for microelectrode studies in asymmetrically heated set-ups, despite nominally identical measurement conditions.

The shape of the impedance spectra (Fig. 3.14) measured in both set-ups shows only minor differences. However, it was reproducibly found that measurements obtained for an asymmetrically heated micro-contact set-up exhibit stronger irreversible changes. Already after 4 min the spectra were different, while data obtained in MiMa show no observable change after 25 min, both displayed in Fig. 3.14. This could also be related to the much stronger degradation of Pt microelectrodes found in a conventional asymmetrically heated set-up, compared to annealing with homogeneous temperature [82]. Exact reasons are not known yet, but a certain role of the temperature gradient is highly probable. Degradation might be driven by gradients in chemical potential which may not only be caused by different oxygen partial pressures, but also by voltages or temperature gradients which again lead to (thermo-)voltages. This first example revealed that both set-ups lead to the same qualitative conclusion in terms of a mechanism change but the asymmetrically heated experiment might be less reliable on a quantitative level.

A second example shows that in other cases also quantitative information fit together: It was already reported in an earlier publication that platinum microelectrodes reduce oxygen via a bulk path below 450 °C [58]. Reconsidering this experimental regime shows that no difference can be found when comparing measurements performed in MiMa and in an asymmetrically heated micro-contact set-up (Fig. 3.15). Here we most probably have less thermovoltage effects due to smaller measurement temperature and thereby less temperature gradients, and the determination of the exact electrode temperature is also less critical due to the low activation energy in this regime. The large spreading of data points is due to fitting inaccuracies caused by the high polarization resistance of platinum microelectrodes at these temperatures. The fitting approach is explained in Ref. [58].
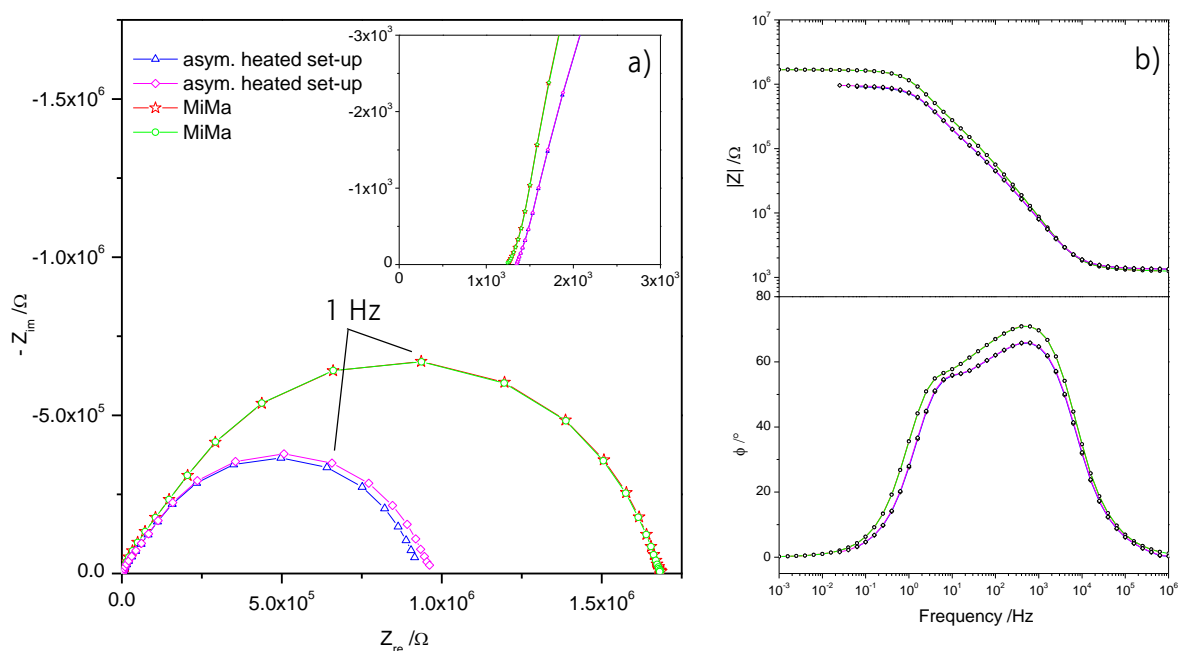
Fig. 3.14 Impedance spectra in Nyquist (a) and Bode plot (b) of exactly the same 145·145 µm^2 squared LSM microelectrode measured in MiMa and in the asymmetrically heated set-up at 758 °C electrode and 900 °C hot stage set temperature, respectively. (Polarization resistances are plotted in Fig. 3.13)

Fig. 3.15 Arrhenius plot of the electrode polarization resistance for Ø=200 µm platinum microelectrodes measured in MiMa and in the asymmetrically heated micro-contact set-up.

3.5.4 Comparison Between Asymmetrically and Symmetrically (MiMa) Heated Set-up for 3PB Path

One and the same LSM/Pt finger-shaped microelectrode with a large 3PB length (Fig. 3.16c) was investigated in the asymmetrically heated set-up and in MiMa. In both cases a Pt/Ir needle was used to electrically contact the LSM/Pt microelectrode. The Pt capping layer on the LSM blocks large parts of the oxygen reduction via a bulk path [32, 127]. The set temperatures of the temperature control units were adjusted to reach almost the same electrolyte resistance R_0 in both set-ups, see inset in Fig. 3.16. When interpreting the same R_0 as an indication of the same average YSZ temperature beneath the microelectrode, the two measurements should lead to very similar results.

a)

b)

c)

400 µm

d)

Platinum

LSM

YSZ
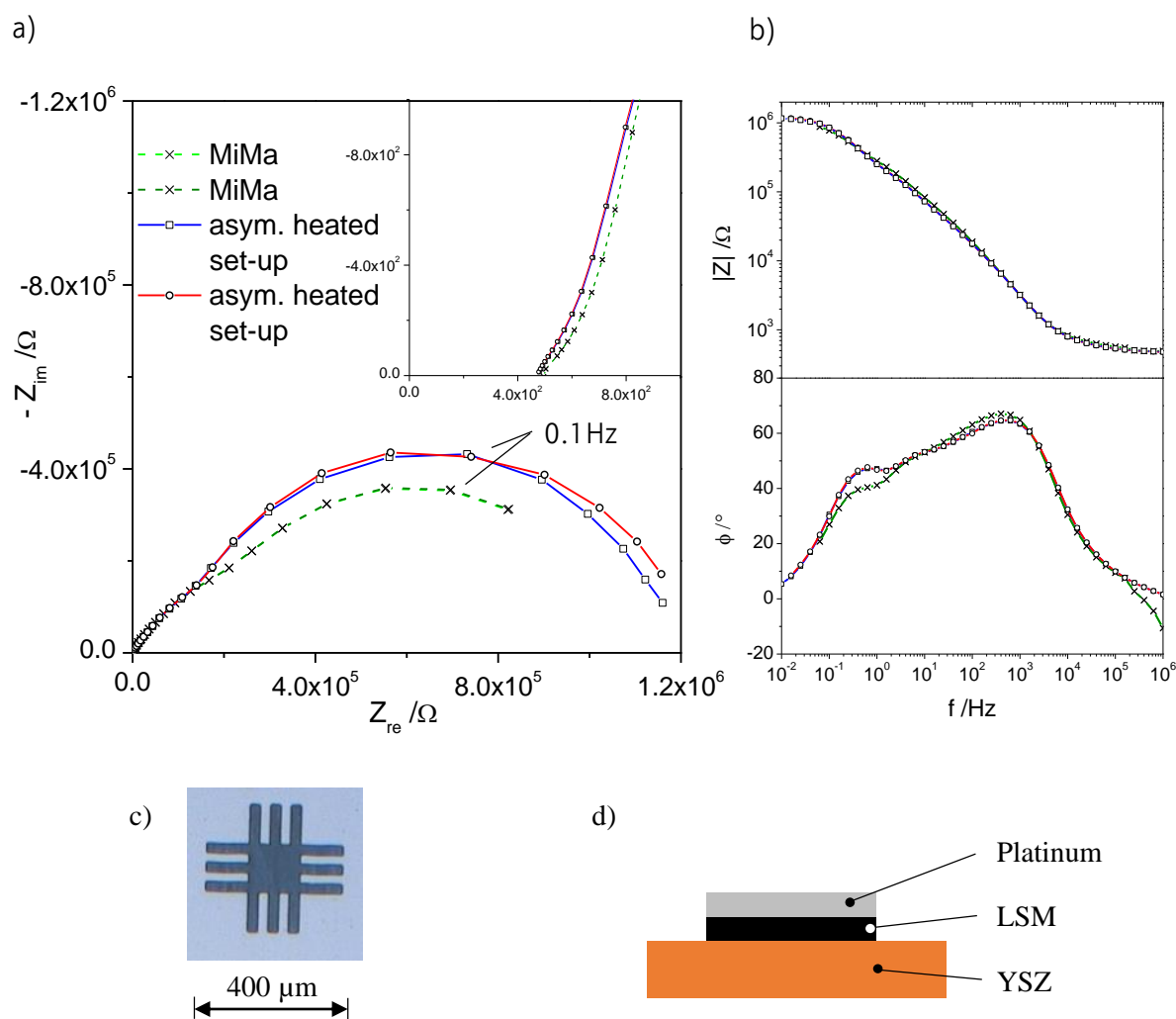
Fig. 3.16 Impedance spectra of a LSM microelectrode covered with Pt at 730 °C (T_{spr} in the asymmetrically heated set-up) in a Nyquist plot (a) and a Bode plot (b) measured in MiMa and in the asymmetrically heated set-up. Two subsequent measurements are shown in each set-up. (c) Photograph of the LSM/Pt microelectrode and (d) sketch of the cross-section.

	R_0 /Ω	R_1 /Ω	R_2 /Ω	R_3 /Ω	C_1 /F	C_2 /F	C_3 /F
MiMa	5.41E+02	9.31E+03	2.37E+05	8.04E+05	2.70E-07	3.30E-07	1.64E-06
MiMa	5.41E+02	9.34E+03	2.38E+05	8.05E+05	2.70E-07	3.30E-07	1.64E-06
asym. heated	4.93E+02	5.55E+03	1.54E+05	1.02E+06	2.91E-07	3.63E-07	1.29E-06
asym. heated	4.91E+02	4.89E+03	1.50E+05	1.06E+06	2.96E-07	3.52E-07	1.27E-06
ratio MiMa/asym.	1.09	1.79	1.56	0.77	0.92	0.92	1.28

Tab. 3.1: Fit results from the spectra in Fig. 3.16 using the equivalent circuit in Fig. 3.1, bottom, capacitances are calculated from CPE elements after [73].

In contrast to the MiMa set-up, spectra measured subsequently in the asymmetrically heated micro-contact set-up slightly drift (Fig. 3.16), as already found for pure LSM microelectrodes (Fig. 3.14). Slight differences of the spectra shapes are visible in Fig. 3.16 and quantified by fitting of the spectra to three serial R-CPE elements, see Fig. 3.1 bottom. The fit results are given in Tab. 3.1, including the ratios of the fit parameters for MiMa and the asymmetrically heated microelectrode measurements. Some differences are found but should not be over-interpreted since the total polarization resistance R_{tot} is very similar in both cases. This is also in line with similar measurements performed on circular Pt microelectrodes. There the 3PB-related path is relevant in the temperature range from 450 to >800 °C [83]. The data obtained in MiMa and in an asymmetrically heated set-up show the same slope in an Arrhenius plot (Fig. 3.17). Slight differences of absolute values might simply be due to an inaccurate temperature calculation for measurements in the asymmetrically heated set-up.
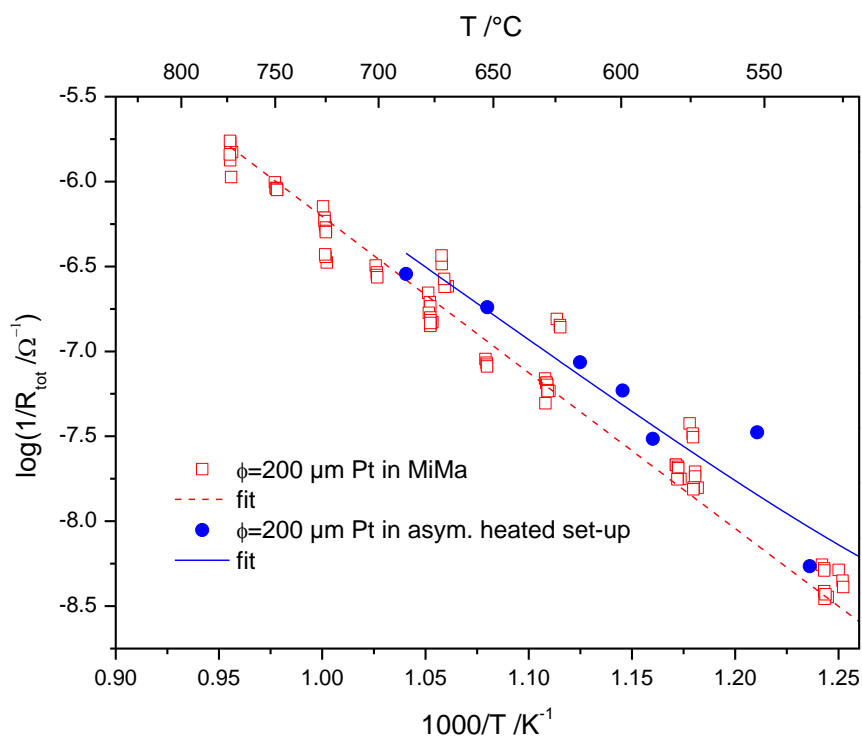
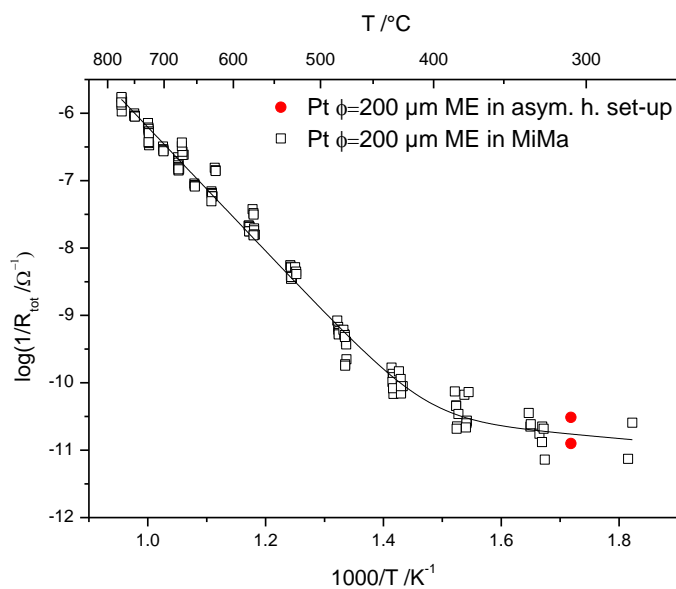**Fig.** 3.17 Arrhenius plot of the electrode polarization resistance for Ø=200 µm platinum microelectrodes measured in MiMa and in the asymmetrically heated micro-contact set-up.

Both experiments on LSM/Pt and Pt, and also the low temperature data in Fig. 3.13 (LSM), show that temperature gradients have only minor impact on the results obtained for the 3PB related surface path. The finite element simulations showed that temperatures at 3PBs are much closer to the temperature of the counter electrode (T_{YSZ}) than the tip contacts. Thermovoltages, on the other hand represent the temperature differences at the contact tip. Those only transfer to a high driving force for a DC driven electrochemical reaction at locations with similarly large deviations from T_{YSZ}. This is not the case for 3PBs but indeed partly true for bulk path-type reactions taking place along the entire electrode surface. Accordingly, neither Pt electrodes at higher temperatures nor LSM/Pt electrodes (all temperatures) are much affected since they are determined

by 3PB kinetics. LSM at lower temperatures also exhibits a 3PB surface path and is not prone to thermovoltage problems as well. (At lower temperature thermovoltages are less pronounced, anyway). Only LSM at high temperatures with its predominant bulk path is severely influenced by the thermovoltages.

3.6   Conclusion

Conventional micro-contact set-ups with asymmetric heating can cause measurement inconveniences and measurement errors. In particular, local cooling by the current collecting tip leads to lateral temperature gradients. Those gradients were quantified and visualized by several tools such as micro-thermocouple measurements, infrared camera pictures, LSM reduction kinetics, or tracer incorporation kinetics. Finite element calculations of temperature distributions are in good agreement with experiments and show that current collecting tips induce a strong temperature decrease at the contacting point (ca. 200 K for 800 °C set temperature). The maximum temperature reduction found beneath the contact tip can mainly be influenced by preventing convection but not by the tip radius. However, temperature gradients are rather sharp and often large parts of the microelectrode are much less affected by the local temperature decrease, provided sharp contact tips and sufficiently large microelectrodes are used. The temperature estimated from the measured YSZ (spreading) resistance is in reasonable agreement with the temperature at the 3PB but may severely overestimate the temperature of inner parts of the microelectrode. Thermovoltages of several 10 mV may arise and can cause an unintended bias load and DC current which may modify

measured polarization resistances. This was indeed found for LSM microelectrodes at high temperatures with predominant bulk path. Electrodes governed by a 3PB surface path (LSM/Pt, Pt) are much less influenced by thermovoltages, since those reflect the strongest possible temperature decrease near the contact tip. Thermally induced electrochemical driving force are much less pronounced at 3PBs. In general measurement errors caused by temperature gradients in asymmetrically heated micro-contact set-ups can be reduced by using thin sharp needles with little thermal conduction, avoidance of convection above the measured sample and choosing low measurement temperatures. Moreover, large microelectrodes exhibit less relevance of local cooling effects by the contacting tip.

For avoiding several problems occurring with set-ups using asymmetrical heating of the sample, a novel micro-contact set-up (MiMa), based on a tube furnace, was constructed. Owing to its symmetrical heating it eliminates all detrimental effects associated with temperature gradients within the sample. Moreover, it allows longtime measurements and temperature cycles. Experiments on LSM and platinum microelectrodes showed that it is possible to analyze a single microelectrode from room temperature up to 1000 °C without losing contact. Microelectrodes were reproducibly measured over weeks from 300 to 950 °C without irreversible degradation effects.

4. Fast Oxygen Exchange and Diffusion Kinetics of Grain Boundaries in $La_{0.8}Sr_{0.2}MnO_3$ and $(La_{0.8}Sr_{0.2})_{0.95}MnO_3$ Thin Films

This chapter corresponds largely to a manuscript submitted to "Phys. Chem. Chem. Phys." as scientific paper [71].

4.1 Abstract

In this chapter the contribution of grain boundaries to the oxygen reduction and diffusion kinetics of $La_{0.8}Sr_{0.2}MnO_3$ (LSM) thin films is investigated. Polycrystalline LSM thin films with columnar grains of different grain sizes as well as epitaxial thin films were prepared by pulsed laser deposition. ^{18}O tracer exchange experiments were performed at temperatures between 570 °C and 810 °C and subsequently analyzed by secondary ion mass spectrometry (SIMS). The isotope concentration depth profiles of polycrystalline films clearly indicated contributions from diffusion and surface exchange in grains and in grain boundaries. Measured depth profiles were analyzed by the finite element modeling, and revealed the diffusion coefficients D and oxygen exchange coefficients k of both the grain bulk and grain boundaries. Values obtained for grain boundaries (D_{gb} and k_{gb}) are almost three orders of magnitude higher than those of the grains (D_b and k_b). Hence, grain boundaries may not only facilitate fast oxygen diffusion but also fast oxygen exchange kinetics. Variation of the A-site stoichiometry (($La_{0.8}Sr_{0.2})_{0.95}MnO_3$) did not lead to large changes of the kinetic parameters. Properties found for epitaxial layers without grain boundaries (D_b and k_b) are close to those of the

grains in polycrystalline layers. The results uncover the importance of grain boundaries in designing thin-film based oxide electrochemical energy conversion devices.

4.2   Introduction

Perovskite-type materials with mixed ionic and electronic conductivity are widely investigated as electrodes for solid oxide fuel cells (SOFC). Sr-doped LaMnO$_3$ (LSM) is known for its use in cathodes for high temperature applications [128], particularly in conjunction with doped zirconia (composite electrode) [36, 37, 129, 130]. LSM exhibits relatively good chemical stability, temperature expansion compatibility with yttria stabilized zirconia (YSZ) and acceptably high electronic conductivity [15, 16]. At high temperatures LSM tends to react with the electrolyte and forms secondary phases at the cathode/electrolyte interface, [6, 10] which can be retarded by an A-site deficiency [10]. However, the ion conductivity at SOFC operation temperatures is quite low [17]. This is crucial for the oxygen reduction reaction (ORR) at the SOFC cathode since this reaction may take place close to the three phase boundary (TPB) but can also run via a bulk path [10, 131]. Owing to its low ionic conductivity, the bulk path may be relevant in LSM only for thin films [40, 42, 44, 70, 113, 131-133] or for porous electrodes upon cathodic polarization [46, 134, 135].

Moreover, there is an open question regarding the bulk path in LSM: how much do grain boundaries contribute to the overall oxygen reduction rate? Some studies dealt with the effect of crystallographic orientation or substrate [60, 136] on ionic conductivity in LSM thin films. Different electronic properties of grain boundaries compared with grain

surfaces were found by scanning tunneling microscopy (STM) studies on LSM layers [137, 138]. This also suggests a different catalytically activity for ORR at the grain boundaries, but quantitative data are not available yet. Impedance spectroscopy studies on thin film microelectrodes may reveal information on the relative importance of bulk path and surface path [70] and could even distinguish whether the bulk path for ORR is limited by the surface reactions or by transport through the bulk [44]. However, information on grain boundary effects can hardly be resolved unambiguously by this technique. ^{18}O exchange experiments followed by secondary ion mass spectrometry (SIMS) analysis - also called isotope exchange depth profiling (IEDP) - is a powerful technique to probe oxygen exchange and oxygen diffusion kinetics and/or to visualize the active ORR sites [14, 28, 33, 58, 64, 69, 124, 139-141] including also some IEDP studies on sintered LSM where it was found that grain boundary diffusion does have an influence on the overall oxygen transport in LSM. Quantitative information on the oxygen exchange properties of the grain boundaries was not deduced from those measurements. Additional studies on oxygen diffusion in grains and grain boundaries of LSM, particularly in LSM thin films with active ORR bulk path, are therefore vital for understanding their role, especially in nanoscale thin-film structures.

In this chapter we report our results of IEDP experiments revealing the strong effect of grain boundaries for ORR and oxygen diffusion in LSM thin films. The ^{18}O isotope exchange experiments were performed from 560 to 810 °C and the isotope depth profiles were analyzed by numerical finite element modeling. In order to investigate the relevance of A-site non-stoichiometry, on stoichiometric ($La_{0.8}Sr_{0.2}MnO_3$) and A-site deficient (($La_{0.8}Sr_{0.2})_{0.95}MnO_3$) LSM thin films were investigated. In order to clearly

demonstrate the effect of grain boundaries, polycrystalline LSM layers with different grain widths as well as epitaxial layers were used. These measurements allowed for the first time the determination of not only the grain boundary diffusion coefficient but also the grain boundary surface exchange coefficient k_{gb} of LSM thin films. To the best of our knowledge the results also establish the first quantification of the contribution of grain boundaries to oxygen surface exchange kinetics on a mixed conducting oxide in general.

4.3 Experimental

4.3.1 LSM Thin Film Preparation

LSM thin films were prepared by pulsed laser deposition (PLD). The stoichiometric compound PLD target, denoted as LSM100, target was produced from $La_{0.8}Sr_{0.2}MnO_3$ (Sigma Aldrich) powder, which was isostatically pressed into pellets and sintered for 12 h at 1200 °C in air. The PLD target of A-site deficient LSM95 (($La_{0.8}Sr_{0.2})_{0.95}MnO_3$) was prepared from powder synthesized by the Pechini method. The preparation route is described in more detail elsewhere [132]. The as-synthesized LSM95 powders were subsequently calcined at 1100 °C for 6 h in air with a ramping rate of 3 °C/min and afterwards pressed into pellets and sintered at 1300 °C in air for 20 h.

All polycrystalline LSM layers were deposited on YSZ (100) (ZrO_2 with 9.5 mol% Y_2O_3, CrysTec GmbH, Germany) single crystal substrates. The deposition was performed in oxygen atmosphere at $4 \cdot 10^{-2}$ mbar oxygen pressure using a KrF excimer laser with a wavelength of 248 nm and a pulse frequency of 10 Hz. The laser beam energy was set

to 400 mJ per pulse and a target-substrate distance of 6 cm was used. Different film growth temperatures ranging from 600 °C to 810 °C were employed to vary the grain width of the thin films with columnar grains. The substrate temperature was measured by an IR pyrometer (Heitronics KT-19.99, Germany).

Epitaxial LSM95 and LSM100 layers were deposited on $SrTiO_3$ (STO) (100) (CrysTec GmbH, Germany) single crystals at 650 °C under $1.3 \cdot 10^{-2}$ mbar oxygen pressure. The films were cooled down to room temperature in 2.7 mbar oxygen pressure. The other PLD parameters were the same as for the polycrystalline LSM layer preparation.

4.3.2 Thin Film Characterization

X-ray diffraction (XRD) 2θ-ω scans and reciprocal space mapping (RSM) of epitaxial and polycrystalline layers were performed with a high resolution four-circle Bruker D8 Discover diffractometer, which is equipped with a Göbel mirror, four-bounce Ge(220) channel-cut monochromator, Eulerian cradle, and a scintillation counter, using Cu $K_{\alpha 1}$ radiation. The thickness of the epitaxial layers was analyzed by X-ray reflectivity (XRR) measurements performed on Rigaku Smartlab diffractometer equipped with 2-bounce Ge (220) channel-cut monochromator using Cu $K_{\alpha 1}$ radiation. From XRR measurements (not shown) the thickness of these epitaxial layers was found to be 28 nm for LSM100 and 29 nm for LSM95.

The thickness of the polycrystalline LSM layers was controlled by deposition time and later determined by scanning electron microscopy (SEM) (FEI Quanta 200 FEG, Netherlands) and transmission electron microscopy (TEM) (FEI TECNAI-20) from cross-

section images. Values ranging from 170 nm to 212 nm were found. The grain width of LSM layers was estimated by two techniques: atomic force microscopy (AFM) (NanoScope V, Bruker Nano) and TEM. In the first case, the surface morphology of LSM95 and LSM100 thin films was characterized using AFM tapping mode. The resulting AFM micrographs were then analyzed by the linear intercept method. In TEM measurements the average column widths were determined from the available images directly.

4.3.3 Isotope Exchange Depth Profile (IEDP) Experiments

The isotope exchange was performed in a gas tight exchange chamber at 200 mbar 97.1% ^{18}O oxygen isotope (Campro Scientific, Germany) at temperatures ranging from 570 °C to 810 °C. The isotope exchange took place for 10 to 60 minutes depending on temperature. After the exchange the sample was quickly quenched to room temperature in ambient air. The unavoidable evacuation step before filling the exchange chamber with tracer gas would annihilate any chemical preequilibration. Therefore such a preequilibration was not performed and a contribution of chemical diffusion could not be avoided. This, however, is expected to be of negligible relevance due to the small concentration of oxygen vacancies in LSM: Any change of the vacancy concentration by chemical diffusion involves only very little amount of tracer molecules. Further information dealing with similar exchange experiments on Sr-doped LaCoO$_3$ thin layers are given in Ref. [141].

The resulting ^{18}O depth profiles were subsequently investigated by time-of-flight secondary ion mass spectrometry (ToF-SIMS) (ION-TOF GmbH, Germany ToF-SIMS 5).

For these SIMS measurements the collimated burst alignment (CBA) mode with Bi_3^{++} primary ions (25 keV) was used, which allows accurate determination of ^{18}O concentrations in a broad intensity range [28, 95, 96]. Negative secondary ions were analyzed in areas of 30x30 µm^2, using a raster of 256x256 measurement points. For the sputtering of material, 1 keV Cs^+ ions were applied with a sputter crater of 300x300 µm^2 and sputtering ion current of 70 nA. The charging of surfaces was compensated by an electron flood gun. The depth profiles of isotope fraction ($f(^{18}O)$) were obtained by normalizing integrated intensities I of ^{18}O and ^{16}O according to

$$f(^{18}O) = \frac{I(^{18}O)}{I(^{18}O) + I(^{18}O)} \qquad 4.1$$

4.4   Results and Discussion

4.4.1 XRD Measurements

The structure and phase purity of the layers was checked by XRD (Fig. 4.1 and Fig. 4.2). The diffraction patterns of LSM100 and LSM95 are shown over the whole 2θ range measured. All visible peaks could be assigned to either the YSZ substrate or the LSM thin films, and a second phase was not observed. Both diffraction patterns are dominated by the intense substrate peaks overshadowing the (011) and (022) peaks of LSM. Furthermore, the K_β peaks of the single crystal YSZ are visible since the Cu K_β radiation was not completely filtered. A rhombohedral distortion of the LSM lattice was not found, but cannot be excluded due to the low intensity of the thin film signals. Pseudo-cubic out-of-plane lattice parameters were calculated from these diffraction

patterns, yielding 3.914±0.004 Å for the LSM100 and 3.946±0.003 Å for LSM95 thin film. A preferential grain orientation can be concluded from these thin film diffraction patterns.

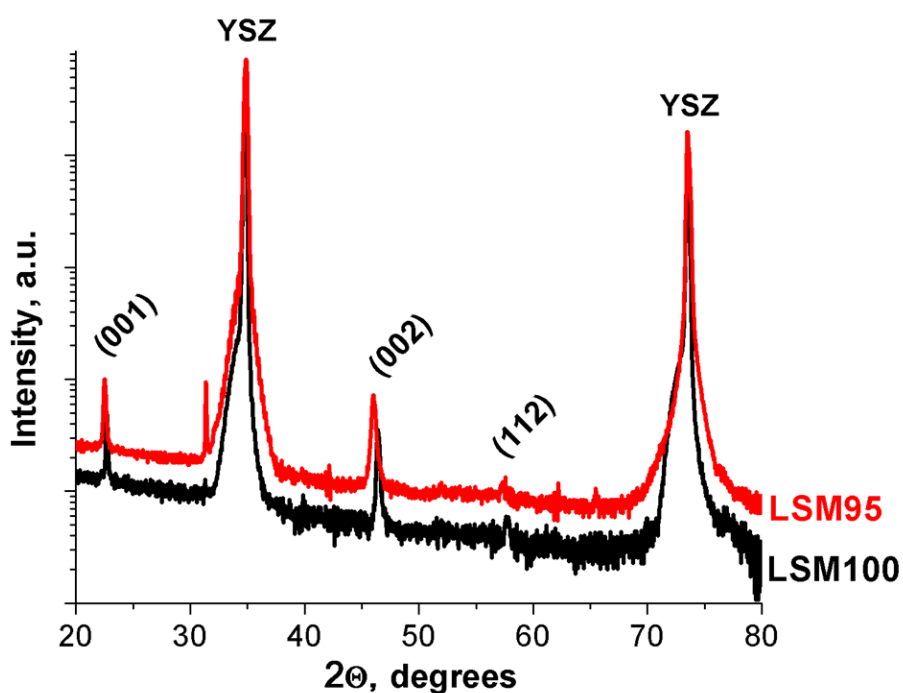**Fig.** 4.1 The θ-2θ scans of polycrystalline LSM95 and LSM100 thin films deposited at 695 °C on YSZ substrates.

Owing to the similar lattice parameters of LSM and STO, preparation of LSM100 and LSM95 on STO substrates leads to epitaxial layer growth [60, 142]. The microstructure of the deposited layers was checked by 2θ-ω scans (Fig. 4.2a) and by reciprocal space mapping (Fig. 4.2 b). The x-ray diffractograms indicate that both LSM layers are with (00l) out-of-plane orientation and epitaxial. The small peaks in 2θ-ω scans around the (001) and (002) peaks (Fig. 4.2a) are thickness fringes, which come from constructive interference of X-rays reflected from the film and the substrate interface. The presence

of such thickness fringes is an indication of the high quality of the film, with a smooth surface and film-substrate interface. As one can see from RSM (Fig. 4.2b), the peaks of LSM100 and LSM95 are located right beneath those of the STO substrate, which indicates that the in-plane lattice parameter of the LSM films match to that of the STO substrate (3.905 Å) epitaxially. Keeping in mind that LSM bulk lattice parameter (3.88 Å) [143] is smaller than STO, this should lead to tensile strain, which was also observed in other studies.
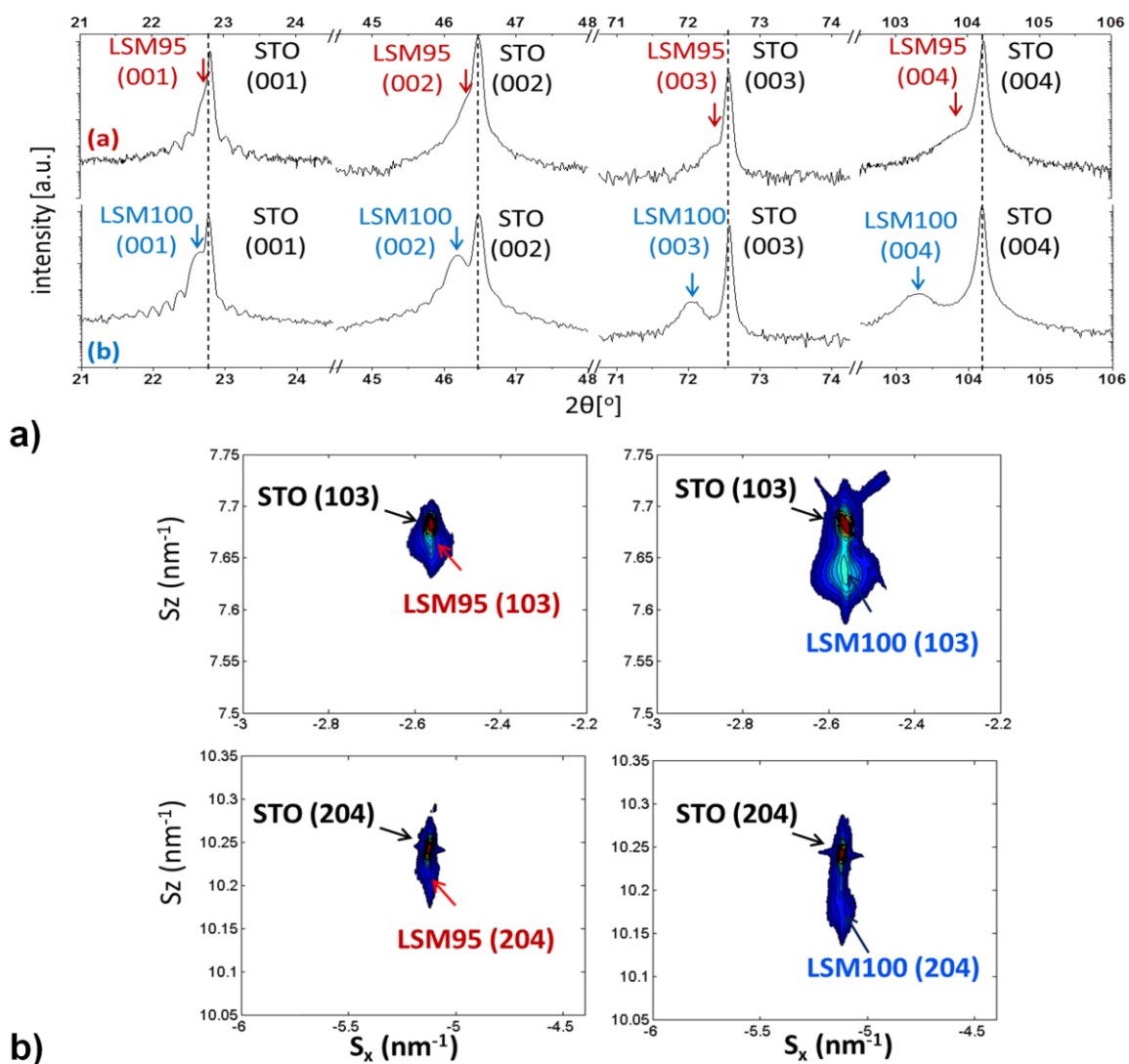
Fig. 4.2 a) High resolution XRD 2θ-ω scans of LSM95 and LSM100 layers on STO substrates; b) Reciprocal space maps of LSM95 and LSM100 on STO (001) substrates, with the STO reference reflections (-1,0,3) and (204).

4.4.2 The Microstructure of LSM Films

The surface morphology of epitaxial and polycrystalline LSM layers deposited at 600, 700 and 810 °C layers was checked by AFM (Fig. 4.3). Layers prepared on STO substrates have a smooth surface with RMS roughness lower than 1 nm. Layers deposited on a YSZ

substrate show a grain microstructure at the surface, with a higher RMS roughness. The films deposited at lower temperatures show finer microstructures. Supported also by TEM results (see Fig. 4.3), these visible structures are identified as the columnar grains, and the coarsening with increasing substrate temperature therefore reflects an increasing grain width due to the higher adatom mobility at the surface during deposition. The grain width was estimated from several line scans of AFM micrographs. This lead to mean grain width values of *ca.* 30 nm for LSM100 deposited at 600 °C, *ca.* 40 nm for LSM100 deposited at 700 °C, *ca.* 60 nm for LSM95 deposited at 600 °C and *ca.* 70 nm for LSM95 deposited at 700 °C. Accordingly, the mean grain size of LSM95 is about 30 nm larger than that of stoichiometric LSM. Layers formed at 810 °C have less pronounced microstructural features and in this case grain width was estimated from TEM cross-section bright-field images. The TEM measurements were performed on LSM100 layers and are shown in Fig. 4.3. The measurements confirmed the columnar grain growth but also revealed some variation in grain width. Keeping the limited statistics in mind, results found from TEM for LSM100 deposited at 600 °C and 700 °C are in a good agreement with AFM results, *i.e.* again *ca.* 30 and *ca.* 40 nm, respectively. The LSM100 layer deposited at 810 °C showed slightly larger grains in TEM and lead to an estimated value of 45 nm. Despite absence of TEM data for the LSM95 layer deposited at 810 °C we also expect a slight increase in grain size compared to the 700 °C layer. The following grain widths were therefore used in the quantitative analysis of the tracer profiles: 30, 40 and 45 nm for LSM100 layers and 60, 70 and 75 nm for LSM95 layers, respectively.
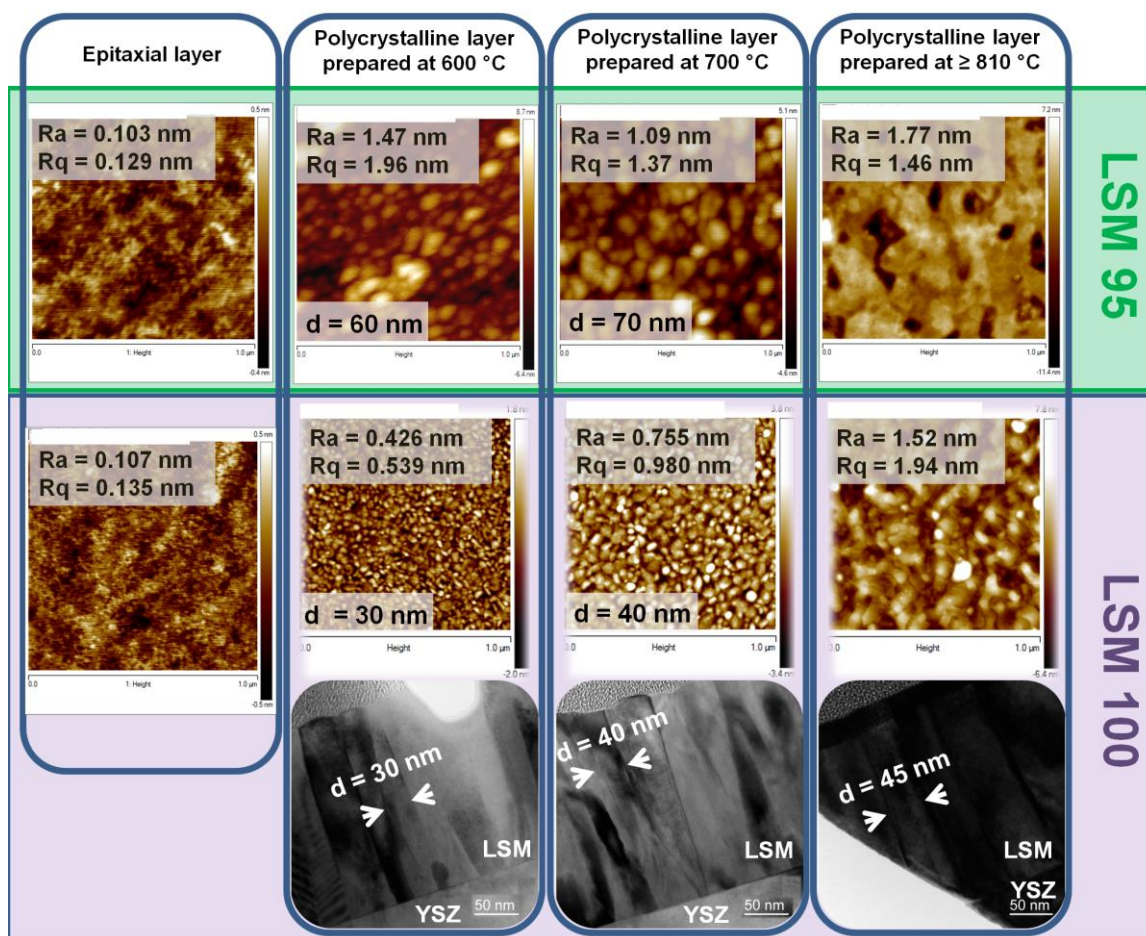
Fig. 4.3 AFM micrographs of LSM95 and LSM100 epitaxial and polycrystalline layers prepared at different temperatures demonstrate distinctly different surface microstructure. The bright-field TEM measurements (bottom) on LSM100 polycrystalline layers show the columnar structure and the dependence of the column diameter on the deposition temperature.

4.4.3 ^{18}O Isotope Exchange on Stoichiometric LSM Films

The isotope exchange experiments were performed at temperatures between 560 °C and 810 °C. The ^{18}O exchange experiments at lower temperatures were performed for 30 min while high temperature anneals in ^{18}O took only 10 min, in order to obtain depth profiles of ^{18}O that still allow for retracting the kinetic parameters. Typical ^{18}O diffusion depth profiles in a polycrystalline LSM thin film (deposited at 600 °C) are shown in

Fig. 4.4a, b for four different exchange temperatures. Depth profiles consist of two main parts – a steep decrease in the very first nanometers, followed by a shallow isotope concentration decrease. Only at the highest temperature these two regimes can hardly be separated and an almost linear profile is found. If the isotope fraction at the LSM/YSZ interface is still above the natural abundance (*e.g.* at 810 °C in Fig. 4.4a) a very shallow profile in YSZ becomes visible, indicating very fast diffusion in YSZ.
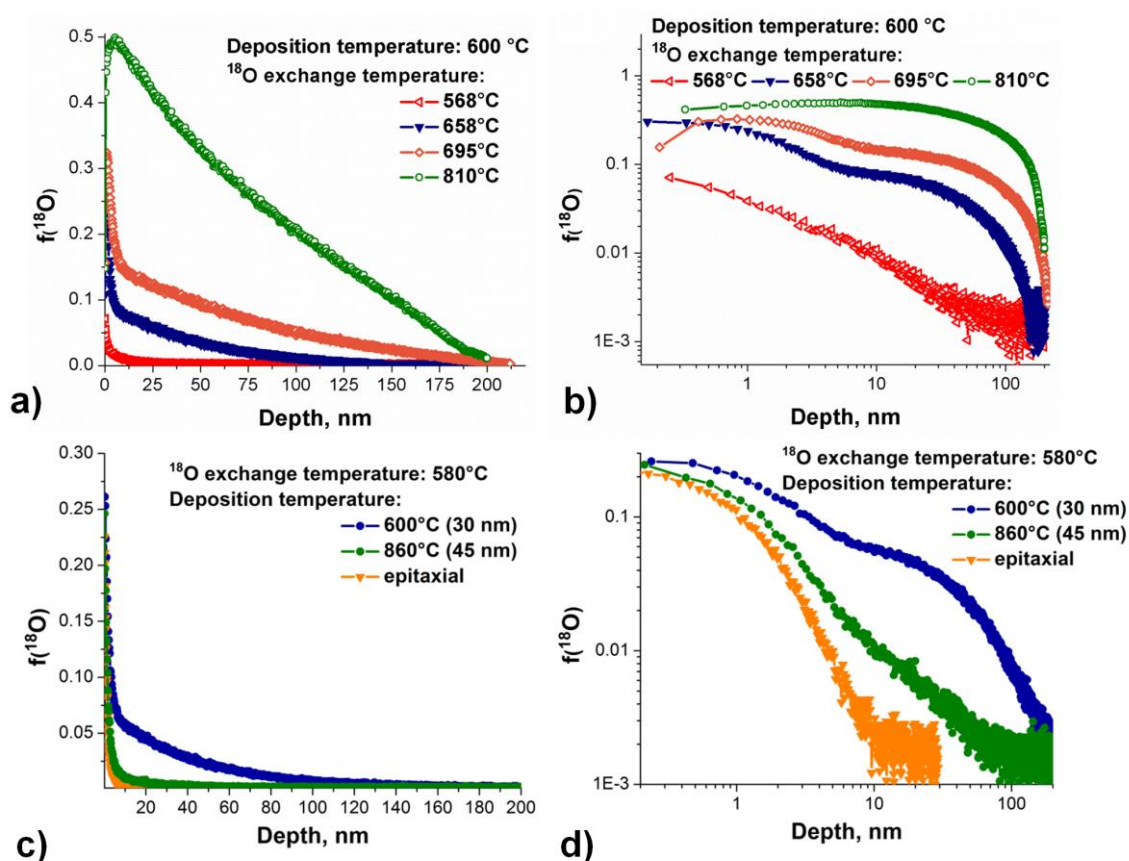
Fig. 4.4 Typical ^{18}O isotope exchange depth profiles of LSM100 thin films obtained with different isotope exchange temperatures ranging from 568 °C to 810 °C (a, b) and varied layer microstructure (30 nm, 45 nm and epitaxial) in linear (c) and logarithmic plots (d).

The grain size, manipulated by the film deposition temperature, also clearly affect the profiles. As an example, Fig. 4.4c, d displays the results for LSM100 layers prepared at

600 °C (d = 30 nm) and 860 °C (d = 45 nm) after oxygen exchange at 580 °C. The near surface parts of the profiles are very similar while a larger grain size causes less ^{18}O concentration in some depth. Profiles measured on epitaxial layers deviate strongly from those of polycrystalline layers. As shown in Fig. 4.4c, d and Fig. 4.5, the very sharp decrease is not followed by a long diffusion tail. At low temperature natural abundance is almost reached at the LSM/substrate interface, despite very thin layers (28-29 nm), pronounced diffusion in STO is not found. At high temperatures, however, very high tracer fraction levels penetrate into the films and the profiles become rather flat, despite short diffusion times.

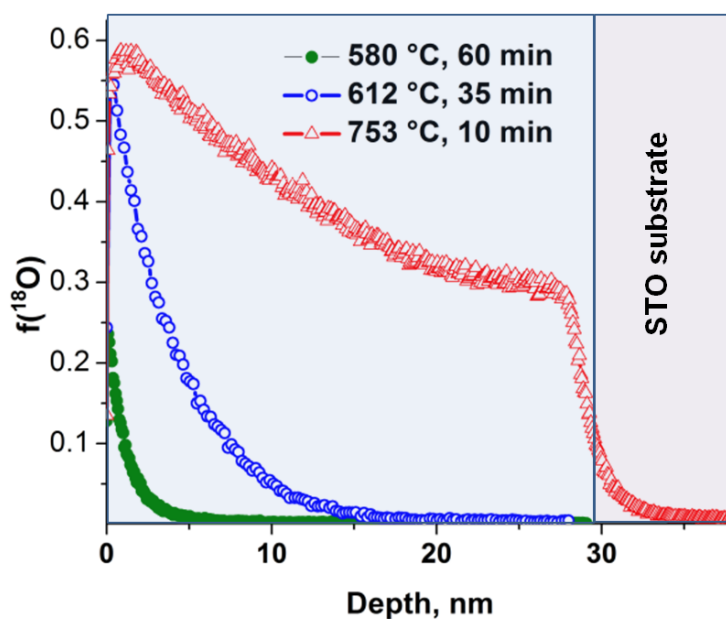**Fig.** 4.5 The ^{18}O isotope exchange depth profiles of epitaxial LSM100 thin films obtained with different isotope exchange parameters.

The absence of the shallow diffusion tail in epitaxial films and the dependence of this part of the diffusion profile on the grain size already suggests an effect of grain boundaries in the overall diffusion kinetics. Profiles strongly resemble those generally

found in the type B regime of Harrison`s grain boundary diffusion classification [14, 64]. Similar isotope exchange depth profiles were also obtained in $SrZrO_3$ pellets, where a fast grain boundary diffusion path was concluded [144]. However, a straightforward analysis of the grain boundary diffusion coefficient according to the model by Whipple/Le Claire [145] (analyzing $\ln c - \ln x^{6/5}$ slopes) is not possible here: First, we do not have semi-infinite conditions in a single phase but fast diffusion in the substrate. Second, we are probably not within the validity range of the model mentioned, above with the total amounts of tracer ions in grain boundaries not being negligible, and diffusion lengths in the grains partly being too large compared to the grain size.

Therefore, a numerical analysis of the measured ^{18}O depth profiles by means of the finite element method (FEM) was performed by using the COMSOL tool. The 3D geometry of the model included three domains (Fig. 4.6), representing diffusion in a grain, along the grain boundary and in the YSZ substrate. The width of the grain boundary (δ) was set to 2 nm and the width of a grain (d) was varied in accordance with the approximative values found in the experiments (see above). For the sake of simplicity, a cylindrically shaped grain was considered, see r.h.s. in Fig. 4.6. The model solves Fick's second law of diffusion in all domains, with diffusion coefficients in LSM grains (D_b), LSM grain boundaries (D_{gb}) and YSZ (D_{YSZ}). The boundary conditions of the FEM model reflect that gas exchange is possible at the surface of grains (exchange coefficient k_b) and grain boundaries (k_{gb}). Diffusion thus takes place in the grain, along the boundary, from the grain boundary to the grain and from the LSM layer to the YSZ substrate. Since the profiles were too shallow in YSZ to deduce a diffusion coefficient, D_{YSZ} was calculated from measured conductivity (σ_{ion}) values. Then FEM calculations with

varying D and k values of grain and grain boundary were performed until the best match was found between the calculated isotope profiles and the experimental ones, across the entire set of experimental data. As an additional parameter in the FEM model, the initial concentration was set to the natural abundance level of 0.00205 for ^{18}O (given by the National Institute of Standards and Technology (NIST)) and the ^{18}O concentration in the gas was assumed to be 97.1% (in accordance with the isotope supplier). The FEM calculations on epitaxial layers were done in a similar manner, though only with a single LSM domain, *i.e.* without grain boundary and without any diffusion in the STO substrate.
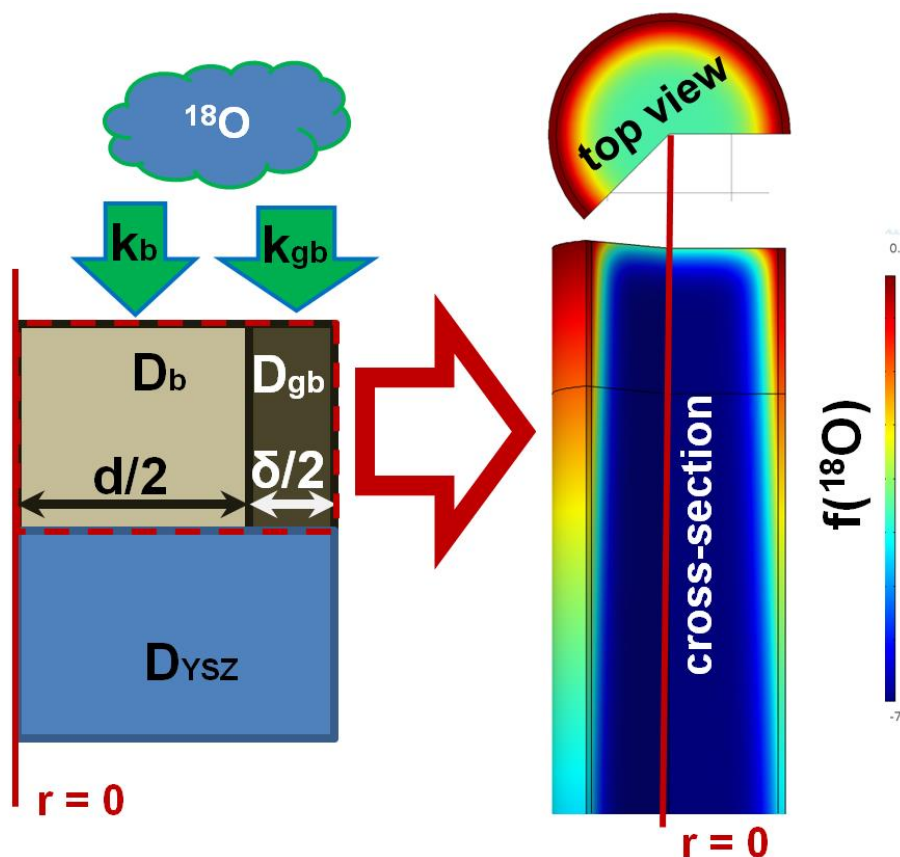

Fig. 4.6 The sketch of the geometry used in the finite element model to analyze the measured isotope depth profiles.

First, the concentration depth profile of a polycrystalline film was fitted with a single diffusion process ($D_b = D_{gb}$ and $k_b = k_{gb}$) (green line). However, in this manner only the steep part of the profile could be described. In a second step, different grain and grain boundary diffusion coefficients were used for the fit ($D_b \neq D_{gb}$ and $k_b = k_{gb}$) (blue line). Again the measured profile could not be reproduced, since the very high ^{18}O concentration in some depth cannot be explained by faster diffusion in the grain boundaries only. This suggests that also a modified surface exchange coefficient for the grain boundaries has to be involved in the model. Finally, full consideration of all fit parameters with different diffusion and different surface exchange coefficients ($D_b \neq D_{gb}$ and $k_b \neq k_{gb}$) leads to a successful fitting (black line in Fig. 4.7). To the best of our knowledge this is the first quantification of the grain boundary surface exchange coefficient of a mixed conducting oxide.

The same type of FEM analysis of the experimental data was performed for all the polycrystalline samples, each with the corresponding grain size. Fig. 4.7c and d displays fit results for two different grain sizes in linear and logarithmic plots, together with that of the epitaxial layer (see also below). The steep isotope depth profile part corresponding to the grain bulk diffusion is the same in all cases while deeper parts strongly depend on the layer microstructure.
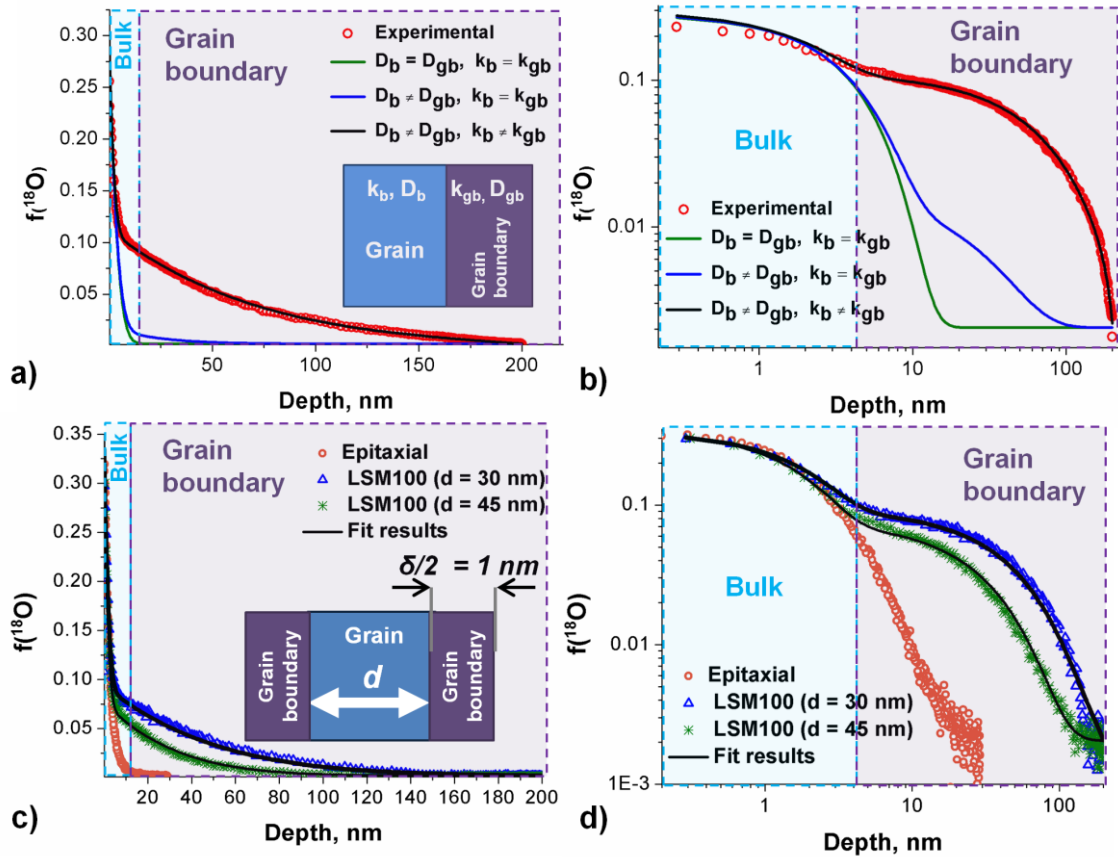
Fig. 4.7 a) The measured isotope exchange depth profile (LSM100, d=30 nm, ^{18}O exchange parameters: T = 695 °C, 10 min) was approximated by the numerical calculation for three cases: only one domain being involved in the model (Db = Dgb and kb = kgb, red line); two domains with different diffusion coefficients used (Db ≠ Dgb and kb = kgb, blue line) and two domains with different diffusion and exchange coefficients are employed (Db ≠ Dgb and kb ≠ kgb) (black line). b) Isotope exchange depth profile and fitting curves of a) in a logarithmic plot; c) Tracer exchange depth profiles of LSM100 layers with varied columnar width – 30 nm, 45 nm and epitaxial layer (18O exchange parameters: 753 °C, 10 min). The black lines are the fitting results obtained with finite element calculations. The first nanometers of the thin films correspond to bulk diffusion and the tail is attributed to grain boundary diffusion. These two contributions are better visible in the logarithmic plot of the isotope exchange depth profile (d).

The obtained diffusion and surface exchange values for the grain and grain boundaries are plotted in Arrhenius diagrams in Fig. 4.8. As one can see, both the diffusion coefficients and the surface exchange coefficients of the grain boundaries are orders of magnitude higher than those of the grain bulk. The enhancement ratios are between 200 to 1000 for D_{gb}/D_b and 200 to 800 for k_{gb}/k_b. Moreover, the diffusion and surface

exchange coefficients do not show a significant dependence on the grain size, all data are more or less on the same Arrhenius-fit. This suggests that grain boundary widths and grain boundary structure/chemistry of all three layers do not drastically depend on the deposition temperatures in the explored range. Moreover, this consistency of the data supports the validity of our proposed model with fast grain boundaries in LSM thin films. This significantly accelerated oxygen exchange and transport kinetics of grain boundaries might become important contributors to the overall kinetics also in porous LSM electrodes with sub-µm grains, at least in regimes with relevant bulk path, *e.g.* upon significant cathodic polarization.
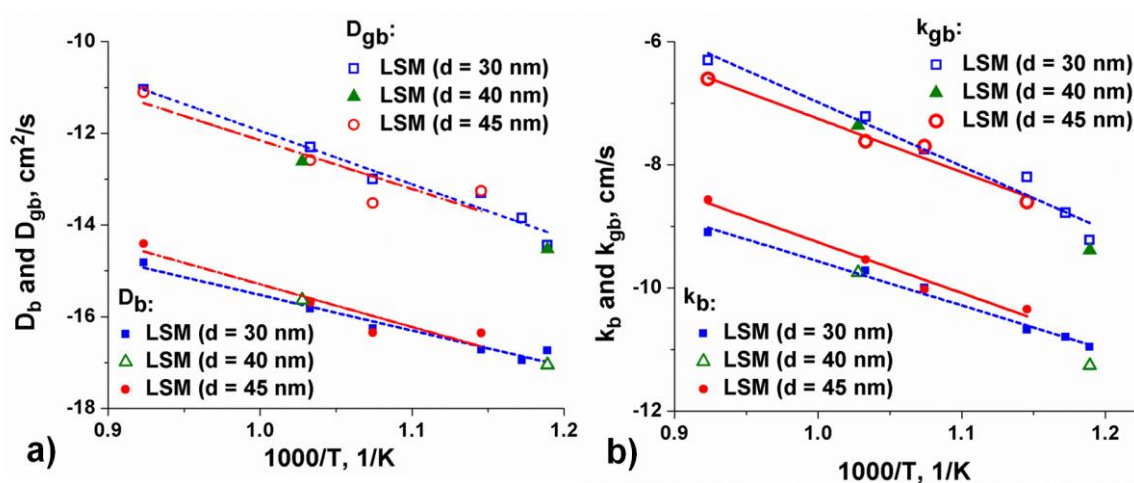
Fig. 4.8 Arrhenius plots of diffusion (a) and exchange coefficients (b) obtained on LSM100 layers with different microstructure. Much higher oxygen exchange and diffusion coefficients of grain boundaries are found.

Still, k and D values slightly spread and the activation energies E_a obtained from Arrhenius plots have to be taken with some care. Fit lines for 30 and 45 nm grains are included in Fig. 4.8. The activation energies for both grain sizes were averaged and all values for bulk (D_b) and grain boundary diffusion (D_{gb}) as well as for both surface exchange coefficients (k_b and k_{gb}) are listed in Table 4.1. A more detailed discussion of

activation energies is given below, together with values found for LSM95 and epitaxial

layers.

	E_{Db} /eV	E_{Dgb} /eV	E_{kb} /eV	E_{kgb} /eV
LSM100, polycrystalline	1.70	2.22	1.53	1.88
LSM95, polycrystalline	2.04	1.78	1.57	1.7
LSM100, epitaxial	2.55		2.04	
LSM95, epitaxial	2.63		1.97	

Tab 4.1 The averaged activation energies of diffusion and surface exchange of grain and grain boundaries of LSM100 and LSM95 thin films.

In the case of epitaxial layers, again only the first part of the depth profile can be fitted

with a single diffusion process, except for 695 °C (Fig. 4.9a red line) and higher

exchange temperatures. Obviously, again a second diffusion mechanism is present,

even though additional effects are less pronounced than for polycrystalline layers.

Owing to the supposed absence of grain boundaries in the epitaxial layers one might

attribute the shallow part of the profile to fast diffusion due to the tensile strain effect.

The obtained D_b and k_b values from the epitaxial films are plotted in an Arrhenius

diagram (Fig. 4.9b). Comparison with data deduced for D_b and k_b from measurements

on polycrystalline layers reveal that values are similar. Moreover, the LSM bulk properties

seem little affected by the preparation conditions and the substrates used here. Strong

strain in LSM layers, might change the situation [146], similar to results found for Sr-
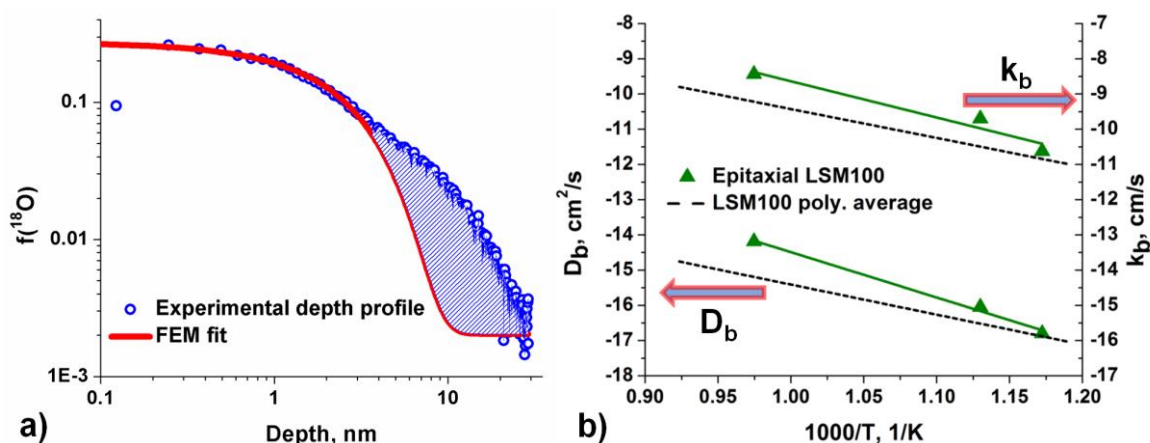
doped $LaCoO_{3-\delta}$ [14].

Fig. 4.9 The first part of the isotope depth profile of an epitaxial layers (LSM100, isotope exchange parameters: 695 °C, 10 min) can be fitted with a single diffusion process. The deviating part (blue area) may emerge due to possible extended defects in the epitaxial films.

4.4.4 Isotope Exchange on A-Site Deficient LSM Layers

The [18]O exchange experiments were also performed on A-site deficient LSM thin films (LSM95) and typical concentration depth profiles are shown in Fig. 4.10a (isotope exchange parameters: t = 10 minutes and T = 695 °C). As in the stoichiometric case, the obtained isotope exchange depth profiles depend on the layer microstructure. The grain widths estimated from the AFM and TEM measurements (60, 70 and 75 nm) were used for the FEM simulation of the depth profile, and D and k values for grain and grain boundaries could again be deduced. The results are plotted in Arrhenius type diagrams (Fig. 4.10b, c). For reasons of comparison averaged data of stoichiometric LSM are also included in Fig. 4.10b and c. Similar to the stoichiometric case, the diffusion coefficient of grain boundaries is approximately two to three orders of magnitude higher than that of a grain bulk. Also a strong difference of k_b and k_{gb} was again found, despite much stronger scattering of k_{gb} data compared to LSM100. Systematic differences between

137

LSM100 and LSM95, however, are not observed. Again the activation energies of D and k were calculated (lines in Fig. 4.10b and c) and averaged values are summarized in Table 1. Profiles of epitaxial LSM95 layers were quantified as described for LSM100 and the resulting D_b and k_b values are included in Fig. 4.10d. Both, diffusion and exchange coefficients are slightly higher for LSM100 but the statistical significance of this difference is not proven yet.
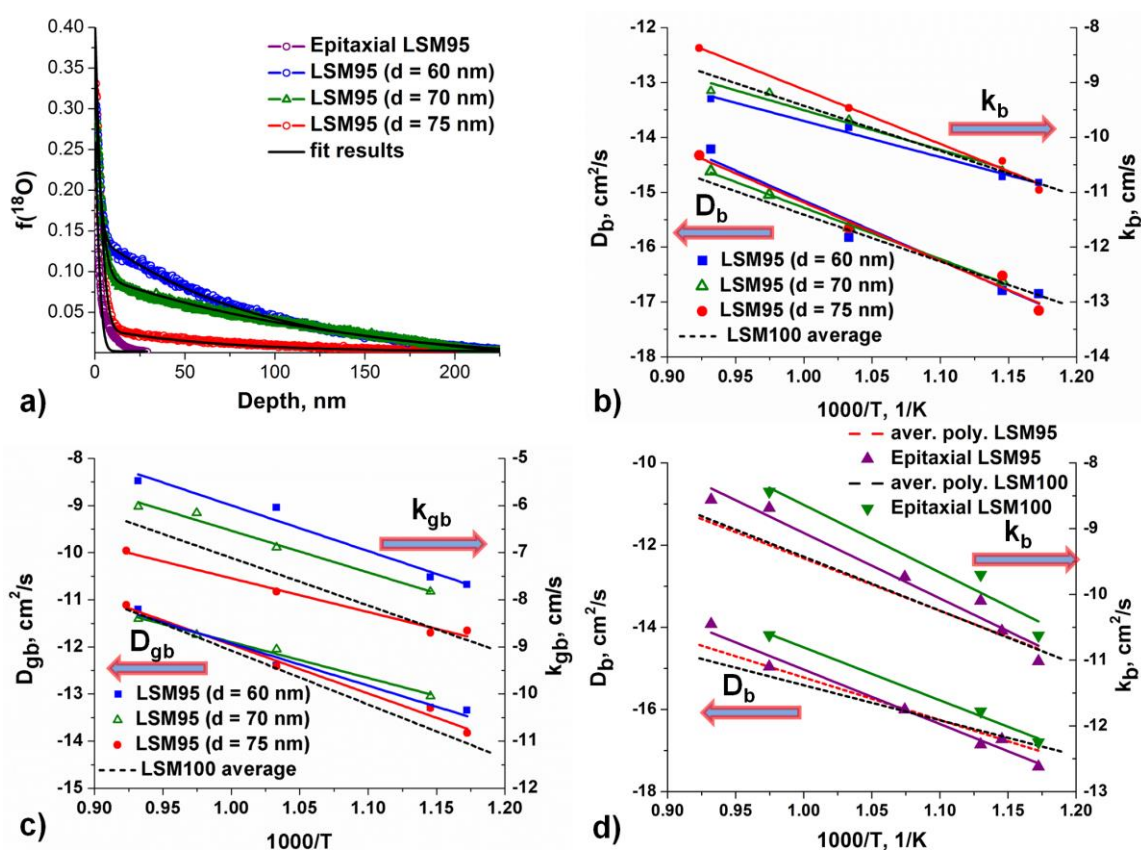

Fig. 4.10 a) Isotope exchange depth profiles of A-site deficient LSM layers in linear plot (LSM95, isotope exchange parameters: 695 °C, 10 min) with varied microstructure. The distinct change of the grain boundary diffusion part in accordance with the microstructure is visible. b) Arrhenius plot of D_b and k_b of A-site deficient LSM95 thin films; c) Arrhenius plot of D_{gb} and k_{gb} obtained on LSM95 layers. Average values for LSM100 are given as well; d)Arrhenius plots of bulk diffusion and bulk exchange coefficients obtained on LSM100 and LSM95 epitaxial layers in comparison with polycrystalline LSM (averaged D and k for polycrystalline layers: LSM100 – red dashed line and LSM95 – black dashed line).

Comparing all activation energies in Table 4.1 one can conclude that activation energies of k values are smaller than those of D. Differences are of the order of 0.2 to 0.4 eV. A statement on the reason behind the differences between activation energies of grains and grain boundaries of polycrystalline layers, however, is not possible yet, due to the scatter present in the fitted data. Approximately, we get 2 eV for D values and 1.7 eV for k values. Even the fact that activation energies of epitaxial layers are somewhat higher should not be over-interpreted. All these measurements and their analysis are far from trivial and include some uncertainties such as very sharp profiles close to the surface at low temperatures, overlap of grain and grain boundary parts, $i.e.$ almost linear profiles at high temperatures (see Fig. 4.4c) and inaccuracies in determining grain widths. In order to check the effect of the grain size and the grain boundary width on the fitting results of an experimentally obtained depth profile of LSM95, data were analyzed with different grain (90, 75 and 60 nm) and grain boundary (0.5, 1 and 2 nm) widths in the FEM model. The resulting values are listed in Table 4.2. The variation of the grain width strongly affects the k values of the grain boundary, while bulk values as well as k_{gb} are much less sensitive. This may explain the strong scatter of the surface exchange values in the LSM95 case, particularly since our model neglects any grain size distribution. The effect of the grain boundary width on k_{gb} and D_{gb} is not surprising and in the range expected when assuming that $\delta \cdot k_{gb}$ and $\delta \cdot D_{gb}$ are the factors defining the amount of incorporated tracer ions.

Grain width d /nm	D_b, cm^2/s	k_b, cm/s	D_{gb}, cm^2/s	k_{gb}, cm/s
90	$2.1 \cdot 10^{-16}$	$3.3 \cdot 10^{-10}$	$3.9 \cdot 10^{-13}$	$1.8 \cdot 10^{-8}$
75	$2.2 \cdot 10^{-16}$	$3.4 \cdot 10^{-10}$	$3.9 \cdot 10^{-13}$	$1.5 \cdot 10^{-8}$
60	$2.2 \cdot 10^{-16}$	$3.6 \cdot 10^{-10}$	$3.9 \cdot 10^{-13}$	$1.0 \cdot 10^{-8}$
Grain boundary width δ /nm				
0.5	$2.2 \cdot 10^{-16}$	$3.4 \cdot 10^{-10}$	$8.0 \cdot 10^{-13}$	$5.0 \cdot 10^{-8}$
1	$2.2 \cdot 10^{-16}$	$3.4 \cdot 10^{-10}$	$4.0 \cdot 10^{-13}$	$2.4 \cdot 10^{-8}$
2	$2.2 \cdot 10^{-16}$	$3.4 \cdot 10^{-10}$	$3.9 \cdot 10^{-13}$	$1.5 \cdot 10^{-8}$

Tab. 4.2 The sensitivity of the results to the variation in grain and grain boundary widths used in the FEM model was analyzed. The experimental results of LSM95 with oxygen exchange at 695 °C (75 nm grain size and 2 nm of grain boundary width) were fitted with varied grain widths (from 60 to 90 nm) and grain boundary widths (from 0.5 nm to 2 nm) in the finite element FEM model.

Finally, the activation energies might be compared with those of a previous tracer diffusion study on polycrystalline LSM pellets [64]. Activation energies for oxygen diffusion in bulk and grain boundaries in the temperature range of 700 °C to 1000 °C were 3.2 eV and 2.8 eV, respectively. In the present study, activation energies are lower which might be due to different types of grain boundaries caused by different preparation. This very different preparation might also cause the severe differences between the absolute k values in Ref. [14] and our k_b, ours are two to three orders of magnitude larger. On the other hand, absolute values of D_b are very close in the temperature regime used in both studies (*e.g.* at *ca.* 800 °C). Hence, one could speculate that at about 700-800 °C a change of the activation energies takes place and causes the different values found in this study (at lower temperatures) and in Ref. [64] (at high temperatures). However, also the very limited temperature range and fit inaccuracies at both ends of our temperature scale might play a role.

4.5   Conclusion

The kinetics of the oxygen exchange reaction and oxide ion diffusion was successfully investigated for stoichiometric and A-site deficient LSM films on YSZ substrates with controlled grain sizes ranging from 30 to 75 nm, as well as LSM epitaxial films on STO substrates. The diffusion profiles in polycrystalline layers indicate contributions of two parallel paths for surface exchange and diffusion of oxygen – in bulk and in grain boundaries. Numerical modelling using the finite element method revealed not only information on grain and grain boundary diffusion, but also on the difference between the kinetics of oxygen exchange on grain surfaces and on grain boundaries. The grain boundary diffusion and surface exchange values obtained from the measurements were approximately two to three orders of magnitude larger than those of the grains. Hence, grain boundaries not only offer fast diffusion paths in LSM but also enable much faster oxygen reduction than the bulk surface. Kinetic parameters of epitaxial layers resemble those of grains in polycrystalline layers. All properties hardly depend on the cation stoichiometry employed in this study (LSM95 and LSM100). These data also suggest that grain boundaries might play a significant role in porous LSM electrodes with active bulk path, *e.g.* upon cathodic polarization, and warrant consideration also in designing thin-film based oxide electrochemical energy conversion devices.

5. Voltage Induced Apparent Uphill Diffusion in LSM Thin Film Microelectrodes

5.1. Abstract

Impedance spectroscopy, DC measurements and ^{18}O tracer experiments were combined to investigate oxygen reduction and ion transport properties of polarized $La_{0.8}Sr_{0.2}MnO_3$ (LSM) thin films. Columnar grown LSM thin film microelectrodes with a thickness of 200 nm and two different grain sizes were prepared on single crystalline yttria stabilized zirconia (YSZ) substrates by pulsed laser deposition (PLD) and microstructured by photolithography. The isotope exchange depth profile method (IEDP) was used to investigate voltage induced changes of diffusion and surface exchange properties of grains and grain boundaries. The ^{18}O tracer exchange experiments were performed at temperatures (T_{exch}) between 500°C and 700°C and subsequently analyzed by time-of-flight secondary ion mass spectrometry (ToF-SIMS). Cathodically polarized microelectrodes showed a strong increase of ^{18}O concentration in the LSM films with an apparent uphill diffusion. All shapes of isotope concentration depth profiles can be explained by a voltage induced change of surface exchange kinetics, a depth dependent change of bulk diffusion properties and fast grain boundary diffusion. Numerical simulation by a 3D finite element model confirmed the interpretation. These measurements also show that a Wagner-Hebb type stoichiometry polarization of the LSM bulk results upon cathodic polarization with a strong increase of the oxygen vacancy concentration towards the LSM/YSZ interface.

5.2. Introduction

The results of the last chapter clearly revealed importance of ion transport along grain boundaries of columnar grown LSM thin films. In electrochemical cells an overpotential of the electrode drives a DC current and this raises the question of the predominant transport path and its rate limiting step for LSM layers upon polarization. Additional experiments on LSM under operating conditions are therefore needed for a clear picture of the oxygen reduction kinetics.

Bias induced ^{18}O incorporation experiments on microelectrodes were already successfully employed for imaging active sits of oxygen reduction [33, 70, 124, 139]. However, a depth dependent analysis of profiles resulting in polarized LSM have not been reported so far. This lack of knowledge could be filled by this study. In order to get a defined overpotential and highly reliable and reproducible data, the symmetrically heated measurement set-up MiMa (**Mi**croelectrode measured in a tube furnace which is normally used for **Ma**croscopic samples) [70] was employed. This also avoids a disadvantage of asymmetrically heated set-ups, namely measurement artefacts caused by inhomogeneous temperature distribution within the microelectrode [33, 70]. DC-measurements in ^{18}O$_2$ atmosphere were combined with quantitative secondary ion mass spectrometry (SIMS) analysis at the resulting depth profiles. Additional impedance measurements were performed on the same microelectrodes. To the best of the authors knowledge such experiments have never been performed before.

5.3. Experimental

5.3.1. Sample Preparation

$(La_{0.8}Sr_{0.2})MnO_3$ powder (Sigma Aldrich, USA) was isostatically pressed, sintered for 12 h at 1200 °C in air and used as target for the PLD process. Films were deposited on polished YSZ (1 0 0) single crystals (9.5 mol% Y_2O_3, CrysTec GmbH, Germany) using a KrF excimer laser (248 nm, COMPex Pro 101 F, Lambda Physics, Germany). Laser beam energy was set to 400 mJ per pulse at 10 Hz pulse frequency. The deposition was performed in $4 \cdot 10^{-2}$ mbar O_2 atmosphere at temperatures (T_{dep}) of 600 °C and 900 °C. The temperature at the YSZ surface was monitored by a pyrometer (Heitronics KT-19.99, Germany). The film thickness of 200 nm was controlled via deposition time and measured by scanning electron microscopy (SEM, FEI Qianta 200 FEG, Netherlands) and digital holographic microscopy (DHM, Lyncee Tec, Switzerland). Microstructure and film growth was investigated by SEM and transmission electron microscopy (TEM, FEI TECNAI F20). All LSM films showed a columnar film growth with varying grain diameters, dependent on the substrate temperature in the PLD [71]. Micro-patterning of the LSM films was performed by photolithography and chemical etching in concentrated hydrochloric acid. This lead to square microelectrodes of 390 µm and 490 µm size. A counter electrode of porous platinum was brushed on the back side of the YSZ substrate.

5.3.2. Impedance Spectroscopy and DC-Measurements

Electrochemical characterization of the LSM microelectrodes was done by means of two point impedance measurements using a POT/GAL 30V 2A test interface together with an Alpha-A High Resolution Dielectric Analyzer (both Novocontrol, Germany) in AC and DC mode (software WINCHEM and WINDETA Novocontrol, Germany). Impedance spectra were recorded at set temperatures of 500 °C, 600 °C, and 700 °C in air before DC-measurements with bias values of -300 mV and -450 mV were started. A frequency range was taken from 10^6 Hz to 10^{-3} Hz (if required) with a resolution of 5 points per frequency decade.

The simplified equivalent circuit shown in Fig. 5.1 was used to quantify the impedance data. Parameterization of the spectra was carried out by the complex nonlinear least square (CNLS) fit software Z-View2 (Scribner, USA).
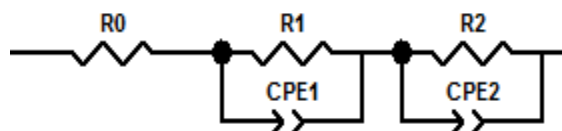

Fig. 5.1 Equivalent circuit used for the complex nonlinear least square fits.

5.3.3. Measurement Set-up and Measuring Procedure

Squared 490·490 μm^2 or 390·390 μm^2 LSM microelectrodes were electrically contacted in the symmetrically heated MiMa as depicted in Fig. 5.2a and b. The set-up was thermally equilibrated in air at measurement temperature before DC measurements and impedance spectroscopy measurements were performed. After finishing these pre-

145

experiments, the vacuum chamber was pumped for 90 seconds until a pressure of roughly $1 \cdot 10^{-2}$ mbar was reached. Then the pump was shut off and 200 mbar of $^{18}O_2$ tracer gas (97.1%, Campro Scientific, Germany) was filled into the chamber within about 10 seconds. Directly after closing the inlet valve (~5 s) cathodic bias was applied and the current measurement was started. Exactly after 10 min the bias was switched off, the vacuum chamber was opened and the sample was quenched in ambient air on a cold metal block. The procedure form switching off the current until quenching takes again 5 to 10 seconds. A control experiment with exactly the same procedure but with fast cooling in $^{18}O_2$ atmosphere while remaining applied bias was performed to prove that no artefacts are produced by shortly exposing the sample to $^{16}O_2$ while it is still at high temperature. In this control experiment, the quartz tube was moved out of the tube furnace after exactly 10 min. The whole set-up was then quenched by water while remaining $^{18}O_2$ atmosphere in the vacuum chamber.

It is often suggested in literature [147-149] to extensively pre-annealed the samples in ^{18}O containing oxygen atmosphere with the partial pressure also used in the exchange experiment afterwards. This is suggested to chemically equilibrate the material and thus to avoid oxygen chemical diffusion during tracer expose. In this experiment the pre-equilibration is hardly possible since the stoichiometry would again change during evacuation, i.e. before the vacuum chamber is filled with $^{18}O_2$ tracer gas. Trying to avoid the problem by a very fast evacuation and refilling process would be in vain, as the time constant of chemical equilibration is too short. This time constant can be estimated from impedance measurements without bias, which is the time constant of the semicircle featuring the chemical capacitance (~1 s at 600 °C). However, compared to tracer

fraction changes caused by the applied cathodic bias, the thermally and partial pressure induces errors during the filling process are negligible. Establishing a steady state upon applied bias before tracer expose is not possible in this experiment, since bias has to be switched off during evacuating the set-up for tracer gas filling. A remaining bias during evacuation is expected to severely enhance the oxygen vacancy concentration in LSM and thereby affects the measurement result [22, 44]. Additionally, cathodic bias at low oxygen partial pressure could irreversibly change LSM thin films. Bulk LSM should be stable until $1 \cdot 10^{-13}$ mbar [31] and for high applied cathodic bias and the low partial pressures during evacuation, such conditions can be reached. In principle a filling with $^{18}O_2$ tracer gas stream in a differently designed set-up without an evacuation step would be possible. However, much more $^{18}O_2$ gas would be needed, which would drastically increase the experimental costs and moreover the exact tracer gas fraction would then hardly be adjustable. We found no conspicuous error induced by our filling method so far [141]. Continuous tracer gas change experiments are available for time dependent equilibration *in situ* monitoring using mass spectrometry [150-153].

All parts in the vacuum chamber in the hot zone are made of quartz or platinum to minimize the ^{16}O-^{18}O oxygen exchange with other materials during the experiment. An exchange during the experiment would decrease the ^{18}O concentration of the gas mixture, which makes a quantitative analysis of SIMS depth profiles impossible. The ^{18}O concentration in the vacuum chamber was checked during the filling and after the experiment with a mass spectrometer (Pfeiffer GSD320 with QMG 220, Germany). The decrease of the tracer gas fraction from initially 97.1% was found between 1 and 2% for all experiments.
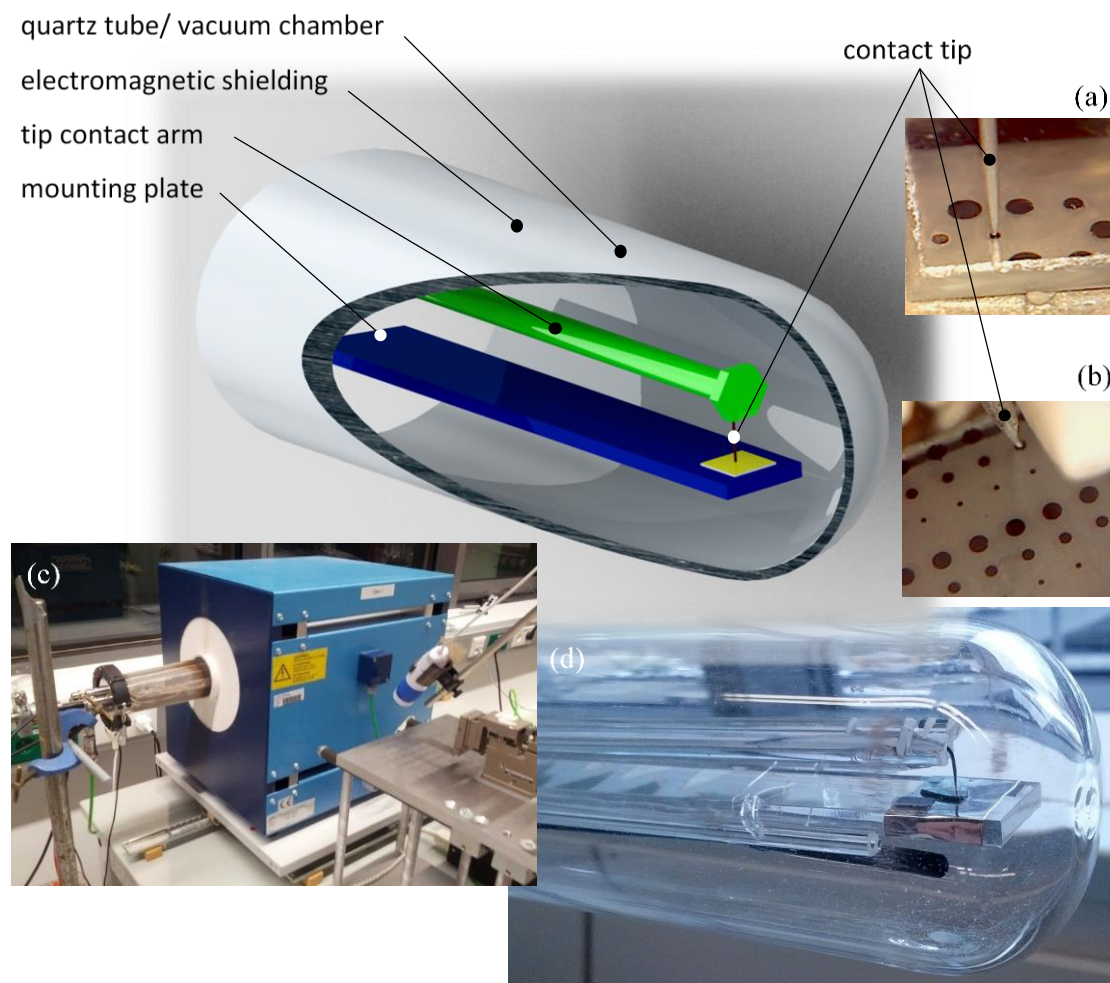
Fig. 5.2 MiMa measurement set-up with 3D sketch of the tip contact arm, mounting plate and quartz tube of the symmetrically heated micro-contact set-up MiMa. Small pictures (a) & (b) show contacted microelectrodes before the tube furnace is moved over the sample. (c) Whole measurement set-up with contacting device. (d) Tip contact arm with Pt/Ir contacting tip on sample located on mounting plate with platinum foil.

5.3.4. Isotope Exchange Depth Profiling (IEDP)

The resulting ^{18}O depth profiles were subsequently investigated by time-of-flight secondary ion mass spectrometry (ToF-SIMS, ION-TOF GmbH, Germany ToF-SIMS 5). For

these SIMS measurements the collimated burst alignment (CBA) mode with Bi_3^{++} primary ions (25 keV) was used, which allows accurate determination of ^{18}O concentrations in a broad intensity range [95, 96]. Negative secondary ions were analyzed in areas of $45 \cdot 45$ μm^2, using a raster of $512 \cdot 512$ measurement points. For the sputtering of material 2 keV Ce$^+$ ions were applied with a sputter crater of $350 \cdot 350$ μm^2 and sputtering ion current of 120 nA. The charging of surfaces was compensated by an electron flood gun. The isotope fraction depth profiles were obtained by normalizing integrated intensities I of ^{18}O and ^{16}O according to

$$f(^{18}O) = \frac{I(^{18}O)}{I(^{18}O) + I(^{18}O)} \; .$$

5.1

5.4.   Results and Discussion

5.4.1. Current Measurements

During the exposure to 200 mbar of $^{18}O_2$ atmosphere a bias of -300 mV or -450 mV was applied for 600 s. Irrespective of the applied bias the measured current response of all microelectrodes deposited at T_{dep}=600 °C showed an exponential decay function (Fig. 5.3a). Current characteristics of microelectrodes deposited at T_{dep}=900 °C showed an additional time dependent feature: The current first decreases very fast, this is followed by a short increase and a final decrease (Fig. 5.3b). The time dependence of these processes, summarized in Tab. 5.1, depends on the applied bias and the experimental temperature. The measured current value increases for a rise of measurement temperature, cathodic bias and decrease of deposition temperature. E.g.

an electrode with small grains exhibits a higher current for the same applied voltage and same experimental conditions, compared to an electrode with large grains. Thus the total electrode polarization resistance scales with grain size (Tab. 5.1).

Measured current values of different LSM microelectrodes were normalized to the microelectrode surface of 490·490 μm^2 and 390·390 μm^2 (c.f. Fig. 5.4). Overpotentials of the microelectrodes were calculated by subtracting the voltage drop in the electrolyte; the ohmic resistance of the electrolyte was obtained by impedance spectroscopy.

LSM thin film microelectrodes were found to incorporate oxygen via a three phase boundary related surface path [32] at temperatures between 500 and 700°C under open circuit conditions. However, a bulk path can be activated by applying cathodic bias at this relatively low temperatures [33, 66]. The polarization resistance of the LSM bulk path in similar LSM thin films at open circuit conditions was shown to decrease with decreasing grain size. Decreasing grain size implies an increasing number of grain boundaries [32, 71]. Thermal ^{18}O tracer exchange experiments revealed grain boundary dominated diffusion is very similar LSM thin films [71].
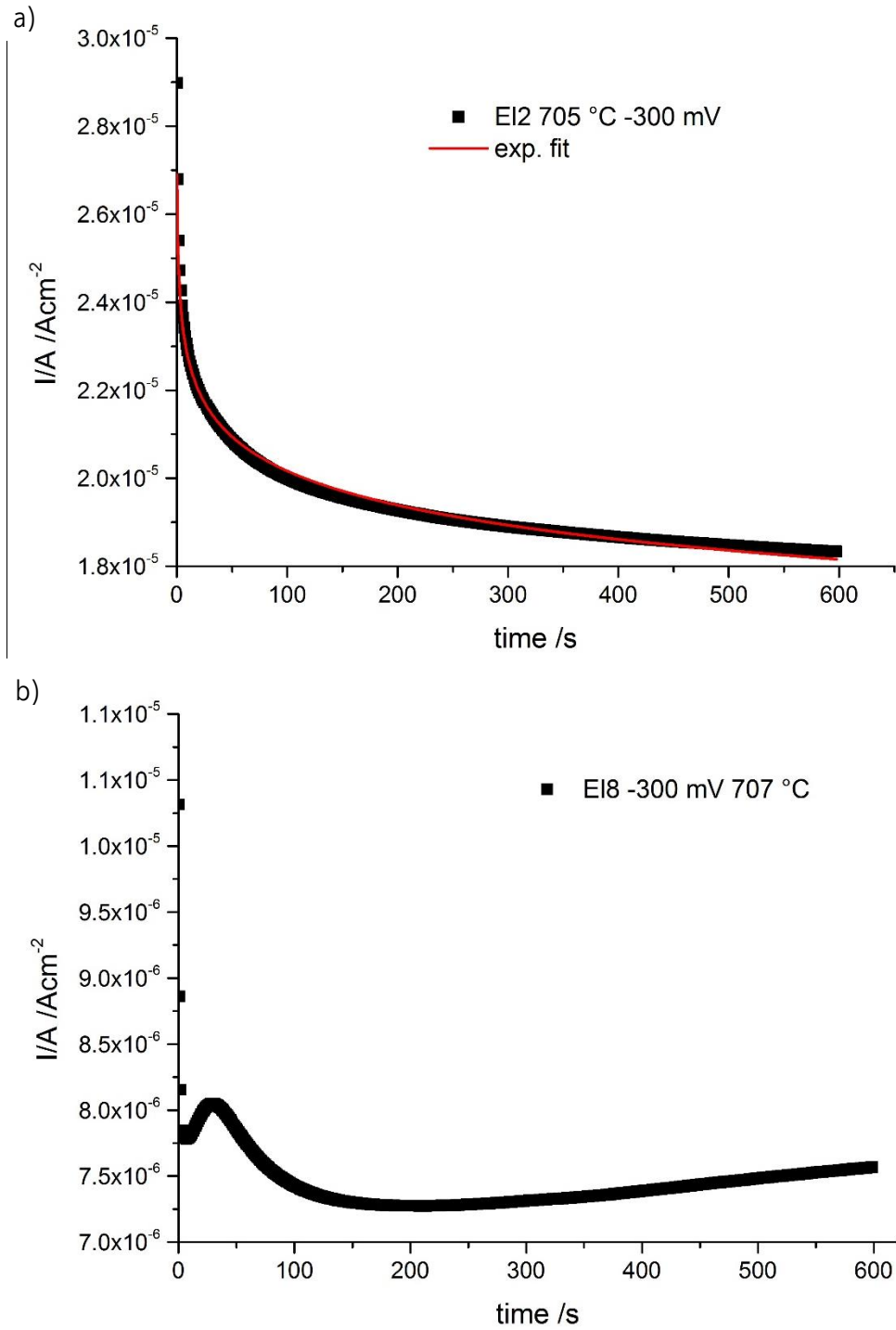
Fig. 5.3 Current response of a) EL4 (T_{dep}=600 °C) and b) El8 (T_{dep}=900 °C). (Voltage of -300 mV was applied for 600 s)

An increase in oxygen vacancy concentration with polarization of an LSM cathode appears to be responsible for the improved performance of LSM cathodes with increasing cathodic overpotential [31, 154, 155]. The oxygen vacancy concentration is of vital importance for the oxygen diffusion in LSM and possibly of equal importance to the oxygen reduction kinetics on LSM [31]. Most probably the applied bias is changing the oxygen vacancy concentration in grains and grain boundaries differently. By applying the cathodic bias, the chemical potential in the grain boundaries is assumed to be adjusted first. The exponential decay of the current after applying the cathodic bias is therefore most probably a stoichiometric polarization process in the LSM grain boundaries. However, charging of the interface capacitance could also play a role in this first equilibration [33]. The second feature, the current increase (Fig. 5.3b), is only present in current characteristics of films with large grains. This could be attributed to a similar stoichiometry polarization process within the grains. Probably the same effect is also present in films with small grains but too fast and, thus, not noticeable since smaller grains exhibit a smaller volume and also shorter diffusion length. This interpretation is based on the findings from thermally annealed ^{18}O depth profiles. There tracer diffusion in LSM grain boundaries is approximately 3 orders of magnitude faster than in LSM grains [71].
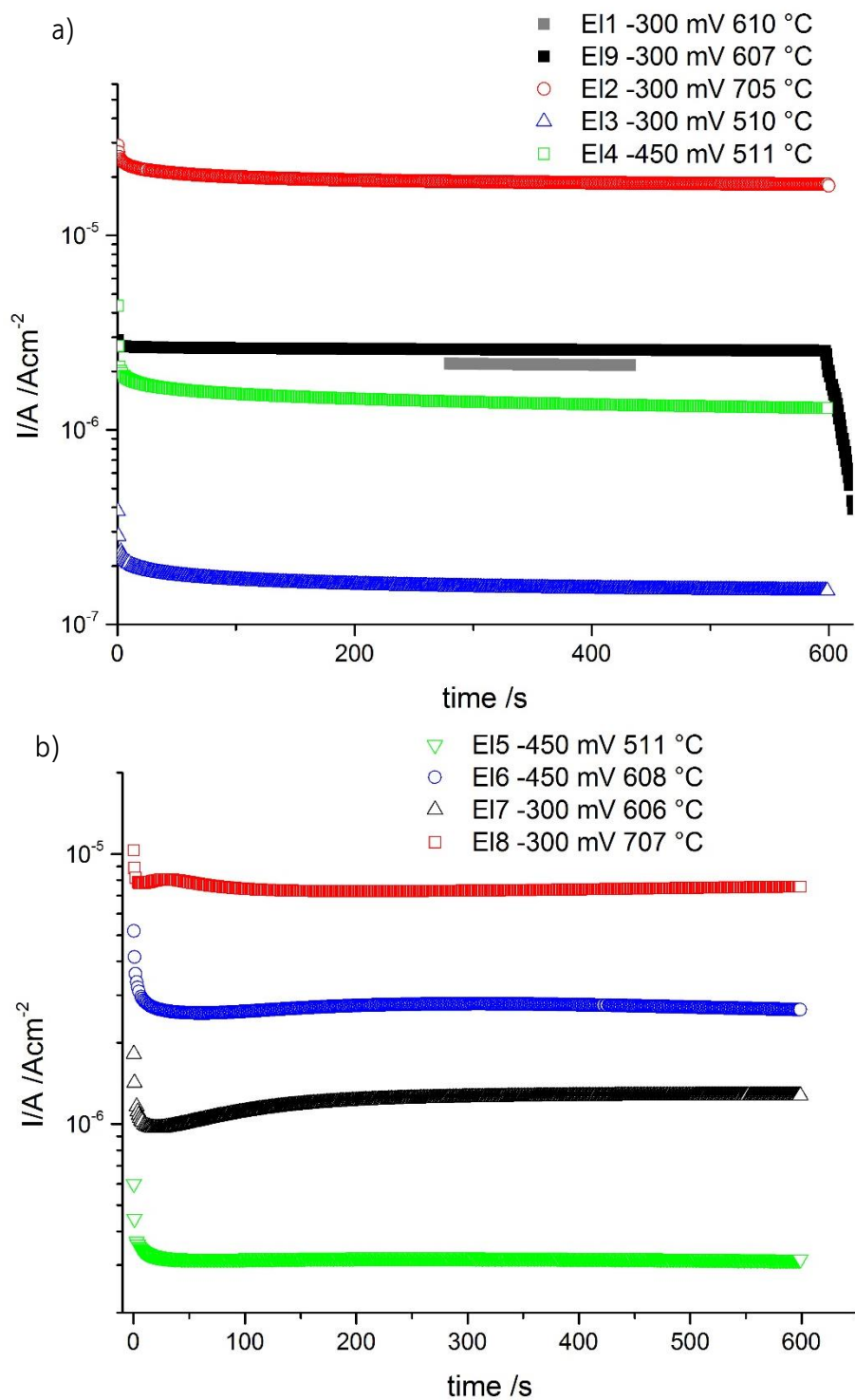
Fig. 5.4 Logarithmic plot of the current recorded during ^{18}O exchange of LSM microelectrodes deposited at 600 °C a) and at 900 °C b). El1 was treated identically, however, current was only recorded for ca. 180 s.

A change of the microstructure substantially influences the measured current for the same applied bias. Changes in grain size have a larger effect at -450 mV than for -300 mV. This indicates that the applied bias has a larger effect on small grains compared to large grains (Fig. 5.5 and Tab. 5.1).
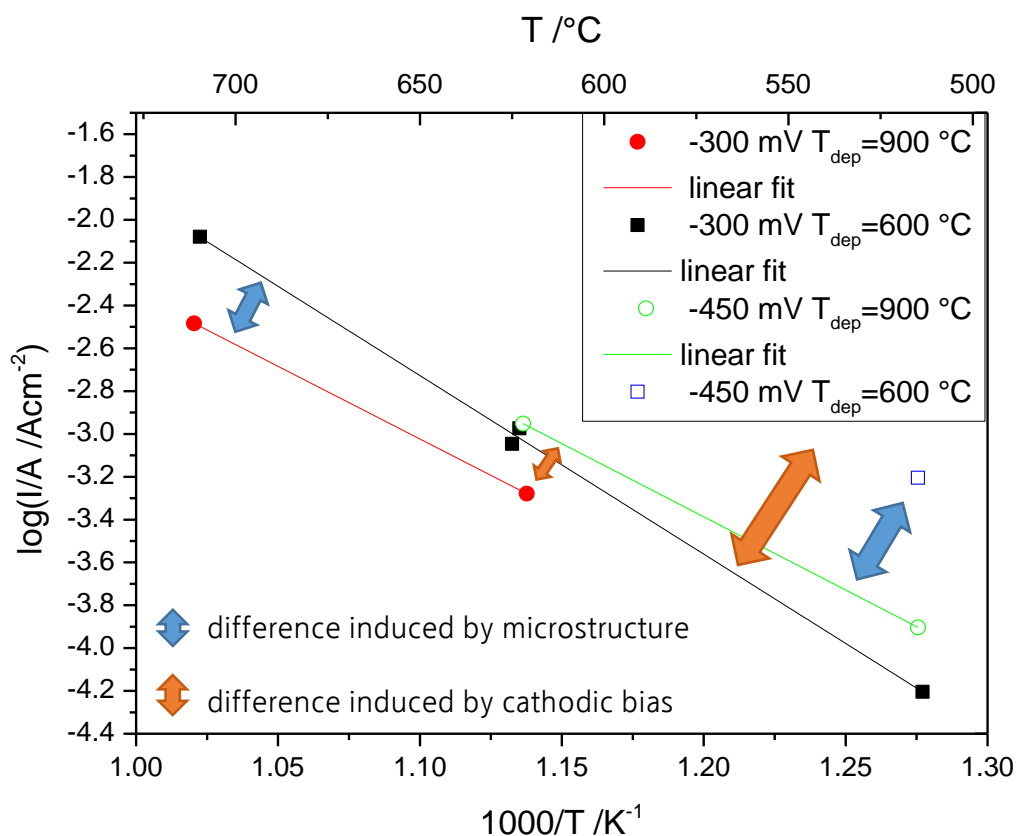

Fig. 5.5 Arrhenius plot of current values from microelectrodes deposited at 600 °C and 900 °C with applied bias of 300 mV and 450 mV.

sample #	el. edge length	T_{exch}	T_{dep}	bias	η	sec. max.	YSZ conc.	I/A /Acm^{-2}
El1	490 µm	600 °C	600 °C	–300 mV	281 mV	-	0.01	$9.00 \cdot 10^{-4}$
El2	490· µm	700 °C	600 °C	–300 mV	265 mV	-	0.057	$8.33 \cdot 10^{-3}$
El3	490· µm	500 °C	600 °C	–300 mV	291 mV	-	0.0025	$6.25 \cdot 10^{-5}$
El4	490 µm	500 °C	600 °C	–450 mV	368 mV	-	0.008	$6.25 \cdot 10^{-4}$
El5	490 µm	500 °C	900 °C	–450 mV	405 mV	230 s	0.0045	$1.25 \cdot 10^{-4}$
El6	390· µm	600 °C	900 °C	–450 mV	430 mV	300 s	0.016	$1.12 \cdot 10^{-3}$
El7	390 µm	600 °C	900 °C	–300 mV	291 mV	>600 s	0.005	$5.26 \cdot 10^{-4}$
El8	390 µm	700 °C	900 °C	–300 mV	291 mV	30 s	0.015	$3.92 \cdot 10^{-3}$
El9	490 µm	600 °C	600 °C	–300 mV	278 mV	-	0.025	$1.06 \cdot 10^{-3}$

Tab. 5.1 Properties of electrodes 1-9, with electrode size (el. edge length), time to reach the second current maximum (sec. max), ^{18}O tracer concentration in YSZ at the LSM/YSZ interface (YSZ conc.), 0.00205 is the natural abundance level.

5.4.2. Impedance Measurements

The impedance spectra of all measured squarish 490·490 µm^2 and 390·390 µm^2 LSM microelectrode consist of a large semicircle in the low frequency range, a shoulder in the medium frequency range and a high frequency intercept. The total polarization resistance strongly decreases with increasing applied bias (Fig. 5.6 and inset). The shape in the Nyquist plot, however, is not significantly changed by the applied bias. Also the high frequency intercept, which can be assigned to the spreading resistance of ion conduction in the YSZ [74, 75], stays invariant upon the applied bias. For low temperatures, the high frequency intercept becomes a separate arc. In all temperature

regimes, the electrode part of the spectra can be fitted to the circuit given in Fig. 5.1. In the Bode plot the two partly separated features (0 mV applied bias) merge to one distorted arc (–300 mV and –450 mV applied bias). Measurement frequencies are indicated in Fig. 5.6. Impedance spectra of all measured electrodes (not depicted) showed similar behavior.

The capacitive properties obtained from the fit are not significantly changed by the applied bias which is surprising since they include contribution from the chemical capacitance of LSM. However, since the chemical potential distribution in the film is adjusted according to the diffusion properties [156], the surface near part with the highest resistance and lowest chemical capacitances might still dominate the impedance spectra.
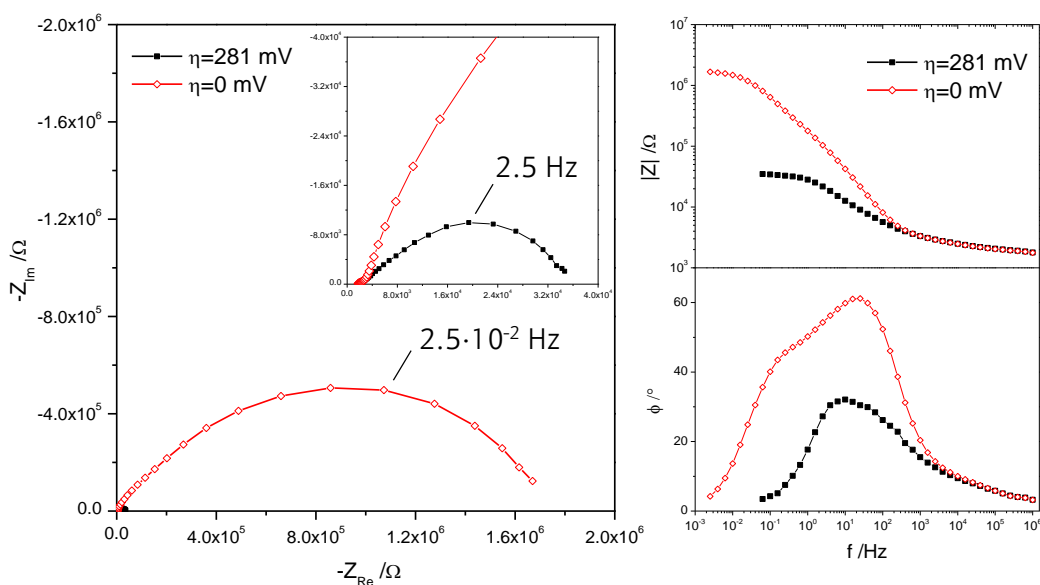

Fig. 5.6 Impedance spectra of LSM microelectrode El1 490·490 μm^2 with and without applied bias at 610 °C. l.h.s.: Nyquist plot, r.h.s.: Bode plot.

5.4.3. ^{18}O Depth Profiles

Tracer depth profiles obtained from electrodes without applied bias show a steep near-surface decrease of ^{18}O concentration (first 10 nm), which is dominated by LSM grains (Fig. 5.7 dotted lines). The following long tail up to the LSM/YSZ interface mainly reflects grain boundary diffusion (see chapter 4). The concentrations at the LSM/YSZ interface was found above the natural abundance of ^{18}O. For all electrodes a very shallow profile in YSZ is visible, indicating very fast diffusion in YSZ. The profile in the YSZ is more relevant than one might expect from its level. The concentration in the LSM, feeding the YSZ, is increasing with time and thereby the LSM microelectrode preparation, and thus the grain size, strongly affects the profile shape in the YSZ (Fig. 7).

After applying a cathodic bias of -300 mV at 600 °C for 10 min to a 490·490 μm^2 LSM (El1) microelectrode (deposited at T_{dep}=600°C) the ^{18}O concentration in the film is strongly enhanced. However, the feature in the first view nanometers looks similar for both types of depth profiles, with -300 mV and without bias (Fig. 5.7 filled lines). At a depth of around 5-10 nm the depth profile shows an apparent bias induced uphill diffusion with increasing ^{18}O concentration, which rises above the surface concentration level (Fig. 5.7b green curve). This hill reaches a maximum roughly in the middle of the film and decreases to a level of 1% tracer fraction at the LSM/YSZ interface, by changing its bending from convex to a concave shaped diffusion profile. The ^{18}O concentration in the YSZ is thus also significantly increased by the bias from 0.28% to 1% for 0 and -300 mV respectively (values for all electrodes are summarized in Tab. 5.1).

Repeating the experiment with the same parameters while only changing the sample to a LSM microelectrode deposited at T_{dep}=900 °C with larger grains (El7) leads to a drastic change of the depth profile (Fig. 5.7b red curve). The near surface feature is essentially the same as for the LSM electrode with small grains. The surface concentration slightly increased from 13.8% to 24% for 0 and -300 mV, respectively. The uphill diffusion with its maximum near the center of the LSM film, however, is much less pronounced compared to the electrode with small grains. The maximum of this dominating feature in the depth profile is shifted towards the interface to a depth of about 115 nm.

When repeating the same experiment with a microelectrode deposited at T_{dep}=900 °C (El6) and increasing the applied bias to -450 mV while leaving all other parameters constant, the picture again changes (Fig. 5.7b blue curve). The near surface concentration is even more increased to 33.5% (24% for -300 mV), without changing the shape in this region. The uphill diffusion is drastically increased but still less pronounced than for the microelectrode deposited at 600 °C and polarized by only -300 mV. The maximum of the dominating uphill diffusion is even more shifted to a depth of 125 nm.

The same exchange experiments were performed for 10 min at a temperature of T_{exch}=500 °C with two similar microelectrodes deposited at T_{dep}=600 °C with bias values of -300 and -450 mV (Fig. 5.7a). Again the near surface profile of polarized electrodes show the same shape as for non-polarized electrodes and the surface concentration is increased depending on the applied bias. The uphill diffusion for a bias of -300 mV is rather small with a maximum located in the first half of the film depth. By applying -

158

450 mV the uphill diffusion part is drastically increased with a maximum at the center of the LSM film thickness.

At T_{exch}=700 °C two electrodes deposited at T_{dep}=600 °C (El2) and T_{dep}=900 °C (El8) were exposed to ^{18}O atmosphere upon polarization by -300 mV. El8 with large grains shows a shift of the near surface feature of about 5 nm into the depth of the LSM film (Fig. 5.7c). The uphill diffusion part in the center of the LSM film of El8 is less pronounced than for the profiles obtained at lower T_{exch} (Fig. 5.7c). El2 deposited at T_{dep}=600 °C with small grains shows already an uphill diffusion without bias. The origin of this probably micro-structure related phenomena will be explained in section 5.4.6. The depth profile of El2 shows a strong decrease of ^{18}O in the first few nanometers. The uphill diffusion part is much higher compared to El8, with a maximum of 71.8%, i.e. much more than its surface concentration, located at a depth of only 70 nm in the LSM film.

The decrease of ^{18}O concentration of El2 and El8 in the first 5 nm in Fig. 5.7c is probably generated due to the quenching procedure in atmosphere at high T_{exch} (700 °C). Probably ^{16}O is incorporated in the near surface region after the bias was switched off and the sample was exposed to air. In Fig. 5.7 some unexpected effects were found. The LSM film thickness of roughly 200 nm seems to differ slightly between the different samples. Different film thicknesses at different microelectrodes can arise by slightly different deposition properties, or by anisotropic sputter conditions in the PLD process, leading to different film thicknesses even on one and the same 10·10 mm^2 YSZ substrate. A microelectrode located in the center of the 10·10 mm^2 YSZ single crystal is expected to be slightly thicker than a microelectrode in the near edge region. Another

possible explanation for apparently different LSM thicknesses are different sputter rates in the SIMS, influenced by charging effects.

In Fig. 5.7a the depth profile of the non-polarized El5 shows a higher ^{18}O concentration value near the LSM/ YSZ interface compared to the polarized electrode. The free YSZ surface surrounding the microelectrode is filled with ^{18}O via thermal incorporation and via the polarized LSM microelectrode. Since both LSM electrodes, the polarized and the non-polarized are assumed to be gas tight, the amount of thermally incorporated ^{18}O should be the same. The bias induced ^{18}O fraction in YSZ is assumed to be higher below the polarized microelectrode, since the ^{18}O is transported through the LSM bulk. At exchange temperatures of T_{exch}=500 °C a back diffusion of ^{18}O from YSZ into non polarized microelectrode is thus probably increasing the ^{18}O concentration in the depth profile towards the LSM/YSZ interface (Fig. 5.7a).
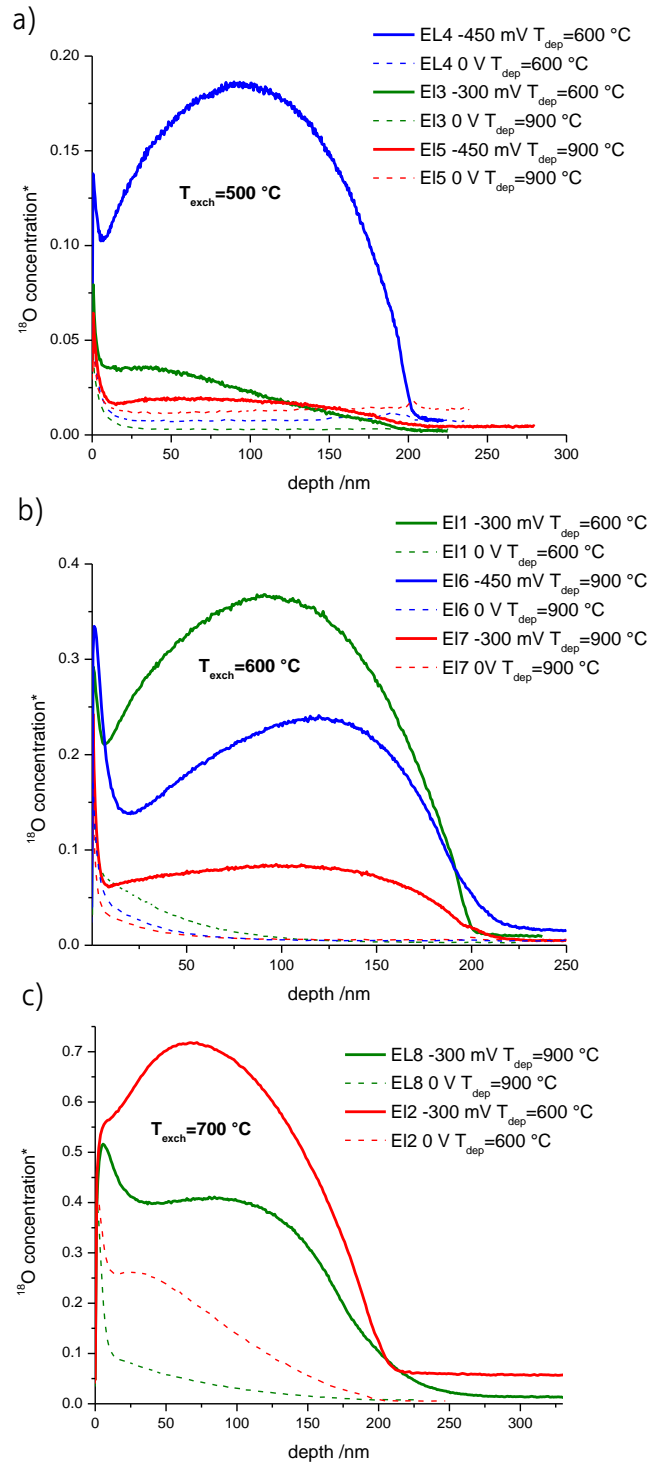
Fig. 5.7 ^{18}O tracer depth profiles of 200 nm thick, columnar LSM films deposited on YSZ at 900 °C and 600 °C. ^{18}O exchange time was 10 min, T_{exch}=500 °C a), T_{exch}=600 °C b), T_{exch}=700 °C c). Obvious differences in amount of tracer incorporation as well as in diffusion profile point to a strong difference of oxygen transport between 0 bias (dotted lines) and applied bias (solid lines).

5.4.4. Simulation of Bias Induced Apparent Uphill Diffusion

Finite element calculations were performed with COMSOL Multiphysics® (COMSOL, Sweden) for a cylindrical LSM grain with surrounding grain boundary on a YSZ electrolyte.
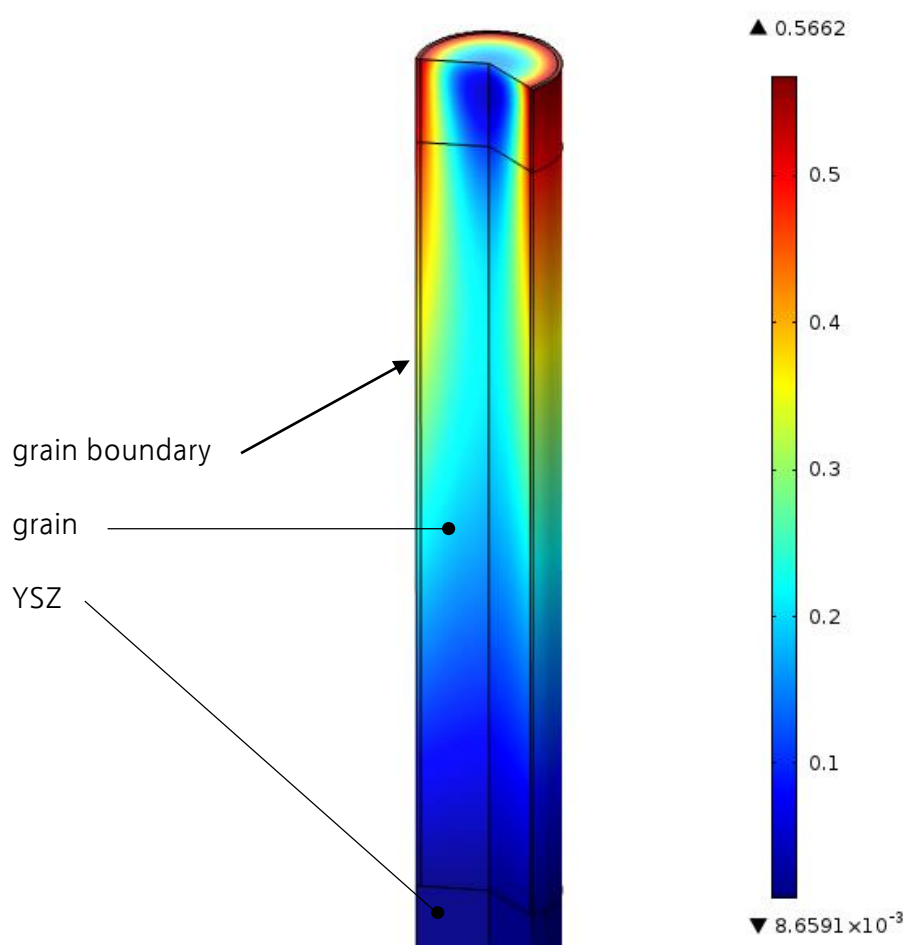

Fig. 5.8 Tracer fraction calculated by a 3D finite element model of a LSM grain with grain boundary and the YSZ substrate. The diffusion coefficient in LSM grain is increasing from the surface to LSM/YSZ interface. The line parallel to the surface in the upper part of the grain confines the region where the finite element mesh is refined to get a better numerical result in the surface near region.

The simulation model was in accordance with the 3D model used in chapter 4. It included three domains (Fig. 5.8) representing diffusion in a grain, along the grain boundary and in the YSZ substrate. Fitting of depth profiles as depicted in Fig. 5.9, with contributions from grains and grain boundaries is already rather complicated because of the large numbers of individual fitting parameters. To minimize the unknown parameters the microstructure of such films was estimated from TEM and SEM measurements. The width of the grain boundary was set to 2 nm.

The model solves Fick's second equation in all domains with diffusion coefficients in the LSM grains (D_b), LSM grain boundaries (D_{gb}) and YSZ (D_{YSZ}). The boundary conditions of the FEM model reflect that gas exchange is possible at the surface of the grains (exchange coefficient k_b) and the grain boundaries (k_{gb}). Thus diffusion takes place from the grain, along the grain boundary, from the grain boundary to the grain and from the LSM layer to the YSZ substrate. Diffusion coefficient D_{YSZ} values were used according to Ref. [157]. In accordance with chapter 4 FEM calculations on thermally annealed films in ^{18}O atmosphere with varying D and k values of grain and grain boundary were done until the best match was found between the calculated isotope profile and the experimental one (c.f. Fig. 5.9). As additional parameter in the FEM model, the natural abundance was set to 0.00205 and the ^{18}O concentration during the experiment was set to 95.6% (in accordance with the 97.1% supplied gas – 1.5% average loss, obtained by mass spectrometer). Only full consideration of all four individual fit parameters ($D_b \neq D_{gb}$ and $k_b \neq k_g$, different diffusion and surface exchange coefficients) leads to a successful fitting (Tab. 5.2 for El1). However, this kind of fit analysis can only be performed for thermally annealed samples without applied bias.
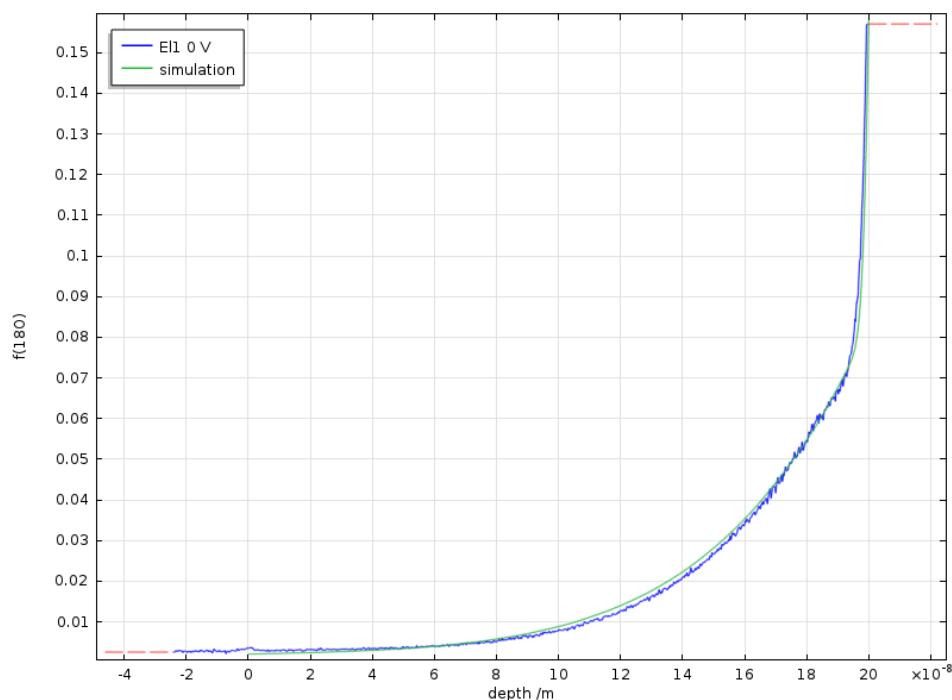
Fig. 5.9 [18]O isotope exchange depth profiles of El1 (T_{exch}= 600 °C, 10 min) with 0 mV bias and finite element fit. Fit values depicted in Tab. 5.2. (r.h.s [18]O atmosphere, l.h.s YSZ).

The FEM calculations of voltage driven tracer diffusion depth profiles were done in a similar manner, with the chemical potential in the model being changed according to the applied cathodic bias (Fig. 5.10). In a diffusion controlled perovskite electrode, the tracer diffusion coefficient is locally changing according to the applied overpotential, which is locally adjusting the chemical potential and thus the oxygen vacancy concentration [156]. The chemical potential of oxygen (μ_O) is expected to change linearly in the LSM layer under applied bias in the case of steady state diffusion [31, 158]. This chemical potential changes can be implemented in the FEM by a linear variation of the tracer diffusion coefficient

$$D_{\mathrm{var}} = D - \frac{z \cdot D \cdot factor}{LSM_h} \, . \qquad\qquad 5.2$$

LSM_h denotes the LSM film height (200 nm), z the depth coordinate, D the diffusion coefficient without bias, and "factor" represents the enhancement factor (Tab. 5.2). Only a voltage induced variation of the bulk diffusion coefficient D_b was assumed for the case of simplicity.

After applying a voltage, the electrochemical potential of the electrons in the LSM electrode changes nearly instantaneously. The oxygen vacancy concentration in vicinity of the LSM surface is no longer in equilibrium with the gas phase, see Fig. 5.10. The chemical potential of oxygen, however, needs some time to adjust according to the slow surface exchange and the diffusion properties of the electrode (Fig. 5.10). Since YSZ blocks electrons totally, this experiment can to a first approximation be described by a Wagner Hebb approach [159] with the vacancy concentration at the LSM/YSZ interface changing according to the full overpotential applied to the electrode [156] (Fig. 5.10). We assume steady state conditions are reached after the measured current drops to an almost constant level, after approximately 30 to 100 seconds (Fig. 5.4). Hence, for most of the time we assume an almost linear chemical potential of oxygen in LSM.

The local depth dependent chemical potential modifies the bulk diffusion coefficient in grains according to Eq. 5.2, cf. Fig. 5.10. Thus, tracer diffusion in LSM grains is slow at the surface and becomes faster towards the LSM/YSZ interface. Near to the surface the ^{18}O concentration in the grain boundaries is expected to be rather high (Fig. 5.8), but only a small fraction is incorporated into the grains owing to the small bulk diffusion

coefficient. In the center of the film the diffusion coefficient in the grain is strongly enhanced and more ^{18}O is incorporated from the grain boundary into the grain (Fig. 5.8). The tracer fraction in the grain boundary becomes smaller with depth and near to the LSM/YSZ interface there is again less tracer transfer from the grain boundary into the grain, despite high bulk diffusion coefficient. This combination of depth dependent transport capacity in the grain and driving force (determined by the tracer fraction in the grain boundary) causes the unusual maximum of tracer concentration in the center of the film, see sketches in Fig. 5.11 and Fig. 5.12.
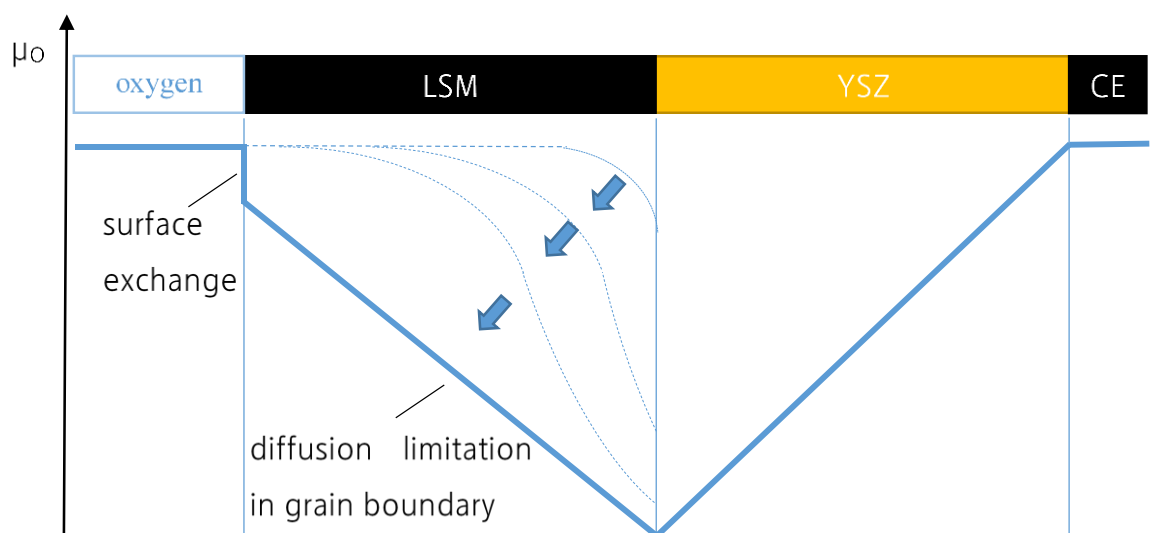
Fig. 5.10 Sketch of the local oxygen chemical potential μ_O in the LSM/YSZ system, with a step function at the surface induced by the surface exchange resistance and a linear slope in the LSM film induced by diffusion limitation. Arrows indicate the time dependent change of μ_O after applying a cathodic bias.
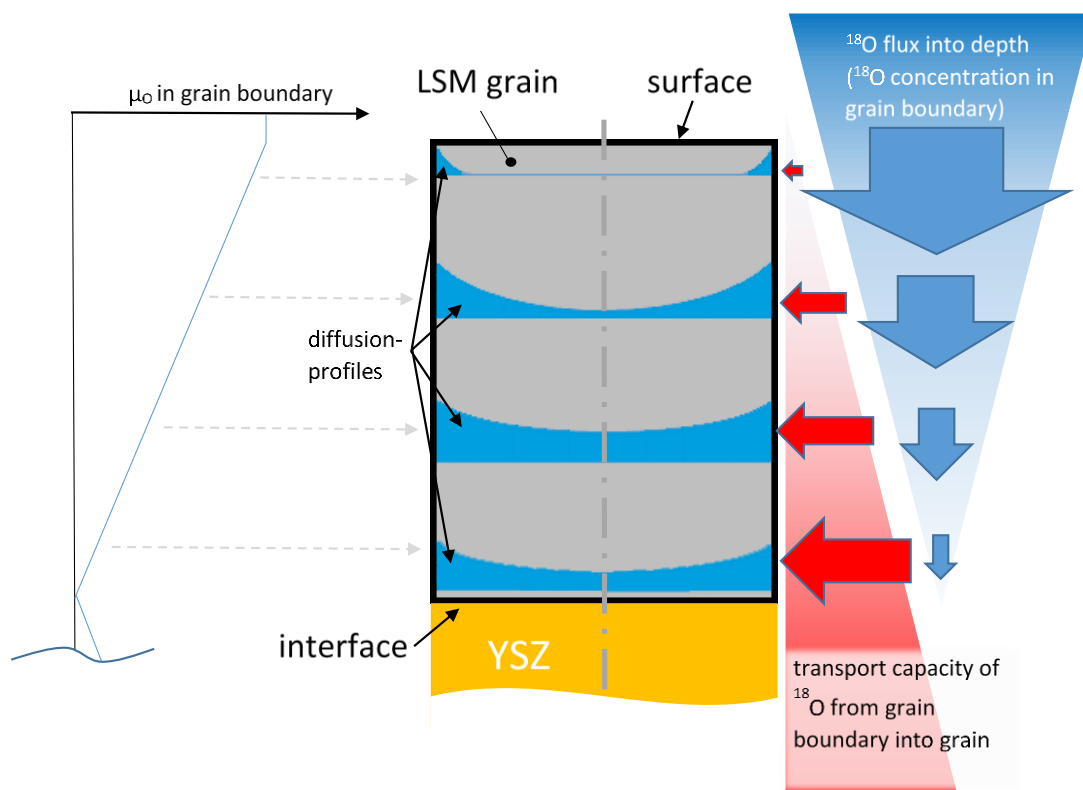
Fig. 5.11 Sketch of depth dependent diffusion profiles in the LSM grain caused by a depth dependent transport capacity induced by the depth dependent chemical potential and by fast diffusion in the grain boundary.
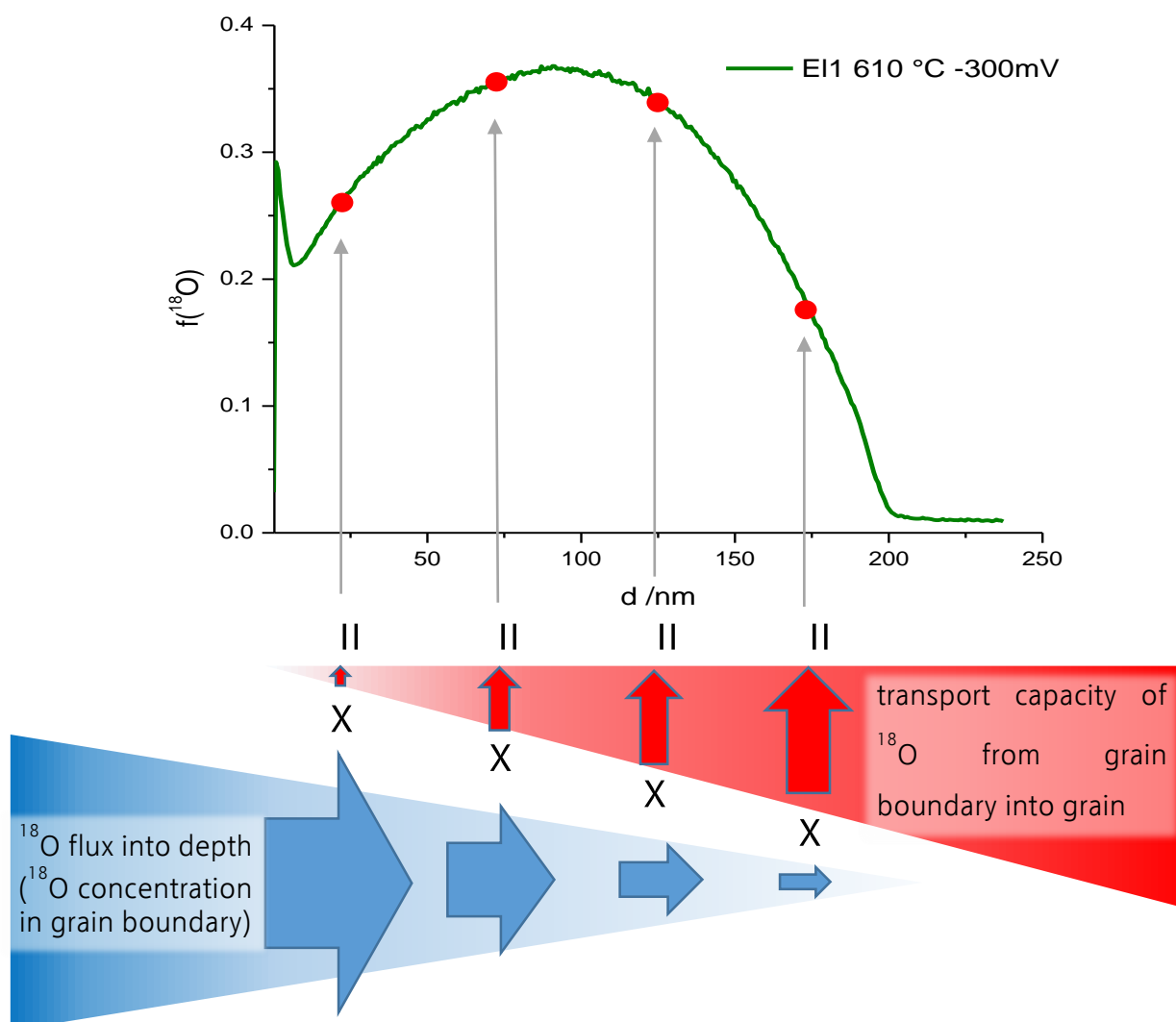
Fig. 5.12 Sketch of the origin of the uphill diffusion with depth dependent decrease of ^{18}O content, and increasing transport capacity.

The simulation to numerically validate this model was carried out in an iterative process, repeating the two steps as follows: First the fit curve was adjusted only to the steep near surface region by changing D_b and k_b, which can attributed to the slow grain incorporation (Fig. 5.13 blue curve, factor x=0). Second D_{gb} and k_{gb} were chosen to reach the measured ^{18}O concentration level at the LSM/YSZ interface.

In the depth of ca. 10 nm, where the grain boundary contribution becomes visible in the depth profile, the uphill diffusion starts for voltage driven profiles. This feature was then adjusted by the bulk enhancement factor as depicted in Fig. 5.13. The shape of the resulting uphill diffusion looks similar to the measured depth profiles. The position and the absolute height, however, are not correct. However, deviations are not surprising since time dependent surface exchange coefficients, depth dependent grain boundary diffusion coefficient and chemical diffusion induced horizontal gradients of the grain diffusion coefficient are neglected in this simulation. The surface and interface concentration, were also only nearly adjusted with reasonable effort. This simulation therefore üresents a clear proof of concept but is not a true quantitative analysis.

El1	D_{gb}	k_{gb}	D_g	k_g	factor
0 V	$8.0 \cdot 10^{-18}$ cm^2/s	$1.5 \cdot 10^{-10}$ cm^2/s	$4.0 \cdot 10^{-21}$ cm^2/s	$2.3 \cdot 10^{-13}$ cm^2/s	–
-300 mV	$2.3 \cdot 10^{-16}$ cm^2/s	$2.0 \cdot 10^{-9}$ cm^2/s	$1.6 \cdot 10^{-20}$ cm^2/s	$8.5 \cdot 10^{-13}$ cm^2/s	0–30

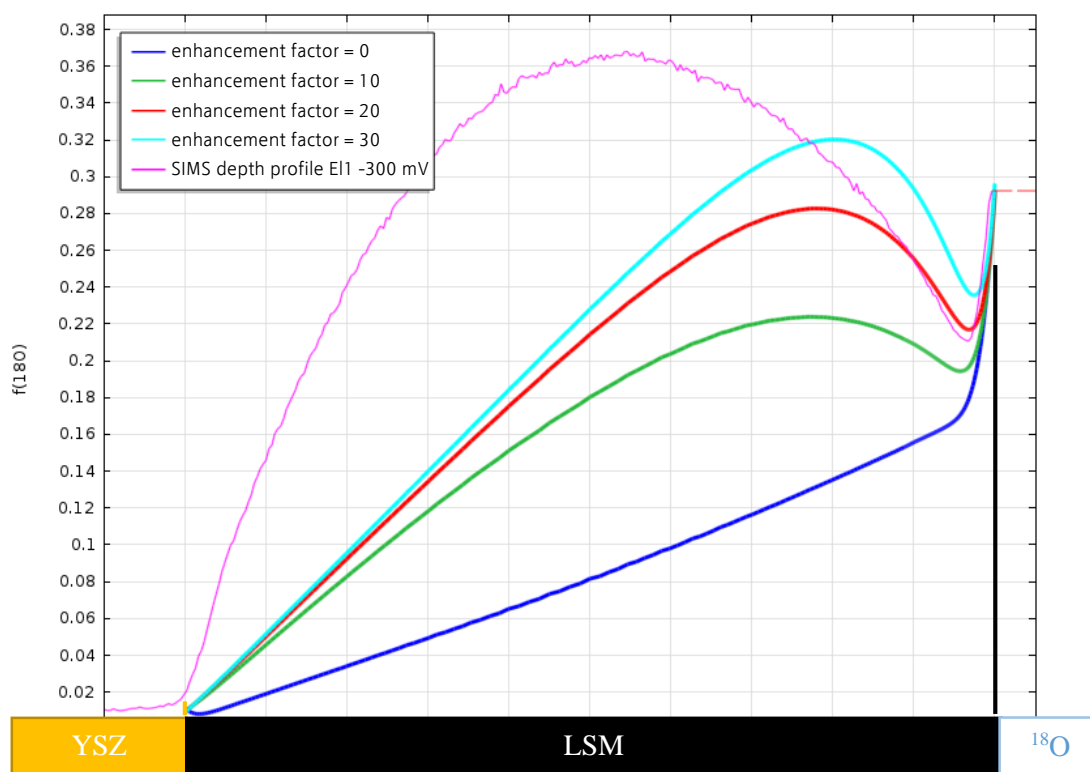**Tab.** 5.2 Fit values used in Fig. 5.9 and 13 for El1 with 0 and -300 mV applied bias.

Fig. 5.13 ^{18}O isotope exchange depth profiles of El1 (T_{exch}= 600 °C, 10 min) with -300 mV and 0 mV bias and sesults of four finite element simulations (factor 0, 10, 20 and 30). The other parameters are depicted in Tab. 5.2.
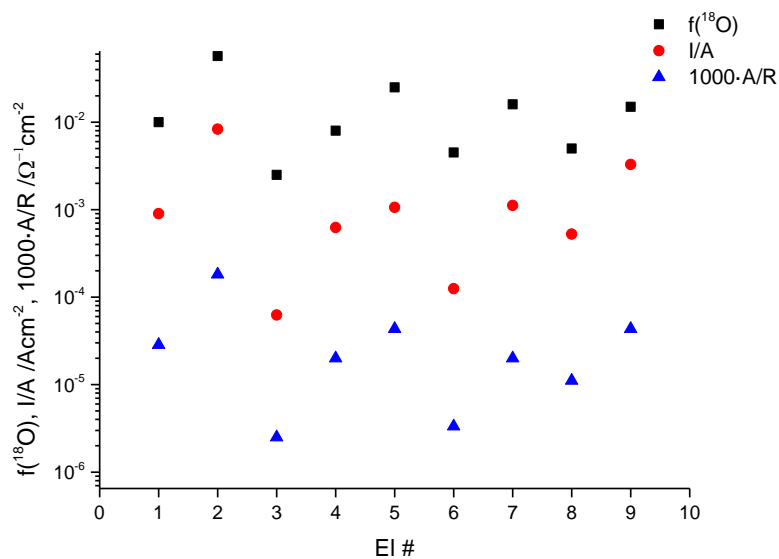
Fig. 5.14 Current normalized to the electrode area (I/A), ^{18}O concentration in YSZ below the electrode (f(^{18}O)) and thousand times the electrical conductance normalized to electrode area (1000·A/R) of electrode number 1-9.

To visualize the results of all three individual examination methods, tracer fraction in YSZ, measured current and electrical conductance (obtained by impedance spectroscopy) of all nine measured electrodes are plotted in Fig. 5.14.
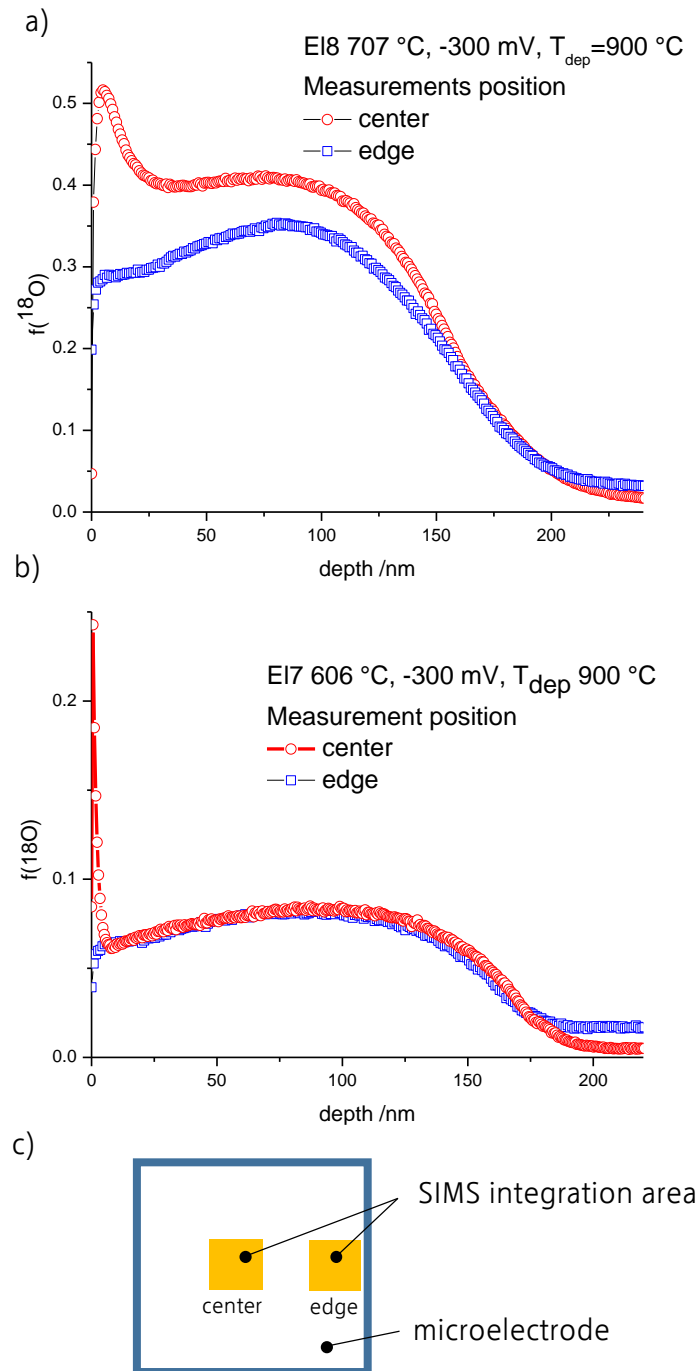
5.4.5. Spatial Resolved Depth Profiles

Fig. 5.15 Depth profiles measured on two different positions of one microelectrode, El8 a) and El7 b). SIMS integration area was located in the center and near the edge/ three phase boundary c).

Locally resolved depth profiles on one and the same microelectrode (El8, -300 mV, T_{exch}=707 °C) showed significantly changed surface concentration at different measurement positions (Fig. 5.15a). Also the shape of the profile changed significantly in the near surface region (first 50 nm). The ^{18}O concentration in the YSZ is increased near the edge of the electrode. Locally resolved depth profiles on El7 (-300 mV, T_{exch}=606 °C) depicted in Fig. 5.15b shows less difference between center and edge. The near edge profile shows a decrease of ^{18}O concentration only in the first 5 nm. The ^{18}O concentration in the YSZ is again higher in the near edge region.

It is known, that LSM thin films show a temperature dependent in-plane sheet resistance with increasing impact towards higher temperatures [32]. This sheet resistance decreases the effective polarization potential with increasing distance to the current collecting tip. The decrease of near surface ^{18}O concentration is more drastic for El8 (707 °C) compared to El7 (606 °C). This suggests, that an in plane sheet resistance is responsible for this difference. Thus, the surface exchange kinetics seems strongly depend upon applied bias. An explanation of the different ^{18}O concentrations in YSZ found on one and the same microelectrode cannot be given so far.

5.4.6. Simulation of Thermally Induced Apparent Uphill Diffusion Without Bias

Some depth profiles obtained from thermally annealed LSM films, e.g. El2 in Fig. 5.7c, showed apparent uphill diffusion even without applied bias. The ^{18}O concentration in non-polarized El2 is increasing in a depth of roughly 10 nm. Such a phenomenon could occur in films with increasing grain boundary distribution density towards the LSM/YSZ

interface. The fast grain boundaries are responsible for the transport of most of the oxygen ions, and hence the total amount of ^{18}O in grains in vicinity of the grain boundaries should increased by a large number of grain boundaries. In simple words, grain boundaries are "conducting" ^{18}O ions while grains "storing" ^{18}O ions.

To proof the concept of changed concentration profiles due to enhanced grain boundary density, a cylindrically symmetric 3D finite element simulation was performed on grains with and without changing grain boundary distribution density. By increasing the number of grain boundaries in a certain depth, as sketched in the 3D finite element model in Fig. 5.8, more volume of the LSM becomes accessible by grain boundaries. Since a SIMS depth profile represents an averaged ^{18}O concentration in a certain depth, the concentration may increase when increasing the number of tracer supplying grain boundaries.

For the simulation a model geometry was used containing a LSM grain with 50 nm in diameter, a height of 200 nm and a 2 nm grain boundary, which corresponds to a PLD deposited thin film at approximately T_{dep}=750 °C (Fig. 5.16a). A similar model was then employed with an additional grain boundary, thus enhancing the grain boundary cross-section (Fig. 5.16b). Since the model is cylindrically symmetric, the diagonal additional grain boundary exhibits a decreasing volume with increasing depth, and thereby less impact of enhanced oxygen ion conduction. This simulation may not represent a real microstructure but is helpful for testing the possibility of uphill diffusion due to structural changes. Indeed, the concentration of the depth profile is significantly changed and the concentration became enhanced in some depth in accordance with an apparent uphill diffusion in the center of the profile (Fig. 5.17).
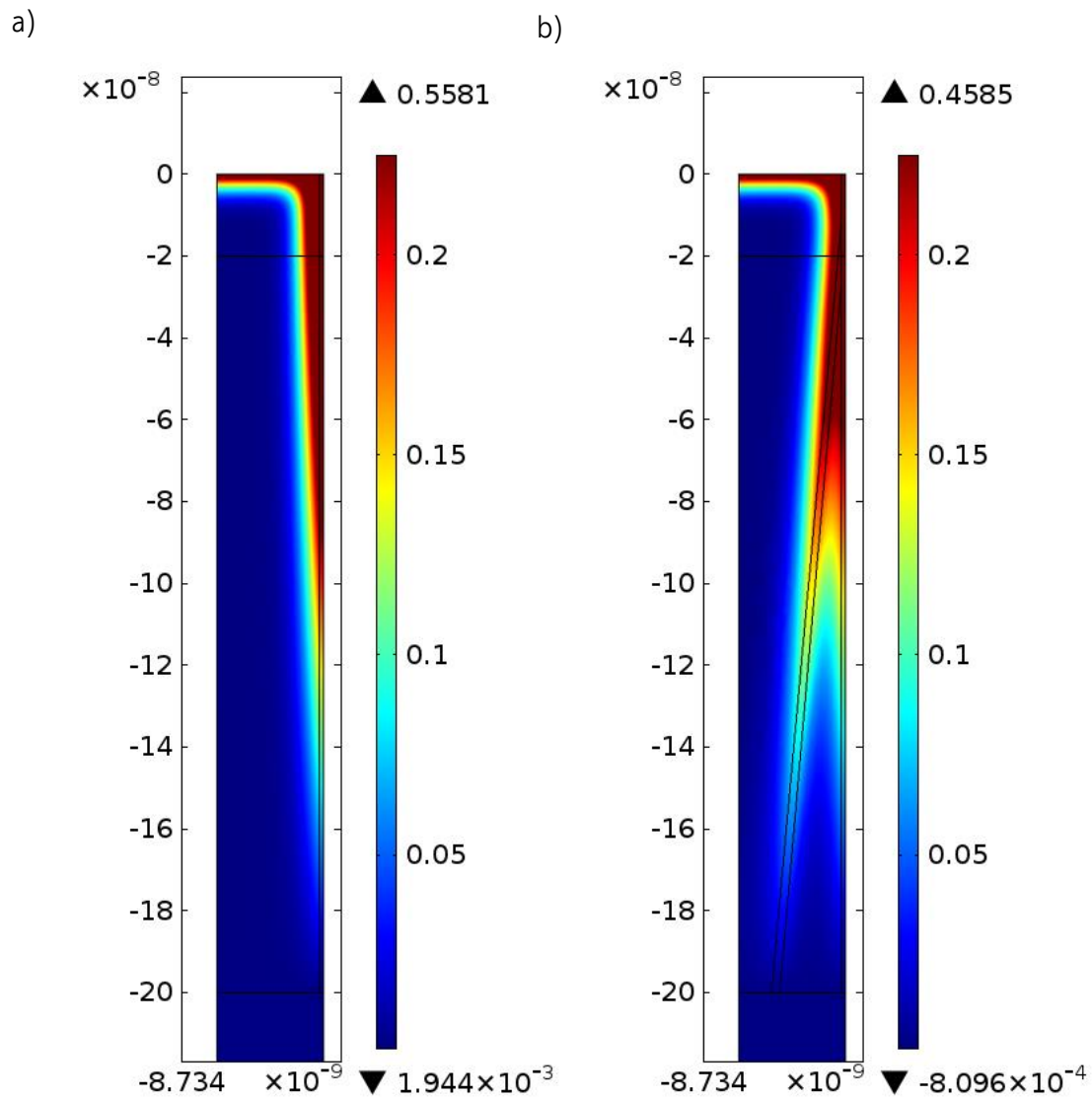
a)
b)

Fig. 5.16 Cross-section of the cylinder symmetrical 3D finite element model of LSM grain with grain boundaries for a columnar grain with fixed grain boundary thickness (a), and an enhanced grain boundary distribution density (b).
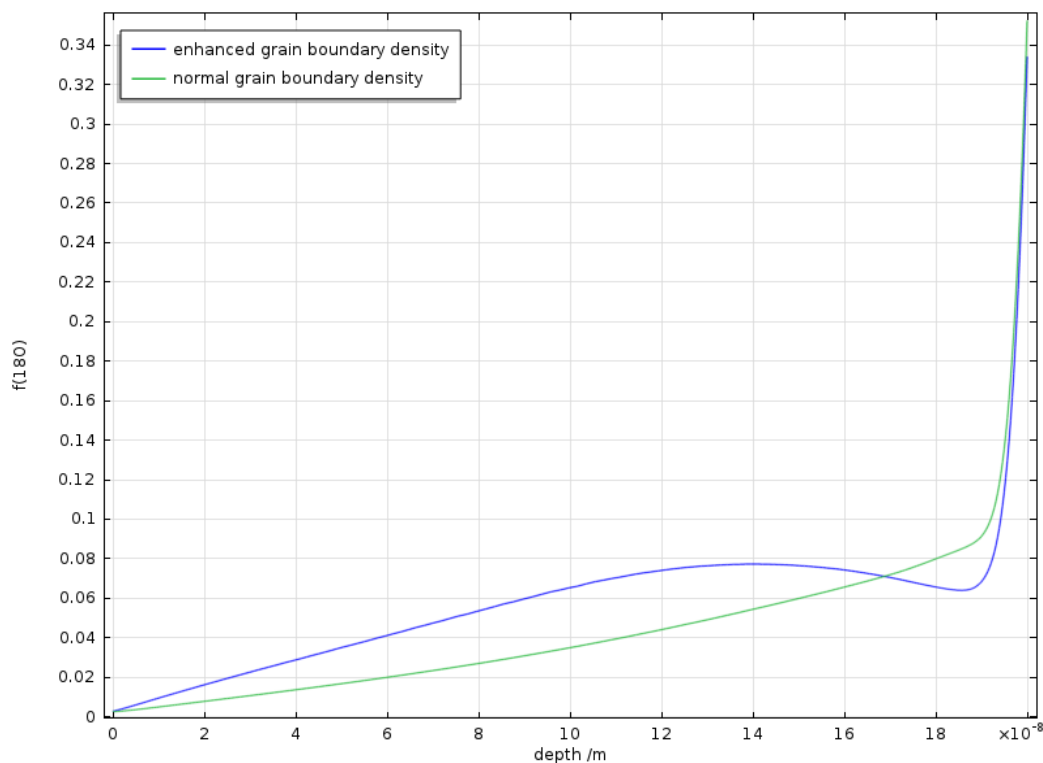
Fig. 5.17 Simulated depth profiles for a columnar LSM grain with one surrounding grain boundary (green line), corresponding to model Fig. 5.16a, and with an enhanced grain boundary distribution density (blue line), corresponding to the model in Fig. 5.16b. (r.h.s. $^{18}O_2$ atmosphere, l.h.s. LSM/YSZ interface)

5.4.7. Tracer Diffusion in a Multi-Layer Deposited Thin Film With Microstructural Changes

In a final experiment a LSM "multi-layer" with 3 layers deposited at T_{dep}=730 °C, T_{dep}=450°C and T_{dep}=730 °C for 3 minutes each was prepared by PLD. Since the grain growth is dependent of the deposition temperature in the PLD, the thin film should exhibit three layers of big, small and big grains. The film was annealed at T_{exch}=793 °C in 200 mbar $^{18}O_2$ for 10 min. The depth profile in Fig. 5.18 shows a tracer decrease in layer (1) similar to that in homogeneously grown columnar samples followed by a

relatively straight profile in the middle of the sample in layer (2) (the low temperature deposited layer) and a bent profile [160] in the last layer (3) up to the LSM/YSZ interface.

The first and the third layer are assumed to have big grains compared to the middle layer, which should exhibit an enhanced grain boundary distribution density. Since the grain boundaries are responsible for the major oxygen transport the middle part becomes less bent due to faster (more) tracer transport. The microstructure change effect is still quite small and not uphill-like, which can be attributed to the insufficient grain boundary distribution density variation, possibly due to grain growth [32] induced at the high deposition temperature of the third layer.
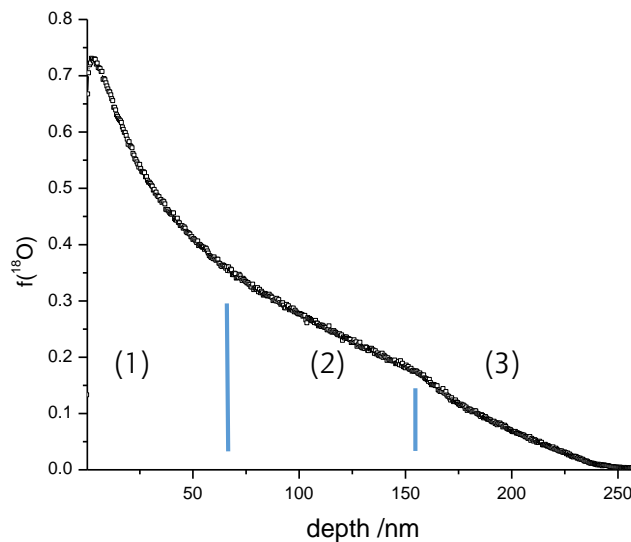

Fig. 5.18 Depth profile of multilayer deposited at 730 °C (1), 450 °C (2) and 730 °C (3). ^{18}O exchange temperature 793 °C for 10 min. Lines indicating changing microstructure.

5.5.   Conclusion

The dependence of oxygen exchange reaction and oxygen ion diffusion upon cathodic bias and microstructural changes was successfully investigated on columnar grown LSM thin films. 200 nm thin LSM microelectrodes on YSZ substrates and two different LSM grain sizes were investigated by means of impedance spectroscopy, DC current voltage measurements and SIMS depth profiling of voltage driven ^{18}O tracer ions. The measured current was enhanced not only by increasing temperature and enhancing cathodic bias, but also by reducing the LSM grain size and thereby increasing the influence of grain boundaries. The diffusion profiles for voltage driven ^{18}O incorporation are partly characterized by very uncommon uphill-like diffusion. This could be explained by assuming a chemical potential and thus a vacancy concentration gradient in LSM grains. Numerical simulations by the finite element method revealed further information on how bias is affecting oxygen transport via grains and grain boundaries. Surface exchange kinetics and diffusion properties are both enhanced by applied cathodic bias.

6. Oxygen Reduction via Grain Boundary Transport in Thin Film Platinum Electrodes on Yttria Stabilized Zirconia

This chapter contains in large part material from a scientific paper published in "Solid State Ionics" [127].

6.1.   Abstract

Model-type sputter deposited platinum microelectrodes with different grain sizes were investigated on single crystalline yttria stabilized zirconia (YSZ) by means of impedance spectroscopy. Measurements on a single platinum microelectrode could be continuously performed for >100 hours and from 250 °C to 800 °C without losing contact. From the temperature dependence, two parallel reaction pathways for oxygen reduction could be identified. Above 450 °C, a surface path with a rate determining step located at the three phase boundary is predominant. Its polarization resistance is independent of the Pt grain size and exhibits an activation energy of 1.83 eV. In the low temperature regime (<450 °C) a bulk path through Pt was verified with an electrode polarization resistance depending on the Pt grain size. The corresponding activation energy is 0.15 eV and the rate limiting step most probably oxygen diffusion along the Pt grain boundaries.

6.2.   Introduction

The system platinum/yttria stabilized zirconia (YSZ) has long tradition in both industrial applications and fundamental research. For example, Pt/YSZ is used in oxygen gas sensors, commonly referred to as lambda probes and mostly applied for exhaust gas analysis in combustion engines [161] and in medical applications [162]. An in-depth understanding of oxygen reduction on Pt/YSZ is crucial for the development of lambda probes with increased performance and higher reliability [10, 163]. Pt on YSZ is also an important model system for electrode kinetic studies in solid oxide fuel cells or solid oxide electrolysis cells (SOFCs or SOECs), with a long history of research. Moreover, in µ-SOFC [164-168] based on thin electrolytes, Pt electrodes are often employed and responsible for a significant part of the total polarization resistance [12].

Pt thin films are frequently applied in studies aiming at a mechanistic understanding of the oxygen reduction reaction [33, 58, 82, 83, 124, 169-173]. Among others, oxygen reduction on Pt thin film micro-electrodes has been shown to proceed via two parallel reaction pathways [58]. In a high temperature regime (>450 °C), a surface path with a rate determining step depending on the three phase boundary (3PB) length was observed. In the lower temperature regime (<450 °C), a bulk path was found and oxygen transport along platinum grain boundaries (GBs) was assumed to be rate limiting. Indications of a transport via GBs can also be found in Refs. [58, 174-176]. An unambiguous proof for its importance in oxygen reduction on Pt/YSZ at low temperatures, however, is still missing.

The goal of this chapter was to verify the nature of the bulk path's rate limiting step – i.e. to clarify the role of oxygen GB diffusion in thin film platinum electrodes. Therefore, electrochemical impedance spectroscopy was performed between 250 and 800 °C on sputter deposited, geometrically well-defined platinum thin film electrodes with different grain sizes.

6.3. Experimental

6.3.1. Sample Preparation

Platinum thin films were prepared by magnetron sputter deposition (MED 020 Coating System, BAL,TEC, Germany) of Pt (99.95% pure, ÖGUSSA, Austria) on polished YSZ (1 0 0) single crystals (9.5 mol% Y_2O_3, CrysTec GmbH, Germany), cf. Ref. [58]. Deposition was performed in argon atmosphere at a pressure of $2 \cdot 10^{-2}$ mbar without additional heating of the substrate. The film thickness of 350 nm was controlled by means of a quartz micro-balance. Micro-structuring of Pt films was performed by lift-off photolithography (ma-N 1420 negative photo resist and ma-D 533S developer for photo resist, both: micro resist technology, Germany) using a quartz photo mask (Rose, Germany) leading to differently sized, circular shaped Pt structures. Size, shape and microstructure of these Pt microelectrodes was investigated by scanning electron microscopy (SEM, FEI Quanta 200 FEG, Netherlands). As counter electrode, Pt paste (Gwent Electronic Materials, UK) was applied onto the back side of the YSZ single crystals. The samples were subsequently annealed in ambient air at 750 °C for 2 h. To obtain electrodes with large grain size, samples were annealed at 800 °C for several

weeks. Thereby Pt grains in the thin films grew from initially sub-µm sizes to several 10 µm as shown in Fig. 6.1. The Ø=100 µm Pt microelectrode shown in Fig. 6.1b, for example, has only 3 large grains. From the absolute number of grains visible at the surface of such microelectrodes, a grain size of several 10 µm was estimated. For not annealed Pt microelectrodes an average grain size of 100-300 nm was estimated from Fig. 6.1a. Thus, the GB distribution density of the small grained Pt microelectrodes is more than 100 times larger than that of electrodes with large grains.
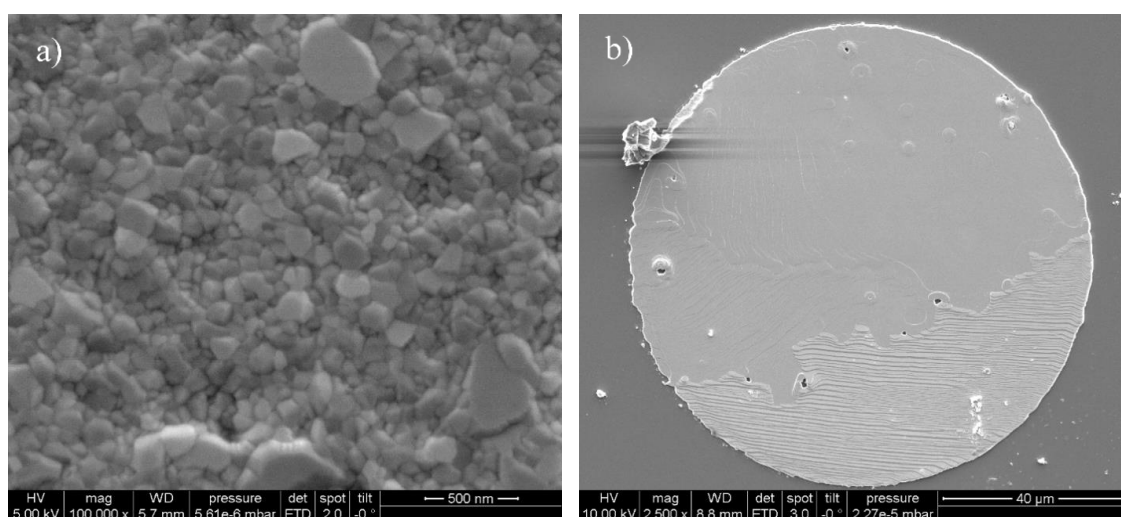

Fig. 6.1: SEM images of platinum microelectrodes a) not annealed with small grains and b) annealed with large grains.

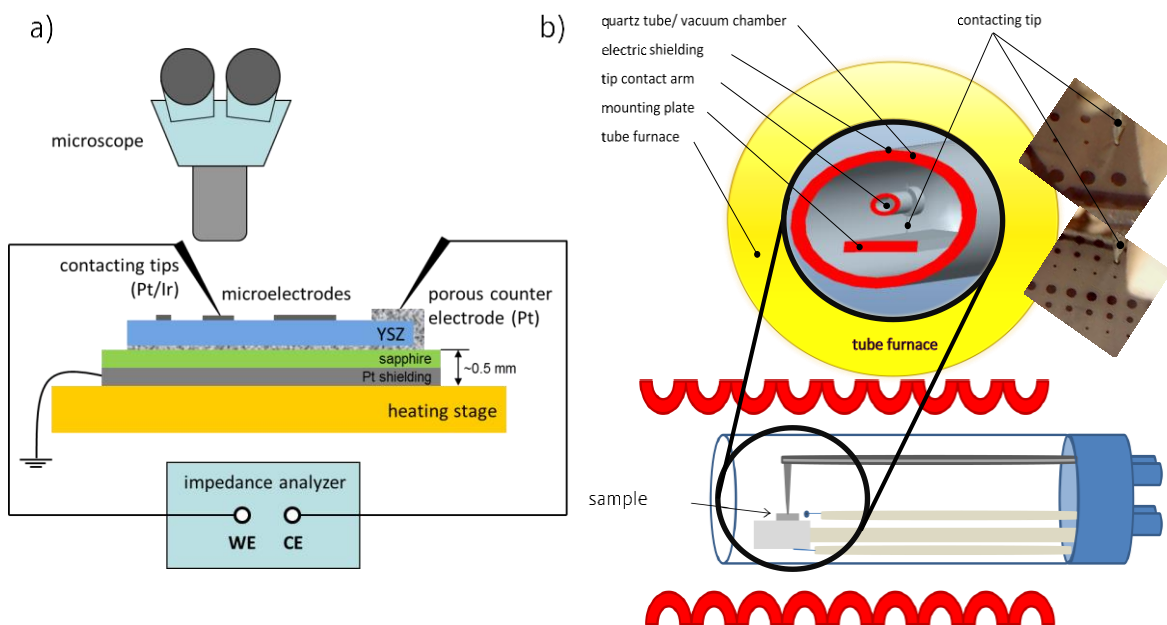## 6.3.2. Measurement Set-ups

Fig. 6.2: a) Conventional asymmetrically heated micro-contact set-up, b) cross-section of the symmetrically heated measurement set-up.

Two different micro-contact set-ups were used for the experiments. The asymmetrically heated measurement set-up (Fig. 6.2a) allows to change the contacted electrode within seconds and thereby to gain statistical information over a large number of different microelectrodes on one and the same sample in a relatively short time. It also enables monitoring of optical changes during the measurement in real time. However, the asymmetrical heating from the bottom side and local cooling (e.g. by convection, radiation, and the contacting tip acting as a heat sink) is known to cause temperature gradients within the sample [83]. Such temperature gradients are responsible for thermo-voltages, which can lead to measurement artefacts in electrochemical

experiments [70]. Avoiding of temperature gradients is therefore highly desired for obtaining reproducible and reliable results.

The second measurement set-up therefore includes a symmetrically heated sample holder, designed to reduce the influence of temperature gradients; it is sketched in Fig. 6.2b. It provides a precisely adjustable and measureable temperature, a homogeneous temperature distribution with minimal temperature gradients in the region of the sample, and it enables long-time measurements on one and the same microelectrode from room temperature up to 1000 °C without losing contact. Since all contacting parts of the symmetrically heated set-up are inside a tube furnace during the measurement, the contacting procedure has to be done prior to the measurement i.e. outside the hot zone. Establishing an electrical contact between tip and microelectrode is performed with a micromanipulator and is monitored by a USB-microscope (Fig. 6.2b, small photographs). Micromanipulator and microscope are removed before the sample with the contacted electrode is transferred into the hot zone of the tube furnace. Detailed information on the two micro-contact set-ups and a discussion on the role of temperature gradients can be found in chapter 3.

6.3.3. Impedance Spectroscopy

Electrochemical characterization of platinum microelectrodes was done by means of two point impedance measurements using an Alpha-A High Resolution Dielectric Analyzer (Novocontrol, Germany). The samples were placed onto the corundum mounting plate located in the middle of the tube furnace of the symmetrically heated set-up (Fig. 6.2b) or onto the heating stage in the asymmetrically heated set-up

(Fig. 6.2a). In both cases, electrochemically etched Pt/Ir tips were used to electrically contact the platinum microelectrodes.

In the symmetrically heated set-up, the porous platinum counter electrode on the back side of the YSZ substrate was contacted via a Pt sheet beneath the sample (Fig. 6.2b). In the asymmetrically heated set-up the counter electrode contact was established on the top side by a second Pt/Ir tip (Fig. 6.2a). Impedance spectra were recorded at temperatures between 250 and 800 °C in the frequency range of 10^6 Hz to 10^{-3} Hz (10^{-2} Hz in the asymmetrically heated set-up) with a resolution of 5 points per frequency decade. Parameterization of the spectra was carried out by the complex nonlinear least square (CNLS) fit software Z-View2 (Scribner, USA) using the equivalent circuit shown in Fig. 6.3d. Therein R_{ysz} represents the spreading resistance of ion conduction in YSZ and the serial R-CPE elements are used to fit the electrode impedance. To account for non-ideal capacitive behavior, constant phase elements (CPE_A and CPE_B) instead of ideal capacitors were employed. It should be noted that by application of this circuit no physical interpretation of the impedance is intended. Rather R_B and CPE_B was simply added to obtain sufficient fit quality and thus being able to extrapolate to low frequencies.
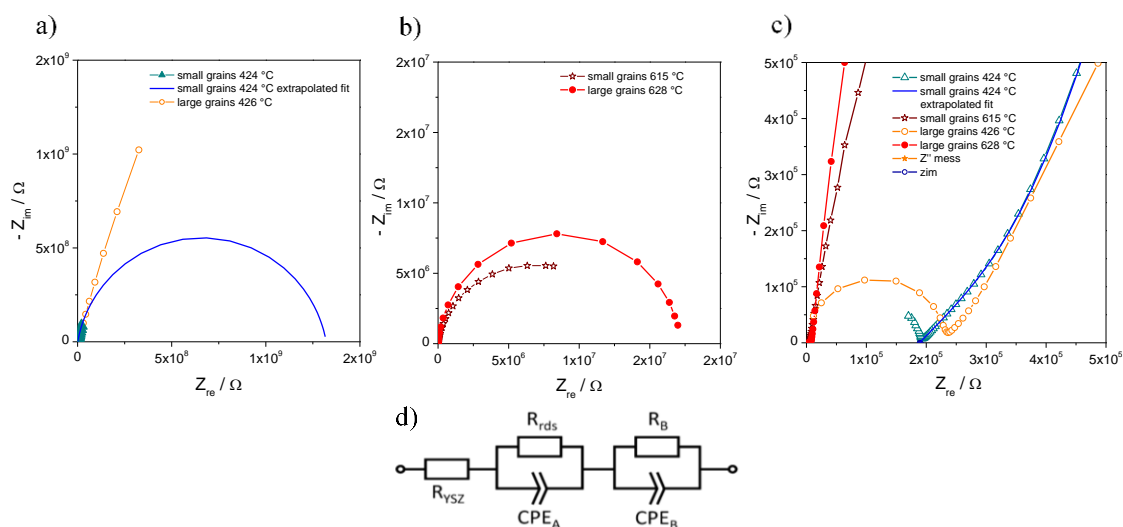
Fig. 6.3: Nyquist plots of two Ø=200 μm platinum microelectrodes with small and large grains, a) measured at 424 °C and 426 °C, and b) measured at 615 °C and 628 °C, respectively. c) Magnification of the high frequency part indicating very similar R_{YSZ} for 424 °C/426 °C. d) Equivalent circuit used for the complex nonlinear least square fits.

6.4.   Results and Discussion

Measurements on annealed electrodes with large grains were performed in the symmetrically heated set-up (Fig. 6.2b). In these experiments, Ø=200 μm microelectrodes were contacted once and measured from 250 °C to 800 °C and back to 250 °C with total measurement times much larger than 100 hours without losing contact. Cross-check experiments on such large grained electrodes were also performed at 320 °C on the asymmetrically heated set-up to exclude systematic errors. Data of measurements on Pt electrodes with small grains, performed in the asymmetrically heated set-up (Fig. 6.2a), were taken from an earlier study [58]. Impedance spectra for electrodes with small and large grains are shown in Fig. 6.3 and both consist of a large

semicircle in the low frequency range, a small shoulder in the medium frequency range (Fig. 6.3c) and a high frequency intercept. For low temperatures, the high frequency intercept, which reflects the spreading resistance of ion conduction in the YSZ [83, 177], develops into a more or less complete arc. Its capacitance and thus also its relaxation time is determined by stray capacitance of the set-up which exceeds the true bulk capacitance of the microelectrode.

In accordance with Ref. [58] we assume that also in case of the low temperature measurements a reliable fit can be achieved despite only a small part of the electrode arc being visible within the frequency range under investigation. The reason is the well-behaved nature of the interfacial capacitance of the system [58]. Fit results show a difference of about three orders of magnitude between R_{rds} and R_B for all measurement temperatures. The total electrode polarization resistance R_{tot} ($R_{tot}=R_{rds}+R_B \approx R_{rds}$) is plotted in the Arrhenius diagram in Fig. 6.4, with filled circles and open squares representing the results on electrodes with small and large grains, respectively. Each point of the small grained Pt electrodes represents an averaged resistance value obtained on three to five $\varnothing$=200 μm microelectrodes measured three times each.

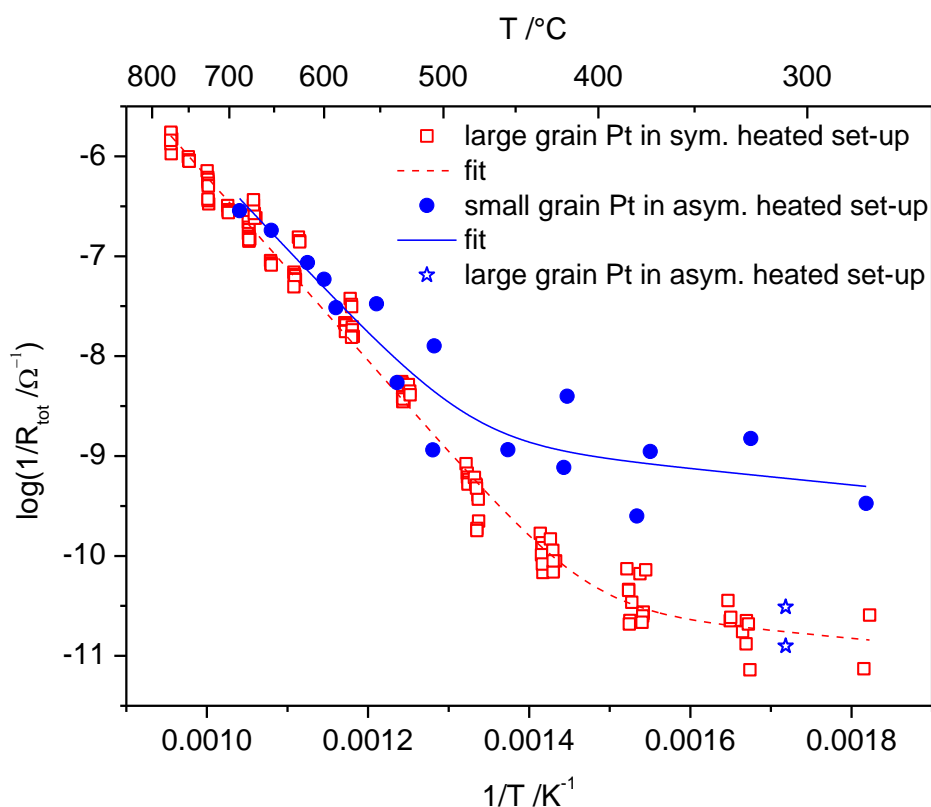**Fig.** 6.4: Arrhenius plot of the inverse electrode polarization resistance measured by impedance spectroscopy on Ø=200 µm platinum microelectrodes. It shows electrodes with grain sizes of several 10 µm measured in the symmetrically heated (open squares) and in the asymmetrically heated set-up (stars) as well as electrodes with grain sizes of 100-300 nm (filled circles) measured in the symmetrically heated set-up.

In this Arrhenius plot both types of Pt microelectrodes—with small and large grains—show a qualitatively comparable behavior: a steeper slope (i.e. higher activation energy) at higher temperatures and a much smaller slope at lower temperatures. Moreover, in the high temperature regime also the absolute polarization resistances of both electrode types are similar whereas at low temperatures the total polarization resistances differ by almost two orders of magnitude. Cross-check experiments of large grained electrodes in the asymmetrically heated set-up showed that this is not an effect

of the measurement set-up (see stars at 300 °C in Fig. 6.4). To quantitatively analyze both data sets in the Arrhenius plot, a fitting was done by using two parallel admittances Y_1 and Y_2 with $Y=1/R_{tot}$. Please note that these two elements (Y_1 and Y_2) do not reflect the two resistors R_{rds} and R_2 from the equivalent circuit but indicate two parallel reaction paths. A detailed argumentation that only two parallel paths can lead to such an Arrhenius plot is given in Ref. [58]. Assuming an exponential temperature dependence of both admittances the resulting fit function reads

$$\log(Y) = \log\left(\frac{1}{R_{tot}}\right) = \log\left(Y_1^0 \cdot e^{\frac{-Ea_1}{k_B T}} + Y_2^0 \cdot e^{\frac{-Ea_2}{k_B T}}\right). \qquad 6.1$$

Therein, the pre-exponential factors Y_1^0 and Y_2^0 as well as the activation energies Ea_1 and Ea_2 are fitting parameters; k_B and T denote Boltzmann's constant and temperature, respectively. The fit is given in Fig. 6.4 and the results obtained for the fit parameters are summarized in Tab. 6.1. Please note the much smaller error of the measurement in the homogeneously heated set-up, which is caused by higher measurement stability.

From the fit curves in Fig. 6.4 and the results in Tab. 6.1 it becomes obvious that the slopes (i.e. the activation energies) for both types of electrodes are almost identical at high temperature. In this temperature region also the pre-exponential factors are in good agreement. At lower temperatures, the slopes and thus the activation energies of electrodes with small and large grains are again virtually identical. The pre-exponential factors, however, differ by almost two orders of magnitude.

	$\varnothing$=200 µm Pt electrodes, small grains, measured in asym. heated set-up	$\varnothing$=200 µm Pt electrodes, big grains, measured in sym. heated set-up
$Ea_{1(high\ temp)}$	1.71±0.02 eV	1.825±0.003 eV
$Ea_{2\ (low\ temp)}$	0.16±0.02 eV	0.150±0.005 eV
Y^0_1	367.5±102.2 Ω^{-1}	983.5±36.9 Ω^{-1}
Y^0_2	$1.5\cdot10^{-8}\pm0.5\cdot10^{-8}$ Ω^{-1}	$3.5\cdot10^{-10}\pm0.3\cdot10^{-10}$ Ω^{-1}

Tab. 6.1: Activation energies and pre-exponential factors from measurement data and fit lines displayed in Fig. 6.4.

In analogy to Ref. [58] the changing activation energy between low and high temperature regime can be interpreted in terms of a change of the reaction path and the rate determining step. It was also shown in Ref. [58] that the polarization resistance at high temperatures scales with the 3PB length, while at low temperatures it scales with the electrode surface area. In accordance with this interpretation, both types of electrodes exhibit a similar polarization resistance in the high temperature regime due to a very similar 3PB length. Surprisingly, the electrodes revealed a strongly different response in the low temperature regime despite having the same surface area. However, their grain boundary distribution density differs by about a factor of more than 100 indicating a crucial role of GBs in the bulk path (see section 2.1 and Fig. 6.1). Moreover, in one of our prior studies [33], diffusion limited kinetics was found in current voltage measurements between 280 and 400 °C on small grained platinum microelectrodes. The combination of all these observations suggests oxygen diffusion along platinum GBs as the rate determining step of oxygen reduction below 450 °C. GB length and 3PB length are of similar length for large grained microelectrodes, and thus we can draw a further conclusion: oxygen reduction via 3PBs (active particularly at high temperatures) and oxygen reduction via GBs (dominating at low temperatures) exhibit very different kinetics. It also means that, except from the transport limitation, oxygen

reduction via GBs is rather fast since all other serial electrochemical steps of the reduction kinetics have polarization resistances which are too low to be seen in this study. Besides this, it is worth to note that the exchange current via the surface path (i.e. the polarization resistance at higher temperature) is independent of the Pt GB distribution density. Thus, a pronounced effect of GB/3PB intersections on the oxygen reduction kinetics can be excluded.

6.5.   Conclusion

Oxygen reduction pathways of sputter deposited platinum microelectrodes with strongly different grain sizes were investigated by means of impedance spectroscopy. Some microelectrodes were analyzed in a symmetrically heated micro-contact set-up to avoid any temperature gradients within the measured sample. Long-time measurements between 250 and 800 °C could thus be performed on single microelectrodes. Two very different activation energies (1.83 eV and 0.15 eV) are found at high and low temperatures, irrespective of the grain size. At low temperatures, a bulk path with oxygen transport through Pt is active and its exchange current scales with the grain boundary distribution density of the investigated microelectrodes. This strongly suggests diffusion along grain boundaries as rate limiting step. In contrast, the polarization resistance at high temperatures reflects a surface path and is not affected by the grain boundary distribution density.

7. Construction of New Measurement Set-ups

During the research work for this thesis many inconveniences of existing tools, measurement setups and experimental stations became obvious. For improvement and enhancing the possibilities for gaining reliable results some new measurement set-ups were built and some novel measurement stations developed. The idea behind all these developments was to design systems that are as simple as possible to use and to maintain. In this chapter several details of the constructions are given.

7.1.　 MiMa

Functionality and measurement results obtained with the symmetrically heated micro-contact set-up MiMa are described in chapter 3. Several slightly different designs of this measurement set-up were realized with corundum and with quartz inner parts. All construction parts, including screws outside the hot zone are made of stainless steel. All current carrying wires inside the chamber are made of platinum. Some measurement stages are equipped with a lambda probe (MicroPoas Setnag, France) and thermo-couple type S. Other stages are equipped with a thermo-couple type K. Different quartz tubes, all with a KF 50 vacuum flange with different diameter for different experiments were used. Figs. 7.1 to 7.6 give photos, sketches and construction details.
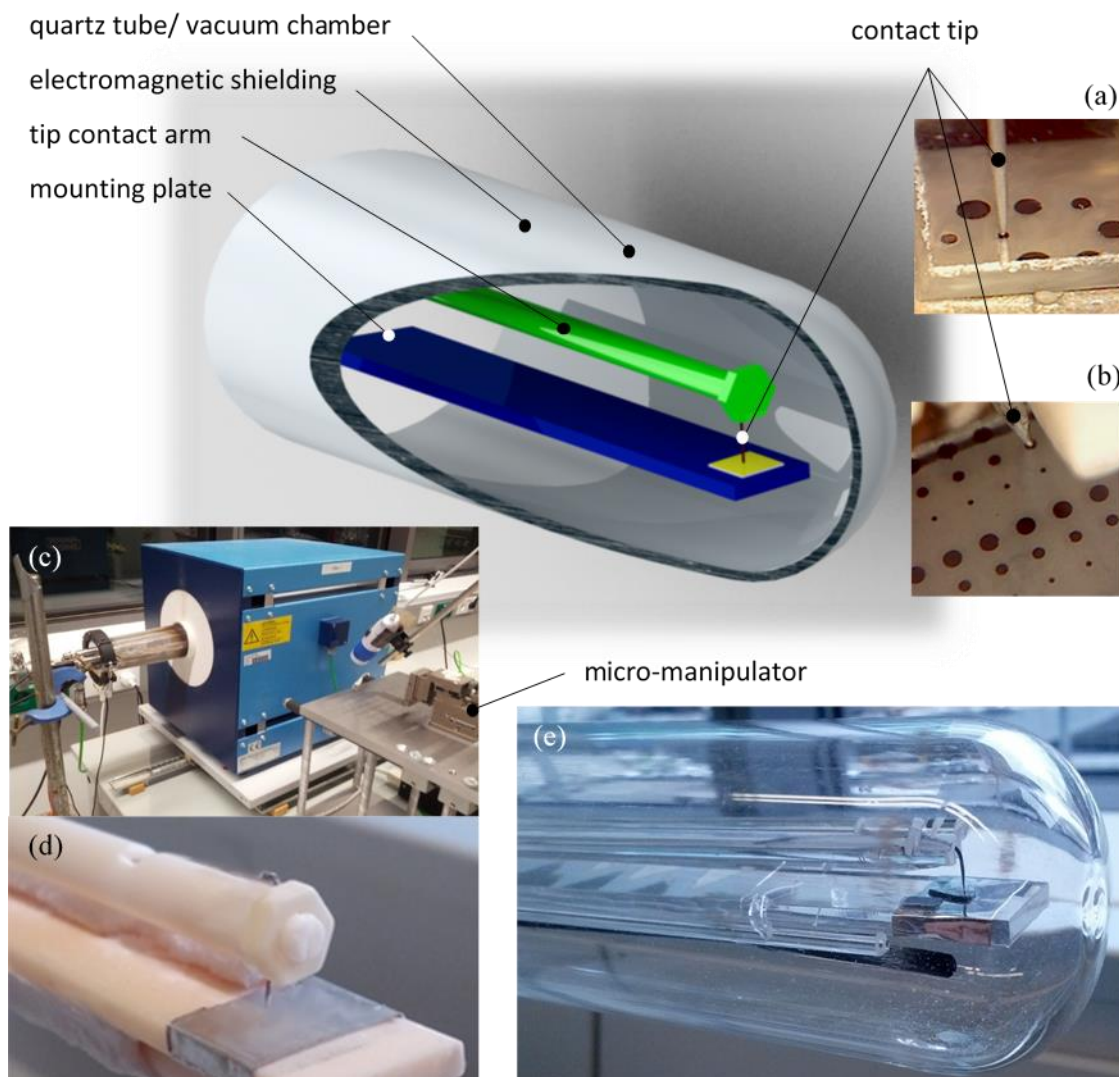
Fig. 7.1 MiMa with tube furnace mounted on rails. 3D sketch of the tip contact arm, mounting plate and quartz tube of the symmetrically heated micro-contact set-up MiMa. Small pictures (a) & (b) show contacted microelectrodes before the tube furnace is moved over the sample. (c) Whole measurement set-up with contacting device. (d) Tip contact arm with Pt/Ir contacting tip on mounting plate with platinum foil (without sample). (e) MiMa fabricated from quartz in the quartz tube with contacted sample.
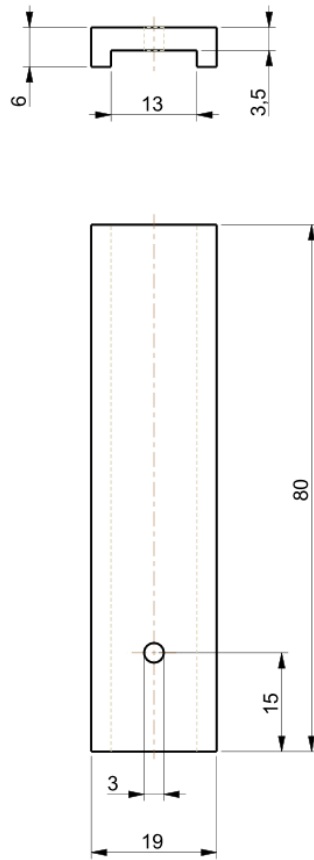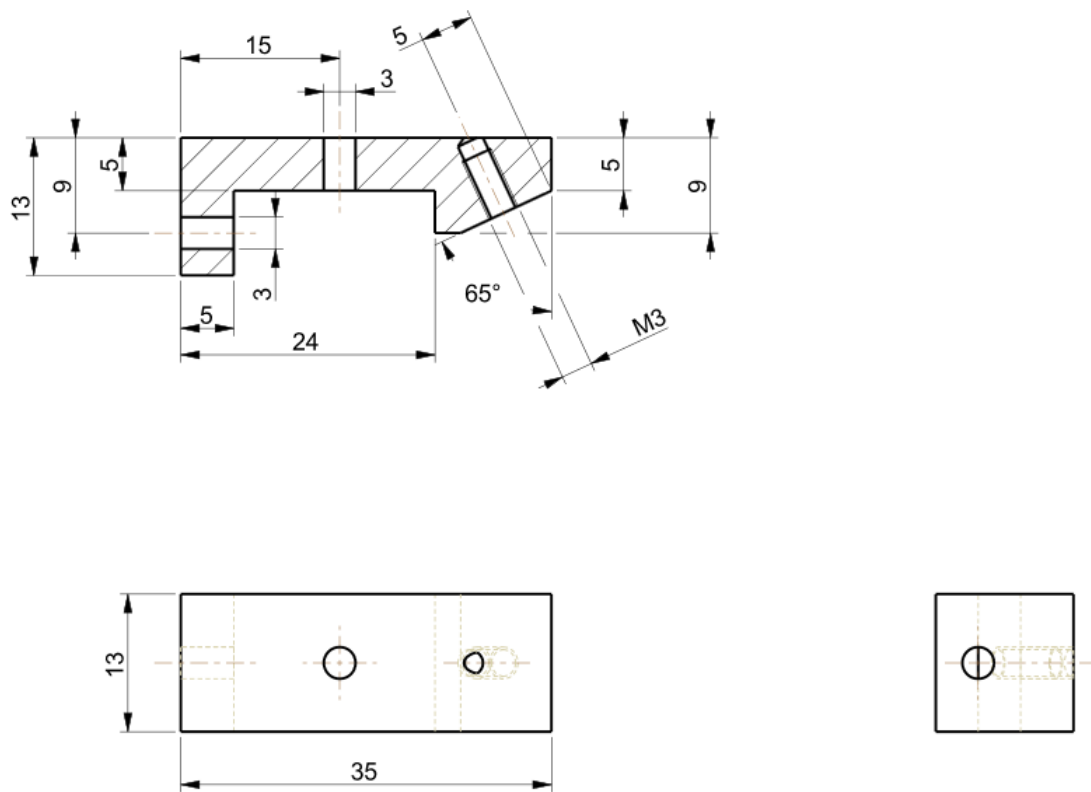
Fig. 7.2 Stainless steel mounting plate holder.

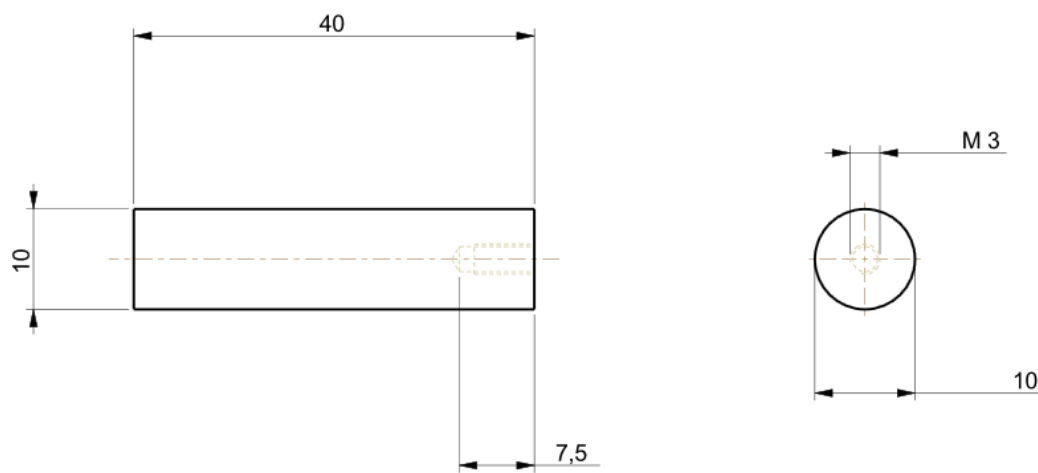Fig. 7.3 Stainless steel main part.

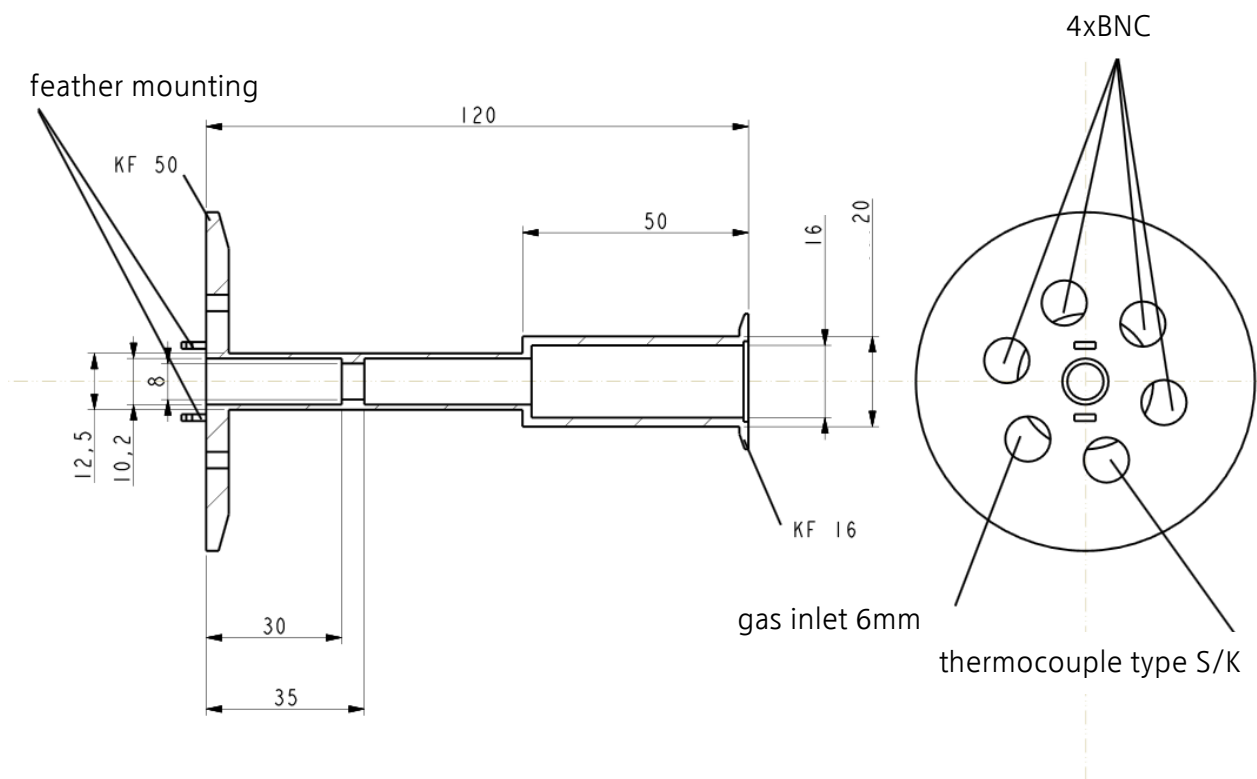Fig. 7.4 Stainless steel flange connector.

Fig. 7.5 Stainless steel vacuum flange with thermocouple type S compensation feed through.
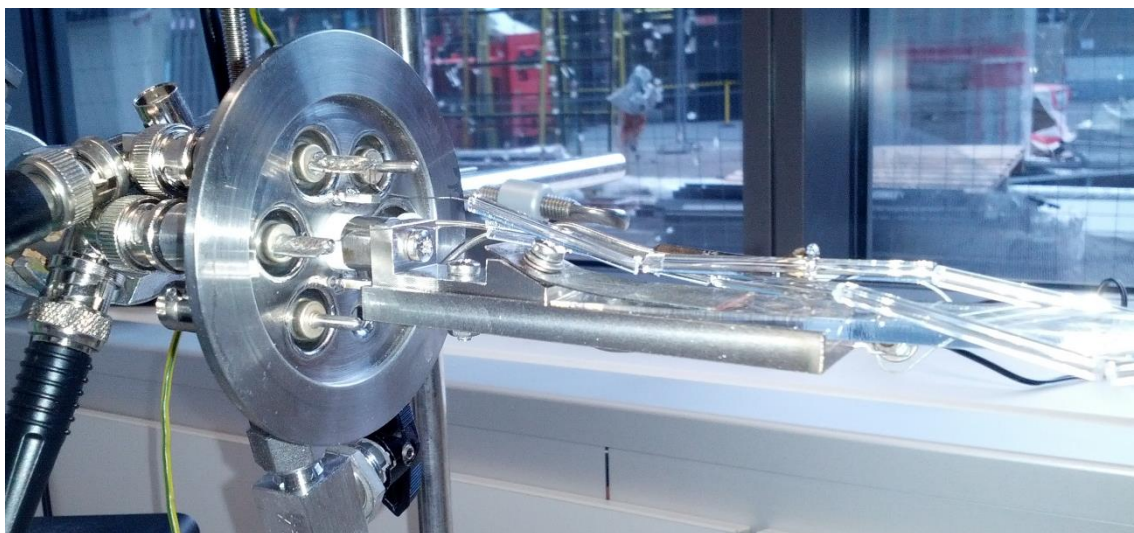

Fig. 7.6 Picture of mounted flange with inner parts of MiMa.

In addition to the parts shown from Fig. 7.1 to 7.4 only a fiew items are needed to build this set-up: a stainless steel leaf spring, a stainless steel screws, Pt wires, crimp contacts for platinum wire mounting, platinum foil, thermocouple, and a Pt/Ir tip for establishing contact to a microelectrode.

7.2 Conventional Sample Holder for Macroscopic Samples

The sample holder is shown in Fig. 7.7 to 7.9 is used in standard electrochemical measurements often performed in the field of solid state ionics. It has the same flange (Fig. 7.5) as MiMa with all inner parts made of quartz.
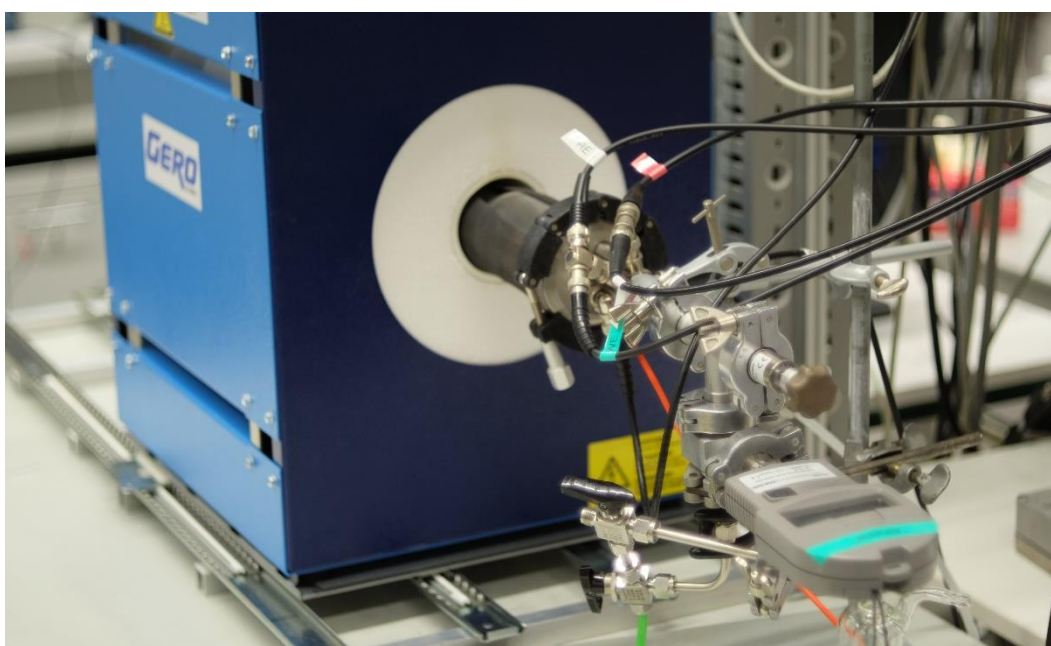

Fig. 7.7 Picture of macroscopic measurement stage
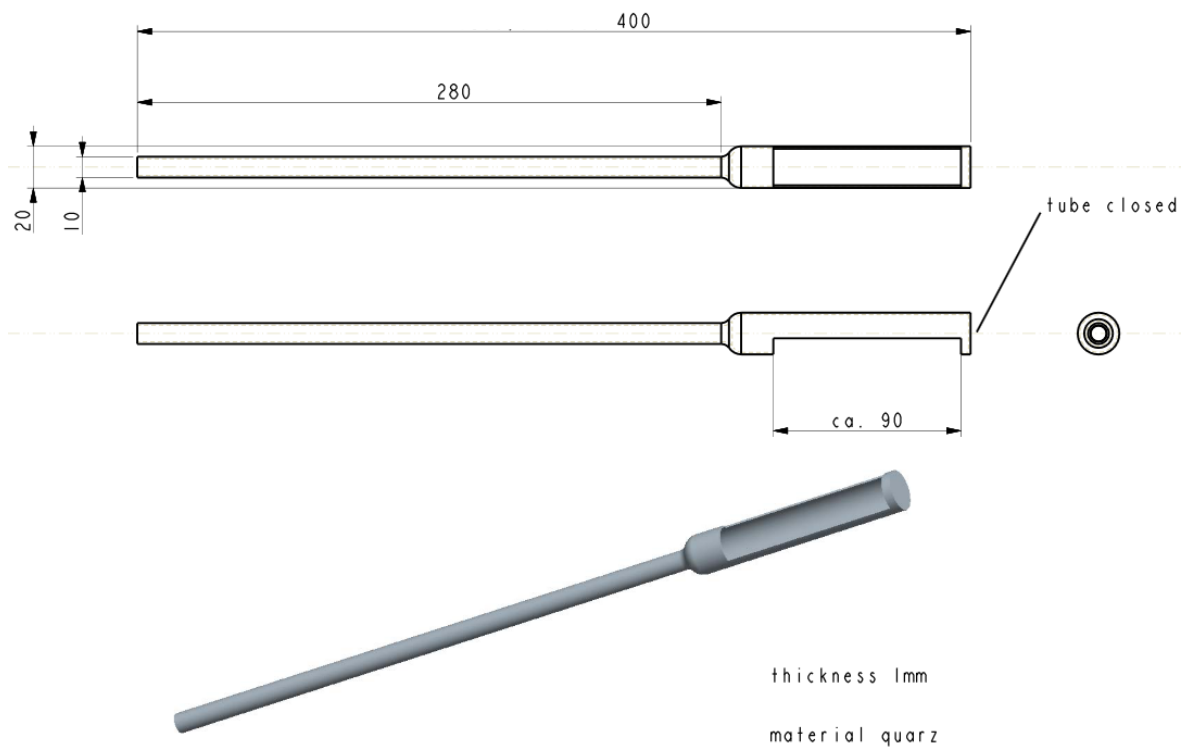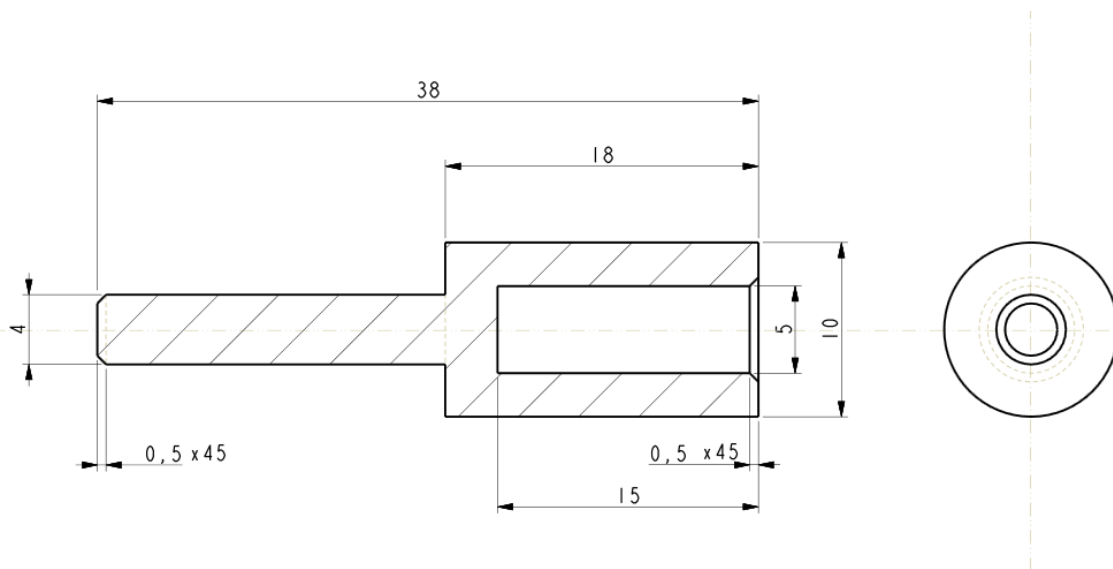
Fig. 7.8 Quartz inner part

Fig. 7.9 Teflon connector for mechanical feed through and quartz rod.

In addition to the shown parts the sample holder includes a mechanical feed through to establish electrical contact to the sample, a ∅=5 mm quartz rod, Pt wires, crimp contacts for platinum wire mounting, platinum foil and thermocouple.

7.3 Van-der-Pauw Measurement Equipment

A symmetrically heated Van-der-Pauw measurement equipment was built with a flange shown in Fig. 7.5 and a quartz inner part show in Fig. 7.8. The measurement set-up is similar to the set-up in section 7.2 without mechanical feedthrough and additional quartz parts with Pt/Ir contact tips. Details are given in Fig. 7.10 and 7.11.
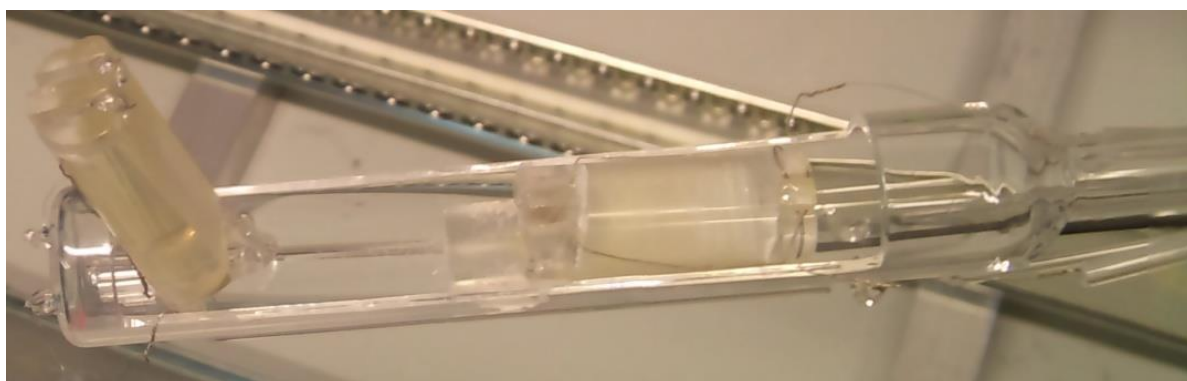
Fig. 7.10 Inner parts of Van-der Pauw set-up.
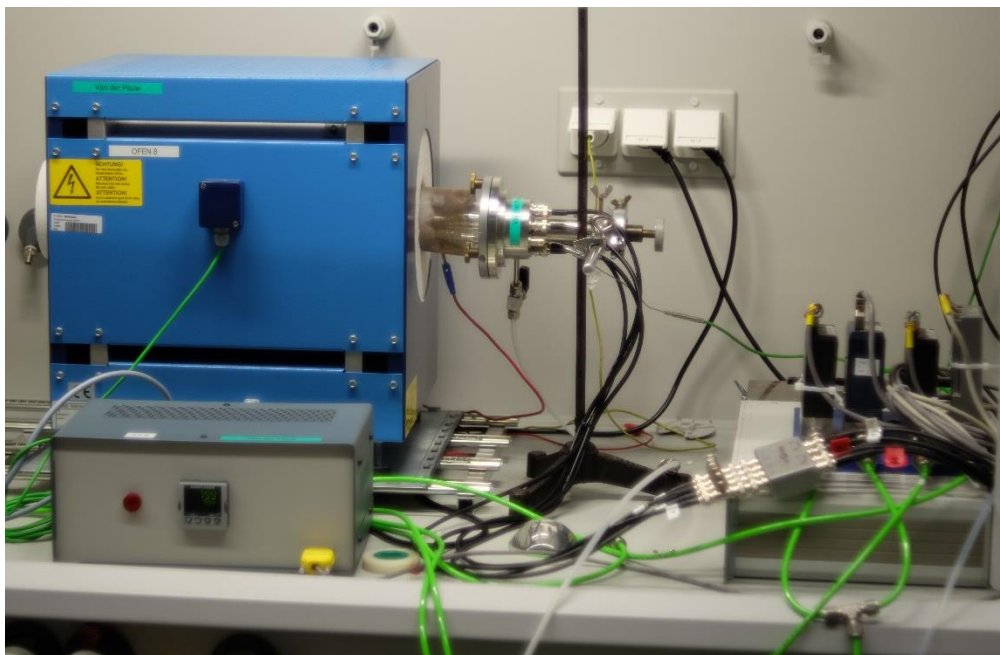
Fig. 7.11 Picture of Van-der Pauw set-up.

7.4 ^{18}O Exchange Chamber With Included Cooling Stage

A tracer gas exchange stage was designed to enable an equilibration of the sample in $^{16}O_2$ gas atmosphere at chosen partial pressure and temperature values before the tracer exchange takes place. After the sample is equilibrated it is transferred into a cooled area. More details about the measurement procedure can be found in Ref. [178]. Construction details and photos are shown in Figs 7.12 to 7.16.
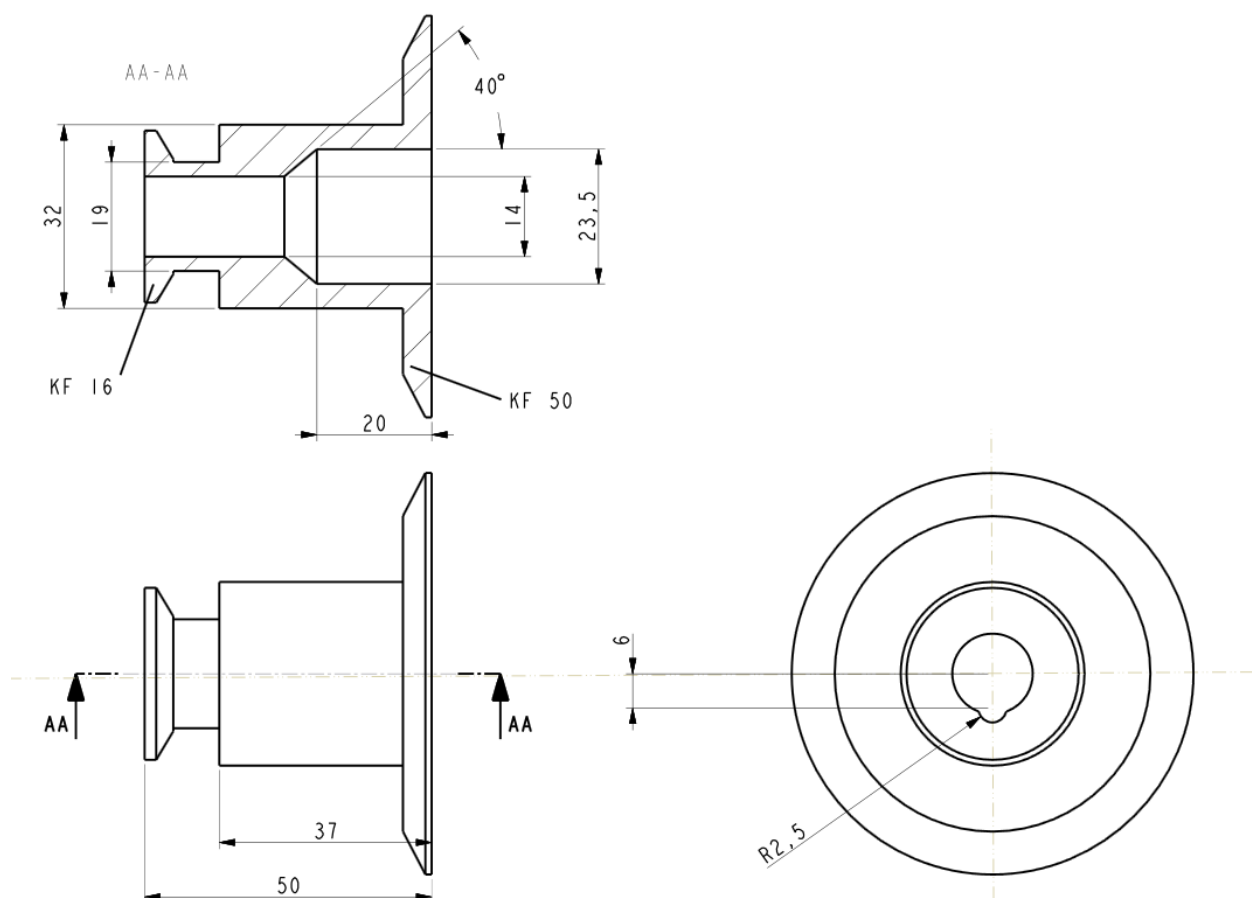
Fig. 7.12 Inner part of the cooling stage from ^{18}O exchange chamber; material: brass.
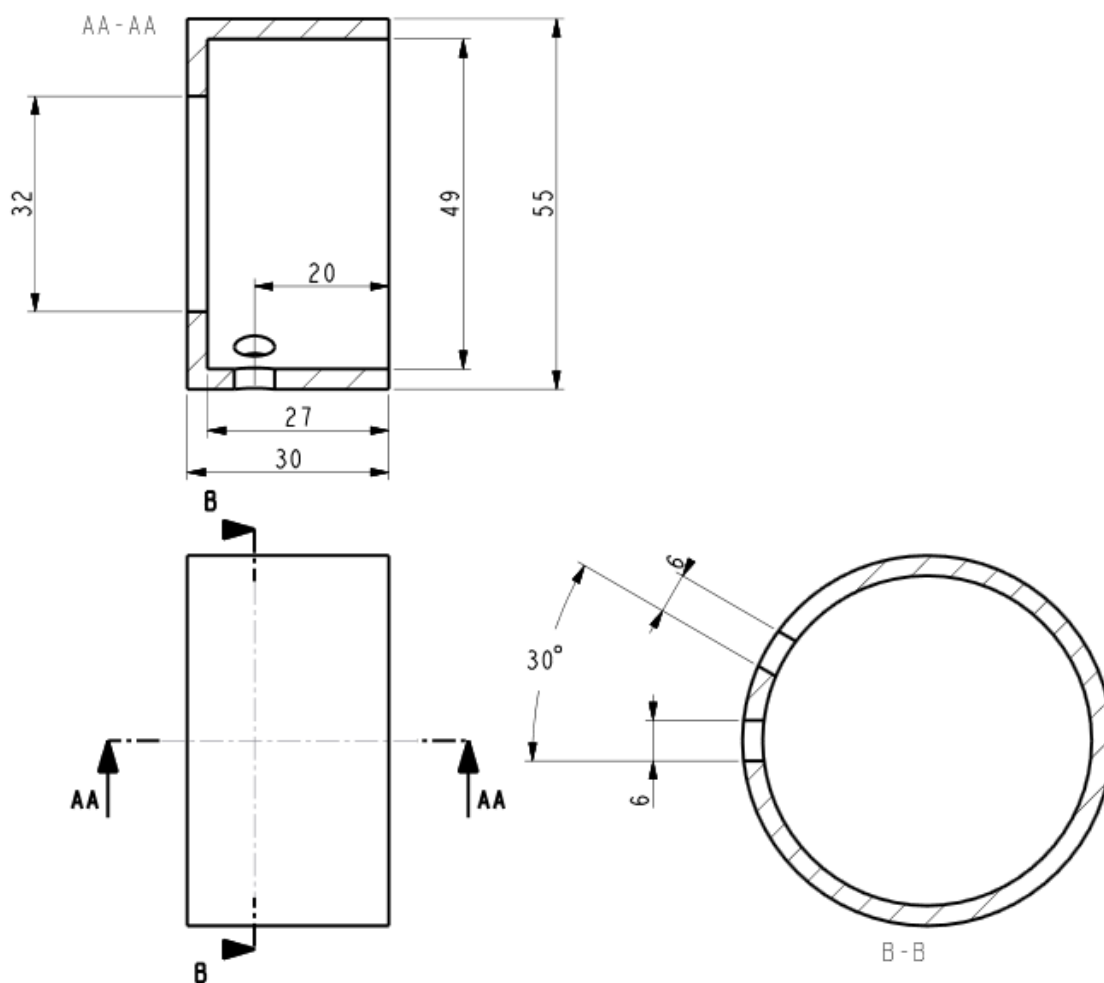
Fig. 7.13 Outer part of the cooling stage of ^{18}O exchange chamber with holes for water supply; material: brass.
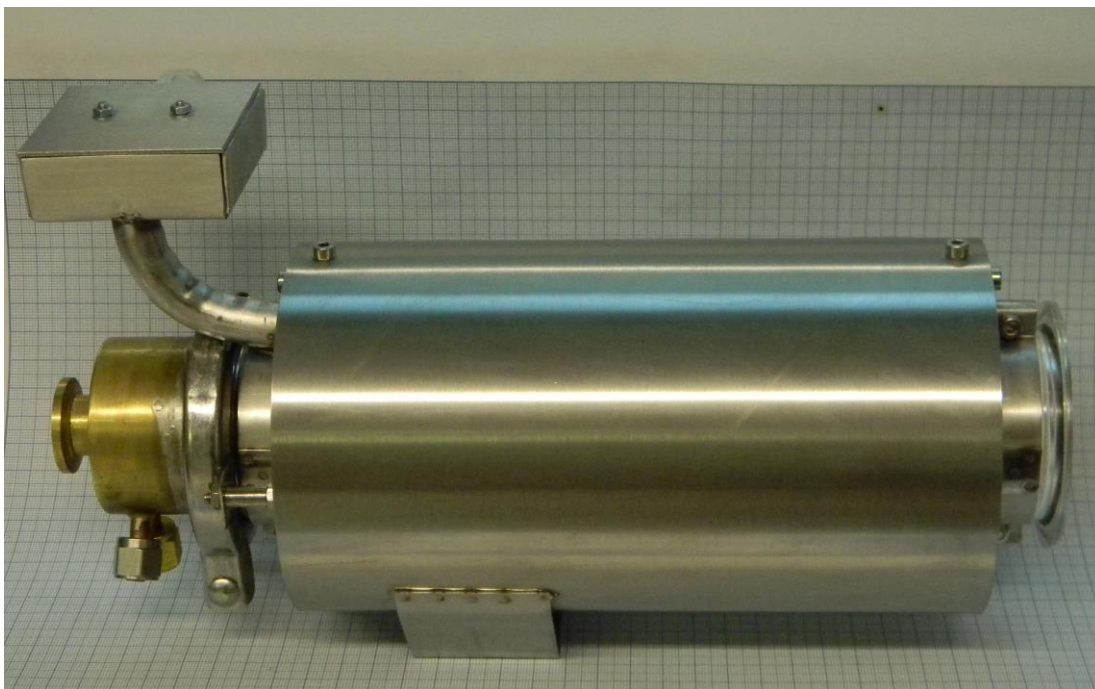
Fig. 7.14 Picture of ^{18}O exchange chamber.
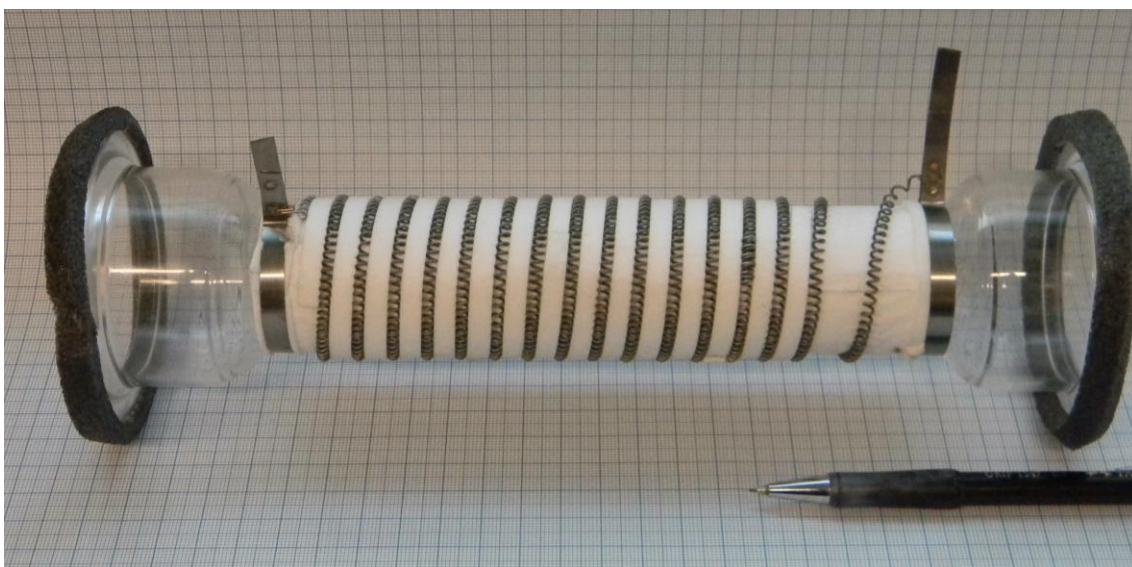
Fig. 7.15 Filament mounted on quartz tube without heat insulation, heat shield and case.
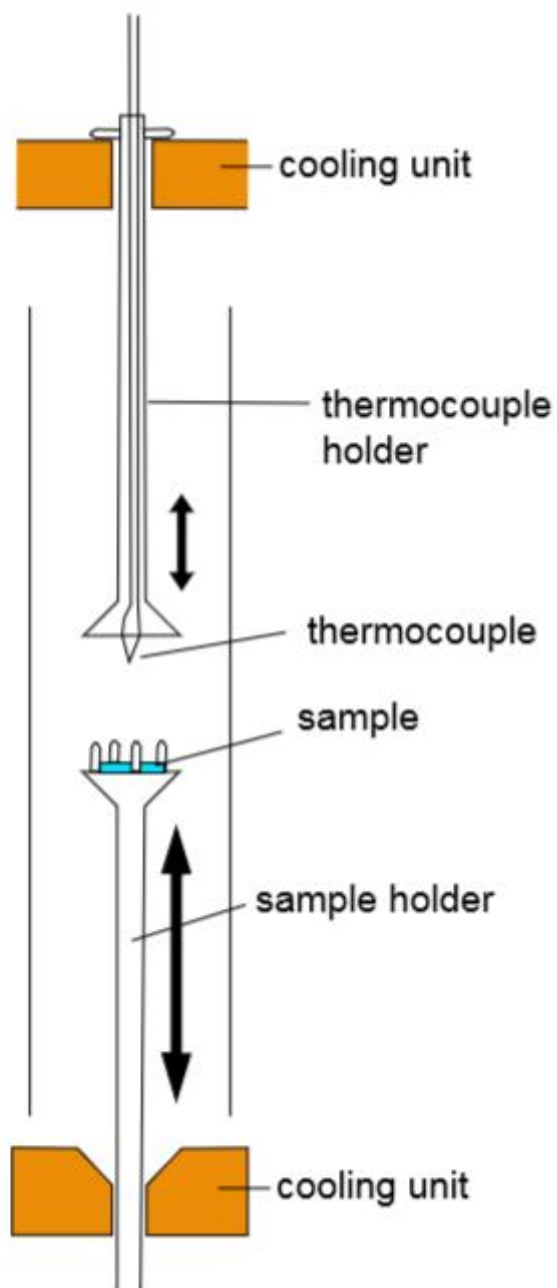
Fig. 7.16 Sketch of inner parts and function of ^{18}O exchange chamber [178].

204

7.5 Conventional Micro-Contact Vacuum Equipment

Similar to the first computer controlled asymmetrically heated micro-contact station named "I-Pot" (**I**mpedance-"vacuum chamber") a second set-up named "II-Pot" (second I-Pot) was built. Construction details can be found in Ref. [179]. All measurements in this thesis performed in an asymmetrically heated micro-contact equipment used in this set-up. Fig. 7.17 displays photos of the set-up.
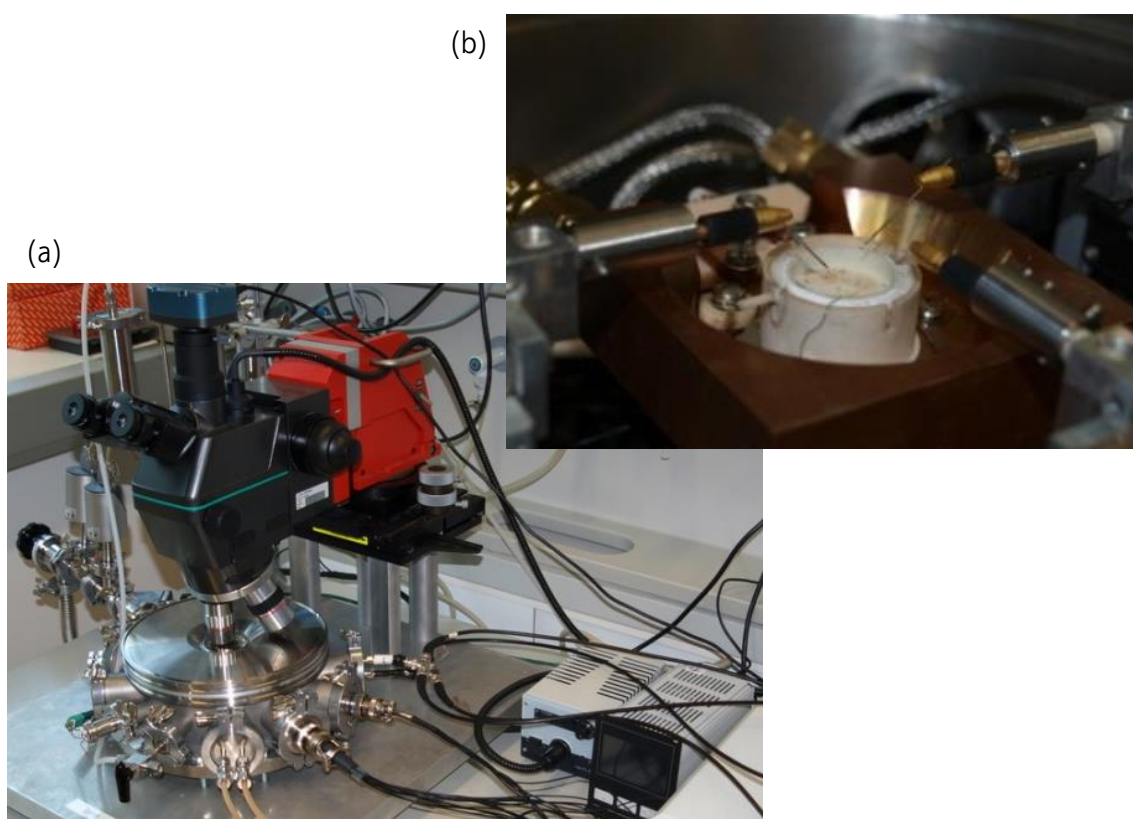
Fig. 7.17 (a) Picture of conventional micro-contact set-up II-Pot. (b) Picture of furnace mounted on metal chiller with contact tip clamps.

8. Summary

Dense lanthanum strontium manganite $(La_{0.8}Sr_{0.2})MnO_3$ and $(La_{0.8}Sr_{0.2})_{0.95}MnO_3$ (LSM) thin films with different microstructures were successfully prepared by pulsed laser deposition (PLD) on single crystals. LSM thin films deposited on yttria stabilized zirconia (YSZ) showed a columnar polycrystalline microstructure with column diameters depending on the deposition temperature. LSM thin films deposited on strontium titanate (STO) showed an epitaxial structure with tensile strain caused by the lattice mismatch of STO and LSM. Electrical measurements were combined with tracer exchange experiments to reveal details of the oxygen reduction mechanism on these LSM thin films. In particular thin films on YSZ were microstructured and characterized by impedance spectroscopy and DC-measurements. Electrode geometries included differently shaped microelectrodes (50-400 µm in diameter) and symmetrically fabricated macroscopic electrodes (5·5 mm^2). Additional finite element calculations and simulations were performed to support theinterpretation of the electrochemical experiments and to fit experimental results.

State of the art microelectrode impedance measurements were further improved by a novel symmetrically heated micro-contact set-up. This novel design allows measurements of a single microelectrode from room temperature up to 1000 °C in changeable gas atmospheres with a pressure range from $1·10^{-2}$ to 2 bar. Measurement inconveniences present in conventional asymmetrically heated set-ups could be reduced and artifacts caused by thermo-voltages could be completely eliminated.

Single microelectrodes were reproducibly measured over weeks from 300 to 950 °C without irreversible degradation effects.

This novel set-up facilitated unambiguous identification of two independent reaction pathways of oxygen reduction on LSM thin film microelectrodes. A surface path for oxygen reduction was found in a low temperature regime, where the polarization resistance scales with the 3PB length, and its resistance has an activation energy of ca. 1.4 eV. At high temperatures, a parallel bulk path with a much higher activation energy of the corresponding resistance namely of the order of 3 eV becomes predominant. The film microstructure - in particular the grain size - affects the LSM bulk path and indicates an important role of grain boundaries in oxygen reduction on LSM. Accordingly, a variation of grain sizes by different deposition temperatures or high temperature annealing causes resistance changes of the LSM bulk path.

When applying an oxygen blocking Pt capping layer on top of a LSM microelectrode, only a small rim at the edge of the electrode remains active. There the relative importance of surface resistance and transport resistance are very different compared to the main part of the LSM electrode. This can change the rate limiting process and shows a reduced activation energy. Possibly the surface reaction dominates the bulk path "across the edges".

To understand the contribution of grain boundaries to the oxygen reduction and diffusion kinetics of the LSM bulk path, polycrystalline LSM thin films with columnar grains of different sizes as well as epitaxial thin films were investigated by means of ^{18}O tracer exchange experiments. The isotope concentration depth profiles of

207

polycrystalline films, obtained by secondary ion mass spectrometry (SIMS) clearly indicated contributions from diffusion and surface exchange in grains and in grain boundaries. Variation of the A-site stoichiometry did not lead to large changes of the kinetic parameters. Numerical modelling using a 3D finite element model revealed two different diffusion coefficients and two different surface exchange coefficients for grains and grain boundaries. The grain boundary diffusion and surface exchange values were approximately two to three orders of magnitude larger than those of the grains. Kinetic parameters of epitaxial layers resemble those of grains in polycrystalline layers.

These results on different oxygen exchange and transport properties of grains and grain boundary inspired further tracer exchange experiments and electrical measurements upon cathodic bias. Therefore thin films were additionally microstructured to obtain microelectrodes. These microelectrodes were then polarized in $^{18}O_2$ atmosphere in the novel micro-contact set-up. The resulting isotope concentration depth profiles clearly revealed a voltage induced change of surface exchange kinetics and a depth dependent change of diffusion properties, both in grains and grain boundaries. Cathodically polarized microelectrodes showed a tremendous increase of ^{18}O concentration in the LSM films with an apparent uphill diffusion. The two parallel and interacting diffusion pathways via grains and grain boundaries were successfully simulated by a 3D finite element model.

For the sake of comparison, also platinum thin film magnetron sputtered microelectrodes on YSZ with two strongly different grain sizes were analyzed by impedance spectroscopy. By using the novel micro-contact set-up, measurements on a single platinum microelectrode could be continuously performed for >100 hours and

from 250 °C to 800 °C without losing contact. From the temperature dependence, again two parallel reaction pathways for oxygen reduction could be identified. Above 450 °C, a surface path with a rate determining step located at the three phase boundary is predominant. In the low temperature regime (<450 °C) a bulk path through Pt was verified with an electrode polarization resistance depending on the Pt grain size. Both pathways showed very different activation energies (1.83 eV and 0.15 eV) at high and low temperatures, irrespective of the grain size. The grain size dependent results strongly suggest oxygen diffusion along grain boundaries as rate limiting step in the low temperature regime.

9. List of Symbols

A	area
AC	alternating current
AFM	atomic force microscopy
Asym. h.	asymmetrically heated micro-contact set-up
BA	burst alignment (a ToF-SIMS mode)
C	capacitance
C_p	heat capacity
C_{Chem}	chemical capacitance
C_{DL}	double layer capacitance
C_{Pt}	platinum interface capacitance
C_{DL+Pt}	double layer with platinum interface capacitance
CBA	collimated burst alignment (a ToF-SIMS mode)
CNLS	complex nonlinear least square
CPE	constant phase elements
d	distance/ grain diameter
d_{ME}	diameter of microelectrode
D	diffusion coefficient
D_{gb}	grain boundary diffusion coefficient
D_b	bulk diffusion coefficient (epitaxial layer and grain)
DC	direct current
DHM	digital holographic microscopy
E_a	activation energy
EDX	energy dispersive X-ray spectroscopy
EIS	electrochemical impedance spectroscopy

f	frequency
$f(^{18}O)$	tracer fraction
FEM	finite element method
FWF	Austrian Science Fund
GB	grain boundary
h	heat transfer coefficient
HT	high temperature
IEA	International Energy Agency
IEDP	isotope exchange depth profiling
IPCC	Intergovernmental Panel on Climate Change
I-Pot	impedance-"vacuum chamber" [pronounces I pot]
II-Pot	second I-Pot [pronounces zwae pot]
III-Pot	Tripod (classical Frittogram)
ISO	International Organization for Standardization
k	oxygen exchange coefficient
k_T	thermal conductivity
k_B	Boltzmann's constant
$\mathbf{k}_{gb}$	grain boundary surface exchange coefficient
k_b	grain surface exchange coefficient (epitaxial layer and grain)
LSC	lanthanum strontium cobaltite
LSM	lanthanum strontium manganite
LSM95	non-stoichiometric LSM
LSM100	stoichiometric LSM
LT	low temperature
L_{3PB}	three phase boundary length
MIEC	mixed ionic electronic conduction
MIMA	micro-contact set-up in furnace for macroscopic samples

n	normal vector
NIST	National Institute of Standards and Technology (USA)
ORR	oxygen reduction reaction
p_{CPE}	fitting parameter of a CPE element (exponent)
PDF	powder diffraction file
PLD	pulsed laser deposition
q	charge
Q_{CPE}	fitting parameter of a CPE element
Q	heat source or sink
r_{tip}	current collecting tip radius
R	resistance
R_0	YSZ spreading resistance
R_{tot}	total polarization resistance
RSM	reciprocal space mapping
SEM	scanning electron microscopy
STM	scanning tunneling microscopy
SIMS	secondary ion mass spectrometry
SOFC	solid oxide fuel cell
STO	strontium titanate
t	time
T	temperature
T_{amb}	ambient air temperature
$T_{hot\ stage}$	hot stage/ furnace temperature
T_{set}	furnace set temperature
T_{TC}	thermo-couple temperature
T_{spr}	effective temperature
T_{YSZ}	YSZ temperature at the counter electrode

TEC	thermal expansion coefficient
TEM	transmission electron microscopy
ToF-SIMS	time-of-flight secondary ion mass spectrometry
XRD	X-ray diffraction
XRR	X-ray reflection
Y	admittance
Y_0	pre-exponential factor of Y
YSZ	yttria stabilized zirconia
Z	impedance
Z_{im}	imaginary part of the impedance
Z_{re}	real part of the impedance
3PB	triple phase boundary
δ	width of the grain boundary
ε	surface emissivity
ε_r	relative static permittivity
ε_0	vacuum permittivity
Φ	electrical potential/ phase angle (Bode plot)
ρ	density
σ_{ion}	ionic conductivity
σ^*	pre-exponential factor of σ_{ion}
σ_0	YSZ conductivity
ω	angular frequency

10.   References

[1]   IEA, *WORLD ENERGY INVESTMENT OUTLOOK* (2014).

[2]   IEA, *WORLD ENERGY OUTLOOK* (2013).

[3]   ipcc, *Climate Change 2014: Impacts, Adaptation, and Vulnerability* (2014).

[4]   A.B. Stambouli, E. Traversa, *Renewable and Sustainable Energy Reviews* **6** (2002) (5) 433.

[5]   N.H. Behling, *Fuel Cells: Current Technology Challenges and Future Research Needs*, Elsevier (2013).

[6]   S. Jiang, *J Mater Sci* **43** (2008) (21) 6799.

[7]   N.Q. Minh, *Journal of the American Ceramic Society* **76** (1993) (3) 563.

[8]   R.M. Ormerod, *Chemical Society Reviews* **32** (2003) (1) 17.

[9]   M. Kubicek, *Dissertation* (2013).

[10]   S.B. Adler, *Chemical Reviews* **104** (2004) (10) 4791.

[11]   S. Jiang, S. Chan, *J Mater Sci* **39** (2004) (14) 4405.

[12]   E. Ivers-Tiffée, A. Weber, D. Herbstritt, *Journal of the European Ceramic Society* **21** (2001) (10–11) 1805.

[13]   S.P.S. Badwal, K. Foger, Materials for solid oxide fuel cells, *Materials Forum* (1997), p.187-224.

[14]   I. Yasuda, K. Ogasawara, M. Hishinuma, T. Kawada, M. Dokiya, *Solid State Ionics* **86–88, Part 2** (1996) (0) 1197.

[15]   J.H. Kuo, H.U. Anderson, D.M. Sparlin, *Journal of Solid State Chemistry* **87** (1990) (1) 55.

[16]   S. Otoshi, H. Sasaki, H. Ohnishi, M. Hase, K. Ishimaru, M. Ippommatsu, T. Higuchi, M. Miyayama, H. Yanagida, *Journal of the Electrochemical Society* **138** (1991) (5) 1519.

[17]   A. Berenov, H. Wood, A. Atkinson, *ECS Transactions* **7** (2007) (1) 1173.

[18]   S. Kuharuangrong, T. Dechakupt, P. Aungkavattana, *Materials Letters* **58** (2004) (12–13) 1964.

[19]   H.U. Anderson, *Solid State Ionics* **52** (1992) (1–3) 33.

[20]   T. Ioroi, T. Hara, Y. Uchimoto, Z. Ogumi, Z.i. Takehara, *Journal of the Electrochemical Society* **144** (1997) (4) 1362.

[21]   A. Endo, M. Ihara, H. Komiyama, K. Yamada, *Solid State Ionics* **86–88, Part 2** (1996) 1191.

[22]   J. Mizusaki, T. Saito, H. Tagawa, *Journal of the Electrochemical Society* **143** (1996) (10) 3065.

[23]   J. Jamnik, J. Maier, *Physical Chemistry Chemical Physics* **3** (2001) (9) 1668.

[24]   J. Mizusaki, H. Tagawa, K. Naraya, T. Sasamoto, *Solid State Ionics* **49** (1991) (0) 111.

[25]   J. Mizusaki, *Solid State Ionics* **52** (1992) (1–3) 79.

[26]   J. Mizusaki, N. Mori, H. Takai, Y. Yonemura, H. Minamiue, H. Tagawa, M. Dokiya, H. Inaba, K. Naraya, T. Sasamoto, T. Hashimoto, *Solid State Ionics* **129** (2000) (1–4) 163.

[27]   B.C. Tofield, W.R. Scott, *Journal of Solid State Chemistry* **10** (1974) (3) 183.

[28]   R.A. De Souza, J.A. Kilner, J.F. Walker, *Materials Letters* **43** (2000) (1–2) 43.

[29]   S.P. Jiang, W. Wang, *Solid State Ionics* **176** (2005) (13–14) 1185.

[30]   S.P. Jiang, Y.D. Zhen, S. Zhang, *Journal of the Electrochemical Society* **153** (2006) (8) A1511.

[31]   F.W. Poulsen, *Solid State Ionics* **129** (2000) (1–4) 145.

[32]   T.M. Huber, A.K. Opitz, M. Kubicek, J. Fleig, *Journal of the Electrochemical Society, in press*.

[33]   A.K. Opitz, M. Kubicek, S. Huber, T. Huber, G. Holzlechner, H. Hutter, J. Fleig, *Journal of Materials Research* **28** (2013) (16) 2085.

[34]   D. Bhattacharyya, R. Rengaswamy, *Industrial & Engineering Chemistry Research* **48** (2009) (13) 6068.

[35]   A. Choudhury, H. Chandra, A. Arora, *Renewable and Sustainable Energy Reviews* **20** (2013) 430.

[36]   J. Nielsen, M. Mogensen, *Solid State Ionics* **189** (2011) (1) 74.

[37]   L.C. Baqué, P.S. Jørgensen, K.V. Hansen, M. Søgaard, *ECS Transactions* **57** (2013) (1) 2027.

[38]   C. Knöfel, M. Chen, M. Mogensen, *Fuel Cells* **11** (2011) (5) 669.

[39]   Y. Jiang, S. Wang, Y. Zhang, J. Yan, W. Li, *Journal of the Electrochemical Society* **145** (1998) (2) 373.

[40]   V. Brichzin, J. Fleig, H.U. Habermeier, J. Maier, *Electrochemical and Solid-State Letters* **3** (2000) (9) 403.

[41]   S.P. Jiang, J.G. Love, *Solid State Ionics* **138** (2001) (3-4) 183.

[42]   R. Radhakrishnan, A.V. Virkar, S.C. Singhal, *Journal of the Electrochemical Society* **152** (2005) (1) A210.

[43]   G.J. La O', B. Yildiz, S. McEuen, Y. Shao-Horn, *Journal of the Electrochemical Society* **154** (2007) (4) B427.

[44]   J. Fleig, H.R. Kim, J. Jamnik, J. Maier, *Fuel Cells* **8** (2008) (5) 330.

[45]   Y. Wu, K.V. Hansen, K. Norrman, T. Jacobsen, M. Mogensen, *ECS Transactions* **57** (2013) (1) 1673.

[46]   A.-K. Huber, M. Falk, M. Rohnke, B. Luerssen, M. Amati, L. Gregoratti, D. Hesse, J. Janek, *Journal of Catalysis* **294** (2012) 79.

[47]   K.-C. Chang, B. Ingram, P. Salvador, B. Yildiz, H. You, *MRS Online Proceedings Library* **1495** (2013).

[48]   E.-C. Shin, P.-A. Ahn, H.-H. Seo, J.-M. Jo, S.-D. Kim, S.-K. Woo, J.H. Yu, J. Mizusaki, J.-S. Lee, *Solid State Ionics* **232** (2013) 80.

[49]   Y. Shirai, S.-i. Hashimoto, K. Sato, K. Yashiro, K. Amezawa, J. Mizusaki, T. Kawada, *Solid State Ionics* **256** (2014) 83.

[50]   K. Shinoda, S. Suzuki, K. Yashiro, J. Mizusaki, T. Uruga, H. Tanida, H. Toyokawa, Y. Terada, M. Takagaki, *Surface and Interface Analysis* **42** (2010) (10-11) 1650.

[51]   J. Malzbender, P. Batfalsky, R. Vaßen, V. Shemet, F. Tietz, *Journal of Power Sources* **201** (2012) 196.

[52]   L.G.J. De Haart, A. Neumann, N.H. Menzler, I.C. Vinke, *ECS Transactions* **35** (2011) (1) 2027.

[53]   L. Blum, L.G.J. de Haart, J. Malzbender, N.H. Menzler, J. Remmel, R. Steinberger-Wilckens, *Journal of Power Sources* **241** (2013) 477.

[54]   M. Kornely, N.H. Menzler, A. Weber, E. Ivers-Tiffée, *Fuel Cells* **13** (2013) (4) 506.

[55]   Q. Liu, S. Bhattacharya, L. Helmick, S.P. Donegan, A.D. Rollett, G.S. Rohrer, P.A. Salvador, *Journal of the American Ceramic Society* **97** (2014) (8) 2623.

[56]   S.J. Dillon, L. Helmick, H.M. Miller, L. Wilson, R. Gemman, R.V. Petrova, K. Barmak, G.S. Rohrer, P.A. Salvador, *Journal of the American Ceramic Society* **94** (2011) (11) 4045.

[57]   R. Chao, R. Munprom, R. Petrova, K. Gerdes, J.R. Kitchin, P.A. Salvador, *Journal of the American Ceramic Society* **95** (2012) (7) 2339.

[58]   A.K. Opitz, A. Lutz, M. Kubicek, F. Kubel, H. Hutter, J. Fleig, *Electrochimica Acta* **56** (2011) (27) 9727.

[59]   H.-T. Chen, P. Raghunath, M.C. Lin, *Langmuir* **27** (2011) (11) 6787.

[60]   L. Yan, B. Kavaipatti, K.-C. Chang, H. You, P. Salvador, *ECS Transactions* **35** (2011) (1) 2063.

[61]   S. Pakalapati, K. Gerdes, H. Finklea, M. Gong, X. Liu, I. Celik, *Solid State Ionics* **258** (2014) 45.

[62]   E. Siebert, A. Hammouche, M. Kleitz, *Electrochimica Acta* **40** (1995) (11) 1741.

[63]   M.E. Lynch, D. Ding, W.M. Harris, J.J. Lombardo, G.J. Nelson, W.K.S. Chiu, M. Liu, *Nano Energy* **2** (2013) (1) 105.

[64]   S. Fearn, J.C.H. Rossiny, J.A. Kilner, J.R.G. Evans, *Solid State Ionics* **211** (2012) 51.

[65]   J. Fleig, F.S. Baumann, V. Brichzin, H.R. Kim, J. Jamnik, G. Cristiani, H.U. Habermeier, J. Maier, *Fuel Cells* **6** (2006) (3-4) 284.

[66]   V. Brichzin, J. Fleig, H.U. Habermeier, G. Cristiani, J. Maier, *Solid State Ionics* **152–153** (2002) 499.

[67]   G.J. La O', R.F. Savinell, Y. Shao-Horn, *Journal of the Electrochemical Society* **156** (2009) (6) B771.

[68]   T. Horita, K. Yamaji, M. Ishikawa, N. Sakai, H. Yokokawa, T. Kawada, T. Kato, *Journal of the Electrochemical Society* **145** (1998) (9) 3196.

[69]   T. Horita, K. Yamaji, N. Sakai, H. Yokokawa, T. Kawada, T. Kato, *Solid State Ionics* **127** (2000) (1-2) 55.

[70]   T.M. Huber, A.K. Opitz, M. Kubicek, J. Fleig, *Solid State Ionics* **268, Part A** (2014) (82-93) 82.

[71]   E. Navickas, T.M. Huber, W. Hetaba, Y. Chen, B. Yildiz, H. Hutter, J. Fleig, *Phys. Chem. Chem. Phys, accepted*.

[72]   F.S. Baumann, J. Maier, J. Fleig, *Solid State Ionics* **179** (2008) (21-26) 1198.

[73]   J. Fleig, *Solid State Ionics* **150** (2002) (1–2) 181.

[74]   J. Fleig, *Advances in Electrochemical Science and Engineering, Volume 8*, Wiley-VCH (2003), p.1-87.

[75]   F.S. Baumann, J. Fleig, H.U. Habermeier, J. Maier, *Solid State Ionics* **177** (2006) (35–36) 3187.

[76]   J. Mizusaki, K. Amano, S. Yamauchi, K. Fueki, *Solid State Ionics* **22** (1987) (4) 313.

[77]   J. Mizusaki, K. Amano, S. Yamauchi, K. Fueki, *Solid State Ionics* **22** (1987) (4) 323.

[78]   J. Fleig, *Zeitschrift für Physikalische Chemie* **221** (2007) (9-10) 1149.

[79]   J. Fleig, *Journal of Power Sources* **105** (2002) (2) 228.

[80]   A. Wedig, M.E. Lynch, R. Merkle, J. Maier, M. Liu, *ECS Transactions* **45** (2012) (1) 213.

[81]   F. Tietz, I. Arul Raj, M. Zahid, D. Stöver, *Solid State Ionics* **177** (2006) (19–25) 1753.

[82]   M.P. Hörlein, A.K. Opitz, J. Fleig, *Solid State Ionics* **247–248** (2013) 56.

[83]   A.K. Opitz, J. Fleig, *Solid State Ionics* **181** (2010) (15–16) 684.

[84]   M.G.H.M. Hendriks, J.E. Ten Elshof, H.J.M. Bouwmeester, H. Verweij, *Solid State Ionics* **146** (2002) (3-4) 211.

[85]   A. Jaccoud, C. Falgairette, G. Fóti, C. Comninellis, *Electrochimica Acta* **52** (2007) (28) 7927.

[86]   R. Baker, J. Guindet, M. Kleitz, *Journal of the Electrochemical Society* **144** (1997) (7) 2427.

[87]   M.G.H.M. Hendriks, J.E. ten Elshof, H.J.M. Bouwmeester, H. Verweij, *Solid State Ionics* **154–155** (2002) (0) 467.

[88]   F.S. Baumann, J. Fleig, H.-U. Habermeier, J. Maier, *Solid State Ionics* **177** (2006) (11–12) 1071.

[89]   C. Falgairette, G. Fóti, *Catalysis Today* **146** (2009) (3–4) 274.

[90]   E. Mutoro, B. Luerßen, S. Günther, J. Janek, *Solid State Ionics* **180** (2009) (17–19) 1019.

[91]   M.W. Breiter, K. Leeb, G. Fafilek, *Journal of Electroanalytical Chemistry* **434** (1997) (1-2) 129.

[92]   M.G.H.M. Hendriks, J.E. ten Elshof, H.J.M. Bouwmeester, H. Verweij, *Solid State Ionics* **146** (2002) (3–4) 211.

[93]   S.P. Jiang, *Solid State Ionics* **146** (2002) (1–2) 1.

[94]   F.S. Baumann, J. Fleig, H.U. Habermeier, J. Maier, *Solid State Ionics* **177** (2006) (11-12) 1071.

[95]   G. Holzlechner, M. Kubicek, H. Hutter, J. Fleig, *Journal of Analytical Atomic Spectrometry* **28** (2013) (7) 1080.

[96]   M. Kubicek, G. Holzlechner, A.K. Opitz, S. Larisegger, H. Hutter, J. Fleig, *Applied Surface Science* **289** (2014) (0) 407.

[97]   T. Kawada, K. Masuda, J. Suzuki, A. Kaimai, K. Kawamura, Y. Nigara, J. Mizusaki, H. Yugami, H. Arashi, N. Sakai, H. Yokokawa, *Solid State Ionics* **121** (1999) (1–4) 271.

[98]   J. Kilner, S. Skinner, H. Brongersma, *Journal of Solid State Electrochemistry* **15** (2011) (5) 861.

[99]   B. Rüger, J. Joos, A. Weber, T. Carraro, E. Ivers-Tiffée, *ECS Transactions* **25** (2009) (2) 1211.

[100]   J.R. Wilson, W. Kobsiriphat, R. Mendoza, H.-Y. Chen, J.M. Hiller, D.J. Miller, K. Thornton, P.W. Voorhees, S.B. Adler, S.A. Barnett, *Nature Materials* **5** (2006) (7) 541.

[101]   J.R. Wilson, A.T. Duong, M. Gameiro, H.-Y. Chen, K. Thornton, D.R. Mumm, S.A. Barnett, *Electrochemistry Communications* **11** (2009) (5) 1052.

[102]   P.R. Shearing, J. Golbert, R.J. Chater, N.P. Brandon, *Chemical Engineering Science* **64** (2009) (17) 3928.

[103]   Z. Jiao, N. Shikazono, N. Kasagi, *Journal of the Electrochemical Society* **159** (2012) (3) B285.

[104]   J.R. Izzo, A.S. Joshi, K.N. Grew, W.K.S. Chiu, A. Tkachuk, S.H. Wang, W. Yun, *Journal of the Electrochemical Society* **155** (2008) (5) B504.

[105]   A. Bieberle, L.P. Meier, L.J. Gauckler, *Journal of the Electrochemical Society* **148** (2001) (6) A646.

[106]   M.V. Rao, J. Fleig, M. Zinkevich, F. Aldinger, *Solid State Ionics* **181** (2010) (25–26) 1170.

[107]   S.B. Adler, B.T. Henderson, M.A. Wilson, D.M. Taylor, R.E. Richards, *Solid State Ionics* **134** (2000) (1–2) 35.

[108]   G. Hsieh, T.O. Mason, E.J. Garboczi, L.R. Pederson, *Solid State Ionics* **96** (1997) (3–4) 153.

[109]   T. Jacobsen, L. Bay, *Electrochimica Acta* **47** (2002) (13–14) 2177.

[110]   J. Nielsen, T. Jacobsen, *Solid State Ionics* **178** (2008) (33–34) 1769.

[111]   W. Zipprich, H.D. Wiemhöfer, *Solid State Ionics* **135** (2000) (1–4) 699.

[112]   D.S. Tsvetkov, V.V. Sereda, A.Y. Zuev, *Solid State Ionics* **192** (2011) (1) 215.

[113]   G.J. La O', Y. Shao-Horn, *Journal of the Electrochemical Society* **156** (2009) (7) B816.

[114] L. Wang, R. Merkle, J. Maier, *Journal of the Electrochemical Society* **157** (2010) (12) B1802.

[115] W. Jung, H.L. Tuller, *Journal of the Electrochemical Society* **155** (2008) (11) B1194.

[116] L. Wang, R. Merkle, G. Cristiani, B. Stuhlhofer, H.-U. Habermeier, J. Maier, *ECS Transactions* **13** (2008) (26) 85.

[117] S. Rodewald, J. Fleig, J. Maier, *Journal of the American Ceramic Society* **84** (2001) (3) 521.

[118] G.J. La O, B. Yildiz, S. McEuen, Y. Shao-Horn, *Journal of the Electrochemical Society* **154** (2007) (4) B427.

[119] J. Nielsen, T. Jacobsen, *Solid State Ionics* **178** (2007) (13–14) 1001.

[120] T. Ryll, J.L.M. Rupp, A. Bieberle-Hutter, H. Galinski, L.J. Gauckler, *Scripta Materialia* **65** (2011) (2) 84.

[121] J. Fleig, H.L. Tuller, J. Maier, *Solid State Ionics* **174** (2004) (1–4) 261.

[122] J. Fleig, J. Maier, *Solid State Ionics* **85** (1996) (1–4) 17.

[123] F.P. Incropera and D.P. DeWitt, *Fundamentals of Heat and Mass Transfer, fifth ed., John Wiley & Sons* (2002).

[124] A.K. Opitz, A. Schintlmeister, H. Hutter, J. Fleig, *Physical Chemistry Chemical Physics* **12** (2010) (39) 12734.

[125] E.O. Ahlgren, F.W. Poulsen, *Solid State Ionics* **82** (1995) (3–4) 193.

[126] E. Ahlgren, F. Willy Poulsen, *Solid State Ionics* **70–71, Part 1** (1994) 528.

[127] T.M. Huber, A.K. Opitz, J. Fleig, *Solid State Ionics, in press*.

[128] S.M. Haile, *Acta Materialia* **51** (2003) (19) 5981.

[129] M. Juhl, S. Primdahl, C. Manon, M. Mogensen, *Journal of Power Sources* **61** (1996) (1) 173.

[130] Q. Su, D. Yoon, Z. Sisman, F. Khatkhatay, Q. Jia, A. Manthiram, H. Wang, *International Journal of Hydrogen Energy* **38** (2013) (36) 16320.

[131] J. Fleig, *Annual Review of Materials Research* **33** (2003) (1) 361.

[132] P. Plonczak, D.R. Sørensen, M. Søgaard, V. Esposito, P.V. Hendriksen, *Solid State Ionics* **217** (2012) 54.

[133] T.P. Holme, C. Lee, F.B. Prinz, *Solid State Ionics* **179** (2008) (27) 1540.

[134] W. Lee, Z. Cai, B. Yildiz, *ECS Transactions* (2012), p.405-412.

[135] M.J. Jørgensen, P. Holtappels, C. Appel, *Journal of Applied Electrochemistry* **30** (2000) (4) 411.

[136] L. Yan, P.A. Salvador, *ACS Applied Materials & Interfaces* **4** (2012) (5) 2541.

[137] K. Katsiev, B. Yildiz, K. Balasubramaniam, P.A. Salvador, *Applied Physics Letters* **95** (2009) (9) 092106.

[138] K. Khabibulakh, B. Yildiz, B. Kavaipatti, P. Salvador, *ECS Transactions* **25** (2009) (2) 2309.

[139] J. Fleig, A. Schintlmeister, A.K. Opitz, H. Hutter, *Scripta Materialia* **65** (2011) (2) 78.

[140] H. Kishimoto, N. Sakai, K. Yamaji, T. Horita, M.E. Brito, H. Yokokawa, K. Amezawa, Y. Uchimoto, *Solid State Ionics* **179** (2008) (27) 1343.

[141] M. Kubicek, Z. Cai, W. Ma, B. Yildiz, H. Hutter, J. Fleig, *ACS Nano* **7** (2013) (4) 3276.

[142] O. Lebedev, G. Van Tendeloo, S. Amelinckx, *International Journal of Inorganic Materials* **3** (2001) (8) 1331.

[143] Y. Takamura, R. Chopdekar, E. Arenholz, Y. Suzuki, *Applied Physics Letters* **92** (2008) (16) 162504.

[144] C. Nivot, C. Legros, B. Lesage, M. Kilo, C. Argirusis, *Solid State Ionics* **180** (2009) (17) 1040.

[145]   A. Le Claire, *British Journal of Applied Physics* **14** (1963) (6) 351.

[146]   H. Jalili, J.W. Han, Y. Kuru, Z. Cai, B. Yildiz, *The Journal of Physical Chemistry Letters* **2** (2011) (7) 801.

[147]   R.A. De Souza, J.A. Kilner, *Solid State Ionics* **106** (1998) (3–4) 175.

[148]   T. Kawada, T. Horita, N. Sakai, H. Yokokawa, M. Dokiya, J. Mizusaki, *Solid State Ionics* **131** (2000) (1–2) 199.

[149]   N. Sakai, K. Yamaji, T. Horita, H. Kishimoto, M.E. Brito, H. Yokokawa, Y. Uchimoto, *Applied Surface Science* **252** (2006) (19) 7045.

[150]   F. Dong, A. Suda, T. Tanabe, Y. Nagai, H. Sobukawa, H. Shinjoh, M. Sugiura, C. Descorme, D. Duprez, *Catalysis Today* **90** (2004) (3–4) 223.

[151]   S. Bedrane, C. Descorme, D. Duprez, *Applied Catalysis A: General* **289** (2005) (1) 90.

[152]   B.A. Boukamp, B.A. van Hassel, I.C. Vinke, K.J. De Vries, A.J. Burggraaf, *Electrochimica Acta* **38** (1993) (14) 1817.

[153]   H.J.M. Bouwmeester, C. Song, J. Zhu, J. Yi, M. van Sint Annaland, B.A. Boukamp, *Physical Chemistry Chemical Physics* **11** (2009) (42) 9640.

[154]   X. Chen, S. Chan, K. Khor, *Electrochemical and Solid-State Letters* **7** (2004) (6) A144.

[155]   X.J. Chen, S.H. Chan, K.A. Khor, *Solid State Ionics* **164** (2003) (1–2) 17.

[156]   J. Maier, *Festkörper-Fehler und Funktion: Prinzipien der physikalischen Festkörperchemie*, Vieweg+ Teubner Verlag (2000).

[157]   P.S. Manning, J.D. Sirman, R.A. De Souza, J.A. Kilner, *Solid State Ionics* **100** (1997) (1–2) 1.

[158]   T. Kawada, J. Suzuki, M. Sase, A. Kaimai, K. Yashiro, Y. Nigara, J. Mizusaki, K. Kawamura, H. Yugami, *Journal of the Electrochemical Society* **149** (2002) (7) E252.

[159]   C. Wagner, *Proc. Int. Comm. Electrochem. Thermodyn. Kinetics (CITCE)* **7** (1957) 361.

[160]   J. Crank, *Oxford, 2nd edn, 1979.*

[161]   N. Docquier, S. Candel, *Progress in Energy and Combustion Science* **28** (2002) (2) 107.

[162]   T.R. Dargaville, B.L. Farrugia, J.A. Broadbent, S. Pace, Z. Upton, N.H. Voelcker, *Biosensors and Bioelectronics* **41** (2013) (0) 30.

[163]   Z.Y. Can, H. Narita, J. Mizusaki, H. Tagawa, *Solid State Ionics* **79** (1995) (0) 344.

[164]   J.L. Hertz, H.L. Tuller, *Journal of the Electrochemical Society* **154** (2007) (4) B413.

[165]   K. Kerman, B.-K. Lai, S. Ramanathan, *Journal of Power Sources* **196** (2011) (5) 2608.

[166]   S.J. Litzelman, J.L. Hertz, W. Jung, H.L. Tuller, *Fuel Cells* **8** (2008) (5) 294.

[167]   J.H. Shim, C.-C. Chao, H. Huang, F.B. Prinz, *Chemistry of Materials* **19** (2007) (15) 3850.

[168]   X. Jiang, H. Huang, F.B. Prinz, S.F. Bent, *Chemistry of Materials* **20** (2008) (12) 3897.

[169]   E. Mutoro, S. Günther, B. Luerßen, I. Valov, J. Janek, *Solid State Ionics* **179** (2008) (33–34) 1835.

[170]   B. Luerßen, E. Mutoro, H. Fischer, S. Günther, R. Imbihl, J. Janek, *Angewandte Chemie International Edition* **45** (2006) (9) 1473.

[171]   G. Beck, H. Fischer, E. Mutoro, V. Srot, K. Petrikowski, E. Tchernychova, M. Wuttig, M. Rühle, B. Luerßen, J. Janek, *Solid State Ionics* **178** (2007) (5–6) 327.

[172]   E. Mutoro, B. Luerssen, S. Günther, J. Janek, *Solid State Ionics* **179** (2008) (21–26) 1214.

[173]   H. Pöpke, E. Mutoro, B. Luerßen, J. Janek, *Solid State Ionics* **189** (2011) (1) 56.

[174]   L.R. Velho, R.W. Bartlett, *MT* **3** (1972) (1) 65.

[175]   R. Stumpf, C.-L. Liu, C. Tracy, *Applied Physics Letters* **75** (1999) (10) 1389.

[176]   T. Ryll, H. Galinski, L. Schlagenhauf, P. Elser, J.L.M. Rupp, A. Bieberle-Hutter, L.J. Gauckler, *Advanced Functional Materials* **21** (2011) (3) 565.

[177]   J.L. Hertz, H.L. Tuller, *Solid State Ionics* **178** (2007) (13–14) 915.

[178]   S. Kogler, *Dissertation, Vienna University of Technology* (2014).

[179]   T.M. Huber, *Master-Thesis, Vienna University of Technology* (2011).

11.   Curriculum Vitae

Tobias Martin Huber
Ph.D. Candidate Electrochemistry
Rottmayrgasse 17/29, 1120 Vienna Austria,
Citizenship: Austria, Date of birth: 15.12.1983

EDUCATION

2011-2014 Vienna University of Technology:

- Ph.D. Candidate at Institute of Chemical Technologies and Analytics, Laboratory of Solid State Ionics and Electrochemistry.

2004-2011 Vienna University of Technology:

- M.S. Physics, Energy and Measurement Technics, passed with distinction.

2008-2009 Uppsala University (Sweden):

- Erasmus stay and project work at Institute of Material Physics Uppsala.

1998-2003 Höhere technische Lehranstalt Hallein /HTL (Federal Secondary College of Engineering Hallein):

- Education in industrial engineering and management specialized in manufacturing computer science, passed with distinction.

RESEARCH EXPERIENCE

Doctoral Research Vienna University of Technology:

- Project to visualize different oxygen reduction reaction pathways of LSM electrodes on YSZ and to show how these processes can be modified, blocked or accelerated. This project included optimizing of electrode preparation, impedance spectroscopy measurements, ^{18}O tracer investigations, finite element simulations and extensive measurement equipment optimization.

Undergraduate Research Vienna University of Technology:

- Platinum and nickel microelectrodes on YSZ were electrochemically analyzed in H_2 via impedance spectroscopy in hydrogen atmosphere. Platinum electrodes were shown to have the rate determining step at the three phase boundary similar to oxygen atmosphere.

Undergraduate Research Sweden Uppsala University

- Hydrogen uptake and release was studied via optical and resistive property changes of 10 nm thin vanadium films to establish a cheap method for hydrogen content measurements and plotting metal-hydride phase diagrams.

PRESENTATIONS

- T. M. Huber, A. K. Opitz, M. Kubicek, A. Welzl, G. Holzlechner, E. Navickas, Y. Chen, B. Yildiz, J. Fleig: "Identifying, Quantifying and Modifying Reaction Pathways of Oxygen Reduction on Lanthanum Manganite (LSM) Model Electrodes"; Oral presentation: E-MRS Spring Meeting 2014, Lille France 2014; 27.5.2014 - 29.5.2014.
- T. M. Huber, A. K. Opitz, M. Kubicek, A. Welzl, G. Holzlechner, E. Navickas, Y. Chen, B. Yildiz, J. Fleig: "Identifying, Visualizing and Modifying Reaction Pathways of Oxygen Reduction on Lanthanum Manganite (LSM) Model Electrodes"; Oral presentation: MRS Spring Meeting 2014, San Francisco USA 2014; 21.4.2014 - 25.4.2014.
- T. M. Huber, M. Kubicek, A. K. Opitz, H. Hutter, J. Fleig: "Separation of Different Oxygen Reduction Paths in Lanthanum Manganite (LSM) Thin Film Model Electrodes"; Oral presentation: Solid State Ionics 19, Kyoto Japan 2013; 3.6.2013 - 7.6.2013.
- T. M. Huber, M. Kubicek, A. K. Opitz, J. Fleig: "A Novel Micro-Contact Equipment for Electrochemical Impedance Spectroscopy"; Poster: Solid State Ionics 19, Kyoto Japan 2013; 3.6.2013 - 7.6.2013.

- T. M. Huber, M. Kubicek, A. Opitz, H. Hutter, J. Fleig: "Reaction Pathways of Oxygen Reduction on Lanthanum Manganite (LSM) Model Electrodes"; Poster: E-MRS Spring Meeting 2012, Strasbourg France; 14.05.2012 - 18.05.2012.

- T. M. Huber, M. Kubicek, A. Opitz, J. Fleig: "New micro-contact equipment for Impedance spectroscopy and first results for Reaction Pathways of Oxygen Reduction on Lanthanum Manganite (LSM) Model Electrodes"; Oral presentation: Topical Issues of Rational Use of Natural Resources, St. Petersburg Russia; 25.04.2012 - 27.04.2012.

- T. M. Huber, M. Dünser, G Pálsson, H. Björgvin: "STORM - Simultaneous optical transmission and resistance measurements"; Oral presentation: Nordic Hydrogen Meeting, St. Petersburg Russia; 14.05.2009 - 16.05.2009.

PUBLICATIONS

- T. M. Huber, M. Kubicek, A. K. Opitz, J. Fleig: "Temperature gradients in microelectrode measurements: Relevance and solutions for studies of SOFC electrode materials" Solid State Ionics 268 (2014): 82-93.

- T. M. Huber, A. K. Opitz, M. Kubicek, J. Fleig: „ The Relevance of Different Oxygen Reduction Pathways of $La_{0.8}Sr_{0.2}MnO_3$ (LSM) Thin Film Model Electrodes." Journal of The Electrochemical Society, in press.

- T. M. Huber, A. K. Opitz, J. Fleig: "Oxygen reduction via grain boundary related bulk path at low temperature in thin film platinum model microelectrodes" Solid State Ionics, in press.

- M. Kubicek, A. Welzl, T. M. Huber, J. Fleig: "Electrochemical Properties of $La_{0.6}Sr_{0.4}CoO_{3-\delta}$ Thin Films Investigated by Complementary Impedance Spectroscopy and Isotope Exchange Depth Profiling" Journal of Solid State Ionics 256 (2014): 38-44.

- A. Opitz, M. Hörlein, T. M. Huber, J. Fleig: "Current-Voltage Characteristics of Platinum Model Electrodes on Yttria-Stabilized Zirconia"; Journal of the Electrochemical Society 159.5 (2012): B502-B513.

- A.K. Opitz, M. Kubicek, S. Huber, T. Huber, G. Holzlechner, H. Hutter, J. Fleig: „Thin film cathodes in SOFC research: How to identify oxygen reduction pathways?" Journal of Materials Research 28.16 (2013): 2085-2105.
- A. Nenning, A. K. Opitz, T. M. Huber, J. Fleig: "A novel approach for analyzing electrochemical properties of mixed conducting solid oxide fuel cell anode materials by impedance spectroscopy" Phys. Chem. Chem. Phys. 16.40 (2014): 22321-22336.

MANUSCRIPTS SUBMITTED

- E. Navickas *, T. M. Huber *, Y. Chen, W. Hetaba, G. Holzlechner, G. Rupp, G. Friedbacher, H. Hutter, B. Yildiz, J. Fleig (* Authors with equal contribution): "Oxygen exchange and diffusion kinetics of grains and grain boundaries in $La_{0.8}Sr_{0.2}MnO_3$-δ thin films" Phys. Chem. Chem. Phys. accepted.

MANUSCRIPTS IN PREPERATION

- T. M. Huber, E. Navickas, G. Friedbacher, H. Hutter, J. Fleig: working title: "Oxygen exchange and diffusion in polarized $La_{0.8}Sr_{0.2}MnO_3$ thin films".

MEMBERSHIPS AND GRANTS

- 2014 European Material Research Society Young Scientist Award 2014

- 2013-2014 Member of WINA+ a support program for young scientists.

- 2012-2014 Member of Solids4Fun Doctoral School of Vienna University of Technology.

- 2011 "Förderstipendium der Technischen Chemie" Grant of Chemistry Department.

12.   Acknowledgements